ASME
SETTING THE STANDARD
1880 2005

Transactions of the ASME, Journal of Heat Transfer (ISSN 0022-1481) is published monthly by The American Society of Mechanical Engineers, Three Park Avenue, New York, NY 10016. Periodicals postage paid at New York, NY and additional mailing offices. POSTMASTER: Send address changes to Transactions of the ASME, Journal of Heat Transfer, c/o THE AMERICAN SOCIETY OF MECHANICAL ENGINEERS, 22 Law Drive, Box 2300, Fairfield, NJ 07007-2300. **CHANGES OF ADDRESS** must be received at Society headquarters seven weeks before they are to be effective. Please send old label and new address. **STATEMENT from By-Laws.** The Society shall not be responsible for statements or opinions advanced in papers or ... printed in its publications (B7.1, Para. 3).

Journal of Heat Transfer

Published Monthly by ASME

VOLUME 128 • NUMBER 1 • JANUARY 2006

MAX JAKOB AWARD PAPER

RESEARCH PAPERS

Evaporation, Boiling, and Condensation

Forced Convection

Micro/Nanoscale Heat Transfer

TECHNICAL BRIEFS

(**Contents continued on inside back cover**)

This journal is printed on acid-free paper, which exceeds the ANSI Z39.48-1992 specification for permanence of paper and library materials. ♾™
♻ 85% recycled content, including 10% post-consumer fibers.

Journal of Heat Transfer **Volume 128, Number 1** **JANUARY 2006**

The ASME Journal of Heat Transfer is abstracted and indexed in the following:

Applied Science and Technology Index, Chemical Abstracts, Chemical Engineering and Biotechnology Abstracts (Electronic equivalent of Process and Chemical Engineering), Civil Engineering Abstracts, Compendex (The electronic equivalent of Engineering Index), Corrosion Abstracts, Current Contents, E & P Health, Safety, and Environment, Ei EncompassLit, Engineered Materials Abstracts, Engineering Index, Enviroline (The electronic equivalent of Environment Abstracts), Environment Abstracts, Environmental Engineering Abstracts, Environmental Science and Pollution Management, Fluidex, Fuel and Energy Abstracts, Index to Scientific Reviews, INSPEC, International Building Services Abstracts, Mechanical & Transportation Engineering Abstracts, Mechanical Engineering Abstracts, METADEX (The electronic equivalent of Metals Abstracts and Alloys Index), Petroleum Abstracts, Process and Chemical Engineering, Referativnyi Zhurnal, Science Citation Index, SciSearch (The electronic equivalent of Science Citation Index), Theoretical Chemical Engineering

Max Jakob Award Paper

Mechanistic Prediction of Nucleate Boiling Heat Transfer–Achievable or a Hopeless Task?

Vijay K. Dhir
Henry Samueli School of Engineering
and Applied Science,
University of California,
Los Angeles, 420 Westwood Plaza,
Los Angeles, CA 90095-1597
e-mail: vdhir@seas.ucla.edu

Over the last half of the twentieth century, a number of purely empirical and mechanism-based correlations have been developed for pool nucleate boiling. Empirical correlations differ from each other substantially with respect to the functional dependence of heat flux on fluid and surface properties, including gravity. The mechanism-based correlations require knowledge of the number density of active sites, bubble diameter at departure, and bubble-release frequency. However, because of the complex nature of the subprocesses involved, it has not been possible to develop comprehensive models or correlations for these parameters. This, in turn, has led to the pessimistic view that mechanistic prediction of nucleate boiling is a hopeless task. However, there is an alternative to the past approaches—complete numerical simulation of the boiling process. Value of this approach for bubble dynamics and associated heat transfer is shown through excellent agreement of predictions with data obtained on microfabricated surfaces on which active nucleation sites can be controlled. [DOI: 10.1115/1.2136366]

1 Introduction

Numerous studies of different modes of boiling have been reported in the literature during the last half of the twentieth century. Of the three modes of boiling—film, nucleate, and transition boiling—film boiling is most amenable to analysis. Nucleate and transition boiling are most complex, and invariably empirical correlations or correlations having a mechanistic basis have been proposed. The correlations serve a useful purpose in their application to engineered systems. However, because of their limited range of applicability, they can rarely be applied with confidence to new situations. In addition, many of these correlations for the global process, are rarely consistent at the subprocess level. Mechanistic models based on basic principles can alleviate this problem. For this purpose, effort has continued to be made by researchers to develop mechanistic models. In this work, we first review the past work on nucleate boiling heat transfer and thereafter provide results from a new approach that is based on direct numerical simulation of the process.

2 Past Studies

Past studies of nucleate boiling have resulted in either empirical correlations for the dependence of wall heat flux on wall superheat and other fluid and solid surface properties or correlations that are based on modeling of the underlying subphenomena.

2.1 Empirical Correlations. The earliest correlation for pool nucleate boiling is that due to Rohsenow [1]. In developing the correlation, Rohsenow reduced the phase-change problem to a single-phase forced convection problem. He proposed that heat from the wall was removed by liquid motion induced by vapor bubbles rising in the liquid pool. Thus, he related the Nusselt number to Reynolds and Pandtl numbers, with the characteristic length being the diameter of the departing bubble. As such, he correlated the data as

$$\frac{\mathrm{Re}_b \mathrm{Pr}_l}{\mathrm{Nu}_b} = C_s \mathrm{Re}_b^m \mathrm{Pr}_l^n \tag{1}$$

or

$$\frac{c_{pl}\Delta T_w}{h_{fg}} = C_s \left[\frac{q\sqrt{\dfrac{\sigma}{g(\rho_l-\rho_v)}}}{\mu_l h_{fg}} \right]^{1/3} \mathrm{Pr}_l^{1 \text{ or } 1.7} \tag{2}$$

The exponents m and n were found empirically. It was also found that a value of $1/3$ for m would fit the data well. The exponent n was given a value of 1 for water and 1.7 for all other liquids. The proportionality constant C_s depended on heater material and fluid combination, but no attempt was made to relate the value of C_s to surface conditions. Liaw and Dhir [2] have shown that C_s varies with contact angle and its value increases as the contact angle is decreased. Equation (2) can be rewritten as

$$\frac{q\sqrt{\dfrac{\sigma}{g(\rho_l-\rho_v)}}}{\mu_l h_{fg}} = C_s^{-3} \left[\frac{c_{pl}\Delta T_w}{h_{fg}} \right]^3 \mathrm{Pr}_l^{-3 \text{ or } -5.1} \tag{3}$$

Almost three decades later, Stephan and Abdelsalam [3] developed a comprehensive correlation for saturated pool nucleate boiling of different liquids. In developing the correlation, they divided the data into four liquid groups: water, hydrocarbons, cryogenic liquids, and refrigerants. The dimensionless heat flux was related to several dimensionless parameters that depended on fluid and solid properties. The important fluid property groups were identified through regression analysis, and the values of exponents of the property group were obtained by matching predictions with data. In developing the correlation, data from different heater geometrics (such as flat plates, horizontal cylinders, vertical cylin-

Contributed by the Heat Transfer Division of ASME for publication in the JOURNAL OF HEAT TRANSFER. Manuscript received August 31, 2005; final manuscript received October 10, 2005. Review conducted by Yogesh Jaluria.

ders, etc.) were used. In addition, surface roughness was assumed to be 1 μm for all heaters. They also developed a generalized correlation applicable to all liquids,

$$\frac{qD_d}{\Delta T k_l} = 0.23\left(\frac{qD_d}{k_l T_{\text{sat}}}\right)^{0.674}\left(\frac{\rho_v}{\rho_l}\right)^{0.297}\left(\frac{h_{fg}D_d^2}{\alpha_l^2}\right)^{0.371} \times\left(\frac{\rho_l-\rho_v}{\rho_l}\right)^{-1.73}\left(\frac{\alpha_l^2\rho_l}{\sigma D_d}\right)^{0.35} \tag{4}$$

where D_d is the bubble diameter at departure.

Cooper [4] has proposed a much simpler correlation for saturated pool nucleate boiling. His correlation employs reduced pressure, molecular weight, and surface roughness as the correlating parameters. The correlation for a flat plate is

$$\frac{q^{1/3}}{\Delta T_w} = 55.0\left[\left(\frac{P}{P_c}\right)^{0.12-0.21\log_{10}R_p}\right]\left(-\log_{10}\frac{P}{P_c}\right)^{-0.55} M^{-0.5} \tag{5}$$

In Eq. (5), R_p is the surface roughness measured in microns. Cooper suggested that for application of the correlation to the horizontal cylinders, the lead constant on the right-hand side should be increased to 95. Also, q is given in watts per square meters.

It should be noted that all of the correlations suggest that wall heat flux varies as ΔT_w^3. Rohsenow's correlation suggests heat flux to vary as the square root of gravity, whereas the other two correlations indicate heat flux to be virtually independent of gravity. Equation (5) accounts for surface roughness, but does not account for the variation in the degree of surface wettability. Rohsenow's correlation implicitly accounts for surface wettability through the proportionality constant C_s, whereas the generalized correlation of Stephan and Abdelsalam bounds the data for a wide range of contact angles. Similarly, while Eq. (5) accounts for heater geometry, the other two correlations are independent of heater geometry.

2.2 Mechanism-Based Correlations. In partial nucleate boiling or in the isolated bubble regime, transient conduction into liquid adjacent to the heater surface is one of the important mechanisms for heat transfer from an upward-facing horizontal surface. After bubble inception, the superheated liquid layer is pushed outward and mixes with the bulk liquid. During the growth phase, the bubble acts like a pump in removing the superheated liquid from the heater surface and replacing it with cold liquid upon departure. This mechanism was originally proposed by Forster and Greif [5]. Combining the contribution of transient conduction on and around nucleation sites, microlayer evaporation underneath the bubbles and natural convection on inactive areas of the heater, an expression for partial nucleate boiling heat flux is obtained as

$$q = \frac{K^2}{2}\sqrt{\pi(k\rho c_p)_l f}D_d^2 N_a \Delta T_w + \left(1-\frac{K^2 N_a \pi D_d^2}{4}\right)\overline{h}_{nc}\Delta T_w + \overline{h}_{ev}\Delta T N_a \frac{\pi D_d^2}{4} \tag{6}$$

Only the first two terms in Eq. (6) were included in the original model proposed by Mikic and Rohsenow [6]. The addition of the last term on the right-hand side of Eq. (6) was suggested by Judd and Hwang [7]. This term accounts for evaporative heat transfer from the microlayer underneath the bubble. For Eq. (6) to serve as a predictive tool, three key parameters, aside from constant K, accounting for the ratio of the area of influence of a bubble to the cross-sectional area of the bubble that must be known, are: number density of active sites N_a, bubble diameter at departure D_d, and bubble release frequency f. During the last four decades, a number of attempts have been made to develop correlations or models for these parameters, but with limited success.

2.2.1 Number Density of Nucleation Sites. Mikic and Rohsenow [6] have proposed that on commercial surfaces, the cumulative number of active sites per unit heater area can be assumed to vary in partial nucleate boiling as,

$$N_a = \left(\frac{D_s}{D_c}\right)^{m_1} \tag{7}$$

where D_s is the diameter of the largest cavities present on the surface and m_1 is an empirical constant. The nucleating cavity diameter D_c is related to wall superheat as

$$D_c = \frac{4\sigma T_{\text{sat}}}{\rho_v h_{fg}\Delta T_w} \tag{8}$$

Bier et al. [8], on the other hand, have deduced an expression for active site density from their heat transfer data as

$$\ln N_a = \ln N_{\max}\left[1-\left(\frac{D_c}{D_s}\right)^{m_2}\right] \tag{9}$$

where $N_{\max}$ is the maximum value of N_a, which occurs at $D_c=0$. The value of m_2 was found to depend on the manner in which the surface was prepared. Kocamustafaogullari and Ishii [9] have correlated the cumulative nucleation site density reported by various investigators for water boiling on a variety of surfaces at pressures varying from 1 to 198 bars as

$$N_a^* = [D_c^{*-4.4}F(\rho^*)]^{1/4.4} \tag{10}$$

where

$$N_a^* = N_a D_d^2; \quad D_c = D_c/D_d; \quad \rho^* = (\rho_l-\rho_v)/\rho_v \tag{11}$$

and

$$F(\rho^*) = 2.157\times 10^{-7}\rho^{*-3.2}(1+0.0049\rho^*)^{4.13} \tag{12}$$

In Eq. (11), the bubble diameter at departure D_d is obtained by using Fritz's correlation [10], and at low to moderate pressures, D_c is given by Eq. (8).

It should be noted that none of the above correlations explicitly account for surface wettability. Wang and Dhir [11] systematically studied the effect of surface wettability by using the same surface-liquid (polished copper surface and water) combination, while controlling the degree of oxidation of the surface. They found the number density of active sites for a given cavity diameter to decrease by a factor of about 25 when the contact angle was reduced from 90 to 18 deg. Subsequently, Basu et al. [12] have correlated nucleation site density data for a variety of liquids and contact angles, for both pool and flow boiling, as

$$N_a = 0.34[1-\cos\phi]\Delta T_w^2 \quad \Delta T_{w,\text{ONB}} \leqslant \Delta T_w < 15\,^\circ\text{C}$$

$$N_a = 3.4\times 10^{-5}[1-\cos\phi]\Delta T_w^{5.3} \quad \Delta T_w > 15\,^\circ\text{C} \tag{13}$$

According to their correlation, the density of active nucleation sites depends only on wall superheat and contact angle.

It is generally believed that heterogeneous nucleation on a surface occurs on defects or cavities that trap gas/vapor. Bankoff [13] was the first to propose that an advancing liquid front will trap gas in a wedge-shaped cavity provided the advancing contact angle was greater than the wedge angle. In their study, Wang and Dhir [14] found that any conical or wedge-shaped cavities on the surface were too shallow to trap any gas. They noted that cavities that trapped gas were spherical in nature. By minimizing the Helmholtz free energy for a liquid/gas/solid system, they developed a criterion for gas entrapment according to which a cavity will trap gas only if the contact angle was greater than the cavity mouth angle. A key weakness in their approach is that it excluded effect of gas diffusion into liquid. Recently, Pesse et al. [15] experimentally studied filling of rectangular microchannels closed at one end. They found that the rate of filling of the channels was dependent on surface forces and the diffusion of gas into liquid. For low

contact angles, multiple interfaces were formed in the channel. It was found that given sufficient time, the microchannels were filled with liquid for all contact angles. Thus, time for which surface remains in contact with liquid is another variable.

Despite numerous efforts, we do not yet have a model/correlation that can be used to predict a priori the number of cavities that will become active at a particular superheat for a given liquid-solid combination. There are several impediments in our ability to have a comprehensive predictive model for density of active nucleation sites. These include the degree to which the surface must be characterized with respect to the number of cavities that are present on the surface, as well as their shape and size. This can be an extremely tedious task. The degree of surface wettability greatly influences how rapidly the cavities are filled with liquid. As such, it is important to know the duration for which the surface is exposed to liquid prior to an experiment. A number of investigators have noted that thermal response of the substrate affects nucleation of cavities at neighboring sites. Judd [16] has found that for active cavities spaced between 1/2 and 1 bubble departure diameter, the formation of a bubble at the initiating site promotes the formation of bubbles at the adjacent sites (site seeding). However, for separation distance between 1 and 3 bubble departure diameters, the formation of a bubble at the initiating site inhibits the formation of bubbles at an adjacent site (deactivation of sites).

Recently, Dinh et al. [17] have claimed that the presence of cavities on the surface is not required for heterogeneous nucleation and that it is the solid surface energy that determines the propensity of nucleation.

2.2.2 Bubble Diameter at Departure. A large number of correlations and mechanistic models have been proposed in the literature for diameter to which a bubble grows before departure. Fritz [10] correlated the bubble departure diameter D_d by balancing buoyancy, which acts to lift the bubble away from the surface, with surface tension force, which tends to hold the bubble to the wall. The resulting correlation is given as

$$D_d = 0.0208\phi\sqrt{\frac{\sigma}{g(\rho_l-\rho_v)}} \tag{14}$$

where ϕ is the contact angle measured in degrees. Significant deviations with respect to prediction from the above equation have been reported in the literature, especially at high pressures. Several other expressions, either obtained analytically or by considering various forces acting on a bubble, have been reported for bubble departure diameter. These expressions, however, are not always consistent with one another with respect to dependence of bubble departure diameter on independent variables. Some investigators report an increase in bubble diameter at departure with wall superheat, whereas others find the bubble diameter at departure to be insensitive to or decrease with wall superheat. In addition, contrary to the commonly held view, the work of Cooper et al. [18] suggests that surface tension may assist bubble departure. Cole and Rohsenow [19] correlated bubble diameter at departure at low pressures as

$$D_d = 1.5\times10^{-4}\sqrt{\frac{\sigma}{g(\rho_l-\rho_v)}}\mathrm{Ja}^{*5/4} \quad \text{for water} \tag{15}$$

and

$$D_d = 4.65\times10^{-4}\sqrt{\frac{\sigma}{g(\rho_l-\rho_v)}}\mathrm{Ja}^{*5/4} \quad \text{for other liquids} \tag{16}$$

where $\mathrm{Ja}^* = \rho_l c_{pl} T_{\mathrm{sat}}/\rho_v h_{fg}$.

Kocamustafaogullari [20] has developed a correlation for bubble departure diameter that includes high-pressure data

$$D_d = 2.64\times10^{-5}\sqrt{\frac{\sigma}{g(\rho_l-\rho_v)}}\left(\frac{\rho_l-\rho_v}{\rho_v}\right)^{0.9} \tag{17}$$

Gorenflo et al. [21] have proposed an expression for bubble departure diameter at high heat fluxes as

$$D_d = C_1\left(\frac{\mathrm{Ja}^4\alpha_l^2}{g}\right)^{1/3}\left[1+\sqrt{1+\frac{2\pi}{3\mathrm{Ja}}}\right]^{4/3} \tag{18}$$

Different values of constant C_1 were used for different liquids. It should be noted that correlations of Fritz [10], Cole and Rohsenow [19], and Kocamustafaogullari [9] suggest that bubble diameter at departure varies at $g^{-1/2}$, where as according to Eq. (18), it varies as $g^{-1/3}$. In addition, the correlation of Gorenflo et al. [21] suggests thermal diffusivity of liquid as well as Jakob number to be important parameters. According to the correlation of Kocamustafaogullari [9], the liquid to vapor density ratio is another important variable.

Despite substantial efforts over a period spanning almost 70 years, we do not yet have a generalized correlation or comprehensive model for bubble departure diameter. The key impediments to these efforts have been the lack of knowledge of temperature and velocity fields that vary both temporally and spatially. The temperature and velocity fields, in turn, affect the growth rate and forces that act on the vapor bubble, respectively. The bubble shape changes continuously, hence, the magnitude of forces acting on it. Surface wettability, contribution of microlayer, and lateral and vertical merger of vapor bubbles influence the bubble departure diameter.

2.2.3 Bubble Release Frequency. Bubble release frequency is the inverse of the sum of waiting and growth periods. Both the waiting time t_w and growth period t_d are difficult to determine quantitatively. Waiting time depends on the temperature field in the solid, as well as in the liquid in the vicinity of the nucleation site. Similarly, growth period depends on the rate of evaporation at the bubble base and around the bubble and the bubble diameter at departure. Often data for bubble release frequency are correlated under the assumption of $t_w \gg t_d$ or vice versa. Correlations have also been developed for vapor superficial velocity or the product of bubble diameter at departure and frequency. Zuber's [22] expression for vapor superficial velocity is often used. According to it,

$$fD_d = 0.59\left[\frac{\sigma g(\rho_l-\rho_v)}{\rho_l^2}\right]^{1/4} \tag{19}$$

Malenkov [23] has proposed that

$$fD_d = \frac{V_d}{\pi\left(1-\dfrac{1}{1+V_d\rho_v h_{fg}/q}\right)} \tag{20}$$

where

$$V_d = \sqrt{\frac{D_d g(\rho_l-\rho_v)}{2(\rho_l+\rho_v)}+\frac{2\sigma}{D_d(\rho_l+\rho_v)}} \tag{21}$$

Predictions from these correlations are valid only for the limited range over which supporting data have been obtained. Difficulties arise in developing a model for bubble release frequency because it is tied to bubble diameter at departure and growth rate, which, in turn, are dependent on mechanisms responsible for heat transfer into and out of the bubble. Waiting and growth periods are influenced by the temperature field in the solid and/or liquid and, as such, require knowledge of the prevailing phenomena. Cavity-cavity interaction, microlayer evaporation contribution, and bubble merger also influence bubble release frequency.

At this juncture, it appears that mechanistic prediction of nucleate boiling is a hopeless task. However, before accepting this conclusion, it is imperative that we attempt an approach that is vastly

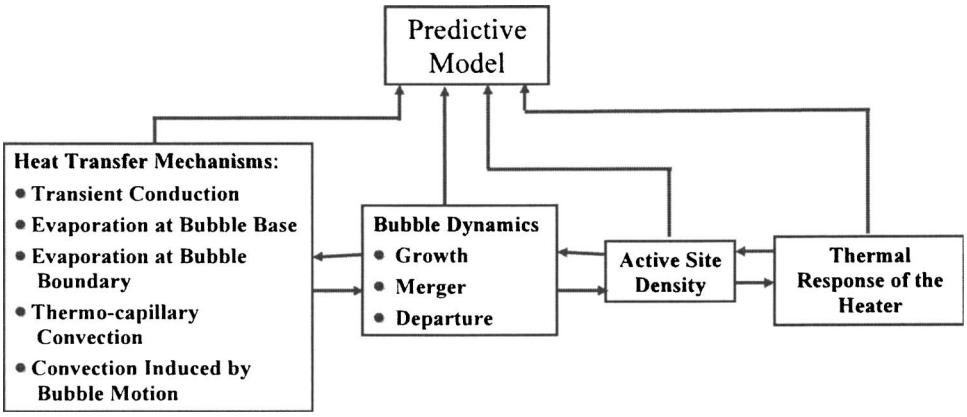

Fig. 1 Mechanistic prediction of nucleate boiling heat transfer

different from what we have employed in the past. This approach and the results obtained from this approach are discussed next.

3 Alternative Approach

In order to have a credible predictive model of nucleate boiling, one must address four subprocesses as indicated in Fig. 1 and their interactions, which tend to be nonlinear. These subprocesses are density of active nucleation sites, bubble dynamics (which includes bubble growth, merger, and departure), and several mechanisms of heat transfer, such as transient conduction into liquid replacing the space originally occupied by a departing bubble, evaporation at bubble base, and bubble boundary. Convection resulting from surface-tension gradient along the interface and that induced by density difference must be included. The convective motion can be altered by agitation created by vapor bubbles. In most experiments, power to the test surface is controlled. Because of spatial and temporal variation in heat transfer on the fluid side, wall temperature will oscillate. To determine the thermal response of the solid, one must solve a conjugate problem for heat conduction in the substrate. At present, we assume the surface temperature to remain constant. As such, the solid is thermally decoupled. In the same vein, a microfabricated surface is employed on which there is control on the cavities that become active. Thus, our focus will be mainly on bubble dynamics and associated heat transfer mechanisms. For this purpose, we rely on complete numerical simulation of the process—a tool that has been developed only recently.

In simulating the process, the region of interest is divided into micro- and macro regions (Fig. 2) as initially proposed by Son et al. [24]. The microregion is the ultrathin liquid film that forms between the solid surface and the evolving liquid-vapor interface. On the inner edge, the microlayer has a thickness of the order of a nanometer, i.e., few molecules of liquid are adsorbed on the surface and do not evaporate. As such, the region further radially inward is considered to be dry. On the outer edge, the microlayer has a thickness of the order of several microns. Heat is conducted across the film and is utilized for evaporation. Lubrication theory is used to solve for the radial variation of microlayer thickness.

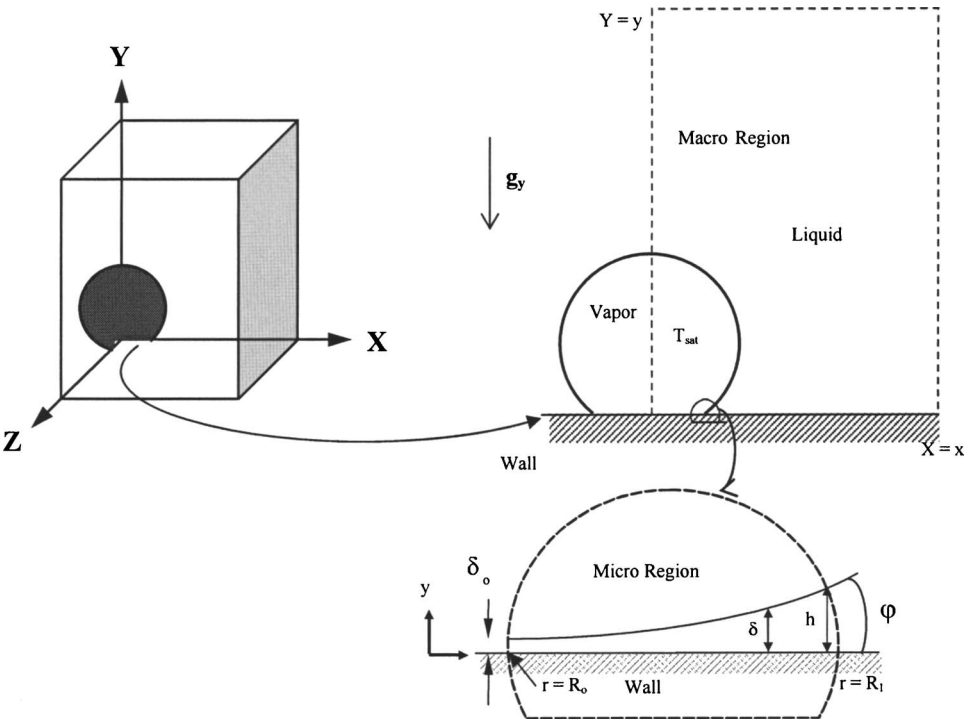

Fig. 2 Macro and micro regions of the mathematical model for numerical simulation

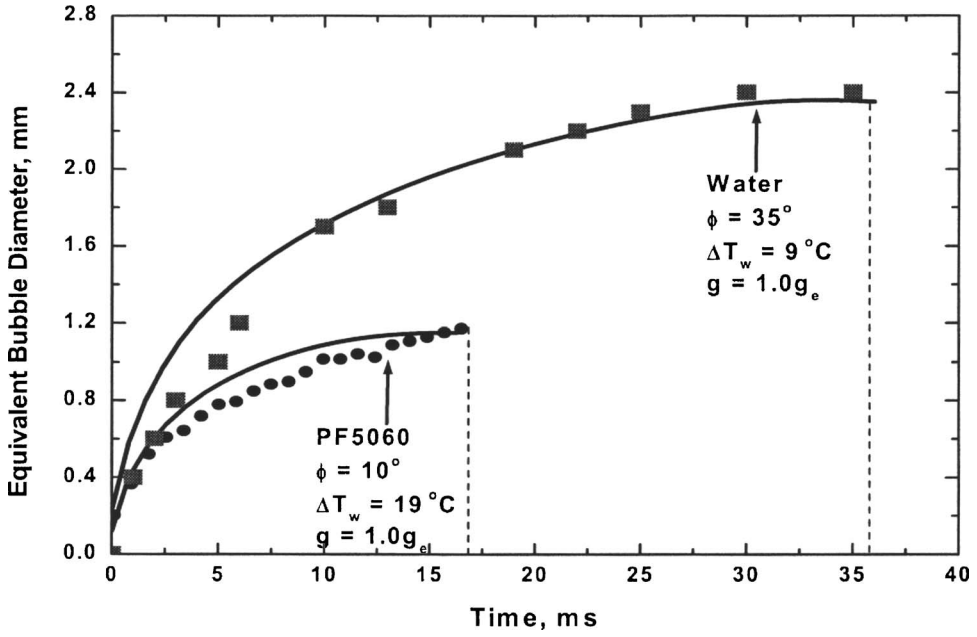

Fig. 3 Comparison of bubble departure diameter and bubble growth time for water and PF5060

The macroregion is the region occupied by vapor and liquid, except the microlayer. For the macroregion, complete conservation equations of mass, momentum, and energy are solved for both phases. Interface position is captured through a level-set function.

Governing equations for micro- and macroregions are given in Son et al. [24] and are not repeated here. In analyzing the microregion, continuum assumption is considered to hold good until the film is a few molecules thick. Long-range forces are evaluated through the Hamaker constant, which is also related to the static contact angle. Ramanujapu and Dhir [25] have shown from experiments that in pool boiling, advancing and receding contact angles are within only ±5 deg of the static contact angle. As such, the use of the static contact angle throughout the bubble evolution process is justified. Capillary pressure gradient is related to change in the curvature of the interface. Recoil pressure resulting from the momentum of vapor leaving the interface being higher than the liquid approaching the interface is included. Inertia terms are neglected in the momentum equation, and convection terms are ignored in the energy equation.

Quasi-static analysis is carried out, and a two-dimensional model for the microlayer is used even in three-dimensional (3D) situations under the assumption that no crossflow occurs in the azimuthal direction.

For the macroregion, it is assumed that fluids are incompressible, flows are laminar, and properties are evaluated at the mean temperature. Vapor is assumed to remain at saturation temperature corresponding to pressure in the bubble. As such, the energy equation is not solved in the vapor space. Finite difference scheme is used in which diffusion terms are solved implicitly, whereas explicit scheme is used for convection terms. Projection method is used to solve for pressure that conserves mass. To prevent numerical oscillations, second-order ENO scheme is adopted for advection terms when solving for the level-set function. In order to increase the rate of convergence, the multigrid method is used. The computational domain is assumed to have a width that is twice the characteristic length, $l_o=[\sigma/g(\rho_l-\rho_v)]^{1/2}$ and symmetry conditions are imposed on the bounding walls.

Numerical simulation results have been validated with experiments conducted on polished silicon wafers. On this wafer, cylindrical cavities were strategically microfabricated. The wafer is heated on the backside with several strain-gage-type heaters. By controlling power to these heaters, any of the cavities could be nucleated. Details of the experiments are given in Qiu et al. [26].

3.1 Single Bubble Dynamics. Son et al. [24] showed a good agreement between predictions from complete numerical simulations and data from experiments with respect to time-dependent vapor bubble shape, growth rate, bubble departure diameter, and growth period. The effect of increased wall superheat, consistent with the data, was to increase the growth rate and reduce the growth period, but increase the bubble diameter at departure. A higher growth rate is due to increased heat transfer at the vapor-liquid interface, whereas the diameter at departure increases because of the increased contribution of liquid inertia. With the increase in liquid subcooling [27], the bubble growth rate decreases and growth period increases, while the bubble diameter at departure decreases.

Fluid properties as well as surface wettability or contact angle are important variables that influence bubble dynamics. Bubble growth histories for water and PF-5060 with widely differing liquid properties as predicted from numerical simulations [28] are plotted in Fig. 3. In the experiments, contact angle for water on silicon was 35 deg, whereas that for PF-5060 was ~10 deg. Bubble diameter at departure and the growth period for PF-5060 are much smaller than those for water. Numerical predictions do quite well in predicting the data for the two fluids. In order to explicitly demonstrate the effect of contact angle, results of numerical simulations carried out by parametrically varying the contact angle for the two fluids are shown in Fig. 4. It was found that results for the two fluids nearly overlap when bubble diameter at departure and growth period are normalized with their corresponding values for a contact angle of 90 deg. Bubble diameter at departure is seen to decrease linearly as the contact angle is reduced up to about 20 deg. This behavior is similar to that predicted from Fritz's [10] correlation. However, for contact angles less than 20 deg when the surface becomes well wetting, the dependence of bubble departure diameter on contact angle is nonlinear. The growth period shows nonlinear behavior for all contact angles. Good agreement of predictions with data obtained using water while varying systematically the surface wettability through oxidation of silicon and with PF-5060 data is seen.

During the growth and departure cycle of a bubble, the wall

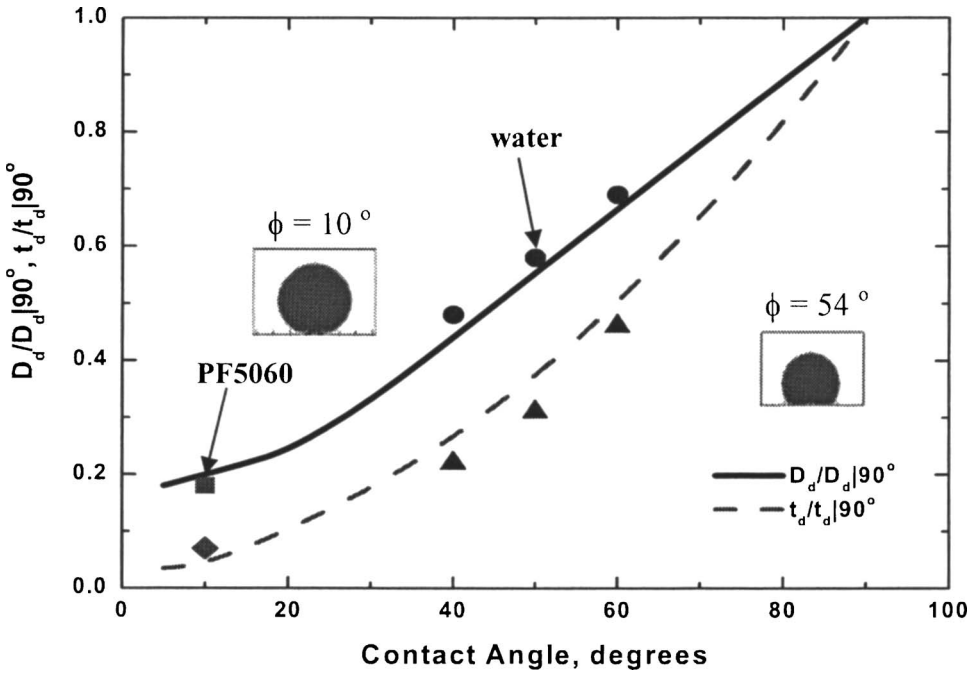

Fig. 4 Variation of the normalized departure diameter and departure time with contact angle (Fluids: water and PF5060, $\Delta T_w = 8°C$, $\Delta T_{sub} = 0°C$, $g = 1.0 g_e$).

heat transfer rate as well as contributions of various mechanisms vary both spatially and temporally. Wall heat flux and contributions of individual mechanisms integrated over the heater area supporting the computational domain are shown in Fig. 5. During the waiting period, which was taken to be 16 ms, heat transfer by transient conduction dominates. Its contribution decreases during the early growth period, but increases again as the bubble base shrinks during the detachment phase of the bubble. Natural convection contribution is highest during the early growth period of the bubble when liquid is pushed out radically. Microlayer contributes only during the period the bubble is attached to the heater surface. Heat transfer rate from the surface peaks just before the vapor bubble lifts off from the heater. Time-integrated values suggest that about 50% of the energy from the wall is transferred by transient conduction, 35% by natural convection, and 15% by microlayer evaporation.

Partitioning of wall energy into vapor and liquid, as determined from numerical simulations, is shown in Fig. 6 for one growth and departure cycle of a bubble. The highest rate at which energy is utilized for vapor production occurs when the vapor bubble base diameter is nearly maximum. Conversely, this corresponds to the lowest energy transfer rate into superheating of the liquid. Time integrated values suggest that about 30% of energy from the wall is utilized in vapor production, whereas 70% goes into superheating of liquid.

3.2 Bubble Merger and Formation of Vapor Columns. Vapor bubble merger in the vertical direction at a single nucleation site occurs when the growth rate of a bubble formed at the nucleation site exceeds the rate at which the lower interface of the

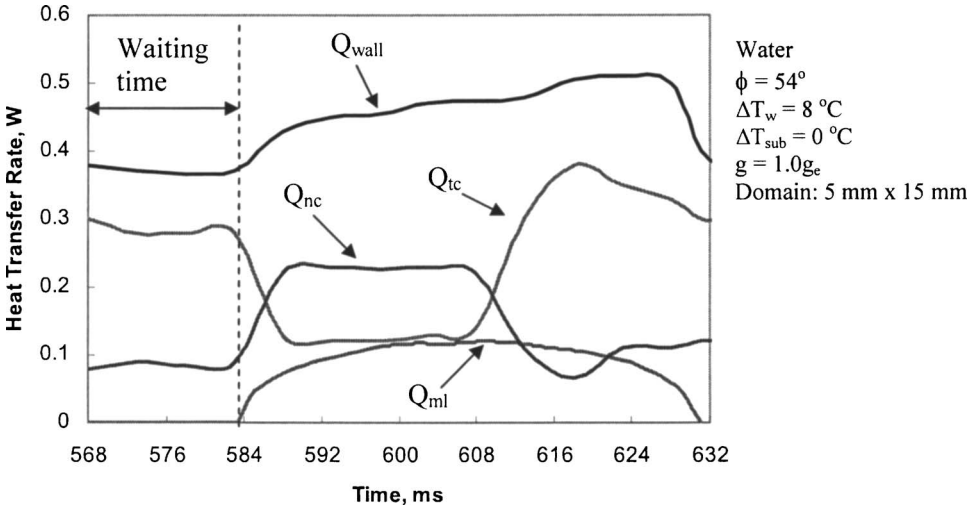

Fig. 5 Partitioning of wall heat transfer into natural convection, transient conduction, and microlayer heat transfer rates

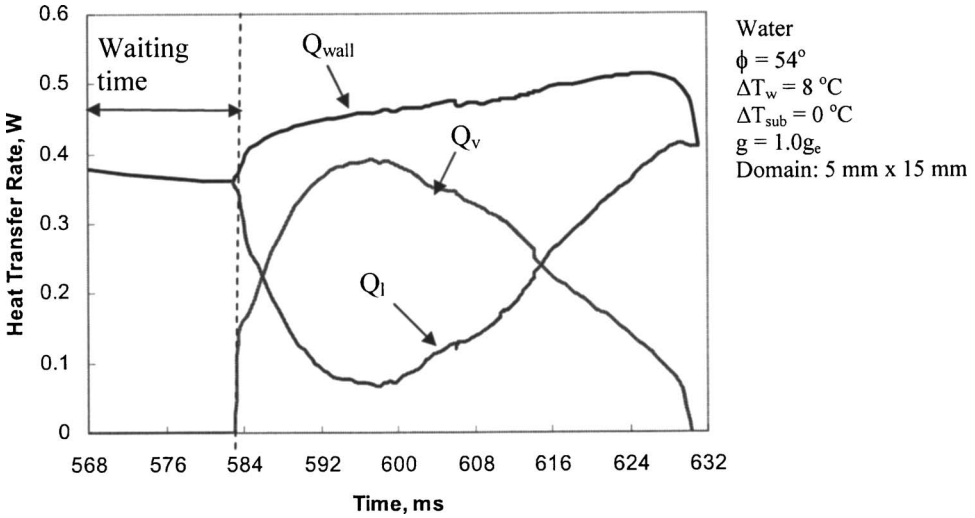

Fig. 6 Variation of the heat transfer rates from wall, into liquid, and into vapor with time

preceding bubble moves away from the heater surface [29]. After merger, the combined vapor mass may detach from the heater surface before the process repeats itself. Such a merger is referred to here as a two-bubble merger process. If, on the other hand, after merger the vapor mass merges with a second succeeding bubble before departure, we call it a three-bubble merger process. The shift from a two- to a three-bubble merger, and so on, depends on the wall superheat and on when vapor leaves the heater in almost a continuous column. Figure 7 shows the results of visual observations and those from numerical simulations for one cycle of the merger of three consecutive bubbles in the vertical direction. The upper set of frames are from visual observations, whereas the lower set of frames are results from numerical simulations.

The individual frames in each figure are from left to right and from top to bottom. After the merger of the departed bubble with the succeeding bubble, the larger vapor mass causes the vapor bubble at the nucleation site to prematurely depart. Thereafter, the second succeeding bubble merges with the vapor mass hovering over the surface. The combined vapor mass goes through several shape changes and departs as a cylindrical bubble. The departing bubble creates a wall jet that impinges on the lower interface of the bubble and forms a dimple. Thereafter, the vapor mass tries to acquire a spherical shape as it moves away from the wall. The rapid acceleration of the vapor mass breaks down the merger process before the cycle repeats itself. The bubble shapes as well as the merger behavior predicted from the numerical simulations is in startling agreement with the visual observations.

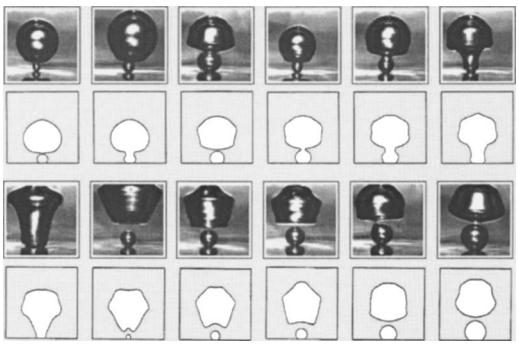

Fig. 7 Comparison of numerical and experimental bubble shapes during vertical merger [29] (Fluid: water, ΔT_w=10°C, ΔT_{sub}=0.0°C, g=1.0g_e, ϕ=38 deg).

3.3 Bubble Merger and Formation of Mushroom Type Bubbles. As the wall superheat is increased, the number density of the active nucleation sites also increases. With increased nucleation site density, vapor bubbles start to merge laterally as well. Mukherjee and Dhir [30] have carried out numerical simulations and experiments for merger of two bubbles nucleating at adjacent sites. In Fig. 8, the upper set of frames show the results of visual observations, whereas the results of numerical simulations are depicted in the lower set of frames. After the merger of two neighboring bubbles, a mushroom-type bubble with two stems attached to the solid surface forms. A liquid bridge exists between the two

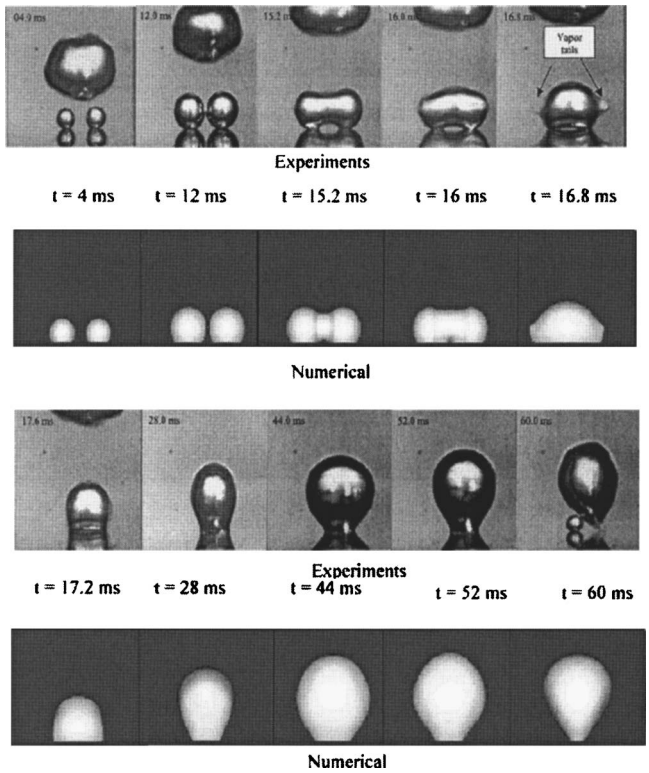

Fig. 8 Comparison of numerically predicted bubble growth with experimental data of Mukherjee and Dhir [30] (Fluid: water, ΔT_w=5°C, ΔT_{sub}=0°C, g=1.0g_e, spacing=1.5 mm)

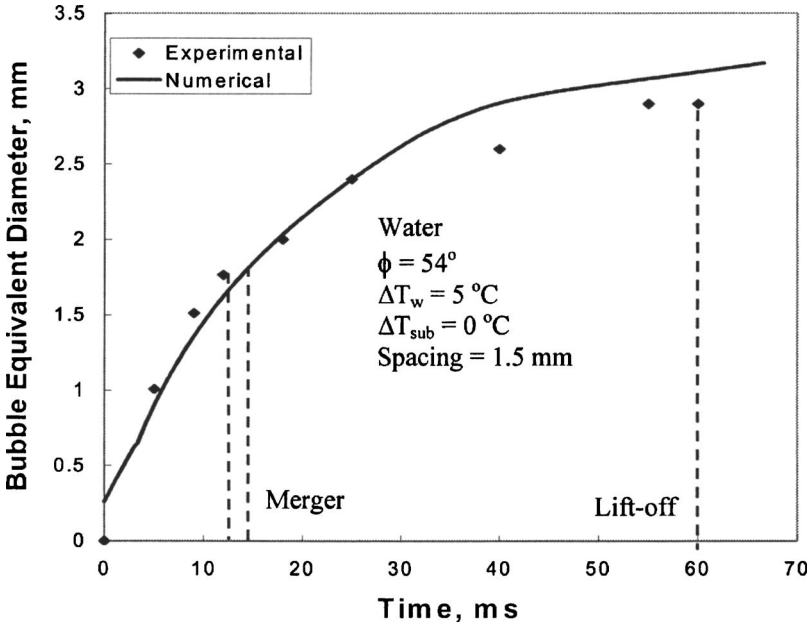

Fig. 9 Comparison of numerically predicted bubble growth with experimental data of Mukherjee and Dhir [30]

stems. As the merged vapor mass tries to acquire a spherical shape as a result of surface tension, vapor tails are formed. The vapor bubble oscillates in size in the plane of the photographs and normal to it before detaching. Numerical simulations capture the essential physics of the process—formation of vapor tails and oscillations in the size of the bubble prior to departure. However, the extent of the trapped liquid in numerical simulations is less than that in experiments.

A quantitative comparison of the predictions from numerical simulations of the growth history of the two bubble merger case with data from experiments is made in Fig. 9. Bubble equivalent diameter in Fig. 9 is the diameter of a perfect sphere having the same volume as the volume of two single bubbles or the merged vapor mass. Numerical simulation results, shown by the solid line, appear to describe well not only the growth history, but also the bubble departure diameter and the growth period.

Abarajith et al. [31] have systematically investigated through numerical simulations, the merger of three inline bubbles and that of three and five bubbles in a plane under low- and microgravity conditions. They found that generally, the predicted vapor bubble departure diameter after merger is smaller than that of a single bubble. In Fig. 10, the numerically predicted growth histories of merger of three inline bubbles and that of a single bubble are compared for earth normal gravity. Equivalent bubble departure diameter and the corresponding growth period for the three-bubble merger case is smaller than that for the single bubble. In order to determine the cause of the premature departure of vapor mass after merger of three bubbles, net force acting on the vapor mass was calculated. This force is taken to be positive when acting upwards and negative when acting downward. Figure 11 shows the variation of the net force on vapor mass during growth and merger of three bubbles and during the growth of a single bubble. For the three-bubble merger case, force changes sign from negative to positive at about 7 ms. This is about the time when the bubble base (Fig. 10) starts to shrink after reaching its maximum value and the vapor bubble enters the detachment phase. However, the single bubble continues to experience negative force and steadily grows for a substantial period beyond when the merged vapor mass starts to detach. The difference between the force acting on the merged vapor mass and the single bubble when the vapor mass, after merger, starts to detach is termed as "lift force." This force is responsible for the premature departure of the vapor mass after merger. The importance of this force increases as the level of gravity decreases.

The computed shapes of the vapor mass during merger of three bubbles placed at the corners of an equilateral triangle are shown in Fig. 12. Departure diameter and the vapor bubble after merger and corresponding growth period depend on the spacing and orientation of nucleating cavities. Figure 13 shows predictions from numerical simulations of bubble diameter at departure as a function of spacing. Both the bubble diameter at departure and the spacing have been normalized with the characteristic length defined as

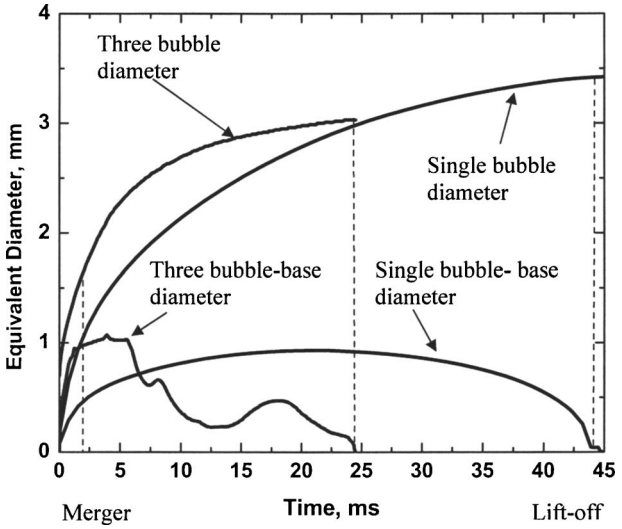

Fig. 10 The variation of equivalent bubble diameter with time for single and three inline bubbles (Fluid: water, ΔT_w=10°C, ΔT_{sub}=0°C, g=1.0g_e, ϕ=54 deg, spacing=1.25 mm)

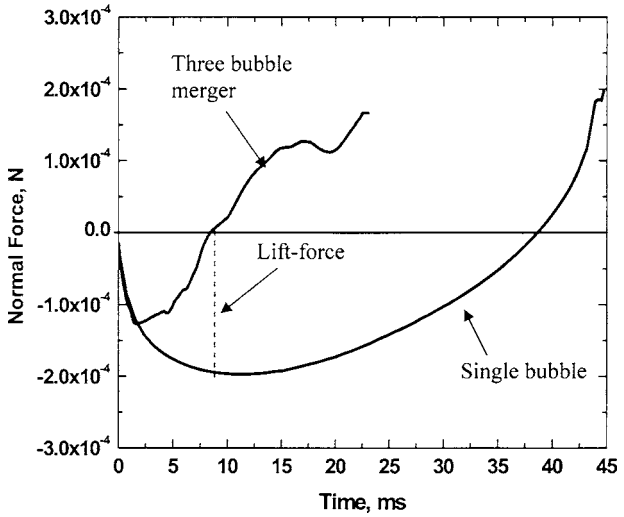

Fig. 11 The variation of force acting in the vertical direction with time for single and three inline bubbles (Fluid: saturated water, ΔT_w=10°C, g=1.0g_e, ϕ=54 deg, spacing=1.25 mm)

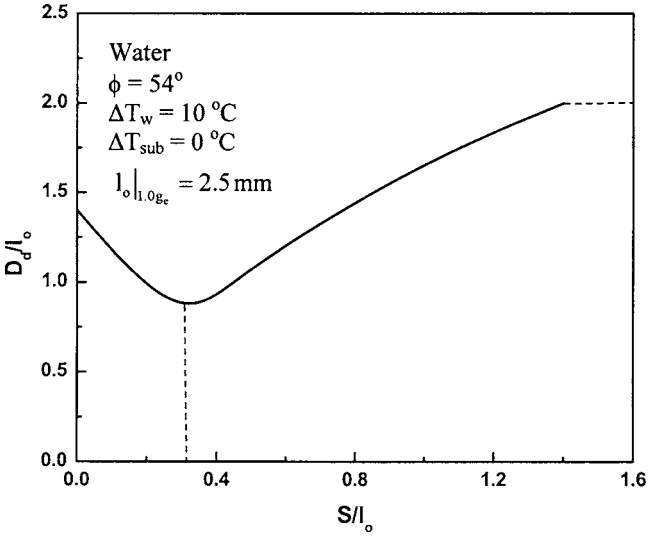

Fig. 13 The variation of nondimensional bubble departure diameter with cavity spacing for bubbles placed on the corners of equilateral triangle (Fluid: saturated water, ΔT_w=10°C, g =1.0g_e)

$$l_o = \sqrt{\frac{\sigma}{g(\rho_l - \rho_v)}} \tag{22}$$

Bubble departure diameter decreases as the spacing between cavities increases until the spacing is equal to $D_{ds}/4$, where D_{ds} is the departure diameter of a single bubble. For a contact angle of 54 deg, with water as the test liquid at one atmosphere pressure, D_{ds} is given as

$$D_{ds} = 1.4 l_o \tag{23}$$

Thereafter, the departure diameter increases until the spacing is large enough so that bubbles do not merge. The limiting values of departure diameter being equal to single bubble diameter, when spacing between cavities is zero, and is equal to $\sqrt[3]{3}D_{ds}$, when the spacing is $1.4l_o$.

The corresponding variation of the growth period is shown in Fig. 14. The growth period is nondimensionalized with the characteristic time defined as

$$t_o = \sqrt{\frac{l_o}{g}} \tag{24}$$

Growth period is found to show a behavior similar to the bubble diameter at departure. It is noted that depending on the magnitude of the spacing, bubble departure diameter can vary by a factor of two, whereas the growth period by a factor of three.

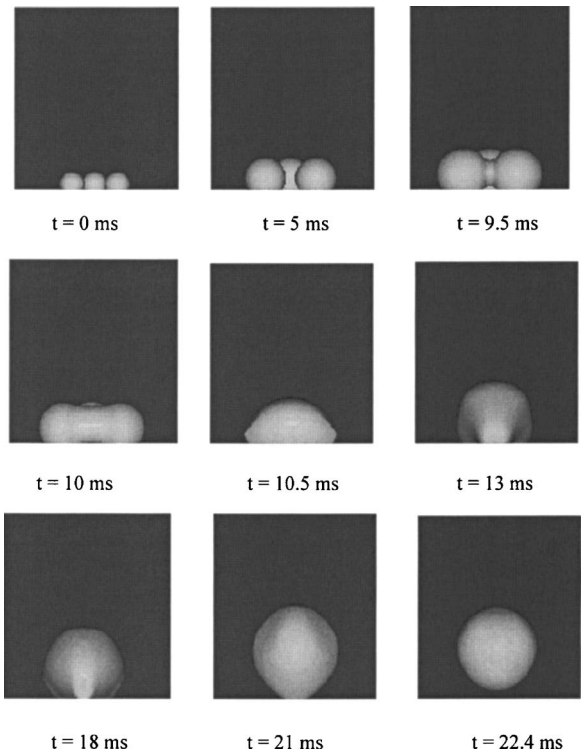

Fig. 12 Growth, merger, and departure of three bubbles located at the corners of an equilateral triangle (Fluid: saturated water, spacing=1.25 mm, ΔT_w=10°C, g=1.0g_e, ϕ=54 deg)

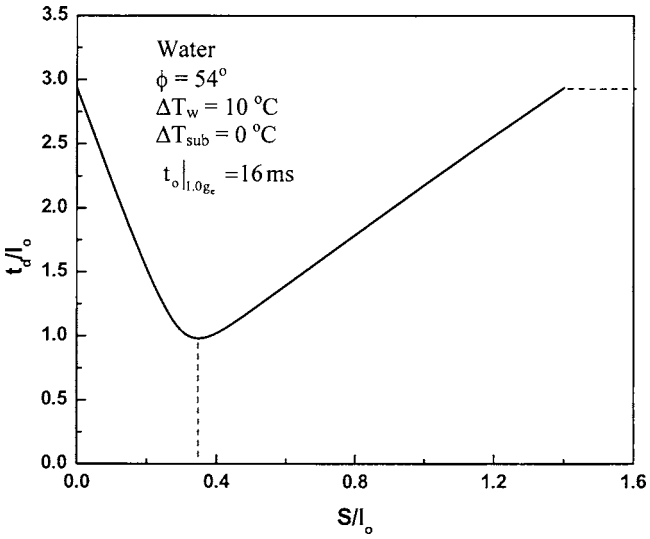

Fig. 14 The variation of nondimensional time period of growth with cavity spacing for bubbles placed on the corners of equilateral triangle (Fluid: saturated water, ΔT_w=10°C, g=1.0g_e)

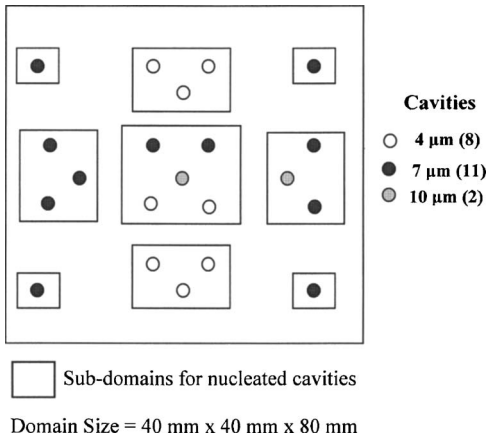

Fig. 15 Simulated commercial surface

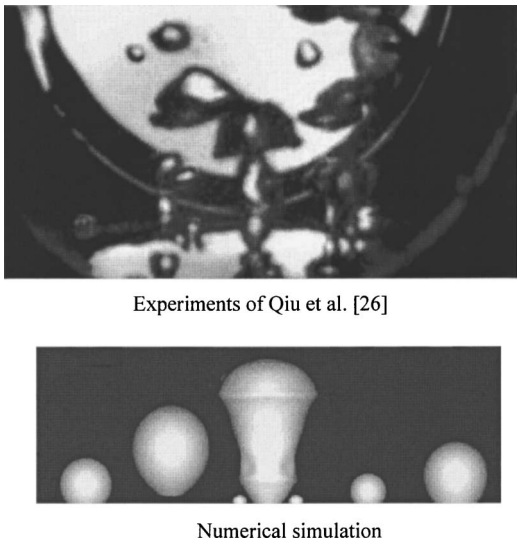

Fig. 16 Comparison of experimental and predicted bubble shapes during nucleate boiling on a simulated commercial surface for (Fluid: saturated water, $\Delta T_w = 7°C$, $g = 1.0 g_e$)

3.4 Nucleate Boiling Heat Flux. Numerical simulations have been carried out [32,33] to predict nucleate boiling heat flux as a function of wall superheat on a surface simulating a commercial surface. On this polished silicon wafer surface, 4 cm × 4 cm in area, cylindrical cavities of 10, 7, and 4 μm dia were fabricated as shown in Fig. 15. Different size cavities were chosen, so that smaller cavities will become active with an increase in wall superheat in a manner similar to that for a commercial surface. In order to accelerate the computations on a large domain, subdomains, as depicted in Fig. 15, were defined around clusters of cavities. While carrying out the computations, no interactions were allowed between neighboring domains. Heat flux in the regions falling between the domains was obtained by interpolating across the values that exist at the boundaries of the domains. The top portion of Fig. 16 shows the visual observation of the boiling phenomenon on the above-described surface when 6–7 cavities were active. The lower figure shows the results of computations at one instant of time. Observed and predicted vapor removal configurations are in a qualitative agreement. Figure 17 shows a comparison of wall heat flux as a function of wall superheat predicted from numerical simulations with data from experiments [26]. The solid line is the prediction from numerical simulations when the number of cavities that are active, and their location is given as an input to the simulations. The reported results are post several bubble growth and departure cycles. Predictions are seen to compare reasonably well with the data. The lower curve in Fig. 17 represents the wall energy that goes into production of vapor. Although the fraction of wall energy utilized in production of vapor varies with wall superheat, almost 40% of the energy is utilized for vapor production at a wall superheat of 12°C. The remaining energy goes into superheating of liquid.

A comparison of the observed and numerically cumputed bubble release pattern when the level of gravity is reduced by almost a factor of 100 is shown in Fig. 18. The same surface was used in the low-gravity experiments as in the experiments conducted at earth normal gravity. The photograph shown in the top portion of Fig. 18 was obtained from the experiments performed in the KC-135 aircraft. Vapor removal configurations predicted

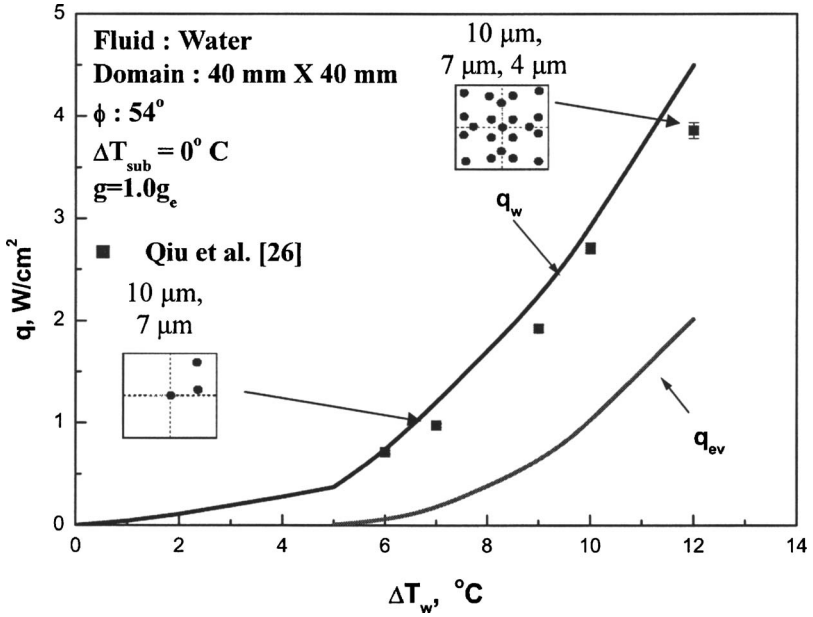

Fig. 17 The variation of wall heat flux with wall superheat for water at $g = 1.0 g_e$

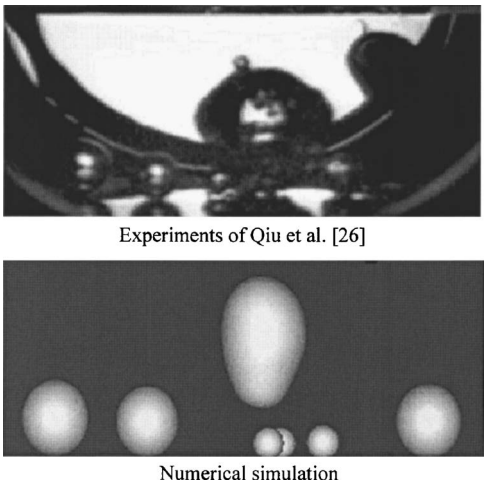

Fig. 18 Comparison of experimental and predicted bubble shapes during nucleate boiling on a simulated commercial surface (Fluid: saturated water, $\Delta T_w=7°C$, $g=0.01g_e$)

from numerical simulations appear to be in general agreement with those found in the experiments. In comparison to earth normal gravity, the departing vapor bubbles are now much larger in size. Predictions and low-gravity heat flux data are compared in Fig. 19. The predictions generally compare well with data, but large scatter in data is seen. Large scatter in data is due to the uncertainty in calculation of heat loss in the KC-135 environment [26]. It is found that in comparison to earth normal gravity, the highest heat flux at the highest wall superheat investigated is almost 25% lower. The lower curve represents partitioning of wall energy into vapor. At 12°C wall superheat, ~80% of energy is predicted to be consumed in vapor production, whereas the remaining 20% goes into superheating of liquid. It should be stressed that, thus far, the numerically analyzed heat fluxes are low. Further efforts in extending these results to high heat fluxes are needed.

The approach developed here can be extended to commercial surfaces provided the location and number density of active nucleation sites is known. The determination of cavities that become active depends on the shape and size of the defects or cavities present on the surface, which, in turn, requires a detailed knowledge of the topography of the surface. The latter information combined with a criterion such as that developed by Wang and Dhir [14] for entrapment of gas can be used as a first-order approximation to determine the number of active cavities at a particular wall superheat. Alternatively, we could use the correlation of Basu et al. [12] to determine the number density of active sites as a function of wall superheat and contact angle, and randomly distribute these cavities before carrying out numerical simulations of the process.

4 Conclusions

1. Various correlations and mechanistic models for nucleation site density, bubble departure diameter, and frequency have not always included the effect of all of the variables that influence these subprocesses.
2. Our ability to predict nucleate boiling heat fluxes mechanistically and theoretically is negatively impacted by the fact that in the past the interacting subprocesses have been treated as disjoint processes.
3. Complete numerical simulation of bubble dynamics and associated heat transfer processes appear to represent a potent approach.
4. As further advances are made in computations of all of the physical processes associated with rapidly evolving vapor-liquid interfaces, it should be possible in the near future to predict mechanistically nucleate boiling even at high heat fluxes on microfabricated surfaces simulating a real surface.
5. In the not-too-distant future, there should be an opportunity to carryout a standard problem in which prediction of dependence of nucleate boiling heat flux on wide range of wall superheats is made prior to experiments.

Acknowledgment

Efforts of all of my graduate students and postdoctoral fellows are gratefully acknowledged. The financial support was provided by NASA under the Microgravity Fluid Physics Program.

Nomenclature

C_1 = empirical constant

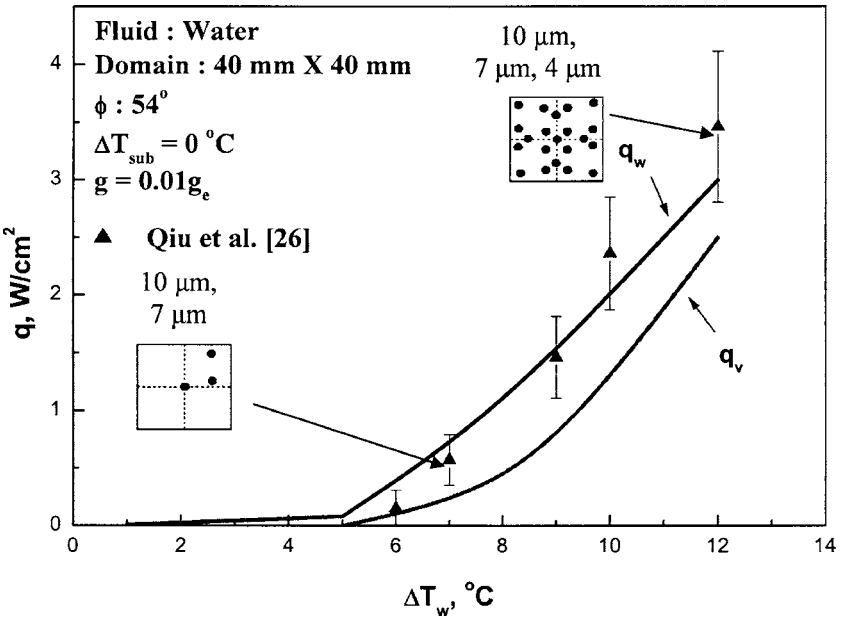

Fig. 19 The variation of wall heat flux with wall superheat for water at $g=0.01g_e$

C_s = empirical constant
c_p = specific heat
D = diameter
D_s = maximum diameter of largest cavity
f = bubble release frequency
g = gravitational acceleration
g_e = earth normal gravity
h = average heat transfer coefficient
h_{fg} = latent heat of vaporization
Ja = Jacob number, $\rho_l c_{pl} \Delta T / \rho_v h_{fg}$
Ja* = modified Jacob number, $\rho_l c_{pl} T_{\text{sat}} / \rho_v h_{fg}$
k = thermal conductivity
K = ratio of area of influence of bubble to cross-sectional area of bubble
l_o = characteristic length scale
M = molecular weight
m = empirical constant
n = empirical constant
N_a = active nucleation site density
$N_{\max}$ = maximum value of N_a
Nu = Nusselt number
P = pressure
P_c = critical pressure
Pr = Prandtl number
q = heat flux
Re = Reynolds number
R_p = surface roughness
T = temperature
t = time
t_d = growth period
t_o = characteristic time scale
t_w = waiting period
ΔT = temperature difference
V = volume

Greek

α = thermal diffusivity
ϕ = contact angle
μ = dynamic viscosity
ρ = density
σ = surface tension

Subscript

b = bubble
c = cavity
d = departure
ev = evaporation
l = liquid
nc = natural convection
ONB = onset of nucleate boiling
sat = saturation
sub = subcooling
v = vapor
w = wall

References

[1] Rohsenow, W. M., 1952, "A Method of Correlating Heat Transfer Data for Surface Boiling of Liquids," Trans. ASME, **74**, pp. 969–976.
[2] Liaw, S. P., and Dhir, V. K., 1989, "Void Fraction Measurement During Saturated Pool Boiling of Water on Partially Wetted Vertical Surfaces," ASME J. Heat Transfer, **111**, pp. 731–783.
[3] Stephan, K., and Abdelsalam, M., 1980, "Heat Transfer Correlation for Natural Convection Boiling," Int. J. Heat Mass Transfer, **23**, pp. 73–87.
[4] Cooper, M. G., 1984, *Saturation Nucleate Pool Boiling—A Simple Correlation*, Institute of Mechanical Engineers, London, IchemE Symposium Series, Vol. 86, pp. 786–793.
[5] Forster, D. E., and Greif, R., 1959, "Heat Transfer to a Boiling Liquid—Mechanism and Correlation," ASME J. Heat Transfer, **81**, pp. 43–53.
[6] Mikic, B. B., and Rohsenow, W. M., 1969, "A New Correlation of Pool Boiling Data, Including the Effect of Heating Surface Characteristics," ASME J. Heat Transfer, **9**, pp. 245–250.
[7] Judd, R. L., and Hwang, K. S., 1976, "A Comprehensive Model for Nucleate Boiling Heat Transfer, Including Microlayer Evaporation," ASME J. Heat Transfer, **98**, pp. 623–629.
[8] Bier, K., Gorenflo, D., Salem, M., and Tanes, Y., 1978, "Pool Boiling Heat Transfer and Size of Active Nucleation Centers for Horizontal Plates With Different Roughness," *Proceedings of the 6th International Heat Transfer Conference*, Vol. 1, Hemisphere, Washington, pp. 151–156.
[9] Kocamustafaogullari, G., and Ishii, M., 1983, "Interfacial Area and Nucleation Site Density in Boiling Systems," Int. J. Heat Mass Transfer, **26**, pp. 1377–1387.
[10] Fritz, W., 1935, "Maximum Volume of Vapor Bubbles," Phys. Z. **36**, pp. 379–384.
[11] Wang, C. H., and Dhir, V. K., 1993, "Effect of Surface Wettability on Active Nucleation Site Density During Pool Boiling of Saturated Water," ASME J. Heat Transfer, **115**, pp. 659–669.
[12] Basu, N., Warrier, G. R., and Dhir, V. K., 2002, "Onset of Nucleate Boiling and Active Nucleation Site Density During Subcooled Flow Boiling," ASME J. Heat Transfer, **123**, pp. 717–728.
[13] Bankoff, S. G., 1958, "Entrapment of Gas in the Spreading of Liquid Over a Rough Surface," AIChE J., **4**, pp. 24–26.
[14] Wang, C. H., and Dhir, V. K., 1993, "On the Gas Entrapment and Nucleation Site Density During Pool Boiling of Saturated Water," ASME J. Heat Transfer, **115**, pp. 670–679.
[15] Pesse, A. V., Warrier, G. R., and Dhir, V. K., 2004, "Experimental Study of the Gas Entrapment Process in Closed-End Microchannels," ASME Paper No. IMECE 2004–60296.
[16] Judd, R. L., 1988, "On Nucleation Site Interaction," ASME J. Heat Transfer, **110**, pp. 475–478.
[17] Dinh, T. N., Tu, J. P., Dinh, A. T., and Theofanous, T. G., 2003, "Nucleation Phenomena in Boiling on Nanoscopically, Smooth Surfaces," *Proceedings of 41st Aerospace Sciences Meeting and Exhibit*, Reno, AIAA, Washington, DC, AIAA Paper No. 2003–1035.
[18] Cooper, M. G., Judd, A. M., and Pike, R. A., 1978, "Shape and Departure of Single Bubbles Growing at a Wall," *Proceedings of 6th International Heat Transfer Conference*, Hemisphere, Washington, 1, pp. 115–120.
[19] Cole, R., and Rohsenow, W., 1969, "Correlation of Bubble Departure Diameters for Boiling of Saturated Liquids," Chem. Eng. Prog., **65**, pp. 211–213.
[20] Kocamustafaogullari, G., 1983, "Pressure Dependence of Bubble Departure Diameter for Water," Int. Commun. Heat Mass Transfer, **10**, pp. 501–509.
[21] Gorenflo, D., Knabe, V., and Bieling, V., 1986, "Bubble Density on Surfaces With Nucleate Boiling—It's Influence on Heat Transfer and Burnout Heat Fluxes at Elevated Saturation Pressures," *Proceedings of 8th International Heat Transfer Conference*, Hemisphere, Washington, Vol. 4, pp. 1995–2000.
[22] Zuber, N., 1959, "Hydrodynamic Aspect of Boiling Heat Transfer," Ph.D. dissertation, University of California, Los Angeles.
[23] Malenkov, I. G., 1971, "Detachment Frequency as a Function of Size of Vapor Bubbles," Inzh.-Fiz. Zh., **20**, pp. 704–708.
[24] Son, G., Dhir, V. K., and Ramanujapu, N., 1999, "Dynamics and Heat Transfer Associated With a Single Bubble During Nucleate Boiling on a Horizontal Surface," ASME J. Heat Transfer, **121**, pp. 623–632.
[25] Ramanujapu, N., and Dhir, V. K., 1999, "Dynamics of Contact Angle During Growth and Detachment of a Vapor Bubble at a Single Nucleation Site," *Proceedings of the 5th ASME/JSME Joint Thermal Engineering Conference*, San Diego, ASME, New York.
[26] Qiu, D. M., Dhir, V. K., Hasan, M. M., and Chao, D., 2000, "Single and Multiple Bubble Dynamics During Nucleate Boiling Under Low Gravity Conditions," *Proceedings of the National Heat Transfer Conference*, Begel House, NY, pp. 62–71.
[27] Singh, S., and Dhir, V. K., 2000, "Effect of Gravity, Wall Superheat, and Liquid Subcooling on Bubble Dynamics During Nucleate Boiling," *Proceedings of Microgravity Fluid Physics and Heat Transfer*, V. K. Dhir, ed., Begell House, New York, pp. 106–113.
[28] Abarajith, H. S., and Dhir, V. K., 2002, "Effect of Contact Angle on the Dynamics of a Single Bubble During Pool Boiling Using Numerical Simulations," *Proceedings of IMECE*, New Orleans, ASME, New York, Paper no. IMECE2002-33876.
[29] Son, G., Ramanujapu, N., and Dhir, V. K., 2002, "Numerical Simulation of Bubble Merger Process on a Single Nucleation Site During Pool Nucleate Boiling," ASME J. Heat Transfer, **124**, pp. 51–62.
[30] Mukherjee, A., and Dhir, V. K., 2004, "Study of Lateral Merger of Vapor Bubbles During Nucleate Pool Boiling," ASME J. Heat Transfer, **126**, pp. 1023–1039.
[31] Abarajith, H. S., Dhir, V. K., and Son, G., 2004, "Numerical Simulation of the Dynamics of Multiple Bubble Merger During Pool Boiling Under Reduced Gravity Conditions," *Proceedings of 7th Japan-U.S. Seminar on Two-Phase Flow Dynamics*, Moriyama, Japan.
[32] Dhir, V. K., Abarajith, H. S., Warrier, G., and Son., G., 2004, "Bubble Dynamics and Nucleate Pool Boiling Heat Transfer—Numerical Simulations and Experimental Validation." J. Energy Heat Mass Transfer, in press.
[33] Dhir, V. K., 2005, "Nucleate Boiling Under Reduced Gravity Conditions." *Proceedings of 6th Minsk International Seminar on Heat Pipes, Heat Pumps, and Refrigerators*, Luikov Heat and Mass Transfer Institute, Minsk, Belarus.

Comparison of Nucleation Site Density for Pool Boiling and Gas Nucleation

Yusen Qi

James F. Klausner[1]

University of Florida,
Department of Mechanical and Aerospace Engineering,
P.O. Box 116300,
Gainesville, FL 32611-6300

It has been well established that the rate of heat transfer associated with boiling systems is strongly dependent on the nucleation site density. Over many years attempts have been made to predict nucleation site density in boiling systems using a variety of techniques. With the exception of specially prepared surfaces, these attempts have met with little success. This paper presents an experimental investigation of nucleation site density measured on roughly polished brass and stainless steel surfaces for gas nucleation and pool boiling over a large parameter space. A statistical model used to predict the nucleation site density in saturated pool boiling is also investigated. The fluids used for this study, distilled water and ethanol, are moderately wetting and highly wetting, respectively. Using distilled water it has been observed that the trends of nucleation site density versus the inverse of the critical radius are similar for pool boiling and gas nucleation. The nucleation site density is higher for gas nucleation than for pool boiling. An unexpected result has been observed with ethanol as the heat transfer fluid, which casts doubt on the general assumption that heterogeneous nucleation in boiling systems is exclusively seeded by vapor trapping cavities. Due to flooding, few sites are active on the brass surface and at most two are active on the stainless steel surface during gas nucleation experiments. However, nucleation sites readily form in large concentration on both the brass and stainless steel surfaces during pool boiling. The pool boiling nucleation site densities for ethanol on rough and mirror polished brass surfaces are also compared. It shows that there is not a significant difference between the measured nucleation site densities on the smooth and rough surfaces. These results suggest that, in addition to vapor trapping cavities, another mechanism must exist to seed vapor bubble growth in boiling systems. [DOI: 10.1115/1.2130399]

1 Introduction

It is well known that nucleation site density is fundamental to the development of mechanistically based nucleate boiling heat transfer models. Enormous effort has been made to predict the nucleation site density in boiling systems using a variety of techniques [1,2]. Corty and Foust [3] recognized that boiling takes place on surfaces with irregularities. They suggested that vapor trapped in these surface irregularities serve as nucleation sites. This hypothesis was confirmed by Clark et al. [4] using micrographs of the heating surface. Under the guidance of heterogeneous nucleation theory, Bankoff [5] was the first to establish a vapor trapping criterion. Using conical cavities as the model, Bankoff proposed that the liquid solid contact angle must be greater than twice the half cone angle for cavities to trap gas or vapor. Cornwell [6] performed a detailed study of the geometry of naturally formed nucleation site cavities in pool boiling to verify that nucleate sites are typically cavities. More recently, Wang and Dhir [7] extended the vapor-trapping criterion to cavities with other shapes.

Yang and Kim [8] suggested that the nucleation site density can be computed from knowing the size distribution of cavities, the distribution of the cavity half cone angles, the minimum cavity mouth radius required for nucleation, and the liquid/solid contact angle. Three nucleation site density data points for pool boiling of water on a mirror-finished stainless steel heating surface appear to agree well with those computed. The comparison is rather limited since the maximum superheat tested was 2.6 °C. Wang and Dhir [7,9] also proposed a statistical method for predicting nucleation site density based on surface microstructure. The nucleation site density data agreed with the predicted data to within ±60% under varying wettability conditions. Hsu [10] suggested there exist both a minimum and maximum cavity radius that will permit the incipience of vapor bubbles. Zeng and Klausner [11] measured nucleation site density in flow boiling. Their data demonstrated that both the maximum and minimum cavity radii are important in flow boiling nucleation. Using stylus systems to record detailed information on surface microstructure, Luke et al. [12–14] studied the effect of surface roughness and topography on boiling nucleation.

Past research suggests that nucleation site density in boiling systems might be predicted by studying the gas bubble density formed on surfaces from supersaturated gas solutions [15,16]. The advantage of using gas nucleation over boiling experiments is that it is easier to count the nucleation sites, and the experiments are potentially easier to operate. Supersaturated gas bubble growth rates in an inorganic fluid are very slow, while they are more rapid in organic fluids due to the low surface tension. When addressing the surface characteristic and wettability effects on heterogeneous nucleation, the gas nucleation technique has inherent advantages. Gas nucleation eliminates the possibility of thermal interference between adjacent sites, which has been suggested as a mechanism for suppressing boiling nucleation. Also, due to the slow growth rate of gas bubbles, dynamic influences related to vapor bubble growth, departure, and turbulence are absent. These advantages of the gas nucleation technique provide sufficient incentive to explore its usefulness for predicting nucleation site density in boiling systems.

Brown [15] was the first to extensively investigate supersatu-

[1]Corresponding author; e-mail: klaus@ufl.edu; tel.: 352-392-3506; fax: 352-392-1071.

Contributed by the Heat Transfer Division of ASME for publication in the JOURNAL OF HEAT TRANSFER. Manuscript received October 7, 2004; final manuscript received May 27, 2005. Review conducted by Raj M. Manglik. Paper presented at the 2004 ASME International Mechanical Engineering Congress (IMECE2004), November 13, 2004–November 19, 2004, Anaheim, California, USA.

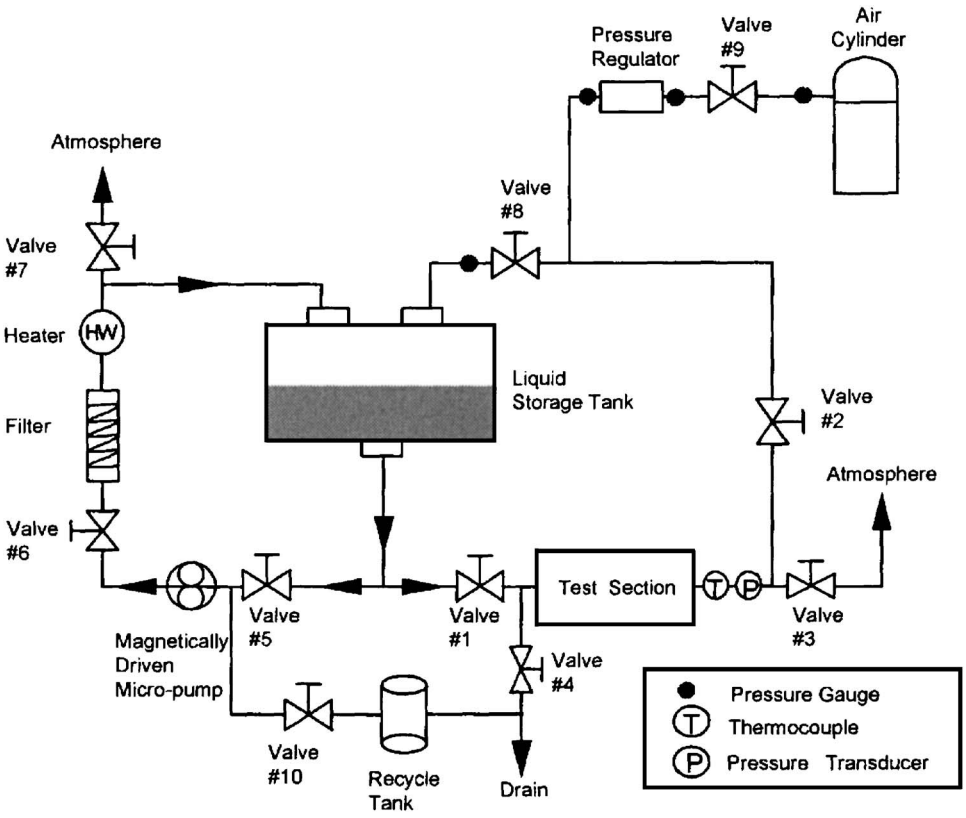

Fig. 1 Gas nucleation facility

rated gas bubble formation at cavity sites where vapor bubbles sit in nucleate boiling systems. Eddington et al. [16–18] have extensively compared nucleation via gas bubbling with that in nucleate boiling. All of the experiments used distilled water as the heat transfer fluid. They found that the nucleation site density with gas diffusion is higher than that measured with nucleate boiling. However, Kenning [2] found that the agreement can be improved by accounting for the nonlinear relation between the saturation pressure and temperature.

In a previous investigation, Qi et al. [19] have made extensive nucleation site density measurements with water on brass and stainless steel surfaces using the gas nucleation technique. Using detailed surface structure data, which includes the statistical distribution of cavity mouth diameters and cavity half cone angles gathered by a vertical scanning interferometer, an attempt was made to predict nucleation site density on coarsely polished surfaces. Due to the large uncertainty in the probability of finding cavities that satisfy the gas trapping criterion, the statistical method was not successful in predicting nucleation site density on surfaces with randomly distributed cavities.

As a further exploration of the gas nucleation technique, this work considers extensive gas nucleation experiments carried through on brass and stainless steel surfaces using distilled water and ethanol. Pressurization changes of up to 8.5 bars have been considered. In order to compare with the gas nucleation data, nucleation site density has been measured for saturated pool boiling using distilled water and ethanol on brass and stainless steel surfaces with the same surface finishes as reported by Qi et al. [19]. High-speed imaging has been used to capture nucleation site density for low to moderate heat flux during pool boiling. The objectives of the current work are to (1) investigate the usefulness of the gas nucleation technique to assist in the prediction of pool nucleate boiling site density, and (2) further investigate the validity of heterogeneous nucleation theory.

2 Experimental Facilities

2.1 Gas Nucleation Facility. A gas nucleation facility, shown in Fig. 1, was designed and fabricated for the present experiments. The facility description and operating procedure have been detailed by Qi et al. [19]. A liquid recycle system and filter have been added to the original facility so that the ethanol is recovered. A brief description of the facility operation is given here. As circulating pressurized liquid is sprayed into the epoxy-lined steel storage tank, it gradually becomes saturated with air. Gas saturated liquid from the storage tank is allowed to fill the test section while dissolved gas remains in solution under high pressure. After the test section is depressurized by opening the discharge valve, nucleation sites form on the test surface, which is photographed with a high-resolution digital camera from a side view. Using back lighting, each bubble directs the light toward the camera lens, and each individual bubble is identified by its bright spot.

A transparent test section that can accommodate 10 bars pressure has been fabricated, and an assembled drawing of the test section is shown in Fig. 2. The visual portion of the test section is constructed from polycarbonate. Two thick metallic plates cover the top and bottom to prevent excessive polycarbonate deformation when under high pressure. All mating surfaces are sealed with viton gaskets.

The pressure in the test section is measured with a Viatran strain gauge-type pressure transducer. The temperature is measured with a single-type *E* thermocouple. The uncertainty of the pressure measurement is ±0.2 kPa and the uncertainty of the temperature measurement is ±0.5°C. At low nucleation site density, the measurement is exact. At higher nucleation site density, the measurement uncertainty is approximately ±2%.

2.2 Pool Boiling Facility. A tilted assembled drawing of the pool boiling chamber is shown in Fig. 3. The boiling chamber

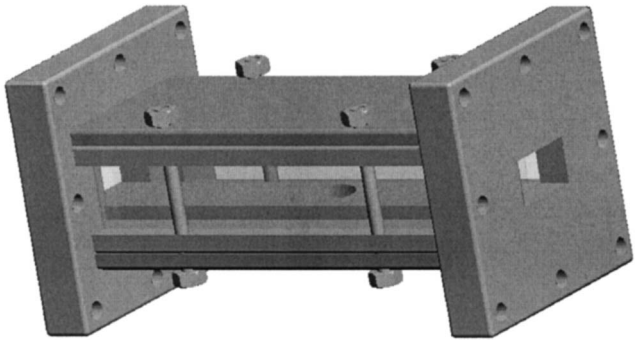

Fig. 2 Test section used in gas nucleation experiments

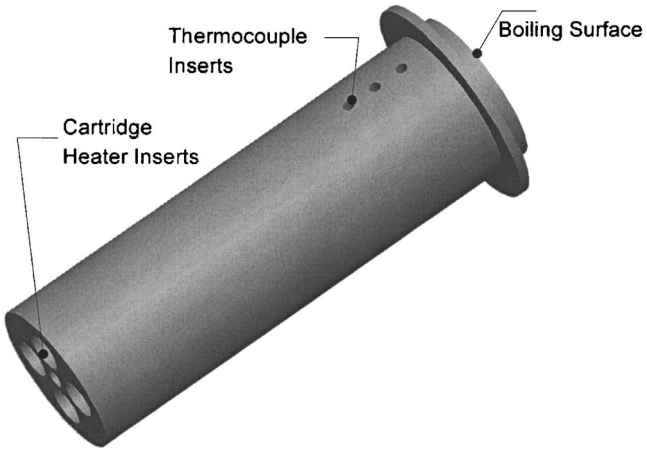

Fig. 4 Cylindrical heater and heat transfer surface used in pool boiling experiments

consists of a low expansion borosilicate glass cylinder with inner diameter 101.6 mm, thickness 6.35 mm and length 0.45 m. The glass cylinder is held vertically in place between two stainless steel plates, on which the circular grooves are cut precisely to fit the glass cylinder. A viton seal is used to prevent leakage between these two plates. A cooling coil that is connected with a small chiller is mounted on the upper part of the boiling chamber to maintain a constant pressure. The water temperature and mass flow rate passing through the cooling coil are adjustable. Heat is supplied to the boiling surface by four high-density cartridge heaters embedded in a cylinder as shown in Fig. 4. The upper surface of the cylinder, which is the boiling surface, is mounted flush with the boiling chamber plate. These four cartridge heaters are rated at 200 W each, which yields a maximum heat flux of 1600 kW/m^2. Type J fine wire thermocouple probes with glass braid insulation are embedded along the length of cylinder at 10, 15, and 20 mm from the boiling surface. The heated cylinder is heavily insulated.

At each vertical location, two thermocouples are embedded with the tip located at a radial distance of 6.35 mm from the outer surface. The temperature reading from the thermocouples on the same vertical plane are averaged. Thus the temperature readings at the three vertical positions are used to evaluate the temperature gradient and surface temperature. For the brass surface, the temperature variation is linear, indicative of one-dimensional heat flow. For the stainless steel sample, the measured temperature distribution along the length of the cylinder is slightly nonlinear, thus a finite volume inverse computational method is used to match the computed temperature distribution with that measured. The computed distribution is used to evaluate the surface tempera-

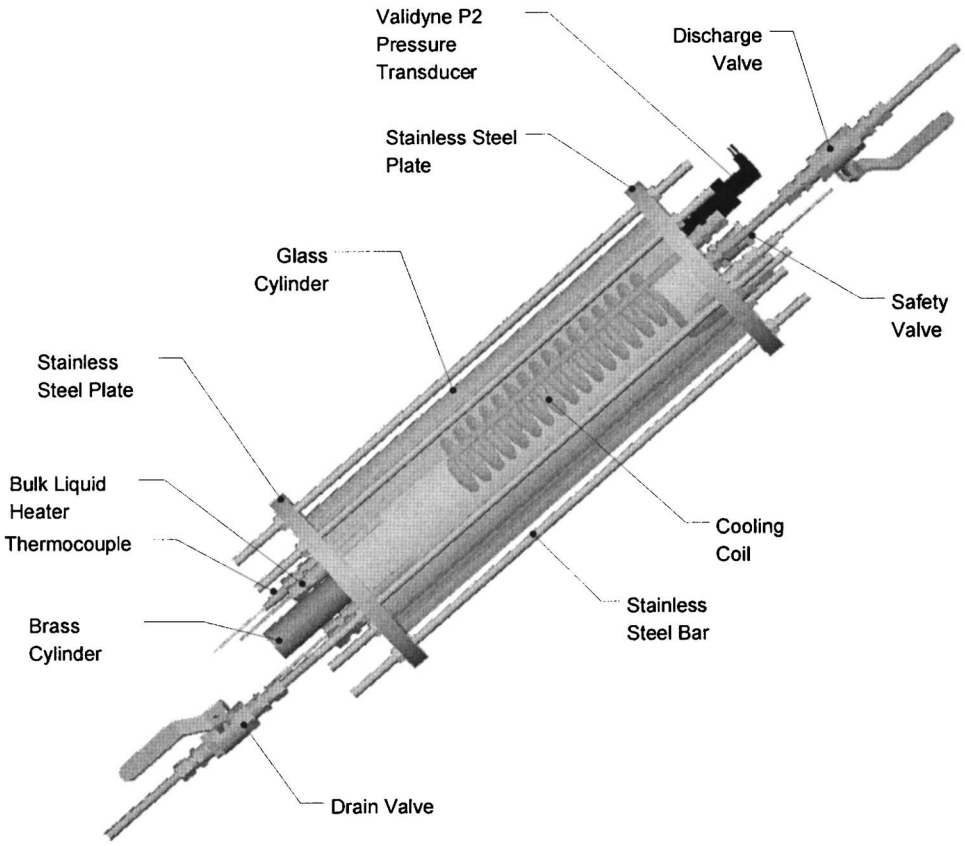

Fig. 3 Assembled view of pool boiling chamber

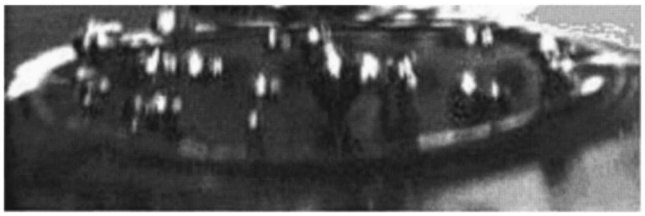

Fig. 5 A typical image of pool boiling nucleation sites

ture and heat flux. The bulk liquid is heated by two heaters with a power of 200 W each. The power to all heaters is controlled by autotransformers. The pressure in the test chamber is measured with a Validyne P2 pressure transducer with an uncertainty of ±0.2 kPa. The uncertainty of temperature measurement is ±0.5°C. The uncertainty of the surface temperature is ±1.5°C. Prior to recording data, the liquid is allowed to boil for 1 h to insure that the system reaches steady state conditions and the surface is degassed. It is not likely that the surface can be completely degassed as will be discussed later.

The bubble growth and departure processes are captured using a high-speed complementary metal-oxide-semiconductor digital camera, Hi-Dcam II from NAC Image Technology, which can run at 20,000 frames per second (fps). The camera images are stored and analyzed using the software accompanied with the camera. A 2000 fps frame rate with a resolution of 1280×256 is appropriate for this study. A typical image of boiling on the heater surface is shown in Fig. 5.

The same Access 12 bit digital data acquisition systems are used with both facilities to record the pressure and temperature measurements. The diameter of the boiling surfaces and the metallic samples inserted in the test section of the gas nucleation facility is 25 mm. All surfaces are prepared in an identical manner. The surfaces are polished initially with 120 grit silicon carbide sandpaper, and then 400 grit sandpaper is applied to reach the final finish. Before the experimental operation, the surfaces are thoroughly cleaned by detergent solution and ethanol. Detailed surface topography data have been obtained and are reported in Qi et al. [19]. The rms roughness of the brass surface is 1.02 μm, while that of the stainless steel surface is 0.88 μm. From the measured distribution of cavity sizes and cavity half cone angles, the mean cavity mouth diameter with standard deviation, denoted as μ_d and σ_d, respectively, and the mean cavity half cone angle with standard deviation, denoted as μ_β and σ_β, respectively, are shown in Table 1.

Table 1 Statistical data on surface structure

Surface	μ_d (μm)	σ_d (μm)	μ_β (rad)	σ_β (rad)
Brass	4.72	3.9	1.31	0.12
Stainless Steel	2.68	1.79	1.18	0.18

The liquid/solid contact angles have been measured using the drop shape method and results are shown in Table 2. The results for water are relatively standard. However, a pure ethanol drop will spread spontaneously when the metallic surfaces are mounted horizontally. Within 100 ms the drops on both surfaces are indiscernible under 10× magnification. Here the digital camera is used to capture the dynamics using a 1000 fps frame rate. When measuring the advancing and receding angle on a 30 deg tilted brass sample, the ethanol drop will reach an indiscernible condition within 0.05 s. The contact angle measurement is not considered reliable and is not reported. The time required for the stainless steel surface is slightly longer, approximately 150 ms. The advancing and receding angles with standard deviations are listed in Table 2 even though uncertainty remains as to whether an equilibrium condition was reached.

3 Nucleation Site Density Measurements With Distilled Water

According to classical heterogeneous nucleation theory, the critical radius at the mouth of a cavity required for incipience is

$$r_c^* = \frac{2\sigma T_{\text{sat}}}{\rho_g h_{\text{fg}} \Delta T_{\text{sat}}} \tag{1}$$

For gas nucleation it is expressed as

$$r_c^* = \frac{2\sigma}{\Delta P} \tag{2}$$

Figure 6 shows the variation of nucleation site density as a function of $\Delta P/2\sigma$ for gas nucleation and $1/r_c^*$ for pool boiling with water on brass. The variation of nucleation site density in Fig. 6 is observed to follow the same trend for both gas nucleation and pool boiling. However, the gas nucleation data are typically higher for the same critical radius. This has also been observed by Eddington and Kenning [17]. Based on heterogeneous nucleation theory there are several possible explanations. One possible explanation is that in the vicinity of a nucleation site, energy is depleted from the heater substrate due to bubble growth and this suppresses the formation of nucleation sites in the surrounding vicinity. This is referred to as thermal interference. Another possible explanation is that a very thin thermal boundary layer results in an upper limitation on the size of cavities that can become active, as analytically detailed by Hsu [10]. No such limitations exist for gas nucleation. As discussed by Cornwell [20], another possibility is that cavities that might otherwise be flooded, could trap vapor during gas nucleation experiments as a result of contact angle hysteresis during pre-pressurization.

Table 2 Contact angle measurements

Surface	Water	Ethanol
Brass	1.27 ± 0.06(rad) 73.1 ± 3.7(deg)	Not reported
Stainless Steel	1.35 ± 0.07(rad) 77.4 ± 4.2(deg)	Advancing 0.14 ± 0.0045(rad) 8.0 ± 0.26(deg) Receding 0.10 ± 0.0083(rad) 5.7 ± 0.47(deg)

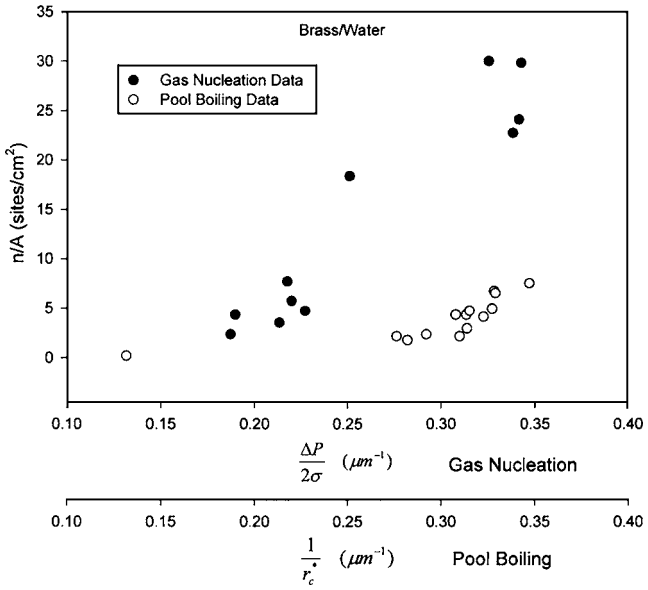

Fig. 6 Variation of nucleation site density for water on brass surface using gas nucleation and pool boiling

In order to further explore the differences in nucleation characteristics, both gas nucleation and pool boiling experiments were also done on the stainless steel surface. The observed variation of nucleation site density with water on stainless steel as a function of $\Delta P/2\sigma$ for gas nucleation and $1/r_c^*$ for pool boiling is shown in Fig. 7. The nucleation site density is slightly higher for gas nucleation than for pool boiling at the same critical radius. In both cases, the nucleation site density increases with decreasing critical radius, as expected.

An attempt is made at predicting pool boiling nucleation site density behavior using a statistical model and heterogeneous nucleation theory as is described next.

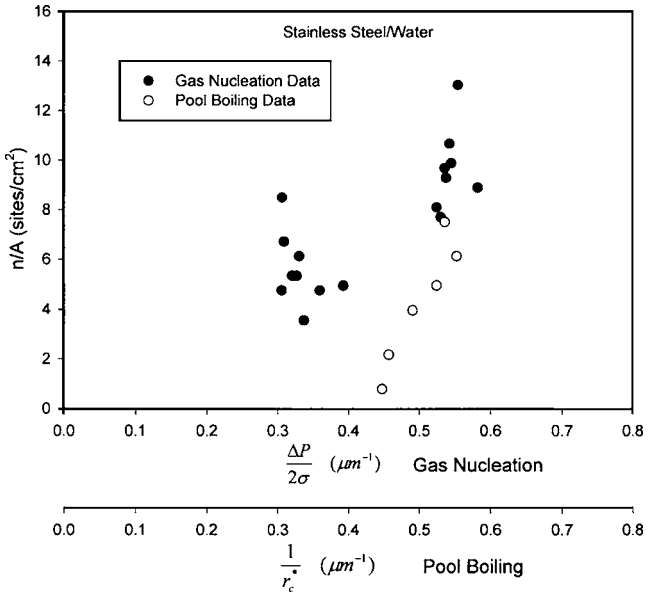

Fig. 7 Variation of nucleation site density for water on stainless steel surface using gas nucleation and pool boiling

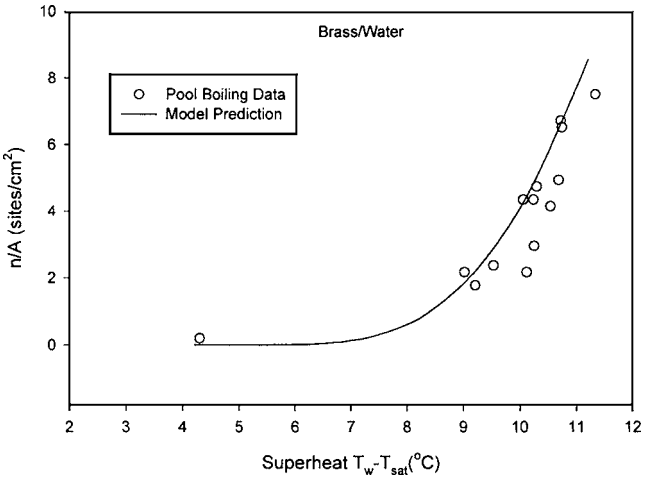

Fig. 8 Comparison between measured and predicted nucleation site density on brass surface using water

4 Nucleation Site Density Prediction

Here the statistical method is used to predict nucleation site density. Following Yang and Kim [8] an estimation of the nucleation site density is given by

$$\frac{n}{A} = \frac{N}{A}\int_{2r_{\min}}^{2r_{\max}} f_{3D}(d)dd \int_0^{\theta/2} g(\beta)d\beta \tag{3}$$

where N/A is the number of cavities per unit area, $f_{3D}(d)$ is the probability density distribution of cavity size, $g(\beta)$ is the probability density distribution of cavity half cone angles, $r_{\min}$ and $r_{\max}$ are the minimum and maximum cavity radius which will permit the incipience of vapor bubbles and θ is the contact angle. The probability density distribution of cavity size approximately follows a Weibull distribution as detailed in Qi et al. [19],

$$f_{3D}(d) = \frac{\lambda}{\omega}\left(\frac{d}{\omega}\right)^{\lambda-1} \exp\left[-\left(\frac{d}{\omega}\right)^{\lambda}\right]; \quad d \geq 0; \quad \omega,\lambda > 0 \tag{4}$$

Here, $\lambda = 1.23$, $\omega = 2.0$ for the brass surface; $\lambda = 1.53$, $\omega = 1.19$ for the stainless steel surface. The probability density distribution of cavity half cone angles is expressed as

$$g(\beta) = \frac{A\left(\frac{\pi}{2} - \beta\right)^2}{B + \left(\frac{\pi}{2} - \beta\right)^6} \tag{5}$$

where $A = 0.019\,13$ and $B = 0.0001$ for the brass surface while $A = 0.091$ and $B = 0.0023$ for the stainless steel surface. According to Hsu [10] $r_{\min}$ and $r_{\max}$ for pool boiling are estimated from

$$r_c^* = \frac{4\sigma T_{\text{sat}} C_2}{h_{\text{fg}}\rho_v(\Delta T_{\text{sat}})_{\text{inc}} C_1}\left[1 \pm \sqrt{1 - \frac{(\Delta T_{\text{sat}})_{\text{inc}}}{\Delta T_{\text{sat}}}}\right] \tag{6}$$

Since ϕ is the angle between the side of the vapor embryo surface and the horizontal, constants $C_1 = (1 + \cos\phi)/\sin\phi$ and $C_2 = 1 + \cos\phi$ are evaluated using the mean cavity half cone angle and contact angles, listed in Tables 1 and 2. $C_1 = 1.0$ and $C_2 = 1.0$ for the brass surface; $C_1 = 0.84$ and $C_2 = 0.83$ for the stainless steel surface. Since finding vapor trapping cavities is a very low probability event and the accuracy from a fitted distribution Eq. (5) is poor, the last integral in Eq. (3) is determined from the measured n/A for gas nucleation. This integral value is 0.0028 for the brass surface and 0.0005 for the stainless steel surface. Figure 8 shows a comparison between the measured and predicted pool boiling nucleation site density for water on brass. Here, the prediction is

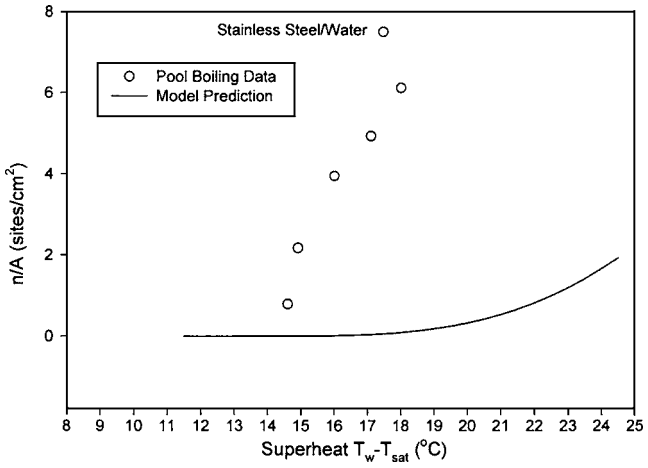

Fig. 9 Comparison between measured and predicted nucleation site density on stainless steel surface using water

in excellent agreement with the measurements. Figure 9 shows a comparison between the measured and predicted pool boiling nucleation site density for water on stainless steel. Here the measured nucleation site density is significantly greater than the prediction. This raises the possibility of another mechanism seeding boiling nucleation in addition to vapor trapping cavities. This possibility is explored in more depth in the section to follow.

5 Nucleation Site Density Measurements With Ethanol

Nucleation site density measurements have also been conducted with ethanol. Figure 10 shows the variation of nucleation site density with ethanol on brass. Due to the high wettability of ethanol, most cavities on the surface are flooded. Only some very small cavities can trap vapor and thus a very high $\Delta P/2\sigma$ is required to activate sites for gas nucleation experiments. The increase in the number of sites activated with increasing pressure is very small, even with an order of magnitude increase in $\Delta P/2\sigma$. In contrast, nucleation sites are easily activated during pool boiling with ethanol on brass. A larger value of $1/r_c^*$ is required for incipience with ethanol on brass compared with water on brass, as

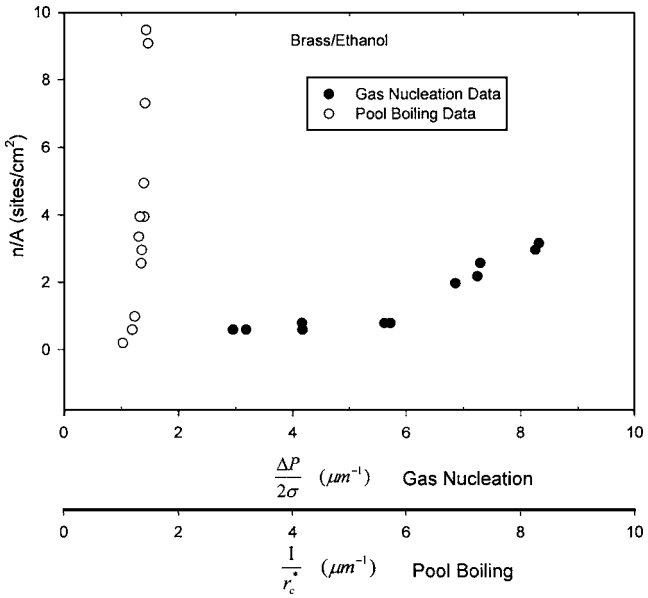

Fig. 10 Variation of nucleation site density for ethanol on brass surface using gas nucleation and pool boiling

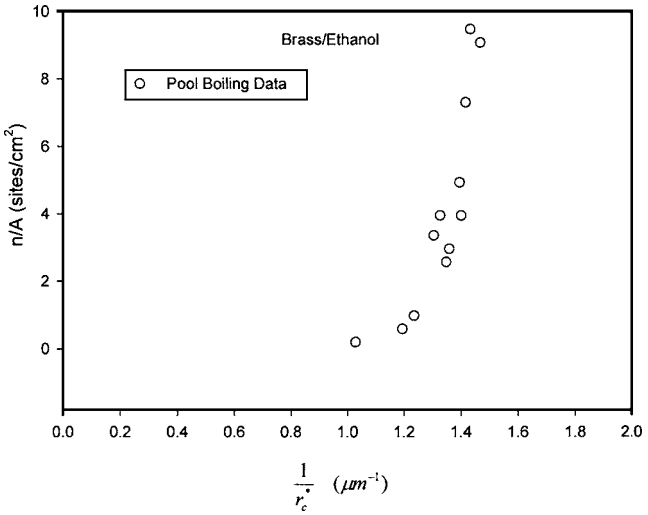

Fig. 11 Variation of pool boiling nucleation site density for ethanol on brass surface

expected due to the higher wettability with ethanol. However, once the incipience point is reached, small decreases in the critical radius result in very large increases in nucleation site density. This is shown more clearly in Fig. 11, where the ethanol on brass pool boiling nucleation site density is shown with a refined scale for the inverse of critical radius. The reason these data are so surprising is the gas nucleation experiments reveal that most cavities are flooded and a very large value of $1/r_c^*$ should be required to activate nucleation sites during pool boiling. Instead, very moderate values of $1/r_c^*$ result in a substantial number of nucleation sites during pool boiling. It would appear that these nucleation sites are activated due to some other mechanism than classical heterogeneous cavity vapor trapping.

Ethanol gas nucleation experiments were done on the stainless steel surface with very high $\Delta P/2\sigma$ (20 μm^{-1}) and due to flooding, at most two nucleation sites were activated. In contrast, Fig. 12 shows the variation of nucleation site density for pool boiling of ethanol on stainless steel with the inverse of the critical radius. A large nucleation site density is achieved at a very moderate critical radius. Slightly smaller critical radius is required for pool boiling on stainless steel than for brass to achieve a certain nucleation site density. However, once incipience is established, the

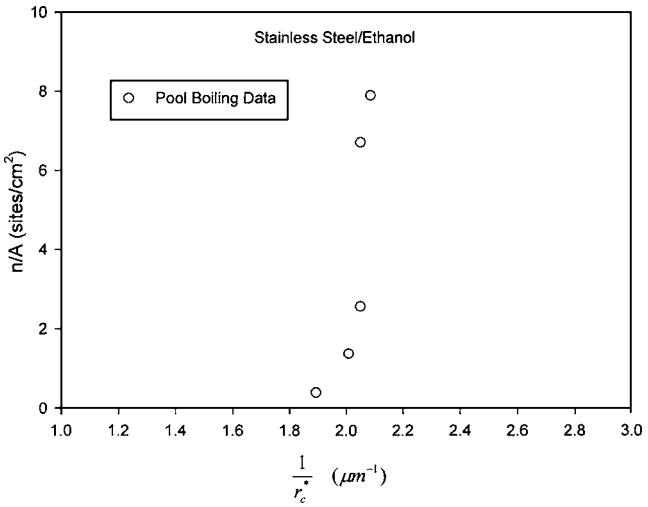

Fig. 12 Variation of pool boiling nucleation site density for ethanol on stainless steel surface

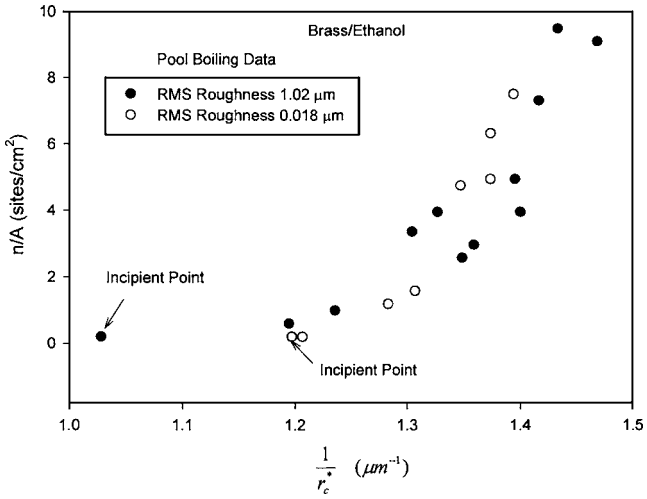

Fig. 13 Variation of pool boiling nucleation site density for ethanol on coarse and polished brass surfaces

pool boiling nucleation site density on stainless steel increases very rapidly with small decreases in the critical radius. This is in stark contrast to the gas nucleation experiments where it is extremely difficult to activate any nucleation sites due to cavity flooding.

If the variation of nucleation site density was controlled by some other mechanism than heterogeneous cavity vapor trapping, then on any given surface the nucleation site density should be independent of the surface roughness. In order to test an extreme case with ethanol, the brass surface was polished to a mirror-like finish. The measured rms roughness is 0.018 μm as compared with the rough brass surface that has a rms roughness of 1.02 μm. The nucleation site densities measured for the rough and polished brass surface are compared in Fig. 13. It is seen that slightly more superheat (1.7°C) is required to achieve incipience with the polished surface. However, once incipience is established, there is essentially no difference in the variation of nucleation sites on the coarse and polished surfaces. These results provide substantial additional evidence that another mechanism other than heterogeneous cavity vapor trapping is involved in seeding pool boiling nucleation sites.

6 Discussion

There was some speculation that some dissolved gas might precipitate out of the ethanol to form microbubbles, and these may be responsible for seeding the nucleation. To further explore the effect of dissolved gas in ethanol, a rigorous degassing procedure was done. The degassing procedure consisted of attaching a vacuum pump to the boiling chamber and pumping down the chamber with and without boiling through several cycles. No chemical analysis was done on the ethanol, so the degree of degassing that was achieved is uncertain. Subsequent to the degassing procedure it was found that the incipient points of ethanol on brass and stainless steel are very similar to those reported in Figs. 11 and 12. Furthermore, no microbubbles were visually observed in the liquid prior to incipience. So, microbubbles have been ruled out as the mechanism driving the present observations.

Recently, Theofanous et al. [21] reported nucleation site density measurements with pool boiling of water on a Ti film surface with a mean roughness of 4 nm. The surface was manufactured by electron beam metal vapor deposition on a glass substrate. It was found that the incipient superheat is approximately 10°C. According to cavity vapor trapping nucleation theory, the nano-scale surface features cannot activate nucleation sites at such low superheat. They speculated that cavity vapor trapping cannot be responsible for nucleation site formation.

Since the pioneering work of Corty and Foust [3] and Griffith and Wallis [22] heterogeneous nucleation theory based on cavity vapor trapping has been almost exclusively relied upon to predict incipience and nucleating characteristics of boiling systems. Based on the wealth of experimental observations reported in the literature and the incontrovertible microscopic measurements by Cornwell [6], there is no valid reason to doubt that vapor trapping cavities are responsible for seeding nucleation sites in boiling systems. However, there is ample evidence from this work and [21] that vapor trapping cavities are not exclusively responsible for seeding nucleation sites. Certainly there is no other **obvious** mechanism that is responsible for seeding nucleation sites when vapor trapping cavities are not available. Nevertheless, after an exhaustive search, a plausible mechanism has been identified that can explain the formation of boiling nucleation sites when vapor trapping cavities are not available. This mechanism is discussed next.

Most recently Tyrrell and Attard [23] obtained an atomic force microscope (AFM) image of very closely packed nanobubbles that cover a smooth hydrophobic surface (glass with 0.5 nm rms roughness) submerged in water. From theoretical considerations, stable spherical nanobubbles cannot exist because the high internal pressure would preclude equilibrium with the surroundings. However, the image reveals that the bubbles are pancake shaped with a large base and small height. The average height is reported to be 20–30 nm with a base diameter on the order of 200 nm. Modeling a nanobubble as the cap of a sphere, the radius of curvature of the cap is on the order of 0.3 μm. Although the dimensions of the AFM image are not quantitatively precise, since the AFM tip influences the shape of the deformable bubble, the uncertainty in the dimensions are on the order of several nanometers. A radius of curvature on the order of 1 μm is required to activate nucleation sites with low superheat. It is not unreasonable to expect that, due to statistical variations in shape and size, pancake shaped nanobubbles exist with the appropriate critical radius of curvature for nucleation, especially since close packed nanobubbles can merge. Although the detailed surface physics controlling the nanobubbles are not well understood, it is clear that there is a strong attractive force holding these pancake shaped bubbles on the solid surface. It has been observed that the nanobubbles easily cover the whole surface within 10–20 min after scraping the surface. Ishida et al. [24] also used AFM to image nanobubbles on hydrophobic surfaces. However, with water on a hydrophilic surface, nanobubbles were not observed. So, whether or not nanobubbles can cover an ethanol submerged surface is uncertain, especially since the mechanism for inducing and sustaining nanobubbles is not known. Nevertheless, the identification of nanobubbles as potential nucleation sites in boiling systems certainly requires further scrutiny.

The experimental observations of nanobubbles on a hydrophobic surface by Tyrrell and Attard [23] and Ishida et al. [24] remain controversial. However, indirect evidence of their existence has been provided by Tretheway and Meinhart [25] who measured a slip length on the order of 0.92 μm between a fluid and a hydrophobic surface. Tretheway and Meinhart [26] attribute the velocity slip to the presence of nanobubbles on the surface. They also report that increasing system pressure can inhibit the formation of nanobubbles and reduce the velocity slip. It is interesting that Mizukami et al. [27] report experiments with pool boiling of ethanol on a 0.3-mm-diam platinum wire in which incipience occurs with low superheat and no pre-pressurization of the boiling chamber. With moderate and high pre-pressurization, very high superheat is required for incipience. If nanobubbles do exist, the suppression of nanobubbles with pre-pressurization is a possible explanation for their results.

7 Concluding Remarks

The reliable prediction of nucleation site density in boiling systems based on first principles has been elusive. Some limited suc-

cess has been achieved by Wang and Dhir [7,9] with water on copper and with water on brass from this study shown in Fig. 8. However, these cases are the exception. Kenning [28] remarked, "At any time, a research community has a set of what should be working hypotheses, but which may become so firmly accepted that they are rarely questioned." The assumption that vapor trapping cavities are exclusively responsible for seeding heterogeneous boiling nucleation sites is one such hypothesis. The fact that pool boiling nucleation sites are easily formed using ethanol, a highly wetting fluid that floods cavities, is suggestive that another mechanism other than heterogeneous nucleation is responsible for the formation of nucleation sites. The existence of nanobubbles offers a plausible mechanism for seeding nucleation sites and requires extensive further scrutiny. Other mechanisms that can explain the collection of experimental observations should also be sought after.

Nomenclature

d = cavity diameter, μm
$f(d)$ = probability density function for finding cavities with diameter d, μm^{-1}
$g(\beta)$ = probability density function for finding cavities with half cone angle β, rad^{-1}
h_{fg} = latent heat of vaporization, J/kg
n/A = nucleation site density, cm^{-2}
N/A = number of cavities per unit area, cm^{-2}
ΔP = change in pressurization, MPa
r_c^* = critical cavity radius, μm
T_{sat} = saturation temperature, °C
ΔT_{sat} = wall superheat, °C
$(\Delta T_{sat})_{inc}$ = wall superheat at the incipient point, °C

Greek Symbols

θ = contact angle, rad
μ_d = mean of the cavity diameter distribution, μm
μ_β = mean of the cavity half cone angle distribution, rad
ρ_g = density of vapor, kg/m^3
σ = liquid/gas interfacial surface tension, N/m
σ_d = standard deviation of the cavity diameter distribution, μm
σ_β = standard deviation of the cavity half cone angle distribution, radians

References

[1] Gorenflo, D., Luke, A., and Danger, E., 1998, "Interactions Between Heat Transfer and Bubble Formation in Nucleate Boiling," *Heat Transfer 1998, Proceedings of 11th IHTC, Korea*, 1, pp. 149–174.
[2] Kenning, D. B. R., 2000, "Experimental Methods: Looking Closely at Bubble Nucleation," *Engineering Foundation Conference*, Boiling 2000, Keynote lecture.
[3] Corty, C., and Foust, A., 1955, "Surface Variables in Nucleate Boiling," Chem. Eng. Prog., Symp. Ser., **51**(17), pp. 1–12.
[4] Clark, H. B., Strenge, P. S., and Westwater, J. W., 1959, "Active Sites for Nucleate Boiling," Chem. Eng. Prog., Symp. Ser., **55**(29), pp. 103–110.
[5] Bankoff, S. G., 1958, "Entrainment of Gas in the Spreading of Liquid Over a Rough Surface," AIChE J., **4**(1), pp. 24–26.
[6] Cornwell, K., 1977, "Naturally Formed Boiling Site Cavities," Lett. Heat Mass Transfer, **4**, pp. 63–72.
[7] Wang, C. H., and Dhir, V. K., 1993, "Effect of Surface Wettability on Active Nucleation Site Density During Pool Boiling of Saturated Water," J. Heat Transfer, **115**, pp. 659–669.
[8] Yang, S. R., and Kim, R. H., 1988, "A Mathematical Model of the Pool Boiling Nucleation Site Density in Terms of the Surface Characteristics," Int. J. Heat Mass Transfer, **31**(6), pp. 1127–1135.
[9] Wang, C. H., and Dhir, V. K., 1993, "On the Gas Entrapment and Nucleation Site Density During Pool Boiling of Saturated Water," J. Heat Transfer, **115**, pp. 670–679.
[10] Hsu, Y. Y., 1962, "On the Size Range of Active Nucleation Cavities on a Heating Surface," J. Heat Transfer, **84**, pp. 207–216.
[11] Zeng, L. Z., and Klausner, J. F., 1993, "Nucleation Site Density in Forced Convection Boiling," J. Heat Transfer, **115**, pp. 215–221.
[12] Luke, A., 1997, "Pool Boiling Heat Transfer From Horizontal Tubes With Different Surface Roughness," Int. J. Refrig., **20**(8), pp. 561–574.
[13] Luke, A., and Gorenflo, D., 1999, "Nucleate Boiling Heat Transfer of HFCs and HCs in Heat Pump Application: State of the Art and New Developments," *Proc. 6th IEA Heat Pump Conference*, Berlin.
[14] Luke, A., and Gorenflo, D., 2000, "Heat Transfer and Size Distribution of Active Nucleation Sites in Boiling Propane Outside a Tube," Int. J. Therm. Sci., **39**, pp. 919–930.
[15] Brown, W. T., 1967, "Study of Flow Surface Boiling," Ph.D. thesis, Department of Mechanical Engineering, Massachusetts Institute of Technology.
[16] Eddington, R. I., and Kenning, D. B. R., 1978, "The Prediction of Flow Boiling Bubble Populations From Gas Bubble Nucleation Experiments," *Proc. 6th Int. Heat Transfer Conf.*, 1, pp. 275–280.
[17] Eddington, R. I., Kenning, D. B. R., and Korneichev, A. I., 1978, "Comparison of Gas and Vapor Bubble Nucleation on a Brass Surface in Water," Int. J. Heat Mass Transfer, **21**, pp. 855–862.
[18] Eddington, R. I., and Kenning, D. B. R., 1979, "The Effect of Contact Angle on Bubble Nucleation," Int. J. Heat Mass Transfer, **22**, pp. 1213–1236.
[19] Qi, Y., Klausner, J. F., and Mei, R., 2004, "Role of Surface Structure in Heterogeneous Nucleation," Int. J. Heat Mass Transfer, **47**, pp. 3097–3107.
[20] Cornwell, K., 1982, "On Boiling Incipience Due to Contact Angle Hysteresis," Int. J. Heat Mass Transfer, **25**, pp. 205–211.
[21] Theofanous, T. G., Tu, J. P., Dinh, A. T., and Dinh, T. N., 2002, "The Boiling Crisis Phenomenon. Part I: Nucleation and Nucleate Boiling Heat Transfer," Exp. Therm. Fluid Sci., **26**, pp. 775–792.
[22] Griffith, P., and Wallis, J. D., 1960, "The Role of Surface Conditions in Nucleate Boiling," Chem. Eng. Prog., Symp. Ser., **56**(30), pp. 49–63.
[23] Tyrell, J. W. G., and Attard, P., 2001, "Images of Nanobubbles on Hydrophobic Surfaces and Their Interactions," Phys. Rev. Lett., **87**, 176104.
[24] Ishida, N., Inoue, T., Miyahara, M., and Higashitani, K., 2000, "Nano Bubbles on a Hydrophobic Surface in Water Observed by Tapping-Mode Atomic Force Microscopy," Langmuir, **16**, pp. 6377–6380.
[25] Tretheway, D. C., and Meinhart, C. D., 2002, "Apparent Fluid Slip at Hydrophobic Microchannel Walls," Phys. Fluids, **14**(3), pp. 9–12.
[26] Tretheway, D. C., and Meinhart, C. D., 2004, "A Generating Mechanism for Apparent Fluid Slip in Hydrophobic Microchannels," Phys. Fluids, **16**(5), pp. 1509–1515.
[27] Mizukami, K., Furutani, H., Abe, F., and Mukasa, S., 1998, "Boiling Inception on Platinum Surface in Water and in Ethanol," *Heat Transfer 1998, Proceedings of 11th IHTC*, Kyongju, Korea, Vol. 29, pp. 461–466.
[28] Kenning, D. B. R., 1999, "What Do We Really Know About Nucleate Boiling?" *ImechE Conf. Trans., 6th UK Nat. Heat Transfer Conf.*, Edinburgh, Keynote Address, pp. 143–167.

Film Condensation of R-134a on Tube Arrays With Plain and Enhanced Surfaces: Part I—Experimental Heat Transfer Coefficients

D. Gstoehl

J. R. Thome[1]
e-mail: john.thome@epfl.ch

Laboratory of Heat and Mass Transfer,
Faculty of Engineering Sciences and Techniques,
Ecole Polytechnique Fédérale de Lausanne,
CH-1015 Lausanne, Switzerland

The aim of the present investigation was to study the effect of condensate inundation on the thermal performance of a vertical array of horizontal tubes with plain and enhanced surfaces. Refrigerant R-134a was condensed at a saturation temperature of 304 K *on tube arrays with up to ten tubes at pitches of* 25.5, 28.6, and 44.5 mm. *Notably, local condensing heat transfer coefficients were measured at the midpoint of each tube, as opposed to mean values. Four commercially available copper tubes with a nominal diameter of* 19.05 mm (0.75 in.) *were tested: a plain tube, a* 26 fpi/1024 fpm *low finned tube, and two tubes, with three-dimensional (3D) enhanced surface structures. At low liquid inundation rates, the tubes with 3D enhanced surface structures significantly outperformed the low finned tube. Increasing liquid inundation deteriorated the thermal performance of the 3D enhanced tubes, whereas it had nearly no affect on the low finned tube, resulting in a higher heat transfer coefficients for the low finned tube at high liquid film Reynolds numbers. All the tests were performed with minimal vapor shear.*
[DOI: 10.1115/1.2130400]

Keywords: condensation, refrigerant, R-134a, plain tube, finned tube, enhancement

Introduction

Condensation on single tubes has been widely studied analytically on plain and low finned tubes (but not three-dimensional (3D) enhanced surface tubes) and in numerous experimental investigations. Although for plain and two-dimensional (2D) finned tubes analytical models and empirical correlations have been developed, no general models have been established for three-dimensional finned tubes, for which the few existing prediction methods are always for one specific surface structure and fluid and, thus, lack generality. In order to judge the thermal performance of three-dimensional finned tubes, industry depends on experimental investigations. Although R-134a is widely used, only few data are available in literature for the 3D surfaces. For example, Chang et al. [1], Jung et al. [2], and Kumar et al. [3] performed measurements of single tube performance for condensation of R-134a on plain and enhanced tubes. Condensation in actual condensers may be very different from condensation on a single tube because the tubes are affected by an inundation of condensate from the neighboring tubes above. The effect on condensate inundation for R-134a was investigated experimentally in several studies. Cheng and Wang [4] conducted experiments on six tubes arranged in two rows, located side by side with three tubes one above the other in each row, set in nearly stationary vapor. Seven kinds of tubes were tested including three low finned tubes. Huber et al. [5–7] presented data for condensation of refrigerant R-134a on a five-rows-wide-by-five-rows-deep staggered tube bundle. They provided data for low finned tubes, enhanced tubes, and also a comparison with R-12. Rewerts et al. [8] studied the effect of R-134a inundation on enhanced tube geometries. They simulated the effect of condensate inundation up to a depth of 30 rows by introducing a two-phase refrigerant mixture into the test section. Kulis et al. [9] presented experimental data for R-134a and R-22 condensing on a staggered bundle of 19 finned tubes. Honda et al. [10,11] investigated the effect of vapor shear during condensation on staggered bundles of low finned and 3D enhanced tubes. Belghazi et al. [12,13] performed measurements with pure R-134a and different zeotropic mixtures with R-134a and R-23 on plain and enhanced tubes.

Without condensate inundation, the tubes with 3D-enhanced surface structures outperformed the low finned tubes, whereas the deterioration in heat transfer with inundation was found to be less pronounced for the low finned tubes. This difference in behavior was often attributed to differences in flow pattern on the low finned and 3D enhanced tubes. However, in many investigations, there was no visual access to observe the condensate flow, especially during bundle tests.

For this reason, the aim of the current investigation is to study condensation on an array of horizontal tubes in a test facility offering complete visual access to observe the condensation process of R-134a. Second, modern heat exchanger design softwares use an incremental thermal design approach, dividing the heat exchanger up into a multitude of small zones and calculating local heat transfer performance in each of these zones. In contrast, up until now, all condensation data have been obtained as mean values along the tube length (not withstanding the varying axial conditions that influence the heat transfer process), which are not optimal for developing local design methods. Since local data are what are really needed to progress further in this research area, a temperature-profile approach already used successfully for in-tube boiling and bundle boiling in the Laboratory of Heat and Mass Transfer (LTCM) at Ecole Polytechnique Fédérale de Lausanne (EPFL) will be applied for the first time here to shell-side condensation (to our knowledge) to obtain local heat transfer coefficients

[1]To whom correspondence should be addressed.

Contributed by the Heat Transfer Division of ASME for publication in the JOURNAL OF HEAT TRANSFER. Manuscript received November 5, 2004; final manuscript received July 12, 2005. Review conducted by Raj M. Manglik.

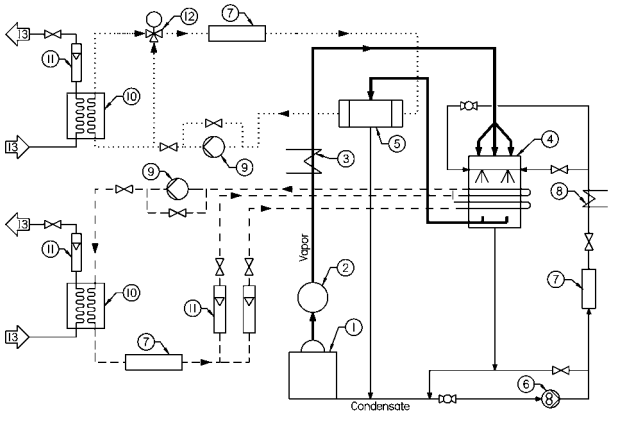

Fig. 1 Schematic of the experimental apparatus

(actually perimeter-averaged values at the midpoint of each tube). Furthermore, the water flow rate is alternated between left and right in each successive tube row to attain the most uniform axial distribution of the condensate feasible and thus create "ideal" measurement conditions, as opposed to a one-tube-pass design that would create an axial migration of condensate toward the lower heat flux end of the bundle and result in a test section design effect on the data.

This paper focuses on the experimental determination of the heat transfer coefficients. New predictive methods based on these experimental results and visual observations of the liquid flow are proposed in Part II of this paper [14]. Visualizations of R-134a flowing on the array under adiabatic and condensing conditions have been shown in Gstoehl and Thome [15].

Description of Experimental Facility and Test Sections

A new falling film heat transfer test facility has been built, which can be operated in condensation or evaporation test mode. A schematic diagram of the test facility in condensation test mode is given in Fig. 1; for the evaporation test mode, refer to Roques [16]. The test facility consists of a natural-circulation loop for R-134a (solid lines) and forced-circulation loops for the cooling water for the test section (dashed lines) and for cooling glycol for the auxiliary condenser (dotted lines).

Refrigerant Loop. The refrigerant circuit is basically comprised of an electrically heated evaporator to maintain the desired saturation condition, an auxiliary condenser to create a vapor flow in the test section, and the test section itself. Refrigerant vapor is generated in the flooded evaporator with immersion heating elements that can provide a heating capacity of up to 60 kW (1). The saturated vapor leaving the evaporator passes through the droplet separator (2). This large volume vessel slows down the vapor flow such that the low velocity allows droplets entrained from the evaporator to settle out and return back to the evaporator. This ensures that the vapor does not contain droplets. After leaving the droplet separator, the vapor passes into the superheater, which is a 1.1 m long section of copper pipe wrapped with an electrical heating tape (3). The heating capacity of the vapor superheater is 1 kW. It was only used at low power to compensate for heat losses to the environment and it was adjusted so that the vapor arrives a little superheated at the test section (<0.3 K). The vapor enters the test section through three large inlets at the top in order to distribute it evenly within the test section (4). In the test section, the vapor is partially condensed on the tubes. The excess vapor leaves the test section in the lower part through four outlets (two on the front side and two at the back side). Then the vapor goes to the auxiliary condenser, where it is condensed completely (5). The condensate formed in the test section and in the auxiliary condenser drains back to the evaporator by gravity.

In order to study the effect of liquid inundation on the performance of the tubes, the test section is equipped with a system to distribute liquid refrigerant onto the top tube. In this way not only can the behavior of the top tube rows of a condenser be investigated without overfeed, but also the conditions on lower tube rows in large condensers can be simulated.

While operating, most of the liquid is in the flooded evaporator, which acts as a liquid reservoir in the circuit (1). From there the refrigerant flows through a filter/dryer to the magnetically driven gear pump (6). Bypass piping together with a frequency controller on the pump are used to achieve the desired liquid flow rate. The liquid refrigerant then passes through a Coriolis mass flowmeter (7) to the liquid heater (8). The liquid heater consists of two electric heating elements in series wrapped tightly around the copper pipe with a heating capacity of 500 W each. The liquid heater is used to bring the refrigerant close to the saturation conditions (with <0.8 K of subcooling). The liquid refrigerant enters the test section by two inlets; one inlet is located on the left and one on the right. Both inlets are equipped with valves to control the distribution in the test section. The liquid refrigerant from the overfeed and the condensate generated on the tubes leave the test section through an outlet at the bottom.

Water Loop. The cooling water flowing inside the test tubes is heated up in the test section and cooled back down with industrial water. This forced-circulation loop for the cooling water is illustrated in Fig. 1 with dashed lines. The circuit is equipped with a centrifugal pump (9). An electronic speed controller together with a bypass and a valve affords good precision in the mass flow adjustment. After the pump, the water goes into a liquid-liquid heat exchanger (10). In this heat exchanger, the test-section water exchanges heat with industrial water (13). This is water from Lake Geneva, available in the laboratory at an almost constant temperature of 280 K (7°C). The cooling capacity of the exchanger is set by adjusting the mass flow rate of industrial water. The total mass flow rate of water circulating in the loop is then measured with a Coriolis mass flowmeter (7).

The main flow of water is then split to the subcircuits of the test section. Each subcircuit has its own float flowmeter (11) and valve to control its flow rate and thus set the water distribution uniformly between the subcircuits. The goal is to have the same flow rate in all subcircuits. There are up to five subcircuits in the main circuit (only two are shown in Fig. 1). A subcircuit usually has two tube passes, i.e., water goes in a test tube in one direction (left to right) and comes back through the test tube just above in the opposite direction within the test section (4). With this setup, the water temperature profiles in the two tubes are opposed. The quantity of liquid refrigerant condensed after each two tubes in the test array is thus nearly uniform along the tube length. In contrast, tests in other published projects often use only one water pass, which creates an imbalance in the condensate distribution along the tubes and hence data dependent on the test setup, which is to be avoided. After the test section, the subcircuits merge and the water flows back to the pump.

Glycol Loop. Glycol is used as a cold source for the auxiliary condenser of the test facility. The glycol is heated up when it passes through the auxiliary condenser and is also cooled by industrial water. This circulation loop of glycol is shown in Fig. 1 as dotted lines. The circuit is equipped with a centrifugal pump (9). An electronic speed controller together with a bypass and a valve are used for the glycol mass flow adjustment. After the pump, a part of the glycol passes to a liquid-liquid heat exchanger (10). In this heat exchanger, the glycol is cooled by industrial water (13). As the industrial water is at constant temperature, the cooling capacity of the heat exchanger is set by adjusting the mass flow of

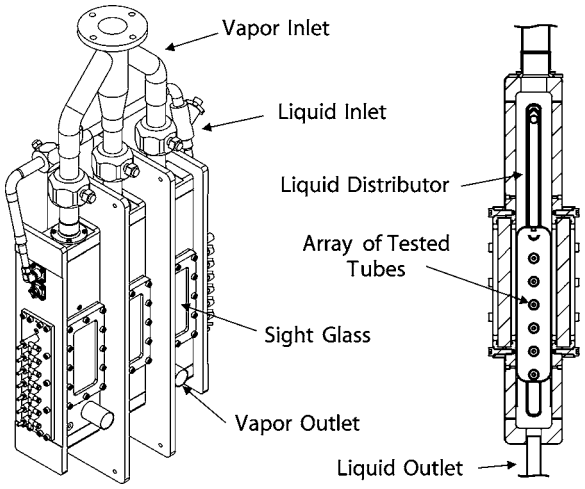

Fig. 2 Test section

the water by a hand valve. The cooled glycol leaving the heat exchanger flows to the motorized three-way valve (12). In this valve cold glycol is mixed with the glycol that did not pass through the heat exchanger to obtain the desired temperature. This recirculation allows a fine adjustment of the glycol temperature. The glycol mass flow is then measured by a Coriolis flowmeter (7). The conditioned glycol then goes to the auxiliary condenser, which is a three-pass condenser with a design capacity of 50 kW.

Test Section. The test section is a rectangular stainless-steel vessel illustrated in Fig. 2. Its internal dimensions are $554 \times 650 \times 69$ mm ($W \times H \times D$). In the present investigation the heat transfer coefficient during condensation on the outside of horizontal tubes is measured. The tubes tested have a nominal outer diameter of 19.05 mm (0.75 in.) and an active length of 554 mm. They are arranged in a vertical array. The end plates, which hold the tubes on the left and right, are removable. This allows the set of end plates to be changed to obtain different distances between the tubes. Depending on the tube pitch, arrays of 6–10 tubes can be tested. In order to have full visual access to observe the condensate flow on the tubes, the test section is equipped with six large windows (120×250 mm). The vapor velocity in the test section is always below 0.2 m/s and vapor feed to vapor condensed ratio was typically about 2.

Special care has been taken to achieve uniform distribution of liquid refrigerant along the top tube in the array. The distributor designed for this purpose is a rectangular box inserted in the test section above the tube array; for details refer to Gstöhl [17] and Gstoehl and Thome [15]. At high liquid flow rates a continuous sheet leaves the distributor, but at low flow rates the distribution of the droplets is not uniform. For this reason a half tube was added just below the distributor. The bottom of the half tube was machined to form a sharp edge. The liquid falls locally along the half tube and overflows on both sides. The sharp edge forces the liquid to leave at the bottom of the half tube. By rotating the half tube, the direction of the liquid leaving the tube at the edge can be adjusted to ensure that the liquid falls exactly on the top of the first test tube. The temperature of the overfeed liquid is controlled by a heater and monitored by thermocouples to maintain its subcooling to <0.8 K.

A new type of heat transfer measurement strategy has been developed in order to obtain local values of the heat transfer coefficient at the midpoint of each tube in the array. In other previous published studies, only the inlet and outlet temperatures of the water have been measured. With that type of measurement, only a mean heat transfer coefficient for the entire tube can be obtained, but with a variation of heat flux and inundation along the tube. In

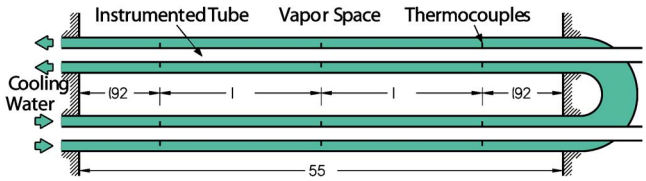

Fig. 3 Schematic of the instrumentation setup for a pair of tubes to measure the temperature profile of the water flowing inside

this study, a stainless-steel tube with an external diameter of $D_{\text{stainless}} = 8$ mm instrumented with six thermocouples is inserted inside each test tube. A schematic of this instrumentation setup is depicted in Fig. 3. The thermocouples are located at the three positions indicated along the axial direction of the tube. At every location, one thermocouple (0.5 mm dia) is facing upward and one is facing downward to measure the temperature of the water flowing in the annulus between the stainless-steel tube and the tested tube. The thermocouple leads are all brought out at one end on the inside of the stainless-steel tube.

In addition, the stainless tube helps to increase the water side coefficient as the flow area for the water is reduced and its entrance length is reduced. In pretests, a difference of 0.2 K or larger was observed between the thermocouple facing upward and the one facing downward at individual locations in the water-side annulus. To increase the accuracy of the measurement of the water temperature, a wire (not shown) with a rectangular cross section (0.9×2.8 mm) has been wound helically (12 mm pitch) around the stainless-steel tube. This promoted mixing, minimized any thermal entrance effect, and further increased the water-side heat transfer coefficient. The difference in readings at one axial location was thus reduced typically to <0.05 K.

The vapor pressure in the test section is measured with two absolute pressure transducers. One is connected to the test section above the array of tubes and one below. The vapor temperature above the tubes is measured with six thermocouples: three are situated on the front and three on the rear of the test section. They are 1 mm in diameter and the junctions are located in the middle between the test section wall and the distributor. The temperature of the liquid entering the test section is measured with one thermocouple inserted in each inlet.

A National Instruments SCXI data acquisition system was used with LABVIEW to receive and store the data from the instrumentation. All instruments were carefully calibrated. The thermocouples were calibrated using a platinum thermometer in temperature steps of 3 K from 276 to 306 K. To verify satisfactory thermocouple calibration, thermocouple measurement checks under adiabatic conditions were made prior to condensation measurements. A second computer equipped with the same SCXI system was used to control the test facility (mainly to maintain the desired saturation pressure by controlling the electrical power of the evaporator). All the important parameters were calculated and displayed online on the two computers to impose optimum test conditions.

Tested Tube Configurations. In order to study the effect of the distance between the tubes, three different tube arrangements have been tested. The tube pitches, center to center, were 25.45, 28.6, and 44.5 mm (the largest representing that typical of actual condensers with staggered tube layouts). With the nominal tube diameter of 19.05 mm (0.75 in.), intertube spacings of 6.4, 9.5, and 25.5 mm are obtained. The distance between the distribution half tube and the top tube was equal to the distance between the tubes to reproduce the same falling effect. At the smallest tube pitch of 25.5 mm, ten tubes were installed. At the tube pitch of 28.6 mm, nine tubes were installed. At the largest tube pitch of 44.5 mm, only six tubes could be mounted.

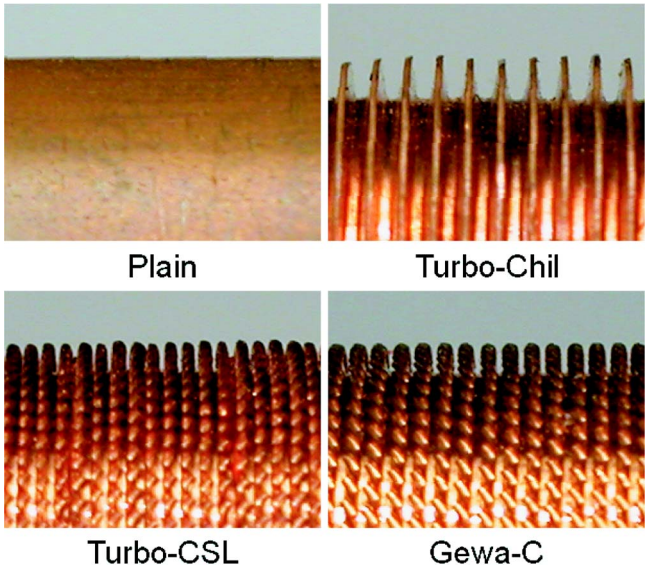

Fig. 4 Tubes tested in this study

Four commercially available copper tubes were tested: a plain tube, a standard 26 fpi/1024 fpm low finned tube (Turbo-Chil) and two condensation tubes with 3D enhanced surfaces (Turbo-CSL and Gewa-C). Close-up pictures of the external tube surfaces are given in Fig. 4.

The two 3D-enhanced condensation tubes are low finned tubes that were obliquely cut through the upper part of the fins. The Turbo-Chil, the Turbo-CSL, and the Gewa-C tube have helical ribs on the inside to increase the water-side heat transfer coefficient. The tube diameter at the fin tip D_o, and the external and internal root diameters, D_{or} and D_i, respectively, are given in Table 1.

The fin pitch of the Turbo-Chil tube determined on micrographs of an axial cut corresponded to a fin density of 27.2 fpi, which is a little higher than the nominal of 26 fpi cited by the manufacturer. It was also observed on micrographs of the Turbo-Chil tube that the heights of the fins were not uniform. The values of the fin height measured on micrographs ranged from 1.24 to 1.47 mm with a mean value of 1.36 mm. The fin thickness at the tip t_t was 0.18 mm, and the fin thickness at the base t_b was 0.51 mm.

Test Conditions

Four types of tubes were tested at three different intertube spacings. During the measurements, the heat flux was kept constant and liquid overfeed rate was increased stepwise up to film Reynolds numbers of 3000. Measurements with increasing overfeed rate were performed at three heat flux levels. The nominal heat fluxes were 20, 40, and 60 kW/m^2 for the three enhanced tubes; for the plain tube lower heat fluxes of 6, 12, and 20 kW/m^2 were tested because of its lower thermal performance. The *nominal heat flux* is approximately the average heat flux of the tube array, whereas the *actual local heat fluxes* are obtained at the midpoints of the tubes, as will be discussed in the next section.

Table 1 Geometrical specifications of the tubes tested

Tube	D_o	D_{or}	D_i
Plain Tube	18.91		16.22
Turbo-Chil	18.94	15.99	14.65
Turbo-CSL	18.90	17.15	15.94
Gewa-C	18.88	17.06	15.54

All dimensions are in mm

Table 2 Experimental database for R-134a at a saturation temperature of 304 K

Tube	Turbo-CSL	Gewa-C	Turbo-Chil	Plain Tube
q, kW/m^2	11.6 to 99.8	12.9 to 95.5	12.7 to 72.9	3.60 to 22.9
T_{sat}-T_w, K	0.44 to 12.8	0.43 to 10.9	0.66 to 5.83	2.50 to 16.3
α_i, kW/m^{2}K	13.1 to 27.3	18.2 to 30.8	16.1 to 24.9	3.5 to 4.4
α_o, kW/m^{2}K	4.10 to 32.1	5.00 to 33.8	10.2 to 24.0	0.9 to 2.6

In addition, measurements without liquid overfeed were taken over the same heat flux range mentioned above. Because of the current two-pass setup, the heat fluxes achieved on the odd and even tubes at one nominal heat flux varied substantially. An overview of the complete database established in the current investigation is given in Table 2. The ranges of the main variables are listed for all types of tubes.

Data Reduction and Accuracies

The local external heat transfer coefficient at the midpoint of each tube is derived from temperature measurements of the cooling water flowing inside the tubes by a modified Wilson plot approach. Using water flowing through the tubes to condense the refrigerant on the outside of the tubes, the water undergoes a temperature change while the phase changing refrigerant stays at the same saturation temperature. This produces a change in local heat flux as the temperature difference between the water and the refrigerant decreases along the length of the tubes. The internally mounted thermocouples measuring the water temperature within the tubes in the axial direction permit the water-temperature profile to be determined as a function of the distance x along the tubes

$$T_{\text{wat}} = f(x) \tag{1}$$

Then, the local heat flux on the outside of the tube can be derived from the water temperature profile as

$$q_o = \frac{\dot{m} c_{p,\text{wat}}}{\pi D_o} \frac{dT_{\text{wat}}}{dx} \tag{2}$$

where $\dot{m}$ is the water mass flow rate and $c_{p,\text{wat}}$ the specific heat of water. The local overall heat transfer coefficient U_o is obtained from its definition

$$U_o = \frac{q_o}{T_{\text{sat}} - T_{\text{wat}}} \tag{3}$$

with the saturation temperature of the refrigerant T_{sat} and the local bulk temperature of the water T_{wat}. The condensing-side heat transfer coefficient α_o can thus be calculated from

$$\alpha_o = \left[\frac{1}{U_o} - \frac{1}{\alpha_i} \left(\frac{D_o}{D_i} \right) - r_w \right]^{-1} \tag{4}$$

where α_i is the water-side heat transfer coefficient and r_w is the thermal resistance of the copper tube wall given by

$$r_w = \frac{D_o}{2\lambda_w} \ln\left(\frac{D_{or}}{D_i} \right) \tag{5}$$

D_i is the inside diameter of the tube, D_{or} is the outside root diameter, and λ_w is the thermal conductivity of the tube material. All values of α_o reported here are based on the nominal surface area of the tubes at their fin tip diameter D_o.

The inside heat transfer coefficient α_i is determined by a modified Wilson plot approach. The essence of this technique is that the form of the relationships for the heat transfer on the internal and external side of the tube are known apart of certain constants. The modified Wilson plot technique consists of measuring the overall heat transfer for several conditions (at different water Reynolds number covering the expected range in the experiments) and correlating all the results to find the unknown constants. The method used in the present study is based on the modified Wilson plot as proposed by Briggs and Young [18].

Typically, the modified Wilson plot method is used to determine a leading empirical constant in the Sieder and Tate correlation [19] for single phase internal flow. One disadvantage of this is that the Sieder and Tate equation is only suitable for fully turbulent flows ($\mathrm{Re_{wat}} > 10{,}000$). For this reason, in the present study the Gnielinski correlation [20] for single phase internal flow is used for the internal heat transfer coefficient. This correlation is suitable for Reynolds numbers corresponding to part of the transition region ($4000 < \mathrm{Re_{wat}} < 10{,}000$) as well as the fully turbulent regime up to $\mathrm{Re_{wat}} = 10^6$. Working with small water Reynolds numbers increases the accuracy in the determination of the local heat flux. The internal heat transfer in the annulus can be written as

$$\alpha_i = C_i \alpha_{\mathrm{Gni}} \tag{6}$$

where C_i is an empirical factor to be found and α_{Gni} according to Gnielinski is

$$\alpha_{\mathrm{Gni}} = \frac{f/8(\mathrm{Re}_{Dh} - 1000)\mathrm{Pr_{wat}}}{1 + 12.7(f/8)^{1/2}(\mathrm{Pr}_{\mathrm{wat}}^{2/3} - 1)} \frac{\lambda_{\mathrm{wat}}}{D_h} \tag{7}$$

and $D_h = D_i - D_{\mathrm{stainless}}$ is the hydraulic diameter for the water in the annulus. For the friction factor f, the correlation $f = (0.79 \ln \mathrm{Re_{wat}} - 1.64)^{-2}$ developed by Petukhov in [19] for plain tubes is used.

The leading constant C_i characterizes the influence of the inside surface enhancement, the annular section, and the copper wire wound around the inner stainless-steel tube on heat transfer. In the present investigation the modified Wilson plot approach to determine the values of C_i for all types of tubes was implemented using nucleate pool boiling on the outside of the tubes. Compared to the alternative modified Wilson plot approach using condensation data, this offers the advantage of large external heat transfer coefficients, which are desirable for determining C_i at large heat fluxes where the measurement uncertainties are smaller. In addition, the heat transfer coefficients in pool boiling increase with heat flux and are nearly uniform around the tube perimeter. In nucleate pool boiling, the heat transfer coefficient can be described by following relation:

$$\alpha_o = C_o q_o^n \tag{8}$$

Substitution of Eqs. (6) and (8) in Eq. (4) and rearranging leads to

$$\left(\frac{1}{U_o} - r_w\right) q_o^n = \frac{1}{C_i}\left(\frac{q_o^n}{\alpha_{\mathrm{Gni}}}\right)\frac{D_o}{D_i} + \frac{1}{C_o} \tag{9}$$

This equation has a simple linear form of

$$Y = \frac{1}{C_i} X + \frac{1}{C_o} \tag{10}$$

With a change of the water velocity, the values of X and Y are altered. The modified Wilson plot technique consists of measuring representative points of this linear relation and performing a linear regression on them. The inverse slope of this fit gives the value of C_i and the inverse of the y-axis intercept yields C_o. Our interest is the value of C_i, as in combination with the Gnielinski correlation the water-side coefficient can be determined according to Eq. (6).

In Eq. (8) the value $n = 0.7$ was used as a first estimate for all types of tubes and then its value was determined afterward by an iterative procedure described in Gstöhl [17]. For the Wilson plot tests, the test section was flooded and water Reynolds number was varied from 6000 to 16,000. The tests were performed at fixed heat duties in order to minimize the effect of the assumption made by Eq. (8). For all four types of tubes, tests were performed at different heat flux levels and for different tubes to obtain the following values of C_i: 1.27 ± 0.1 for the plain tube, 2.94 ± 0.2 for the Turbo-Chil tube, 3.83 ± 0.2 for the Turbo-CSL tube, and 3.99 ± 0.2 for the Gewa-C tube.

Alternatively, assuming a heat flux dependency of $-1/3$ typical of plain and low finned tube models (suggested to us by Rose [21]), a modified Wilson plot analysis was also performed on the single plain tube and low finned tube data (top tube row data without overfeed), resulting in values of $C_i = 1.25$ and $C_i = 2.82$, respectively, which agree well with those from the pool boiling results. However, for all tubes the values of C_i determined using nucleate pool boiling were used in the data processing.

In the data reduction, the physical properties of R-134a were evaluated using the software REFPROP at a saturation temperature that was derived from the mean value measured by the two pressure transducers. The physical properties of water were determined with the software EES.

With the help of Eqs. (2)–(7), the heat transfer on the outside of the tube can be calculated from the measured water-temperature profile, the water mass flow rate, and the saturation temperature of the refrigerant. For a given water-temperature profile, the outside heat transfer coefficient can be calculated at any location along the axis of the tube. However, in this study the coefficient α_o is only evaluated at the midpoint along each tube, where the most accurate measurement can be made.

The water-temperature profile is approximated by a second-order polynomial fit of the six thermocouples at the three axial locations.

A propagation of error analysis was performed to estimate the accuracies of the local heat transfer coefficients [17]. The estimated accuracies for all types of tubes at the three nominal heat flux levels are given in Table 3.

The uncertainty in the local heat transfer coefficient decreases with increasing heat flux. For a higher heat flux, the temperature differences become larger, which means that the relative error of a temperature difference decreases for a constant absolute error in the temperature measurement. In laminar film condensation, the external heat transfer coefficient is determined by the thickness of the condensate film. A low heat flux or a low inundation rate creates a thin condensate film and hence a high heat transfer coefficient. In this case, the error in the measurement of the external heat transfer coefficient caused by the uncertainty of the internal heat transfer coefficient increases as the heat flux decreases.

The propagation of error analysis has been applied to each experimental data point. For all measurements, the experimental un-

Table 3 Mean relative errors in local heat transfer coefficients at the three nominal heat flux levels

	$\Delta\alpha_o/\alpha_o$		
Tube	q_o=20kW/m^2	q_o=40kW/m^2	q_o=60kW/m^2
Turbo-CSL	10.6%	6.1%	4.4%
Gewa-C	10.7%	6.3%	4.3%
Turbo-Chil	13.0%	8.8%	6.1%
	q_o=6kW/m^2	q_o=12kW/m^2	q_o=20kW/m^2
Plain Tube	12.0%	7.4%	5.7%

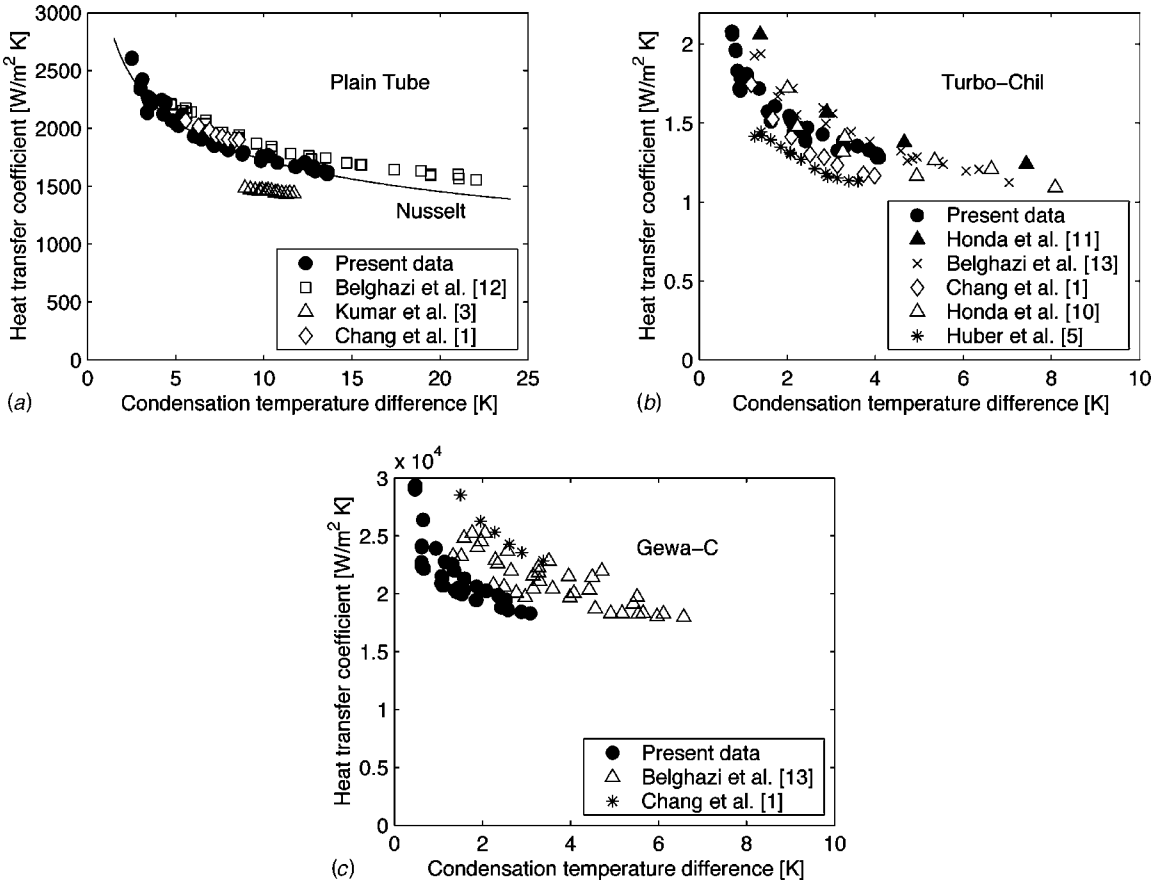

Fig. 5 Condensation on the top tube without liquid overfeed

certainty of the heat transfer coefficient α_o is, on average, ±8.3%, with 90% of points having an uncertainty less than ±12.8%, and all points less than ±20.5%.

The dominating parameters in the propagation of error analysis were found to be the measurements of the water temperatures and the internal heat transfer coefficient (due to the error on C_i). In order to minimize the experimental errors during the experiments, the propagation of error analysis was implemented directly in the LABVIEW software on the data acquisition computer. This allowed the mass flow rate to be adjusted (to adjust α_i) during the measurements to obtain minimum experimental errors depending on the measured heat fluxes.

Experimental Results

Comparison of Single Tube Data With Other Investigations. R-134a is now a widely used refrigerant, but only few data are available in literature for direct comparison to the tubes tested here. A comparison of the present experimental data to experimental data of R-134a of other investigations is made in Fig. 5. The data points of these investigations were digitized from the publications.

For plain tubes in Fig. 5(*a*), Belghazi et al. [12] performed measurements on a 13×3 bundle of smooth horizontal tubes. They also reported data of the heat transfer coefficient on the first row for condensation of R-134a at a saturation temperature of 40°C. Their values are slightly higher than the values for the plain tube in the present study. This might be because the tubes they tested were 16.8 mm dia as opposed to 18.91 mm used in the present investigation. Smaller tubes tend to have a higher heat transfer coefficient as the condensing length is shorter (i.e., as per Nussselt's theory). Kumar et al. [3] performed single tube tests with R-134a condensing on a plain tube which was 21.35 mm dia. The data they obtained at a saturation temperature of 39°C are lower than in the present study because of the increased condensing length. Chang et al. [1] conducted experiments to study the condensation heat transfer characteristics of horizontal enhanced tubes. He tested a plain tube and different enhanced tubes, including a 26 fpi low fin tube and a Gewa-C tube. Their experimental points for the plain tube with a diameter of 19.03 mm at a saturation temperature of 40.6°C are close to those of the current investigation. There is also an effect of the saturation temperature, due to the change in physical properties. However, according to Nusselt's theory an increase of the saturation temperature from 31°C in the current study to 40°C results in only a 4% decrease of the heat transfer coefficients.

For the plain tube, a comparison with Nusselt's well-known equation for condensation on a single tube is also shown in Fig. 5(*a*), evaluating the physical properties at the saturation temperature. On average, all data measured on the top tube in the array are 1.0% above Nusselt's prediction. Taking into account the subcooling of the condensate by the use of an effective latent heat of evaporation $h'_{LV}=h_{LV}[1+0.68c_{p,L}(T_{\text{sat}}-T_w)/h_{LV}]$ [22] and evaluating the physical properties at an effective film temperature, $T_w+0.25(T_{\text{sat}}-T_w)$ as proposed by Drew [23], the current data are overpredicted on average by 2.2%. This difference is in the range of the scatter of the measured values and smaller than the uncertainty in the measurement of the heat transfer coefficients. For this reason, the effect of subcooling was not taken into account and the physical properties were evaluated at the saturation temperature for all further comparisons.

A comparison for the Turbo-Chil tube is given in Fig. 5(*b*) on the right. More data are available in the literature for condensation of R-134a on 26 fpi low fin tubes than for plain tubes. Honda et al. [11] studied the condensation of R-134a on a staggered bundle

of finned tubes, including the effect of vapor shear. For the comparison here, only their data at the lowest vapor velocity (7 m/s) were taken. The geometrical specification of their tube is close to the Turbo-Chil tested in the present investigation, but their measured values of the heat transfer coefficient are a little higher, which might be due the small dimensional differences. Belghazi et al. [13] gave data for the heat transfer coefficient on the top row in their bundle of Gewa-K26 tubes, 26 fpi low fin tubes from Wieland. Their experimental data for their low finned tube are a little higher than the present data. This might be due to the larger fin height of their tubes, which is 1.5 mm as opposed to 1.36 mm of the tubes used in the present study. Chang et al. [1] tested a 26 fpi low finned tube with a fin height of 1.16 mm. Their experimental data are a little lower than the present data at higher condensate temperature differences. Honda et al. [10] tested a bundle of smaller diameter low finned tubes. Their tubes were 15.6 mm dia, but had approximately the same fin height of 1.43 mm. Their data are a little higher than the present data, but lower than their data for the larger tubes. Condensation on low finned tubes is controlled by surface tension with the fin height as the characteristic length, not the tube diameter. Huber et al. [5] studied condensation of R-134a on a 5×5 staggered bundle of 26 fpi low fin tubes. Their tubes were 18.8 mm dia and had a fin height of 1.45 mm. They provided the experimental data in a tabular format. The heat transfer coefficients for the first row are listed in their publication, but only the average bundle heat flux is mentioned. For the comparison here, the condensation temperature difference was calculated based on the average bundle heat flux. Their data were a little lower than the present data.

A comparison of the heat transfer performance of the 3D enhanced tubes Turbo-CSL and Gewa-C to independent data is difficult. These geometries are only produced by the individual manufacturers and few data are available. No published data are currently available in the literature for the Turbo-CSL tube to our knowledge. A comparison of the heat transfer performance for the Gewa-C is also given in Fig. 5. Belghazi et al. [13] tested a Gewa C+ tube and Chang et al. [1] tested a Gewa-C tube. The geometric specifications (tube diameter, fin pitch, fin height) are very close to the ones of the Gewa-C tube used in the present investigations, but the fins of the Gewa C+ tube were notched differently and the heat transfer coefficients measured in these studies are higher than the present data. In both studies, the differences may be the fact that they measured mean values for the whole length of tube as opposed to local values obtained in the present study.

A comparison for the Turbo-Chil top tube data and a selection of correlations for condensation on a single horizontal low finned tube available in the literature is shown in Fig. 6. For the calculation of the heat transfer coefficient of the Turbo-Chil tube, the actual fin pitch (0.94 mm), the mean value of the fin height (1.36 mm), and the diameter at the fin root (15.99 mm) were used in the calculations. The heat transfer coefficient was then related to the nominal area of the low finned tube using the diameter at the fin tip D_o. For all calculations, the physical properties of the refrigerant have been evaluated at the saturation temperature, except for the model of Sreepathi et al. [24], who mentioned that they evaluated the physical properties at $T_w+0.5(T_{sat}-T_w)$. The mean relative errors compared to the measured data for the low finned tube are also given in Fig. 6. Surprisingly, the simple model of Beatty and Katz [25] is very close to the measured data, even though this model does not take into account the effects of surface tension. They assumed that the entire tube surface was active for condensation and that no condensate retention occurred, and they neglected the surface tension drainage from the fin toward the fin root. In the present situation, the overestimation of active surface area seems to compensate for the underestimation of the increase in heat transfer on the fins due to thinning of the liquid film by surface tension. The fin efficiency, following the recommendation of Beatty and Katz, was set to one, which gives higher values for the heat transfer coefficient than when using the actual fin efficiency.

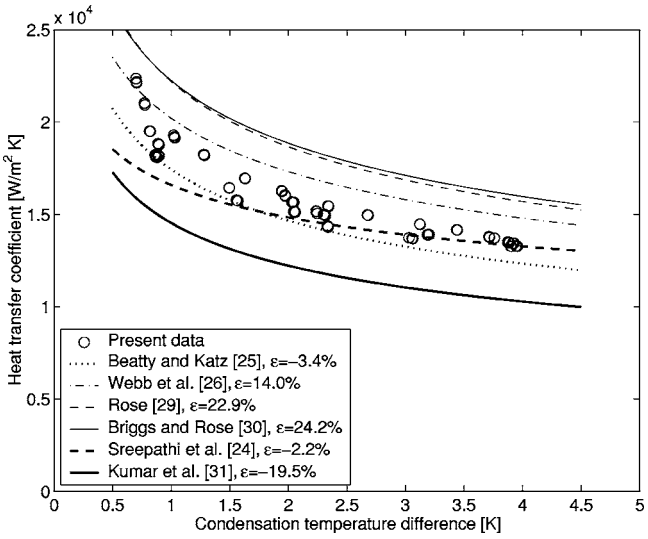

Fig. 6 Comparison of single low finned tube data with different correlations (*e*=mean relative error)

An early model for condensation on horizontal integral-fin tubes, including the effect of surface tension, was proposed by Webb et al. [26]. In this method, they use an Adamek fin profile to predict the heat transfer coefficient on the fins involving the determination of the fin shape parameter ς. In the present evaluation of their model, the condensation on the fins was predicted using their earlier simplified linear pressure gradient model described in [27] as suggested by Thome [28] in order to avoid the determination of the shape parameter from the data. However, Rudy and Webb [27] showed that this linear pressure gradient model lacks general validity; they do not recommend its use. Evaluating their model in this way overestimates the measured heat transfer coefficient by 14%.

More recently, Rose [29] proposed a semi-empirical method for condensation on a low finned tube with a trapezoidal fin shape. This method overestimates the measured heat transfer coefficient by ~23%. Briggs and Rose [30] extended the model by adding the fin efficiency, but they assumed only rectangular fin profiles. For the evaluation of this model, a rectangular fin shape with average fin thickness $t=(t_t+t_b)/2$ was used. The values obtained from this model are very close to the previous values of the model of Rose, but larger because of the fin shape effect.

Sreepathi et al. [24] developed a correlation for a trapezoidal fin shape including fin efficiency effects. As seen on Fig. 6, this model slightly underpredicts the present data at low condensate temperature differences and slightly overpredicts the data at high condensate temperature differences. The mean deviation with respect to all measured data is only −2%. By the way, neglecting the effect of fin efficiency, this model would overestimate the measured data by ~9%.

Kumar et al. [31] recently presented a very easy-to-use correlation. This correlation underestimates the present data by ~20%, which is smaller than the deviation of 35% they observed in a comparison with data from 13 other investigators. Considering that all these methods typically claim to be accurate to about ±20%, the deviations are within expectations and no conclusion about which is the best model can be drawn here.

Because of the complex surface structure of the 3D enhanced tubes, no analytical models and only few semi-empirical correlations exist for these types of tubes. Kumar et al. [31] also used

Table 4 Coefficients in Eq. (11) for condensation on a single tube without liquid overfeed

Tube	a	b
Plain Tube	1.20	-0.33
Turbo-Chil	10.32	-0.29
Turbo-CSL	8.50	0.16
Gewa-C	9.99	-0.21

data of spine-shaped integral fin tubes for development of their correlation used for the comparison to the finned tube above. They manufactured these tubes by cutting axial slots on the surface of a finned tube. Belghazi et al. [13] proposed a method for their 3D enhanced Gewa C+ tube data, which is a notched fin tube. However, those methods are for their specific geometries and not for general application.

Empirical Single Tube Correlations. No attempt has been made to provide a new analytical model for condensation on a single tube here. The previous section showed that there are existing methods for the plain and low finned tubes in good agreement with the data. Instead, the experimental data are used to provide empirical correlations for all four types of tubes for later use in Part II [14] and by others. Based on the Nusselt theory, an equation of following form is assumed:

$$\frac{\alpha_o}{\lambda_L}\left[\frac{\mu_L^2}{\rho_L(\rho_L-\rho_V)g}\right]^{1/3} = a\,\mathrm{Re}^b \tag{11}$$

The bracketed term together with its exponent is a characteristic length, and the complete term to the left of the equal sign corresponds to the Nusselt number Nu^* with this characteristic length. The values of the multiplier a and the exponent b in Eq. (11) for all types of tubes are listed in Table 4. The values of a and b obtained from the fit for the plain tube are very close to the theoretical values of the Nusselt theory, which are 1.21 and $-1/3$, respectively, while the others also closely fit their respective data.

A comparison of the present empirical correlations for the single tube performance of all four types of tubes is depicted in Fig. 7. The ranges of the film Reynolds numbers shown correspond approximately to the measured ones. For the plain tube the film Reynolds numbers are available only in the lower range, as the measured heat fluxes for this tube were smaller. The Turbo-CSL tube shows the highest single tube performance followed by the Gewa-C and the low-finned tube. At a film Reynolds number of 50, the 3-D enhanced tubes perform about 12 times the plain tube, whereas the low fin tube has an enhancement ratio of about 9.

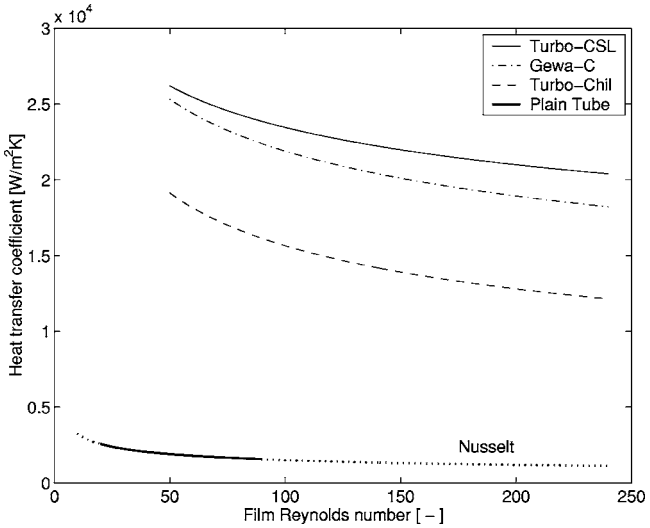

Fig. 7 Comparison of single tube performance without liquid overfeed

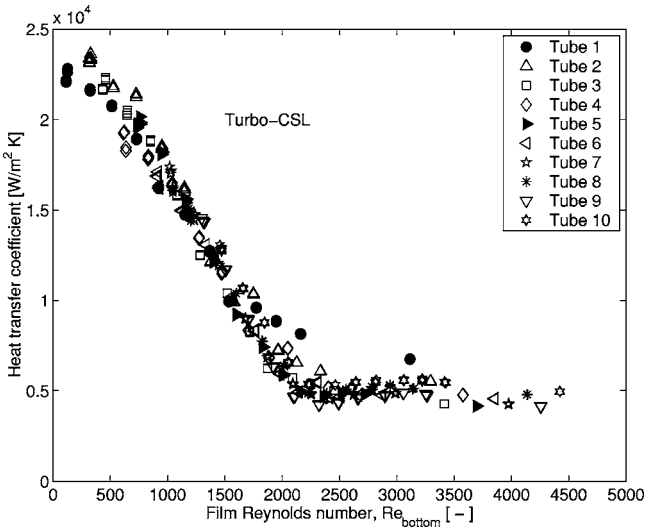

Fig. 8 Measurements with liquid inundation on the Turbo-CSL tube with a tube pitch of 25.5 mm at a nominal heat flux of 40 kW/m^2

Measurements With Liquid Inundation. Measurements with liquid overfeed on the top of the array of tubes were performed at three tube pitches and three heat fluxes for each type of tubes. The nominal heat fluxes were 20, 40, and 60 kW/m^2 for the enhanced tubes and 6, 12, and 20 kW/m^2 for the plain tube.

As shown in Fig. 7, the tubes with a 3-D enhanced surface structure, the Turbo-CSL and Gewa-C tubes, have the highest single tube heat transfer performance. The result of one series of measurements with liquid overfeed of the Turbo-CSL tube is given in Fig. 8. The heat transfer coefficient is plotted versus the film Reynolds number of the condensate leaving the bottom of each tube in analogy to the single tube tests. These measurements were performed with the smallest tube pitch of 25.5 mm at a mean heat flux of 40 kW/m^2. Starting with no liquid overfeed ($\Gamma = 0$ kg/ms), the mass flow rate was increased in 12 steps to a maximum mass flow rate of $\Gamma = 0.135$ kg/ms, with a smaller step width at low mass flow rates. The film Reynolds numbers are determined from an energy balance with the assumption that all the liquid condensed on a tube flows onto the tube below. The film Reynolds number is the local value at the midpoint of the tube where the local heat transfer coefficient is determined. Different symbols are used for the ten tubes in the array to illustrate the evolution of heat transfer performance of every tube during one series of measurements when the liquid inundation rate is increased. Without overfeed (lowest film Reynolds number for each symbol), the heat transfer coefficient decreases from a value of about 23 kW/m^2 K on the first tube to a value of 13 kW/m^2 K on the tenth tube in the array.

In general, the heat transfer coefficient is high at low film Reynolds numbers and decreases with increasing film Reynolds number. At a film Reynolds number of ~2200, the heat transfer coefficient reaches a plateau and flattens out. This trend is observed on all ten tubes in the array, proving the consistency of the experimental setup with overfeed to simulate a large number of tube

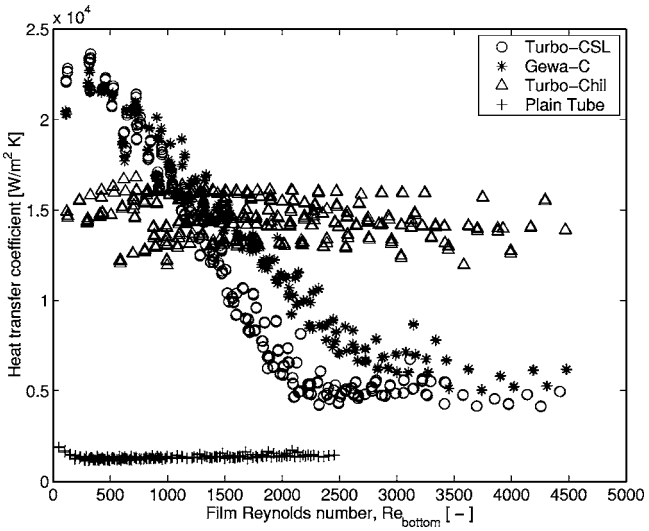

Fig. 9 Comparison of the four types of tubes with tube pitch of 25.5 mm at a nominal heat flux of 40 kW/m^2 (12 kW/m^2 for the plain tube)

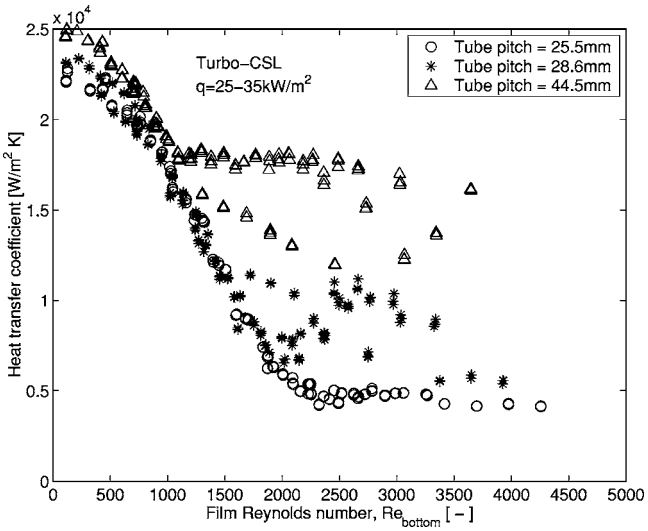

Fig. 10 Tube spacing influence of the Turbo-CSL tube at a nominal heat flux of 40 kW/m^2 over a limited heat flux range

rows. Only the top tube deviates a little from the others. At low film Reynolds numbers, its heat transfer coefficients are a little below the other tubes, and at high film Reynolds numbers its values are higher than the other tubes. This might be explained by the fact that the liquid flow leaving the distribution half tube differs from the liquid flow leaving the enhanced tube. The film Reynolds number leaving the tenth tube during the measurement with the highest inundation rate would correspond approximately to the 30th row in a heat exchanger at this specific heat flux.

During each series of measurements, the nominal row heat flux was held constant, but as mentioned above, the experimental setup has two tube passes. Thus, heat flux varied substantially between the even and odd rows in the bundle. In addition, as seen in Fig. 8, the external heat transfer coefficient is higher on the upper tubes in the array as the inundation is less, resulting in a higher heat flux on the upper tubes for the same condensation temperature difference. These two effects lead to a wide range of heat flux on the tubes in the array at the imposed nominal row heat flux. For example, for the measurements shown in Fig. 8 at a nominal heat flux of 40 kW/m^2 with an overfeed rate of $\Gamma = 0.027$ kg/ms, the heat flux variation by row starting at the top tube to the tenth tube is as follows: 36, 57, 35, 49, 33, 44, 30, 38, 26, and 36 kW/m^2. About half the scatter of the points in Fig. 8 is, in part, due to this difference in heat flux, which is not differentiated in this graph.

Similar graphs were obtained for all three nominal heat fluxes and for all types of tubes and tube pitches. For all four types of tubes, the measured values at one nominal heat flux at the smallest tube pitch are plotted in Fig. 9. For the Gewa-C tubes, basically the same behavior as for the Turbo-CSL tubes is observed. The heat transfer coefficients start at a high level at low film Reynolds numbers and decrease with increasing film Reynolds numbers, reaching also a plateau. At low film Reynolds numbers the heat transfer coefficients are slightly higher for the Turbo-CSL tube. With increasing film Reynolds number the heat transfer coefficients of Turbo-CSL decrease faster than those of the Gewa-C. The heat transfer coefficients of the Gewa-C tube flatten out at a higher film Reynolds compared to the Turbo-CSL and the value of this plateau is slightly above the value of the Turbo-CSL.

For small inundation rates, the heat transfer coefficients for the 3D enhanced tubes are high compared to the finned tube (Turbo-Chil). Increasing the inundation rates deteriorates the performance the 3D enhanced tubes while the heat transfer coefficient of the low finned tube varies little with the inundation rate. The cross over in performance with the low finned tube suggests that in large bundles it may be judicious to use low finned tubes in the lower rows when the Reynolds number is larger than 1250.

For the plain tube, the measurements were performed at lower heat fluxes. The measured heat transfer coefficients at a nominal row heat flux of 12 kW/m^2 are given in Fig. 9 for comparison. At low film Reynolds numbers the heat transfer coefficient decreases with increasing film Reynolds numbers. At a film Reynolds number of $\sim$500, the coefficient starts to increase slowly with increasing film Reynolds number.

Figure 10 depicts the measured heat transfer coefficients of the Turbo-CSL tube as a function of the film Reynolds number for all three tube pitches. For clarity, only the data in the heat flux range from 25 to 35 kW/m^2 are shown to partly eliminate the effect of heat flux. Although the scatter in the data for the tube pitch of 28.6 and 44.5 mm is larger than for the smallest tube pitch, it can be seen that for all three tube pitches the heat transfer coefficient decreases with increasing film Reynolds number and flattens out at a certain film Reynolds number. The larger the tube pitch the earlier this happens, and thus the higher the value of the plateau in the heat transfer coefficient. At the tube pitch of 44.5 mm typical of a staggered tube layout, the plateau is reached at $Re_{bottom} = 1100$ and this gives higher performance than for the low finned tube; thus, in fact, it is not judicious to change to low finned tubes lower in the bundle. At low film Reynolds numbers (below 1000) in Fig. 10 the heat transfer coefficient increases with increasing tube pitch, apparently due to the higher velocity of the impinging liquid and the larger fraction of condensate between adjacent tubes that is not on the tubes.

The influence of the tube pitch on the Gewa-C tube is illustrated in Fig. 11. A similar behavior as observed for the Turbo-CSL can be seen. The heat transfer coefficient deteriorates less with increasing tube pitch at high Reynolds numbers and the plateau at 44.5 mm is again reached at about $Re_{bottom} = 1100$. At low film Reynolds numbers the behavior differs, however, as the heat transfer coefficients for all tube pitches are close together apart from some values of the middle tube pitch that lie above.

For both 3D enhanced tubes it was observed that liquid left the array of tubes sideways at high film Reynolds numbers [15]. The change in heat transfer performance shown above is thus apparently linked to this observation as the film Reynolds numbers where the changes occur coincide approximately to the film Reynolds number where the some liquid starts to leave the array of

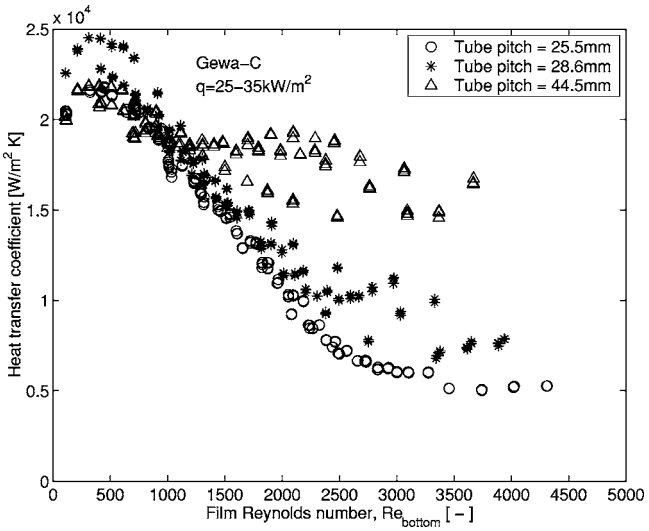

Fig. 11 Tube spacing influence of the Gewa-C tube at a nominal heat flux of 40 kW/m^2 over a limited heat flux range

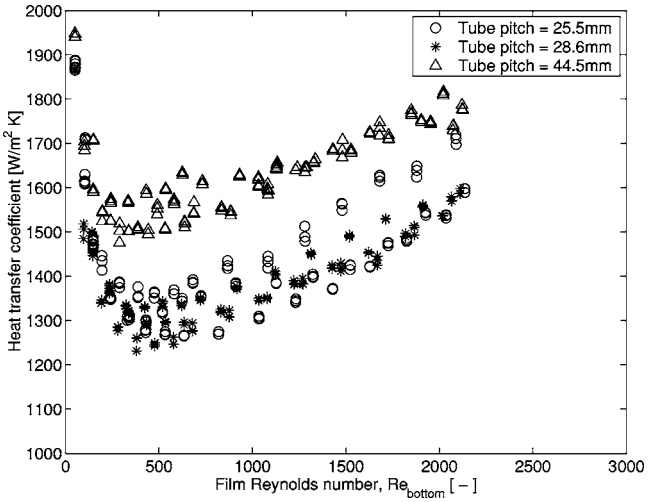

Fig. 13 Tube spacing influence of plain tube at a nominal heat flux of 12 kW/m^2 on the top three tubes in the array

tubes sideways. Furthermore, it is also plausible that with increased tube pitch the condensate starts to leave the array sideways at lower film Reynolds numbers and the amount of liquid leaving is larger resulting in higher heat transfer coefficients for the larger tube pitches (resulting in higher levels of the plateaus).

For the low finned tube, the heat transfer coefficient stays approximately fixed over the whole film Reynolds number range for all three tube pitches as depicted in Fig. 12. No prominent trend in the heat transfer coefficient as a function of the tube pitch was observed for this tube.

In Fig. 13, the heat transfer coefficient for the plain tube for all three tube pitches is given. For a clear representation of the effect of tube pitch, only the heat transfer coefficients for the top three tubes are shown. At low film Reynolds numbers, the heat transfer coefficients are similar for all three tube pitches. At high Reynolds numbers, the heat transfer coefficient is highest for the largest tube spacing (most likely due to increased amount of liquid "slinging" sideways off the tubes), which results in a lower effective liquid Reynolds number on the tubes below compared to the plotted Reynolds numbers that assume all the liquid remains on the tubes. The effective film Reynolds may even decrease going downward in the array as the amount of liquid that leaves the array increases. The differences observable for the tube pitch of 25.5 and 28.6 mm are within the experimental uncertainty.

For every type of tube and tube pitch, measurements have been performed at three nominal heat fluxes. For a detailed discussion of all these results, refer to Gstöhl [17]. In general, the heat transfer coefficients decrease with increasing heat flux for the four different tubes. This decrease is less pronounced for increasing inundation rates for the enhanced tubes.

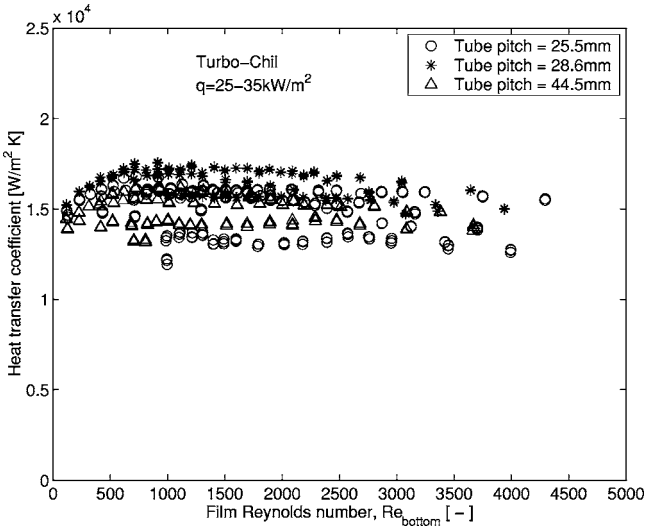

Fig. 12 Tube spacing influence of the Turbo-Chil tube at a nominal heat flux of 40 kW/m^2 over a limited heat flux range

Conclusions

A new data-reduction method to determine local external condensation heat transfer coefficients at the midpoint of each of the tubes in the array was shown, and a propagation of error analysis was performed to estimate the uncertainty of the measurements. Four types of tubes were tested at the tube pitches of 25.5, 28.6, and 44.5 mm: a plain tube, a 26 fpi/1024 fpm low finned tube (Turbo-Chil), and two tubes with 3D enhanced surface structures (Turbo-CSL and Gewa-C). Measurements with liquid overfeed onto the top of the array were performed for each type of tube at three different heat flux levels. Additionally, measurements without liquid overfeed were made by varying the heat flux. Thus, a large new database of *local* condensation heat transfer coefficients have been presented here with a total of approximately 15,000 data points.

The measured heat transfer coefficients on the plain tube without liquid inundation were in good agreement with the Nusselt theory. For the low finned tube without liquid inundation, good agreements with other data and the prediction methods of Sreepathi et al. [24] and Beatty and Katz [25] were found.

For small inundation rates, the heat transfer coefficients for the 3D enhanced tubes were high compared to the finned tube. Increasing the inundation rates deteriorated the performance the 3D enhanced tubes until a minimum plateau was reached at a certain film Reynolds number, whose level was dependent on tube pitch. The heat transfer coefficients of the Turbo-CSL were slightly higher than those of the Gewa-C for small inundations, but the decrease with increasing inundation rate was less pronounced for the Gewa-C compared to the Turbo-CSL. The heat transfer coefficient of the finned tube varied little with the inundation rate. The heat transfer performance of the plain tube decreased first sharply and then increased again slowly with increasing inundation rates.

For low inundation rates, the heat transfer coefficients were similar for the three tube pitches. For the 3D enhanced tubes, the heat transfer coefficient achieved a constant level at a lower film Reynolds number for the larger tube pitch. This level was higher for the larger tube pitch. The heat transfer coefficient of the finned tube varied little with the tube pitch. For the plain tube, an increase in heat transfer coefficient was observed for the largest tube pitch.

The heat transfer coefficients decreased with increasing heat flux for the four types of tubes. This decrease was less pronounced for increasing inundation rates, apart from the plain tube.

The observed behavior in heat transfer performance of the 3D enhanced tubes and the plain tube is most likely linked to our visual observations that some liquid left the array of tubes sideways [15], which should be accounted for in future predictive methods for condensation on a vertical array of tubes.

Acknowledgments

The authors acknowledge the financial support to the EPFL/LTCM Falling Film Research Club members: Axima Refrigeration AG, Dunham-Bush Inc., UOP Inc., Wieland-Werke AG, and Wolverine Tube Inc., and, in particular, Wieland-Werke AG and Wolverine Tube Inc. for providing the tube samples.

Nomenclature

C = multiplier
c_p = specific heat at constant pressure, J/(kg K)
D = tube diameter, m
f = friction factor of Petukhov [19]
Ga = modified Galileo number $(\rho\sigma^3/(\mu^4\,\mathrm{g}))$
g = acceleration due to gravity [9.81], m/s^2
h_{LV} = latent heat of evaporation, J/kg
Nu^* = Nusselt number $(\alpha(\mu_L/\rho_L(\rho_L-\rho_V)\mathrm{g})^{1/3}/\lambda_L)$
$\dot{m}$ = mass flow, kg/s
Pr = Prandtl number $(\mu c_p/\lambda_L)$
q = local heat flux relative to a surface, W/m^2
Re = film Reynolds number $(4\Gamma/\mu)$
$\mathrm{Re}_{\mathrm{wat}}$ = cooling water Reynolds number $(4\dot{m}/(\pi(D_i+D_{\mathrm{stainless}})\mu))$
r_w = thermal resistance of the tube wall, m^2 K/W
T = temperature, K
t = thickness, m
U = local overall heat transfer coefficient, W/(m^2 K)
x = coordinate in axial direction, m

Greek Symbols

α = heat transfer coefficient, W/(m^2 K)
$\Delta\alpha$ = uncertainty in heat transfer coefficient, W/(m^2 K)
ε = mean relative error
Γ = film mass flow rate on one side per unit length of tube, kg/(m s)
λ = thermal conductivity, W/(m K)
μ = dynamic viscosity, N s/m^2
ρ = density, kg/m^3

Subscripts

b = fin base
bottom = at the bottom of the tube
Gni = Gnielinski
h = hydraulic
i = internal side
L = saturated liquid
o = external side at fin tip
or = external side at fin root
sat = saturated conditions
stainless = stainless-steel tube
t = fin tip
V = saturated vapor
w = wall
wat = water

References

[1] Chang, Y. J., Hsu, C. T., and Wang, C. C., 1996, "Single-Tube Performance of Condensation of R-134a on Horizontal Enhanced Tube," ASHRAE Trans., **102**(Pt 1), pp. 821–829.
[2] Jung, D., Kim, C.-B., Cho, S., and Song, K., 1999, "Condensation Heat Transfer Coefficients of Enhanced Tubes With Alternative Refrigerants for CFC11 and CFC12," Int. J. Refrig., **22**, pp. 548–557.
[3] Kumar, R., Varma, H. K., Mohanty, B., and Agrawal, K. N., 2000, "Condensation of R-134a Vapor Over Single Horizontal Circular Integral-Fin Tubes With Trapezoidal Fins," Heat Transfer Eng., **21**(2), pp. 29–39.
[4] Cheng, W. Y., and Wang, C. C., 1994, "Condensation of R-134a on Enhanced Tubes," ASHRAE Trans., **100**(Pt 2), pp. 809–817.
[5] Huber, J. B., Rewerts, L. E., and Pate, M. B., 1994, "Shell-Side Condensation Heat Transfer of R-134a. Part I: Finned-Tube Performance," ASHRAE Trans., **100**(Pt 2), pp. 239–247.
[6] Huber, J. B., Rewerts, L. E., and Pate, M. B., 1994, "Shell-Side Condensation Heat Transfer of R-134a. Part II: Enhanced Tube Performance," ASHRAE Trans., **100**(Pt 2), pp. 248–256.
[7] Huber, J. B., Rewerts, L. E., and Pate, M. B., 1994, "Shell-Side Condensation Heat Transfer of R-134a. Part III: Comparison With R-12," ASHRAE Trans., **100**(Pt 2), pp. 257–264.
[8] Rewerts, L. E., Huber, J. B., and Pate, M. B., 1996, "The Effect of R-134a Inundation on Enhanced Tube Geometries," ASHRAE Trans., **102**(Pt 2), pp. 285–296.
[9] Kulis, F., Compingt, A., Mercier, P., and Rivier, P., 1995, "Design Method for Shell and Tube Condensers in Refrigeration Units," *Heat Transfer in Condensation*, Eurotherm Seminar 47, Paris, pp. 133–138.
[10] Honda, H., Takamatsu, H., Takada, N., and Yamasaki, T., 1995, "Design Method for Shell and Tube Condensers in Refrigeration Units," *Heat Transfer in Condensation*, Eurotherm Seminar 47, Paris, pp. 110–115.
[11] Honda, H., Takata, N., Takamatsu, H., Kim, J. S., and Usami, K., 2002, "Condensation of Downward-Flowing HFC-134a in a Staggered Bundle of Horizontal Finned Tubes: Effect of Fin Geometry," Int. J. Refrig., **25**, pp. 3–10.
[12] Belghazi, M., Bontemps, A., Signe, J. C., and Marvillet, C., 2001, "Condensation Heat Transfer of a Pure Fluid and Binary Mixture Outside a Bundle of Smooth Horizontal Tubes: Comparison of Experimental Results and a Classical Model," Int. J. Refrig., **24**, pp. 841–855.
[13] Belghazi, M., Bontemps, A., and Marvillet, C., 2002, "Condensation Heat Transfer on Enhanced Surface Tubes: Experimental Results and Predictive Theory," ASME J. Heat Transfer, **124**, pp. 754–761.
[14] Gstoehl, D., and Thome, J. R., 2006, "Film Condensation of R-134a on Tube Arrays With Plain and Enhanced Surfaces. Part II: Empirical Prediction of Inundation Effects," ASME J. Heat Transfer, **128**(1), pp. 33–43.
[15] Gstoehl, D., and Thome, J. R., 2006, "Visualization of R-134a Flowing on Tube Arrays With Plain and Enhanced Surfaces Under Adiabatic and Condensing Conditions," Heat Transfer Eng., **27**, in press.
[16] Roques, J.-F., 2004, "Falling Film Evaporation on a Single Tube and on a Tube Bundle," Ph.D. thesis No. 2987, Swiss Federal Institute of Technology, Lausanne, http://library.epfl.ch/theses/?display=detail&nr=2987
[17] Gstöhl, D., 2004, "Heat Transfer and Flow Visualization of Falling Film Condensation on Tube Arrays With Plain and Enhanced Surfaces," Ph.D. thesis No. 3015, Swiss Federal Institute of Technology, Lausanne, http://library.epfl.ch/theses/?display=detail&nr=3015
[18] Briggs, D. E., and Young, E. H., 1969, "Modified Wilson Plot Techniques for Obtaining Heat Transfer Correlations for Shell and Tube Heat Exchangers," Chem. Eng. Prog., **65**(92), pp. 35–45.
[19] Incropera, F. P., and DeWitt, D. P., 1996, *Fundamentals of Heat and Mass Transfer*, 4th Edition, Wiley, New York, Chap. 8.
[20] Gnielinski, V., 1976, "New Equations for Heat and Mass Transfer in Turbulent Pipe and Channel Flow," Int. Chem. Eng., **16**(2), pp. 359–368.
[21] Rose, J. W., 2004, personal communication.
[22] Rohsenow, W. M., 1956, "Heat Transfer and Temperature Distribution in Laminar Film Condensation," Trans. ASME, **79**, pp. 1645–1648.
[23] McAdams, W. H., 1954, *Heat Transmission*, 3rd Edition, McGraw-Hill, New York.

[24] Sreepathi, L. K., Bapat, S. L., and Sukhatme, S. P., 1996, "Heat Transfer During Film Condensation of R-123 Vapour on Horizontal Integral-Fin Tubes," J. Enhanced Heat Transfer, **3**(2), pp. 147–164.
[25] Beatty, K. O., and Katz, D. L., 1948, "Condensation of Vapors on Outside of Finned Tubes," Chem. Eng. Prog., **44**(1), pp. 55–70.
[26] Webb, R. L., Rudy, T. M., and Kedzierski, M. A., 1985, "Prediction of the Condensation Coefficient on Horizontal Integral-Fin Tubes," ASME J. Heat Transfer, **107**, pp. 369–376.
[27] Rudy, T. M., and Webb, R. L., 1983, "Theoretical Model for Condensation on Horizontal Integral-Fin Tubes," AIChE Symp. Ser., **79**(225), pp. 11–18.
[28] Thome, J. R., 2004, *Condensation on External Surfaces*, Engineering Databook III, Wolverine Tube, Huntsville, AL, Chap. 7, http://www.wlv.com/products.
[29] Rose, J. W., 1994, "An Approximate Equation for the Vapour-Side Heat Transfer Coefficient for Condensation on Low-Finned Tubes," Int. J. Heat Mass Transfer, **37**(5), pp. 865–875.
[30] Briggs, A., and Rose, J. W., 1994, "Effect of Fin Efficiency on a Model for Condensation Heat Transfer on a Horizontal, Integral-Fin Tube," Int. J. Heat Mass Transfer, **37**(Suppl. 1), pp. 457–463.
[31] Kumar, R., Varma, H. K., Mohanty, B., and Agrawal, K. N., 2002, "Prediction of Heat Transfer Coefficient During Condensation of Water and R-134a on Single Horizontal Integral-Fin Tubes," Int. J. Refrig., **25**, pp. 111–126.

Film Condensation of R-134a on Tube Arrays With Plain and Enhanced Surfaces: Part II—Empirical Prediction of Inundation Effects

D. Gstoehl

J. R. Thome[1]
e-mail: john.thome@epfl.ch

Laboratory of Heat and Mass Transfer,
Faculty of Engineering Sciences and Techniques,
Ecole Polytechnique Fédérale de Lausanne,
CH-1015 Lausanne, Switzerland

New predictive methods for R-134a condensing on vertical arrays of horizontal tubes are proposed based on visual observations revealing that condensate is slung off the array of tubes sideways and significantly affects condensate inundation and thus the heat transfer process. For two types of three-dimensional (3D) enhanced tubes, the Turbo-CSL and the Gewa-C, the local heat flux is correlated as a function of condensation temperature difference, the film Reynolds number, the tube spacing, and liquid slinging effect. The measured heat transfer data of the plain tube were well described by an existing asymptotic model based on heat transfer coefficients for the laminar wavy flow and turbulent flow regimes or, alternatively, by a new model proposed here based on liquid slinging. For the 26 fpi *low finned tube, the effect of inundation was found to be negligible and single-tube methods were found to be adequate.* [DOI: 10.1115/1.2130401]

Keywords: condensation, refrigerant, R-134a, plain tube, finned tube, enhancement, prediction, inundation

Introduction

Tubes in shell-and-tube condensers, widely used in refrigeration, heat pumps, and chemical process industries, are subjected to condensate inundation from the neighboring upper tubes. In general, the top tube without condensate inundation in a vertical array of horizontal tubes has the highest heat transfer performance. The condensate of this tube falls on the tube below, and thus, with increasing row number starting from the top, the amount of condensate increases and thermal performance decreases. Numerous studies have been performed in order to quantify the effect of condensate inundation on the thermal performance, mainly concerning plain tubes. In Nusselt's theory [1] the mean heat transfer coefficient $\overline{\alpha_N}$ of a vertical array of horizontal tubes compared to the heat transfer coefficient of the top tube α_1 in the array is given by

$$\frac{\overline{\alpha_N}}{\alpha_1} = N^m \tag{1}$$

where $m=-1/4$ and N is the row number counting from the top. In thermal design, this equation was found to be too conservative, resulting in condensers that were consistently oversurfaced. For this reason, Kern [2] suggested a less conservative relationship by using $m=-1/6$ based on practical experience. Nusselt's theory assumes a constant condensation temperature difference on all the tubes in the array, which cannot be achieved in a practical system. Katz and Geist [3] were among the first to measure the row effect of integral low fin tubes. Their experiments indicated that the decrease in condensing film coefficients with the number of tubes in a vertical row of six tubes is less for finned tubes than would be predicted by the application of Nusselt's theory. They found a row effect exponent $m=-0.04$ for 16 fpi (630 fpm) integral low fin tubes.

Kutateladze and Gogonin [4] showed that results of condensation experiments on a bank of plain tubes can be correlated as a function the film Reynolds number based on the condensate flow rate

$$\mathrm{Nu}^* = f(\mathrm{Re}) \tag{2}$$

Honda et al. [5] used the same approach and extended it to include the effect of vapor shear for condensation on bundles of horizontal plain tubes. For condensation on a vertical column of horizontal low finned tubes, Honda et al. [6] proposed a theoretical model based on the flow characteristics (column and sheet). Numerous experimental investigations have been carried out in order to characterize the tube row effect for different tube geometries and refrigerants. Data have been mostly reported row by row or based on the film Reynolds number. However, only few provided a method to describe the tube row effect and these are discussed below.

Webb and Murawski [7] studied the row effect on a vertical bank of five horizontal tubes, testing four types of enhanced tubes. They proposed curve fits in the form of $\alpha_N = a\mathrm{Re}^{-n}$. A 26 fpi tube showed no row effect ($n=0.00$) similar to the present results in Part I [15]. The greatest row effect was displayed by a three-dimensional (3D) enhanced tube ($n=0.58$). They also gave the corresponding exponents m in Eq. (1). Their values of the exponent m are based on constant inlet water temperature in all tubes. In addition, they reported the observed condensate drainage patterns including a map for the flow mode transitions. Memory et al. [8] performed measurements on a vertical in-line column of four plain and roped tubes. Their data lie between the equations of Kern [2] and Eissenberg [9], the former lying above the latter, indicating that the inundation affected the roped bundle more than the smooth bundle. McNaught and Chu [10] ran experiments for four different low finned tube bundles and characterized the tube row effect by the exponent on the film Reynolds number. For

[1]To whom correspondence should be addressed.

Contributed by the Heat Transfer Division of ASME for publication in the JOURNAL OF HEAT TRANSFER. Manuscript received November 5, 2004; final manuscript received July 12, 2005. Review conducted by Raj M. Manglik.

R-134a, which is widely used today, Cheng and Wang [11] conducted experiments condensing on a vertical column of three horizontal tubes, with seven kinds of tubes. For the plain tubes, they found an exponent of $m=0.2$. Kulis et al. [12] presented experimental data for R-134a and R-22 condensing on a staggered bundle with 12 active tubes. A tube row effect depending on tube geometry and heat flux was observed. The higher the heat flux, the smaller was the adverse tube row effect. The Eissenberg tube row effect matched their data best. Rewerts et al. [13,14] studied the effect of R-134a and R-123 inundation on enhanced tube geometries. The test bundle consisted of five instrumented tubes in a five-row test bundle surrounded by inactive tubes in the staggered tube arrangement. They simulated the effect of condensate inundation up to a depth of 30 rows by introducing a two-phase refrigerant mixture into the test section. They observed that some tubes were characterized by a change in heat transfer above a certain film Reynolds number. They correlated each range by an equation of the form like Webb and Murawski [7].

Large differences in the effect of inundation were found for different types of tubes and test conditions. In general, the tube row effect was less pronounced for low finned tubes compared to 3D enhanced tubes. Very often these differences were attributed to different flow patterns of the condensate on the array of tubes, but in many studies there was little or no visual access to observe the condensation process itself. For this reason, heat transfer measurements have been performed in Part I on an array of horizontal tubes in a test facility offering complete visual access to observe the condensation process, with observations reported in Gstoehl and Thome [15]. Some videos from this work are also viewable online in Thome [16]. R-134a was condensed at a saturation temperature of 304 K on tube arrays with up to ten tubes at pitches of 25.5, 28.6, and 44.5 mm. Four commercially available copper tubes with a nominal diameter of 19.05 and 544 mm in length were tested: a plain tube, a 26 fpi/1024 fpm low finned tube (Turbo-Chil), and two tubes with three-dimensional enhanced surface structures (Turbo-CSL and Gewa-C). Measurements were performed at three nominal heat flux levels, which were 20, 40, and 60 kW/m^2 for the three enhanced tubes and 6, 12, and 20 kW/m^2 for the plain tube (the nominal heat flux is the average heat flux in the array from an energy balance on the water side as, due to the two-pass setup, the heat flux varied substantially in the array). Liquid refrigerant was fed onto the array corresponding to film Reynolds numbers up to 3000.

The objective of this paper is to present new predictive methods based on these heat transfer measurements presented in Part I [15] and on visual observations, which are shown in detail in Gstoehl and Thome [17]. First, the two 3D enhanced tubes are addressed, followed by the plain tube and then the low finned tube.

3D Enhanced Tubes

The heat transfer coefficients as a function of the film Reynolds numbers for both 3D enhanced tubes, the Turbo-CSL and Gewa-C, are basically characterized by two distinct zones [15]. In the first zone, the heat transfer coefficient decreases with increasing film Reynolds number. Above a certain film Reynolds number, the heat transfer coefficient then decreases much slower or achieves a constant value. Most likely this second behavior is linked to the fact that condensate was observed to leave the array of tubes sideways (liquid "slinging") and reduces the inundation rate below that expected as illustrated on Fig. 1. Under ideal conditions, the condensate impinges exactly at the top of the lower tube and the amount of condensate flowing on one side of the tube is exactly one-half of the total flow rate. At the bottom of the tube the horizontal momentum of the joining films is canceled out and the condensate leaves the tube vertically downward. If the amount of condensate flowing on both sides is not equal because of a small asymmetry, the condensate maintains some horizontal momentum and hence creates an instability. Flowing down in the array, this behavior can be amplified up to a point where the falling film does not even always hit the tube below as its trajectory fluctuates in direction. This liquid "slinging" effect has also been noted and described by Wei and Jacobi [18] for adiabatic flows on plain tube arrays. Visual observations in [17] showed that the film Reynolds number at which the heat transfer behavior changed corresponded approximately to the film Reynolds number where the condensate starts to leave the tube row sideways.

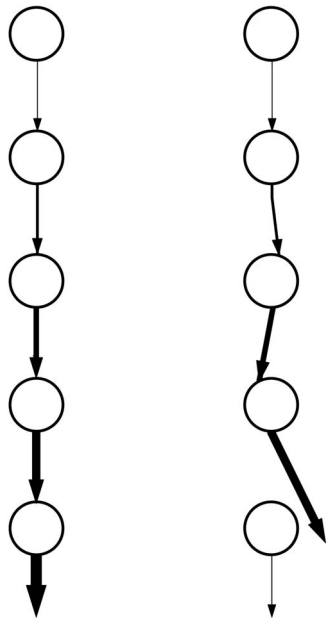

Fig. 1 Ideal flow (left) and liquid "slinging" (right)

Results Without Condensate "Slinging." As a first step in correlating the heat transfer behavior of the 3D enhanced tubes (the Turbo-CSL and Gewa-C tubes), only the measurements where no condensate is leaving the tubes sideways are considered (the data before the plateau) for now. For this condition, for a given film Reynolds number, the heat transfer coefficient is dependent on the heat flux, i.e., increasing the heat flux (and hence film Reynolds number) decreases the heat transfer coefficient.

During laminar film condensation, the heat transfer coefficient is dependent on the condensation temperature difference. Newton's concept of using a heat transfer coefficient defined as the ratio of heat flux to the temperature difference (saturation temperature minus base wall temperature) is debatable in such a case as also mentioned by Rose [19]. In other words, for calculating the heat flux for a given temperature difference, the heat transfer coefficient is multiplied by the temperature difference. When the heat transfer coefficient itself depends on the temperature difference (as is the case here), nothing is gained by separating the correlation for calculating the heat flux into a heat transfer coefficient and a condensation temperature difference (i.e., the idea behind Newton's law of cooling is that the heat transfer coefficient in convection is *not* a function of temperature difference, which in two-phase processes is normally not true). However, the heat transfer community is used to working with heat transfer coefficients, and for this reason it makes sense to use it for comparison purposes.

For fundamental understanding, it is helpful to look at the local heat flux q_o as a function of the condensation temperature difference as the dependent variable since integrating the local heat fluxes in a tube bundle gives its overall heat duty. During the measurements, the heat flux decreases with increasing liquid inundation for the same condensation temperature difference. In order to study this, data were limited to the points where the film Reynolds number of the liquid falling onto the top of the tube Re_{top} are in a small range (for example, 600–800). In this way, the

Table 1 Coefficients in Eq. (4) for condensation on the tube array with a tube pitch of 25.5 mm with no condensate leaving sideways and relative errors of the prediction methods

Tube	a [W/m^2]	b [-]	c [W/m^2]	ε [%]	σ [%]
Turbo-CSL	25500	0.91	-9.7	-1.0	9.2
Gewa-C	25200	0.87	-6.5	-0.3	7.2
Turbo-CSL	25350	0.89	-9.4	-1.0	9.3
Gewa-C	25350	0.89	-6.8	-0.4	7.3

local data measured on different tubes in the array at the three different heat flux levels (≈50 data points) can be correlated by an equation of the following form

$$q_o = C(\Delta T^b) \tag{3}$$

For the Turbo-CSL tube, an analysis was performed starting at film Reynolds numbers equal to 0 up to 2000, where the condensate starts to leave sideways, always limiting the data to small ranges in film Reynolds number. Little variation was found in the value of the exponent b for all these small ranges, while the value of C decreased approximately linearly with increasing film Reynolds number. A similar behavior was also observed for the Gewa-C tube up to a film Reynolds number of 2500. For this reason, an equation as follows is suggested to describe the performance of the 3D enhanced tubes:

$$q_o = (a + c\ \mathrm{Re}_{\mathrm{top}})\Delta T^b \tag{4}$$

A least-squares optimization scheme was used with all measurements for each of the 3D enhanced tubes with inundation and no condensate leaving sideways in order to determine the values of the three constants in Eq. (4). The values of a, b, and c for the Turbo-CSL and Gewa-C tube are listed in Table 1 for a condensation temperature difference ΔT in Kelvin (first and second line). The values of a and b are nearly identical, and the difference in thermal performance of the two enhanced tubes comes mainly from the value of c.

In order to make a quantitative comparison between the experimental results and the predictions, the following statistical values are used. The relative error between measurement and prediction for each data point is defined by

$$\varepsilon_i = \frac{\mathrm{prediction}_i - \mathrm{measurement}_i}{\mathrm{measurement}_i} \tag{5}$$

The mean relative error is

$$\varepsilon = \frac{1}{N}\sum_{i=1}^{N} \varepsilon_i \tag{6}$$

The standard deviation is

$$\sigma = \left[\frac{1}{N-1}\sum_{i=1}^{N} (\varepsilon_i - \varepsilon)^2\right]^{1/2} \tag{7}$$

The standard deviation gives a measure of how the relative errors are distributed around the mean relative error. For a Gaussian distribution of relative errors, 68% would be within $\pm\sigma$ and 95% within $\pm 2\sigma$.

The values obtained for both types of types of tubes are also listed in Table 1. The mean relative error for the Turbo-CSL tube is −1.0% with a standard deviation of 9.2%. For the Gewa-C tube, the mean relative error is −0.3% with a standard deviation of 7.2%.

As the values of the coefficients a and b for both types of tubes were found to be very similar, the next step was to characterize the difference in the heat transfer performance of the two 3D enhanced tubes by only the coefficient c. Thus, the values of the coefficients a and b were next set to the mean values obtained for both tubes, (a=25,350 W/m^2, b=0.89), and then values of c were determined for both types of tubes. With this second method the values of c, which characterizes the deterioration of the heat transfer coefficient with increasing inundation, are −9.4 W/m^2 and −6.8 W/m^2 for the Turbo-Chil and the Gewa-C tube, respectively (third and fourth line in Table 1). The mean relative error for the Turbo-CSL tube becomes −1% with a standard deviation of 9.3%. For the Gewa-C tube, the mean relative error is −0.4% with a standard deviation of 7.3%. These values for c and also the mean relative errors and the standard deviations are very close to the first "tube-specific" method. As these two 3D enhanced condensing tubes have rather similar geometries, this result is hence perhaps not so surprising. Since only one fluid, R-134a at 31°C, has been tested here, no attempt has been made to nondimensionalize Eq. (4); this method does have a convenient, simple form for fitting data for other 3D tube-fluid combinations, however.

For comparison purposes, a prediction of the heat transfer coefficient as a function of the condensation temperature difference ΔT and the liquid inundation $\mathrm{Re}_{\mathrm{top}}$ can be calculated using Eq. (4) and $\alpha_o = q_o/\Delta T$ (referred to as the second method above). Comparisons of the measured and the second method predicted heat transfer coefficients for the Turbo-CSL and the Gewa-C tubes are depicted in Fig. 2. For both tubes, the predicted values are centered within the measured data points. The heat transfer coefficients are about the same at low film Reynolds number for both types of tubes (coefficient a). With increasing film Reynolds number, the heat transfer coefficients of the Turbo-CSL tube decrease faster than those of the Gewa-C tube, characterized by the coefficient c.

Results With Condensate "Slinging." During the measurements, it was observed due to the instabilities in the condensate in between tubes, that some condensate leaves the tubes sideways and does not contact the lower tubes. For the 3D enhanced tubes, this occurred at the transition to the sheet mode or in the sheet mode. At the transition, a continuous sheet is temporarily formed. When it breaks down, some condensate leaves the array of tubes sideways. This breakdown phenomenon is less frequent when the film Reynolds is increased as the sheet becomes continuous. However, the continuous sheet is always unstable, moving a little forward and backward. For a further increase in film Reynolds number, this unstable movement is amplified and regular oscillations with frequencies of about 1.5 Hz are observed. At high film Reynolds numbers, the amplitude becomes so large that a significant fraction of the condensate leaves the tubes sideways (the amount of which, however, was not able to be measured experimentally). This phenomenon was regular, and it seamed that the amount of liquid leaving the array of tubes on the front was the same than leaving on the back, indicating that is was not caused by imperfections of the experimental setup. As seen before, heat transfer deteriorates with increasing inundation. When some of the condensate leaves the array of tubes sideways, the tubes below receive less condensate on their top than otherwise expected, which has a beneficial effect on their heat transfer.

For this reason, a heat transfer model based on the present visual observations is proposed to account for the fraction of condensate leaving sideways in the sheet mode. In an ideal situation, the condensate flows in a continuous sheet from the bottom of one tube onto the top of the tube below. The actual condensate does not however fall vertically in a stable sheet, but instead, it oscillates back and forth (front and back). With increasing mass flow rate, the amplitude of oscillation increases. This behavior is modeled as follows. The condensate is assumed to leave the bottom of the tube with a certain angle relative to the vertical, as illustrated in Fig. 3. This angle varies in time. The maximal angle of deflec-

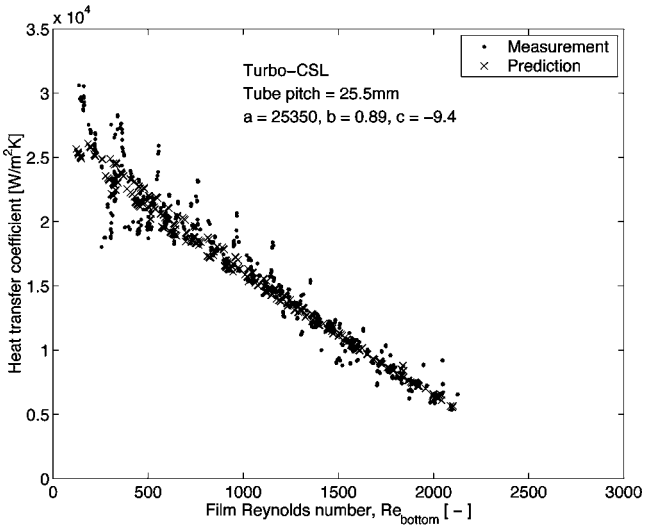

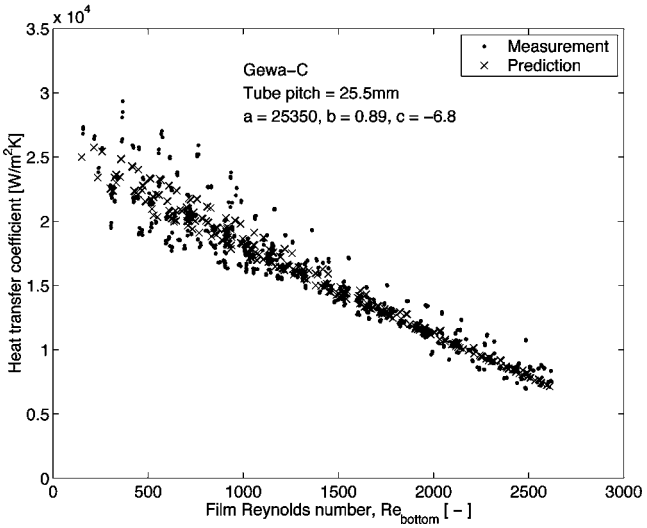

Fig. 2 Prediction of heat transfer coefficient of the 3D enhanced tubes at a tube pitch of 25.5 mm (second method)

tion of the condensate is denominated θ. It is assumed that the angle θ is a function of the film Reynolds number based on our visual observations

$$\theta = f(\mathrm{Re}) \tag{8}$$

θ_{crit} is the angle that delineates contact with the next tube row. As long as $\theta < \theta_{\mathrm{crit}}$, the condensate sheet oscillates on the top of the lower tube, but all the condensate stays on the tube. When $\theta > \theta_{\mathrm{crit}}$, a fraction of the condensate misses the lower tube. The critical angle θ_{crit} depends on the geometry of the tube array as follows:

$$\theta_{\mathrm{crit}} = \arcsin\left(\frac{r_o}{p - r_o}\right) \tag{9}$$

where r_o is the tube radius and p is the tube pitch. The portion of condensate that leaves the tube is assumed to be proportional to the ratio of $(\theta - \theta_{\mathrm{crit}})/\theta$. This means that the film Reynolds number on the top of the nth tube in the array can be expressed as

$$\mathrm{Re}_{\mathrm{top},n} = \frac{\theta_{\mathrm{crit}}}{\theta}\mathrm{Re}_{\mathrm{bottom},n-1} \tag{10}$$

Once the actual amount of condensate that falls on the top of the tube is known, Eq. (4) can be used to determine the heat flux on the tube. For application of this model, the calculation is started

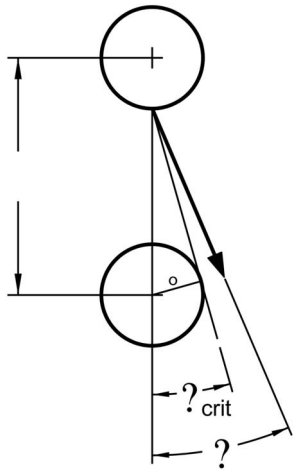

Fig. 3 Schematic of condensate leaving the tube sideways

on the top tube of the array. As long as no condensate leaves ($\theta < \theta_{\mathrm{crit}}$), Eq. (4) is used to determine the heat flux on the tube and then by an energy balance gives the amount of condensate leaving the bottom of the tube. All the condensate flowing off the bottom of the tube is assumed to fall on the top of the tube below ($\mathrm{Re}_{\mathrm{bottom},n-1} = \mathrm{Re}_{\mathrm{top},n}$). In this way the heat transfer can be determined on one tube after another stepping downwards in the array. As soon as part of the condensate starts to leave (when $\theta > \theta_{\mathrm{crit}}$, Eq. (10) is used to determine the amount of condensate that arrives on the tube below and subsequently Eq. (4) to determine the heat flux on the tube.

With these assumptions, the only remaining unknown in the problem is the relationship between the angle θ and the film Reynolds number in Eq. (8). To simply matters, a linear function is assumed

$$\theta = d\ \mathrm{Re} + e \tag{11}$$

The present tube-specific model using all the measured data for one type of tube were used to determine the coefficients d and e in Eq. (11) by a least-squares method. The results for the Turbo-CSL and the Gewa-C tube are listed in Table 2 as the first method.

Comparisons of the measured and predicted heat transfer coefficients for all measurements for the 3D enhanced tubes are depicted in Fig. 4. The predicted heat transfer coefficient flattens out at three levels corresponding to the three tube pitches (and hence three different values of θ_{crit}). For these points, the amount of liquid condensed on the tube is nearly equal to the amount of liquid that leaves sideways and thus the heat transfer coefficient of the tube below does not decrease. The values of θ_{crit} for the three tube pitches tested here were 36, 30, and 16 deg. The "plateaus" in the predicted heat transfer coefficients for the three different tube pitches can be seen and interpret the associated data quite well. Each level of the plateaus corresponds to a certain percentage of condensate leaving the array of tubes sideways. The plateau observed at the smallest tube pitch of 25.5 mm (the lowest plateau) corresponds approximately to 3% of the condensate leaving the array sideways. At the largest tube pitch of 44.5 mm, ~10% of the condensate does not fall on the tube below and leaves the array of tubes sideways. About 80% of the whole database for the two 3D enhanced tubes are predicted within the range of ±15% error using this method.

The relation for the maximum angle of deflection of the condensate leaving at the bottom of the tube was assumed to be linear (Eq. (11)). According to the coefficients listed in Table 2, which were determined using the entire database, the liquid sheet is already deflected at small film Reynolds numbers ($\mathrm{Re} \approx 0$), as the values of the coefficient e are positive for both types of tubes.

Table 2 Coefficients in Eqs. (4) and (11) and relative errors of the prediction methods, including the condensate "slinging" effect

Tube	Method	a [W/m^2]	b [-]	c [W/m^2]	d [rad]	e [rad]	ε [%]	σ [%]
	1st	25500	0.91	-9.7	0.00027	0.08	-2.4	12.9
Turbo-CSL	2nd	25500	0.91	-9.7	0.00031	0	-3.4	12.9
	3rd	25350	0.89	-9.4	0.00031	0	-3.2	12.8
	1st	25200	0.87	-6.5	0.00018	0.14	-1.9	10.1
Gewa-C	2nd	25200	0.87	-6.5	0.00024	0	-2.7	10.5
	3rd	25350	0.89	-6.8	0.00024	0	-3.1	10.6

Apart from the fact that sheets are only formed at higher film Reynolds number, this does not correspond to the observations. In an evaluation using small subsets of data, the values of e were found to be negative for both types of tubes. In this case it was assumed that there was no deflection as long as the angle calculated with Eq. (11) was negative. This assumption, that the condensate starts to oscillate above a certain threshold value in the Reynolds number ($\theta > 0$), is closer to the actual situation than the correlations given above ($e > 0$). Thus, for simplicity, in a next step the relationship between the angle θ and the film Reynolds number was forced to pass through the origin ($e = 0$). The results of the new optimization of the value d are listed in Table 2 as the second method in comparison with the values mentioned above for both types of tubes. Approximately, the same standard deviation of the relative error compared to the whole database is obtained, while the mean relative error is about 1% larger for the second method ($e = 0$).

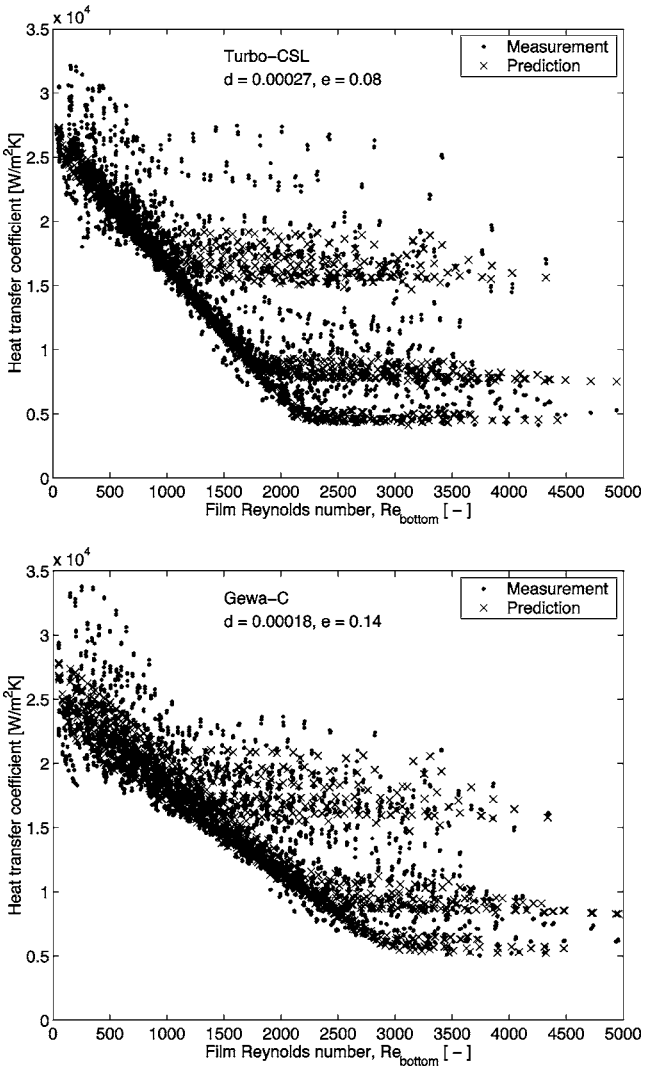

Fig. 4 Prediction of heat transfer coefficients of the 3D enhanced tubes (first method)

Above it was shown for the measurements without condensate leaving sideways that the values of the coefficients a and b are similar for both types of tubes and the prediction error increases little if the same mean values are used for both types of tube. An optimization using these mean values of a and b lead to equal values of d for both types of tubes as shown by the third method. The relative mean error and standard deviation of this third method is also listed in Table 2. The relative mean error is a little smaller for the Turbo-CSL tube and increases only by 0.4% for the Gewa-C tube. The standard deviations are very close to those of the second method.

A further attempt to simplify the proposed model is to assume that the relationship between the angle θ and the film Reynolds number can be approximated to be the same for both types of tubes used in the present investigation. Using a value of $d = 0.00028$ as the best compromise of the values determined above, the inaccuracies increase significantly. The mean relative error for the Turbo-CSL tube becomes −8.8% with a standard deviation of 13.3%. For the Gewa-C tube, the mean relative error becomes 2.1% with a standard deviation of 14.4%. For this reason, this last approximation is not recommended. The results thus far are promising for this limited database (two tubes, three tube pitches, wide range of film Reynolds numbers, but only one fluid), proving that the observed behavior in heat transfer and liquid "slinging" can be described by the new method proposed above. Although the method is empirical, it uses a minimum of constants and includes some geometric characteristics of the tube layout in the liquid "slinging" process. For real condensers with neighboring tubes catching some of the slinging liquid while vapor may entrain some too, the above method can eventually be amplified to capture those effects.

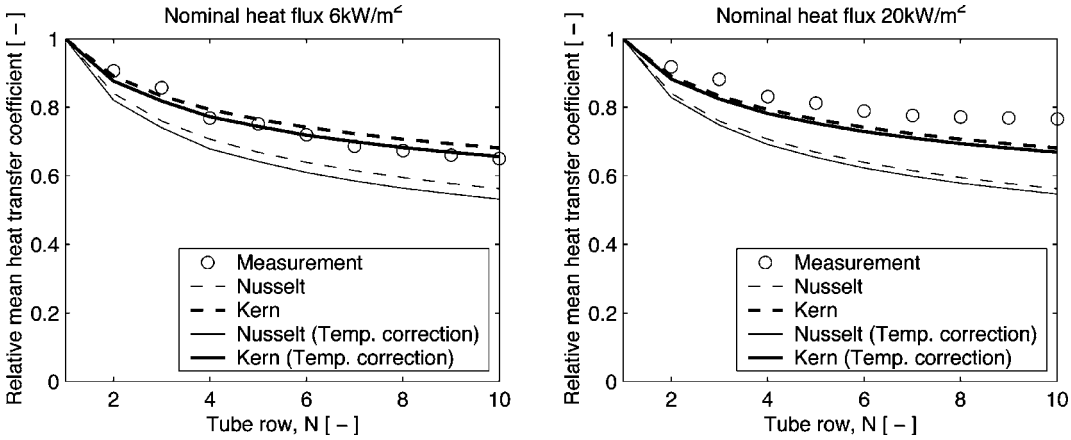

Fig. 5 Tube row effect for the plain tube at a tube pitch of 25.5 mm at a nominal heat flux of 6 and 20 kW/m²

Plain Tube

Tube Row Effect. In the literature, the inundation of condensate from tube row to tube row is often referred to as the tube row effect. The condensate from the above tubes drains onto the tubes below, increasing the amount of condensate flowing on each tube in addition to the new condensate formed on that particular tube. With increasing row number, starting from the top, the heat transfer performance of the tubes decreases and, as such, the mean heat transfer coefficient of the entire array. The performance of the entire array, or an individual tube, is often compared to the performance of the top tube. For high-accuracy calculations, this approach is not useful, as generally in a bundle, not only the inundation varies but also the condensing temperature difference $(T_{sat}-T_w)$ and the flow pattern. However, in order to make a comparison to other studies, the experimental results without liquid overfeed will be presented below as a function of position in the tube array.

In the present investigation the surface temperature of the tubes in the array at their midpoint was not uniform, mainly due to the experimental setup with a two-pass water flow inside the tubes. Thus, the surface temperature of the tubes in the even row numbers was lower than on the odd tubes just above. In an attempt to characterize this nonuniformity of surface temperature in Nusselt's theory, a similar expression with a correction for the nonuniformity of the surface temperature has been derived by Gstöhl [20]

$$\frac{\overline{\alpha_N}}{\alpha_1} = N^m \left(\frac{\overline{\Delta T_N}}{\Delta T_1} \right)^m \tag{12}$$

where ΔT_1 is the local condensation temperature difference at the midpoint of the top tube and $\overline{\Delta T_N}=(\Delta T_1+\Delta T_2+\ldots+\Delta T_N)/N$ is the mean condensation temperature difference on the entire tube array from those at the midpoints of each tube (ΔT_1, ΔT_2, etc.).

For this calculation, the mean heat transfer coefficient of the entire array of tubes was defined as the mean heat flux divided by the mean temperature difference

$$\overline{\alpha_N} = \frac{\overline{q_N}}{\overline{\Delta T_N}} = \frac{\alpha_1 \Delta T_1 + \alpha_2 \Delta T_2 + \cdots + \alpha_N \Delta T_N}{\Delta T_1 + \Delta T_2 + \cdots + \Delta T_N} \tag{13}$$

Figure 5 depicts mean heat transfer performance of the entire array as a function the tube row. The mean heat transfer coefficients divided by the heat transfer coefficient of the top tube for measurements at nominal heat fluxes of 6 and 20 kW/m² are given. For comparison, the predictions, according to Nusselt and Kern for uniform surface temperature and both expressions with the correction for non-uniform surface temperature are also given. At the lower heat flux, the measurements are in agreement with the expression of Kern with the correction for nonuniform surface temperature. During the measurements, the surface temperature on the top tube is higher than on the other tubes because its performance is highest. For this reason, assuming a uniform surface temperature leads to a weaker tube row effect compared to the tube row effect taking into account the nonuniformity of surface temperature. At the higher heat flux, the condensation temperature differences are larger than for the low heat flux, so the differences between the mean temperature and the temperature of the top tube are smaller and thus the temperature correction is smaller. At the heat flux of 20 kW/m², the observed data are higher than predicted by Kern's expression.

Using the experimental data and Eqs. (1) and (12) to find the optimal exponents *m*, Tables 3 and 4 list the values of these exponents in the tube row expressions determined for the three tube pitches and for the three nominal heat fluxes. The values in brackets were determined using only the top six tubes at every tube pitch in order to compare directly to the largest tube pitch, which

Table 3 Tube row effect for the plain tube without surface temperature correction (exponents in Eq. (1)) for all tubes in the array and on the first six tubes (values in brackets)

	Nominal heat flux		
Tube pitch	6 kW/m²	12 kW/m²	20 kW/m²
25.5mm	-0.18 (-0.17)	-0.15 (-0.14)	-0.13 (-0.13)
28.6mm	-0.16 (-0.15)	-0.15 (-0.15)	-0.11 (-0.11)
44.5mm	-0.21	-0.13	-0.10

Table 4 Tube row effect for the plain tube with surface temperature correction (exponents in Eq. (12)) for all tubes in the array and on the first six tubes (values in brackets)

	Nominal heat flux		
Tube pitch	6 kW/m²	12 kW/m²	20 kW/m²
25.5mm	-0.16 (-0.15)	-0.14 (-0.13)	-0.12 (-0.12)
28.6mm	-0.15 (-0.13)	-0.14 (-0.14)	-0.11 (-0.11)
44.5mm	-0.18	-0.12	-0.09

only had six tubes. Neglecting the effect of wall temperature, nonuniformity leads to a weaker tube row effect. The differences for the different tube spacings are small. Generally, the tube row effect is stronger for lower heat fluxes. On average, Tables 3 and 4 suggest an exponent of $-1/7$ as opposed to $-1/4$ of Nusselt and $-1/6$ of Kern. Equation (12) captures the effect of the nonuniformity in wall temperature within the array and can easily be implemented in a row by row design procedure.

Waves and Turbulent Film Condensation. The heat transfer results on the present single plain tube are well described using Nusselt's equation for laminar film condensation as shown in Table 4 in Part I [15]. In this theory, heat transfer is a function of the film Reynolds number leaving the bottom of the tube

$$\frac{\alpha_o}{\lambda_L}\left[\frac{\mu_L^2}{\rho_L(\rho_L-\rho_V)g}\right]^{1/3} = 1.208\ \mathrm{Re}_{\mathrm{bottom}}^{-1/3} \tag{14}$$

It is known that the Nusselt theory has a limited range of applicability, as purely laminar condensate flow is only encountered at very low film Reynolds numbers. Little is known for condensation on horizontal tubes, but it has been intensively studied for condensation on a vertical plate. For this reason, a comparison of observations in literature for condensation on vertical plates (or tubes) are mentioned below. Observations of film condensation on vertical plates indicate that the interface becomes unstable and forms ripples or waves. These waves increase heat transfer by enlarging the interfacial area and by reducing the mean thickness of the film.

According to Butterworth [21], the film Reynolds number for the onset of interfacial waves on a vertical plate occurs at about a film Reynolds number of 30. Another criterion for the onset of waves is related to the Archimedes number Ar_L, which is defined as

$$\mathrm{Ar}_L = \frac{\rho_L^2\sigma_L^{3/2}}{\mu_L^2 g^{1/2}(\rho_L-\rho_G)^{3/2}} \tag{15}$$

The laminar falling film condensation heat transfer on vertical plates is enhanced when

$$\mathrm{Re} > 9.3\mathrm{Ar}_L^{1/5} \tag{16}$$

For R-134a with an $\mathrm{Ar}_L = 1.6$ at the present test conditions, waves should occur according to this criterion for film Reynolds numbers above 10.

In the present investigation the film Reynolds number at the bottom of the top tube ranged from 20 to 80 without inundation. The heat transfer coefficients measured on the top tube were in very good agreement with Nusselt's theory for laminar film condensation [15]. However, the coefficients measured on the second and the following tubes were underpredicted. This observation is explained by the difference in flow pattern (as a continuous sheet was never observed as assumed by Nusselt) and by the occurrence of interfacial waves in analogy to condensation on a vertical plate.

To account for the effect of waves on heat transfer, Kutateladze [22] suggested an empirical correction of $0.8(\mathrm{Re}/4)^{0.11}$ for condensation on a vertical plate as mentioned by Thome [23]. Kutateladze and Gogonin [4] used an empirical correction term (referring to Labuntsov [24]) in the Nusselt equation for the enhancement of heat transfer on a vertical surface by the waves of $(\mathrm{Re}/2)^{0.04}$ over the range of film Reynolds numbers from 10 $< \mathrm{Re} <$ 200.

During the present heat transfer measurements, the condensate flow on the plain array was very unstable as noted previously and due to the occurrence of liquid "slinging" some condensate left the tubes sideways. For clearness, and to reduce the effect of liquid slinging to a minimum, only the results of the top three tubes are considered in the following first step in the analysis.

Figure 6 depicts the measured data on the top three tubes at all tube pitches and heat fluxes. The prediction by the Nusselt theory and predictions using an empirical multiplier to account for the waves are also plotted. At low film Reynolds numbers the lower limit of the measured data is well described by the Nusselt theory. These points are the measured values on the top tube without liquid inundation (shown in [15]). On the top tube, the measured data are very close to Nusselt theory up to film Reynolds numbers of about 80. For the second and third tubes in the array, the measured heat transfer coefficients are underestimated by Nusselt theory. Both empirical corrections for the waviness of the film lie within the measured data, showing that these corrections determined for condensation on vertical surfaces work well for condensation on horizontal tubes. The correction of [22] seems to be closest to the measured data. The tendency of the Kutateladze [22] and Kutateladze and Gogonin [4] methods to underpredict the data at the high film Reynolds numbers is thought to be caused by the liquid slinging observed.

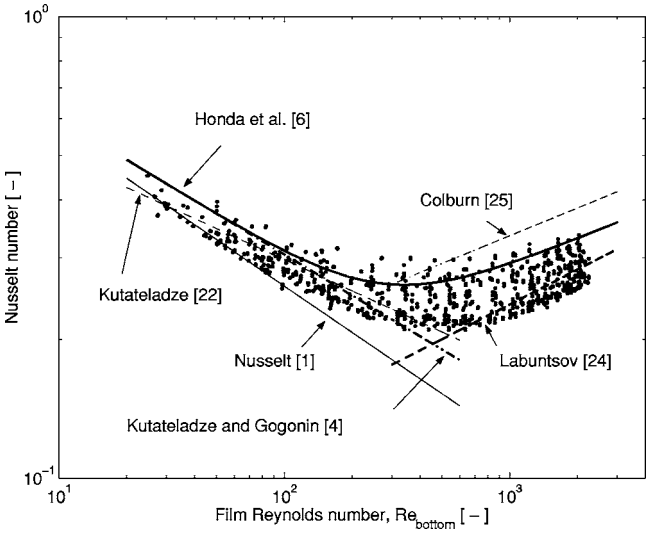

Fig. 6 Local heat transfer coefficients on the top three plain tubes in the array. Comparison with correlations for the wavy and turbulent flow regimes on a vertical plate.

At high film Reynolds numbers the condensate flow may become turbulent. The transition threshold for the bundle is adapted from a vertical-plate turbulent transition criterion of 1600 (but also values of 1200, 1800, and 2000 have been proposed as remarked by Thome [23]).

Colburn [25] set the transition at a film Reynolds number of 2000 when comparing his experimental data to the Nusselt theory. Applying an analogy to turbulent liquid flow in pipes, Colburn proposed the following correlation for the local turbulent condensing coefficient on a vertical plate:

$$\frac{\alpha}{\lambda_L}\left[\frac{\mu_L^2}{\rho_L(\rho_L-\rho_V)g}\right]^{1/3} = 0.056\ \mathrm{Re}^{0.2}\,\mathrm{Pr}_L^{1/3} \tag{17}$$

Butterworth [21] instead recommends adapting the Labuntsov expression [24] for turbulent film condensation on a vertical plate to horizontal tubes for predicting local turbulent film condensation on horizontal tube bundles as follows:

$$\frac{\alpha_o}{\lambda_L}\left[\frac{\mu_L^2}{\rho_L(\rho_L-\rho_V)g}\right]^{1/3} = 0.023\ \mathrm{Re}^{0.25}\,\mathrm{Pr}_L^{0.5} \tag{18}$$

For film Reynolds numbers above 1000 in Fig. 6, the prediction by the correlation of Labuntsov is within the scatter of the experimental data, whereas the correlation of Colburn clearly overpredicts the measured data.

Honda et al. [5] assumed an asymptotic model for predicting condensation of stagnant R-113 vapor on a vertical column of horizontal tubes as follows:

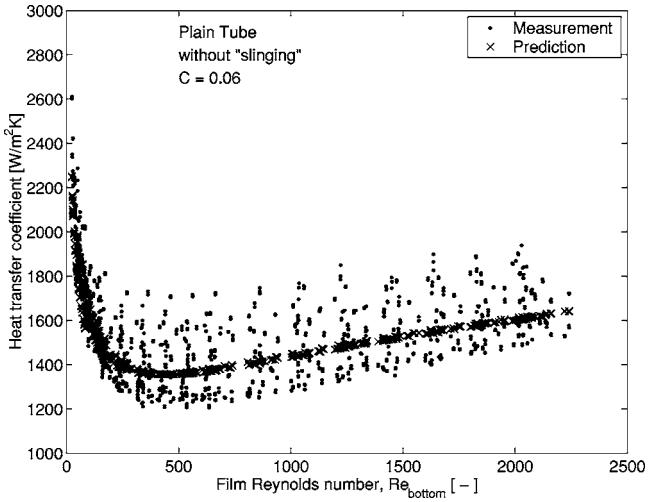

Fig. 7 Prediction of heat transfer coefficients of the plain tubes (asymptotic model)

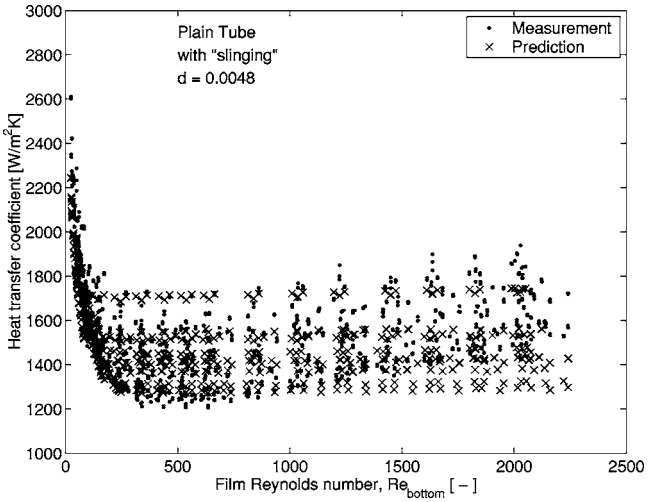

Fig. 8 Prediction of heat transfer coefficients of the plain tubes (with slinging)

$$\frac{\alpha_o}{\lambda_L}\left[\frac{\mu_L^2}{\rho_L(\rho_L-\rho_V)g}\right]^{1/3} = [(1.2\ \mathrm{Re}^{-0.3})^4 + (0.072\ \mathrm{Re}^{0.2})^4]^{1/4} \tag{19}$$

The first term in Eq. (19) is the Nusselt solution with the enhancement factor for the waves from Kutateladze and Gogonin [4]. The second term is a correlation for turbulent condensation, similar to the expression of Colburn. The experimental data of Honda et al. [5] did not cover the turbulent flow regime; they used the R-12 and R-21 data of Kutateladze and Gogonin [4] to develop their correlation, neglecting the Prandtl number effect, which comes into play in the turbulent flow regime. However, the Prandtl number of R-134a ($\mathrm{Pr}_L=3.4$) in the present study is close to the Prandtl number of R-12 and R-21 ($\mathrm{Pr}_L\approx 3.5$) in the investigation of Kutateladze and Gogonin [4], and therefore, it is not feasible to determine the effect of the Prandtl number here. For the comparison shown in Fig. 6, the effect of the Prandtl number for R-134a is also not been taken into account. It can be seen at low film Reynolds numbers that Eq. (19) is asymptotic to the correlation of Kutateladze and Gogonin, and at high film Reynolds numbers, it lies between the correlations of Colburn and Labuntsov, overpredicting most of the experimental data at high film Reynolds numbers.

In analogy to the correlation of Honda et al., the following equation was used to obtain a better fit to the present R-134a data on the top three tubes where the multiplier of the expression for the turbulent flow regime was found to be $C=0.060$:

$$\frac{\alpha_o}{\lambda_L}\left[\frac{\mu_L^2}{\rho_L(\rho_L-\rho_V)g}\right]^{1/3} = [(1.2\ \mathrm{Re}^{-0.3})^4 + (C\ \mathrm{Re}^{0.2})^4]^{1/4} \tag{20}$$

Assuming a Prandtl number effect, such as Colburn in Eq. (17), then the term $C\,\mathrm{Re}^{0.2}$ in Eq. (20) can be replaced by $0.04\mathrm{Pr}_L^{1/3}\mathrm{Re}^{0.2}$, using the Prandtl number of R-134a to obtain a general form. A comparison of this modified Honda correlation with the experimental data is depicted in Fig. 7. The predictions lie well centered within the experimental data and follow the trends of the data. However, this correlation, neglecting the effect of the tube pitch, fails to predict the scatter in the measurements, which is partly due to the different tube spacings in the data set. The mean relative error is −1.2% with a standard deviation of 7.9%. Approximately, 80% of the measurements are within ±10% error.

Thus, it is seen that the observed behavior of heat transfer on an array of horizontal plain tubes can be described by a model combining a zone where the heat transfer is increased compared to the Nusselt theory by the occurrence of interfacial waves with a zone for turbulent condensation, where the heat transfer increases with increasing film Reynolds number. However, this behavior was especially observed for the top three tubes in the array. For the lower tubes the heat transfer coefficient was almost constant for film Reynolds numbers above 300, which suggests the above approach is missing something, which is notably the slinging effect.

Predictive Method Taking Into Account for Condensate Slinging. As mentioned before, during the measurements on the plain tubes, a considerable amount of condensate left the array of tubes sideways. For this reason, the importance of modeling the observed heat transfer behavior by taking into account the fact that some condensate leaves the tubes is self evident. In analogy to the heat transfer model for the 3D enhanced tubes proposed above, the heat transfer on the array of plain tubes is modeled as follows. The maximum angle of deflection is assumed to be proportional to the film Reynolds number

$$\theta = d\mathrm{Re} \tag{21}$$

The calculation is started on the top tube in the array. When condensate is leaving sideways ($\theta > \theta_{\mathrm{crit}}$), the actual film Reynolds number on the top of the lower tubes is determined by Eq. (10). The heat transfer on each tube is calculated based on the Nusselt theory taking waviness into account by the empirical correction used by Kutateladze and Gogonin [4] as in Honda et al. method, Eq. (19), by

$$\frac{\alpha_o}{\lambda_L}\left[\frac{\mu_L^2}{\rho_L(\rho_L-\rho_V)g}\right]^{1/3} = 1.2\ \mathrm{Re}_{\mathrm{bottom}}^{-0.3} \tag{22}$$

As the film Reynolds number leaving at the bottom of the tube is not known in advance, an iterative calculation is necessary. The value of the coefficient $d=0.048$ was determined using all data of the measurements on the top three tubes for all three tube pitches. This value of d is much larger than the ones determined on the 3D enhanced tubes, meaning the maximum angle of deflection increases faster with increasing film Reynolds number, so that the condensate leaves the array of tubes at lower film Reynolds numbers, which corresponds to the visual observations. The increased slinging effect of the plain tube compared to the 3D tubes can be explained by the increased liquid adhesion by the capillary forces acting on the film of the 3D enhanced tubes.

A comparison of predicted heat transfer coefficients to the measurements is depicted in Fig. 8. At low film Reynolds numbers, the predicted heat transfer coefficient decreases according to Eq. (22). With increasing overfeed rates, the amount of condensate

Table 5 Tube row effect for the low finned tube (exponent m in Eq. (1)) for all tubes in array

	Nominal heat flux		
Tube pitch	20 kW/m^2	40 kW/m^2	60 kW/m^2
25.5mm	-0.06	-0.03	-0.02
28.6mm	-0.07	-0.02	-0.01
44.5mm	-0.05	-0.03	-0.02
Average	-0.06	-0.03	-0.02

that leaves the array of tubes increases, resulting approximately in a constant inundation on the tubes and subsequently a constant heat transfer coefficient. The mean relative error is −2.5% with a standard deviation of 7%. Approximately 80% of the measurements are predicted within an error of ±9% using this method that assumes there is no transition to turbulent flow. This simple model fails to predict the trend of the slight increase in heat transfer with increasing film Reynolds number, which was assumed to be due to turbulent heat transfer in the first model above. However, the second model, based on the assumption that some condensate is leaving the array, accounts for the effect of tube spacing, which leads to approximately the same scatter as that observed during the measurements as can be observed in Fig. 8. This effect of the tube spacing and "slinging" was completely ignored in all other previous models.

The two methods proposed above have been developed using only the data of the top three tubes. In a comparison with all data for all the tubes in the array, the modified model of Honda et al. given by Eq. (20), ignoring the effect of slinging, overpredicts the experimental data with a mean relative error of 10% and a standard deviation 12%, whereas the second model taking into account the effect of slinging gives a mean overprediction of 7.4% with a standard deviation of 13%. This means that the second model, including the slinging effect and its tube pitch influence, is more suitable to describe the measured data in the present case. This is not surprising, as during the measurements, condensate was always seen leaving the array of plain tubes at high overfeed rates.

However, an optimization of the two models using all the data of the ten tubes (4245 data points) leads to values of $C=0.052$ and $d=0.0027$ for the first and second models, respectively. With these coefficients the mean relative error of the first model is 0.6% with a standard deviation of 10% and the mean error of the second model is −1.3% with a standard deviation of 12%. Hence, both methods give similar results, but the second one that includes liquid slinging and tube pitch may be the better of the two. A new third model that introduces the liquid slinging effect into the Honda model could be envisioned. In a tube bundle, the "slinging liquid" will deposit on nearby tubes or be entrained in the vapor flow as a mist and could thus be incorporated into a complete bundle model. However, at present no local (as defined here) bundle heat transfer data are currently available in the literature and implementation of this third step will be investigated in the future.

Low Finned Tube

In the literature, the tube row effect on low finned tubes is often described using the equation derived by Nusselt's theory for plain tubes and adapting the value of the exponent. For comparison purposes, the tube row effect on the low finned tubes was quantified in the same way as for the plain tube using Eq. (1), ignoring the nonuniformity in wall temperatures. Table 5 lists the values of the exponent m in the tube row expression for the three tube pitches and for the three nominal heat fluxes. In order to determine the exponent m for the data without overfeed, all ten tubes were used for the smallest tube pitch. For the middle and the large tube pitches, all nine and all six tubes were used, respectively. The values determined using only the top six tubes for all tube pitches are very close to the ones listed in Table 5. The observed tube row effect is very small for the finned tube ranging from $m=-0.01$ to $m=-0.07$ (refer to Fig. 12 in Part I [15]). There is little difference for the different tube pitches and the average values of m are also shown, which suggests average exponents ranging from $-1/16$ to $-1/50$. Generally, the tube row effect is stronger for lower heat fluxes as was also observed in Tables 3 and 4 for the plain tube. The very weak tube row effect is explained by the observed differences in condensate flow pattern. On the finned tube, the condensate flows very unsteady and never forms complete sheets [17]. In addition, the fins prevent the axial spreading of the liquid such that large portions of the tube are not affected by inundation from the tube above. Taking into account the nonuniform surface temperature according to Eq. (12) had a negligible effect on the values of the exponent m.

As the tube row effect on the low finned tube was found to be very small, a comparison to existing single tube correlations is made neglecting the tube row effect. Similar to the comparison to the single tube data [15], the model of Sreepathi et al. [26] gives the best prediction of the experimental data, with a mean relative error of −1.8% and a standard deviation of 8%. Interestingly, the relative errors are smaller at high film Reynolds numbers on the lower tubes, where the tube row effect is expected to be highest. As the data here are only for one fluid/one fin density combination, no general conclusion can be made about the "best" overall method here.

For design purposes, often the tube row effect in the following form is recommended for use:

$$\frac{\alpha_N}{\alpha_1} = N^{m+1} - (N-1)^{m+1} \tag{23}$$

where α_N is the local heat transfer coefficient on the Nth tube. Based on the mean value of $m=-0.03$ determined from all the data, an exponent of 0.97 is obtained for Eq. (23). However, even this weak tube row effect applied to the whole database of measurements without overfeed leads to an underestimation of the heat transfer coefficient on the lower tubes in the array; thus, the mean relative error becomes 5.3% with a standard deviation of 7.8%.

Alternatively, the data on all tubes in the array for all tube pitches can be correlated by a simple correlation of the following form:

$$q_o = C(\Delta T^b) \tag{24}$$

For the measurements without overfeed, the coefficients were found to be $C=17700$ W/m^2 and $b=0.79$ with mean relative error of 0.3% and a standard deviation of 7.9%. The accuracy of this very simple curvefit is about the same as the model of Sreepathi et al. [26].

Extending the analysis to the whole database, including the measurements with liquid overfeed, the same behavior as described above for the measurements without overfeed are obtained. Even when the film Reynolds number is increased up to 4500 the model of Sreepathi et al., neglecting the effect of tube rows, predicts the experimental data best. The mean relative error increases to −3.2% with a standard deviation of 7.9%. The heat transfer performance can also be correlated by Eq. (24), with the coefficients $a=18{,}000$ W/m^2 and $b=0.78$ (mean relative error 0.3%, standard deviation 7.7%). No new general model for condensation on tube arrays of low finned tubes is proposed here since, even though ~4000 data points were taken, only one fluid and one fin density are represented for very wide range of test conditions.

Conclusions

The heat transfer performances of all four types of tubes have been analyzed here. For the 3D enhanced tubes, the Turbo-CSL and the Gewa-C, the heat transfer coefficient as function of the film Reynolds number was characterized by two distinct zones. At low film Reynolds numbers, the heat transfer coefficient decreased almost linearly and above a certain film Reynolds number the heat transfer coefficient decreases much slower or achieves a constant value. For both types of 3D enhanced tubes, the local heat flux on a tube in the array was correlated as function of condensation temperature difference and the liquid inundation in the form of the film Reynolds number falling on the tube. The coefficients in the correlation were found to be close for both tubes apart from the coefficient, which corresponds to the slope in the deterioration in heat transfer performance with increasing film Reynolds number. The heat transfer coefficient of the Gewa-C tube decreases less rapidly with increasing film Reynolds number. Visual observations revealed that condensate left the array of tubes sideways, and hence, a new model was proposed to account for this. This simple approach was able to describe the observed heat transfer behavior with a minimum of empirical constants. All measurements at the three different tube pitches of both 3D enhanced tubes were predicted by the new method with a mean error of 3% and standard deviations of $<13\%$. Notably, this new 3D tube method is easily applied to new tube/fluid combinations with a limited experimental database to find the values of a, b, c, and d.

For the plain tube, the measured heat transfer coefficients on the top tube without liquid inundation were found to be in good agreement with Nusselt's theory even for film Reynolds numbers, leaving the bottom of the tube corresponding to the wavy (ripple) flow regime. For the measurements without additional liquid overfeed, the tube row effect was expressed like in Nusselt's expression as the ratio of the mean heat transfer coefficient of the array to the heat transfer coefficient of the top tube. The mean value of the exponent in the expression was found to be $m=-0.15$ (equivalent to $-1/7$) as opposed to Nusselt's theoretical value of $-1/4$. A new modified tube row expression taking into account the nonuniform surface temperatures of the tubes in the array lead to a similiar value of $m=-0.14$ (i.e., again about $-1/7$), indicating that the effect of differences in the surface temperature on the tubes in the array were small in the present case.

It was shown that the measured data on the plain tubes could be described by an asymptotic model of Honda [5] based on heat transfer in wavy flow and turbulent flow regimes or even better with a slight modification using the extensive database from Part I [15]. Alternatively, is was shown that the data could also be just as well described by a liquid slinging model based on visual observations that a fraction of the condensate leaves the array of tubes, in analogy to the model proposed for the 3D enhanced tubes.

For the low finned tube, in analogy to the plain tube, the best exponent in the tube row expression of $m=-0.03$ (i.e., $-1/33$) was determined for the tube row effect of liquid inundation. Neglecting the effect of inundation completely, all data measured on the low finned were underpredicted by the model of Sreepathi [26] by only -3% mean error with a standard deviation of 8%.

Finally, the effects of intertube flow patterns (drop, column, and sheet) that were expected to play a role in the tube row effect turned out to not be of notable direct importance.

Acknowledgments

The authors acknowledge the financial support to the EPFL/LTCM Falling Film Research Club by the following members: Axima Refrigeration AG, Dunham-Bush Inc., UOP Inc., Wieland-Werke AG, and Wolverine Tube Inc., and, in particular, Wieland-Werke AG and Wolverine Tube Inc. for providing the tube samples.

Nomenclature

- Ar = Archimedes number, defined by Eq. (15)
- c_p = specific heat at constant pressure, J/(kg K)
- g = acceleration due to gravity [9.81], m/s^2
- m = row effect exponent in Eqs. (1) and (12)
- N = Number of rows counting from top row
- Nu^* = Nusselt number $\{\alpha(\mu_L/[\rho_L(\rho_L-\rho_V)g]^{1/3}/\lambda_L\}$
- Pr = Prandtl number $[\mu c_p/\lambda_L]$
- p = center to center tube pitch, m
- r = tube radius, m
- T = temperature, K
- q = local heat flux relative to a surface, W/m^2
- Re = film Reynolds number $[4\Gamma/\mu]$
- x = coordinate in axial direction, m

Greek Symbols

- α = local heat transfer coefficient, $W/(m^2\,K)$
- ΔT = condensation temperature difference, $T_{sat}-T_w$
- ε = mean relative error, defined by Eq. (6)
- Γ = film mass flow rate on one side per unit length of tube, kg/(m s)
- λ = thermal conductivity, W/(m K)
- μ = dynamic viscosity, $N\,s/m^2$
- θ = maximum deflection angle, rad
- θ_{crit} = critical deflection angle, defined by Eq. (9), rad
- ρ = density, kg/m^3
- σ = standard deviation, defined by Eq. (7)
- σ = surface tension, N/m

Subscripts

- bottom = at the bottom of the tube
- L = saturated liquid
- N = number of rows measured from top row
- o = external side at fin tip
- sat = saturated conditions
- top = at the top of the tube
- V = saturated vapor
- w = wall

References

[1] Nusselt, W., 1916, "Die Oberächenkondensation des Wasserdampfes," Z. Vereins deuts. Ing., **60**(27-28), pp. 541–546 and pp. 569–575.

[2] Kern, D. Q., 1958, "Mathematical Development of Tube Loading in Horizontal Condensers," AIChE J., **4**(2), pp. 157–160.

[3] Katz, D. L., and Geist, J. M., 1948, "Condensation on Six Finned Tubes in a Vertical Row," Trans. ASME, **70**, pp. 907–914.

[4] Kutateladze, S. S., and Gogonin, I. I., 1979, "Heat Transfer in Film Condensation of Slowly Moving Vapor," Int. J. Heat Mass Transfer, **22**, pp. 1593–1599.

[5] Honda, H., Uchima, B., Nozu, S., Nakata, H., and Fujii, T., 1989, "Condensation of Downward Flowing R-113 Vapor on Bundles of Horizontal Smooth Tubes," Heat Transfer-Jpn. Res., **18**(6), pp. 31–52.

[6] Honda, H., Nozu, S., and Takeda, Y., 1989, "A Theoretical Model of Film Condensation in a Bundle of Horizontal Low Finned Tubes," ASME J. Heat Transfer, **111**, pp. 525–532.

[7] Webb, R. L., and Murawski, C. G., 1990, "Row Effect for R-11 Condensation on Enhanced Tubes," ASME J. Heat Transfer, **112**, pp. 768–776.

[8] Memory, S. B., Mazzone, R. W., and Marto, P. J., 1992, "Enhanced Laminar Film Condensation of R-113 Using Wire-Wrap on a Horizontal Roped Tube Bundle," Inst. Chem. Eng. Symp. Ser., **129**(1), pp. 249–262.

[9] Eissenberg, D. M., 1972, "An Investigation of the Variables Affecting Steam Condensation on the Outside of a Horizontal Tube Bundle," Ph.D. thesis, University of Tennessee.

[10] McNaught, J. M., and Chu, C. M., 1993, "Heat Transfer Measurements in Condensation on Bundles of Low-Finned Tubes: Effects of Fin Frequency," *Eng. Foundation Conf., Condensation and Condenser Design*, St. Augustine, Florida, pp. 367–376.

[11] Cheng, W. Y., and Wang, C. C., 1994, "Condensation of R-134a on Enhanced Tubes," ASHRAE Trans., **100**(2), pp. 809–817.

[12] Kulis, F., Compingt, A., Mercier, P., and Rivier, P., 1995, "Design Method for Shell and Tube Condensers in Refrigeration Units," *Heat Transfer in Condensation*, Eurotherm Seminar 47, Paris, pp. 133–138.

[13] Rewerts, L. E., Huber, J. B., and Pate, M. B., 1996, "The Effect of R-123 Condensate Inundation and Vapor Shear on Enhanced Tube Geometries," ASHRAE Trans., **102**(2), pp. 273–284.

[14] Rewerts, L. E., Huber, J. B., and Pate, M. B., 1997, "The Effect of Noncondensable Gas on the Condensation of R-123 on Enhanced Tube Geometries," ASHRAE Trans., **103**(1), pp. 149–163.
[15] Gstoehl, D., and Thome, J. R., 2006, "Film Condensation of R-134a on Tube Arrays With Plain and Enhanced Surfaces: Part I—Experimental Heat Transfer Coefficients," ASME J. Heat Transfer, **128**(1), pp. 21–32.
[16] Thome, J. R., 2004, *Video Gallery of Flow Phenomena*, Engineering Databook III, Wolverine Tube, Huntsville, AL, Chap. 1, http://www.wlv.com/products
[17] Gstoehl, D., and Thome, J. R., "Visualization of R-134a Flowing on Tube Arrays With Plain and Enhanced Surfaces under Adiabatic and Condensing Conditions," Heat Transfer Eng. (accepted for publication).
[18] Wei, Y.-H., and Jacobi, A. M., 2002, "Vapor-Shear, Geometric, and Bundle Depth Effects on Intertube Falling-Film Modes," *Proc. of 1st International Conference on Heat Transfer, Fluid Mechanics and Thermodynamics*, *HEFAT2002*, 8–10 April, Kruger Park, South Africa, **1**(1), pp. 40–46.
[19] Rose, J. W., 2004, "Heat-Transfer Coefficients, Wilson Plots and Accuracy of Thermal Measurements," Exp. Therm. Fluid Sci., **28**, pp. 77–86.
[20] Gstöhl, D., 2004, "Heat Transfer and Flow Visualization of Falling Film Condensation on Tube Arrays With Plain and Enhanced Surfaces," Ph.D. thesis No. 3015, Swiss Federal Institute of Technology, Lausanne, http://library.epfl.ch/theses/?display=detail&nr=3015
[21] Butterworth, D., 1990, *Hemisphere Handbook of Heat Exchanger Design*, Hemisphere, New York, Chap. 2.6.2.
[22] Kutateladze, S. S., 1963, *Fundamentals of Heat Transfer*, Academic Press, New York.
[23] Thome, J. R., 2004, *Condensation on External Surfaces*, Engineering Databook III, Wolverine Tube, Huntsville, AL Chap. 7, http://www.wlv.com/products
[24] Labuntsov, D. A., 1957, "Heat Transfer in Film Condensation of Pure Vapours on Vertical Surfaces and Horizontal Tubes," Teploenergetika, **7**, pp. 72–80.
[25] Colburn, A. P., 1934, "Notes on the Calculation of Condensation Where a Portion of the Condensate Layer is in Turbulent Motion," Trans. AIChE, **30**, pp. 187–193.
[26] Sreepathi, L. K., Bapat, S. L., and Sukhatme, S. P., 1996, "Heat Transfer During Film Condensation of R-123 Vapour on Horizontal Integral-Fin Tubes," J. Enhanced Heat Transfer, **3**(2), pp. 147–164.

Estimation of Time-Varying Inlet Temperature and Heat Flux in Turbulent Circular Pipe Flow

Cha'o-Kuang Chen
e-mail: ckchen@mail.ncku.edu.tw

Li-Wen Wu

Yue-Tzu Yang

Department of Mechanical Engineering,
National Cheng Kung University,
Tainan 70101,
Taiwan, Republic of China

This study addresses the conjugate heat transfer problem of hydrodynamically developed turbulent flow in a circular pipe. An inverse method is used to estimate the time-varying inlet temperature and the outer-wall heat flux simultaneously on the basis of temperature measurements taken at two different locations within the pipe flow. The present approach rearranges the matrix forms of the governing differential equations and then applies a whole domain estimation with the function specification method and the linear least-squares-error method to determine the two boundary conditions of the pipe flow. The dimensionless temperature data obtained from the direct problem are used to simulate the temperature measurements. The influence of temperature measurement errors upon the precision of the estimated results is investigated. The proposed method provides several advantages compared to traditional methods: (1) it yields a solution within a single computational iteration, (2) no prior information is required regarding the functional form of the quantities of interest, (3) no initial guesses of the unknown parameter values are required, and (4) the inverse problem can be solved in a linear domain. This study also considers the influence of the location of the temperature measurement sensors upon the accuracy of the calculated results. The numerical results confirm that the proposed method provides an efficient, robust, and accurate means of estimating the inlet temperature and outer-wall heat flux simultaneously in turbulent pipe flow.
[DOI: 10.1115/1.2130402]

Keywords: conjugate heat transfer, inverse method, numerical method, turbulent, pipe flow

1 Introduction

It is well known that conjugate heat transfer, in which interaction occurs between the conduction effects in a solid wall and the convection effects within a fluid flowing around it, occurs in many engineering devices. A familiar example is that of a heat exchanger, in which an interaction takes place between the conduction in the pipe wall and the convection in the fluid flowing over the wall. A further practical example is the flow of a fluid over fins. In this case, valuable design information can be obtained by simultaneously analyzing the conduction in the fin and the convection in the fluid. Finally, a significant example is that of the cooling rods within a nuclear reactor.

In the case of thin-walled pipes, the boundary conditions at the external surface are the same as those at the internal solid-fluid interface, and hence, early researchers neglected wall conduction effects and considered that the conditions on the external surface of the pipe were also imposed upon the surface of the inner wall. However, for conjugate heat transfer in thick-walled pipes, the boundary conditions imposed at the external surface are different from those at the internal surface. The problem of conjugate heat transfer has already been examined by a number of researchers [1–4]. Generally, it has been shown that a substantial amount of heat is transferred to the fluid in the unheated sections of the pipe as a result of wall conduction effects. These effects are more pronounced when the solid-to-fluid thermal conductivity ratio, k_{sf}, is high and the inner-wall radius ratio, $R_{iw}=r_{iw}/r_{ow}$, is low. In this situation, the thermal boundary conditions existing at the internal surface are not known a priori, and hence, the energy equations must be solved under the conditions of temperature and heat flux continuity.

Recently inverse heat conduction problems (IHCPs) have been analyzed for situations where a direct measurement of the thermal boundary behavior is difficult, or indeed impossible, to carry out. A typical application of such problems is the case where it is desired to measure the temperature of a surface, but where that temperature is so high, that were a thermocouple to be installed, it would rapidly be destroyed. Using direct measurement results to evaluate the heat loss in situations of this type is very complex. Various analytical and numerical approaches have been proposed to overcome these technical limitations. For example, Chen et al. [5] presented a hybrid method using the Laplace transform technique and the finite-difference method with a sequential in-time concept to estimate the unknown surface temperature of a plane plate in a two-dimensional IHCP using temperature measurements taken from within the plate. A method utilizing a boundary element inverse technique has also been developed for the estimation of the local heat transfer coefficients on the surface of arbitrarily shaped solids [6,7]. Lin et al. [8] applied the finite-difference method and the linear least-squares-error method to estimate the thermal behaviors at the center and surface of a heated cylinder positioned normally to a turbulent air stream. Several researchers have also investigated the inverse problem related to the estimation of the thermophysical properties of a heat-conducting medium. Kim and Lee [9] adopted the parameter estimation technique to predict the temperature-dependent thermal conductivity and volumetric heat capacity of a fluid flowing in a circular duct. Finally, Sawaf et al. [10] applied an iterative procedure based upon the Levenberg–Marquardt method and minimizing the sum of squares function to estimate the linearly temperature-dependent thermal conductivity and specific heat capacity of an orthotropic solid.

Contributed by the Heat Transfer Division of ASME for publication in the JOURNAL OF HEAT TRANSFER. Manuscript received September 30, 2004; final manuscript received July 16, 2005. Review conducted by Karen Thole.

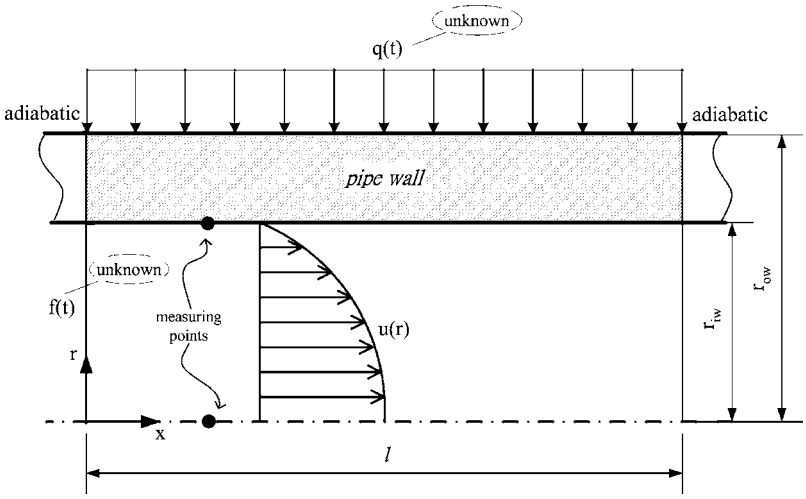

Fig. 1 System under consideration. Note that the velocity profile is fully developed and that the inlet temperature is constant. [*q*(*t*) and *f*(*t*) denote the outer-wall heat flux function and the inlet temperature function, respectively].

Many researchers have used the temperature history and distribution within a fluid to determine the boundary conditions of the fluid flow. For example, Su et al. [11,12] estimated the spatially non-uniform wall heat flux in a thermally developing hydrodynamically developed turbulent flow in a circular pipe by means of finite element interpolation and the Levenberg–Marquardt method. Meanwhile, Park and Lee [13] employed an inverse technique using the Karhunen–Loève Galerkin procedure to evaluate numerically the unknown functions of the wall heat flux for laminar flow inside a duct. Bokar and Özisik [14] applied the conjugate gradient method of minimization with an adjoint equation to estimate the time-varying inlet temperature for laminar flow inside a parallel-plate duct. Finally, Li and Yan [15,16] applied the same inverse method to estimate the space- and time-dependent wall heat flux for unsteady turbulent forced convection within a circular tube and a parallel-plate channel, respectively. However, the approaches described above all involve an iterative computational procedure. Furthermore, they neglect the effects of axial heat conduction within the wall in the vicinity of the solid-fluid interface.

The present study proposes an efficient technique which combines the function specification method, the whole domain estimation approach and the linear least-squares-error method to estimate the unknown outer-wall heat flux and the inlet temperature simultaneously for conjugate heat transfer within a hydrodynamically developed turbulent pipe flow. Yang and Chen [17] developed the linear least-squares-error method for solving boundary conditions in inverse heat conduction problems. The proposed inverse method is used to solve the two-dimensional conduction equation for the pipe wall and the two-dimensional convection equation for the flowing fluid simultaneously. The method requires no prior knowledge of the functional forms of the unknowns and yields solutions for the unknown conditions within a single computational iteration. The results confirm that the proposed method is capable of developing precise predictions of the unknowns and is relatively insensitive to temperature measurement errors. As when using traditional IHCPs to solve unknown conditions (e.g., local heat flux, local Nusselt numbers, temperature, geometry, heat transfer coefficients, etc.), it is shown that the precision of the results estimated using the proposed method increases as the locations of the temperature measuring points approach those of the unknown quantities.

This paper commences by introducing the governing equations for the direct problem, and then proceeds to present the matrix formulation of the inverse problem. The paper then discusses the effects of measurement errors and measuring point location upon the accuracy of the estimated results for the outer-wall heat flux and the inlet temperature. Finally, the paper presents some brief conclusions.

2 Physical Model and Governing Equations

The present study considers a system in which a Newtonian fluid of constant properties flows with steady turbulent motion in a circular pipe. At time $\tau=0$, the inlet temperature, $\Theta(0,R,\tau)$, commences to vary as a function of time in the form $F(\tau)$. The heat flux imposed on the external surface of the pipe, $Q(\tau)$, also varies as a function of time. In the present simulations, the calculations of these two distributions are performed simultaneously. Due to the symmetrical characteristic of the current problem, the domain need only consider one half of the pipe flow. Furthermore, this flow can be assumed to be two dimensional. The pipe wall is assumed to be homogeneous with a constant thermal conductivity, k_s, and a finite thickness. Meanwhile, the fluid is assumed to be incompressible, homogeneous, and to have a constant thermal conductivity, k_f. Finally, the pipe length is such that a fully developed flow is established at the entrance and exit regions.

Figure 1 presents a schematic representation of the current pipe flow and conjugate heat transfer system. The governing equations for the temperature field of the pipe flow are expressed by the following differential equations:

In the wall region:

$$\frac{\partial\Theta(X,R,\tau)}{\partial\tau}-\frac{\alpha_{sf}}{R}\frac{\partial}{\partial R}\left(R\frac{\partial\Theta(X,R,\tau)}{\partial R}\right)-\frac{\alpha_{sf}}{L^2}\frac{\partial}{\partial X}\left(\frac{\partial\Theta(X,R,\tau)}{\partial X}\right)=0 \tag{1a}$$

$$\frac{\Theta_s(0,R,\tau)}{\partial R}=0 \quad \text{at } X=0, \quad R_{iw}\leqslant R\leqslant 1, \quad \tau>0 \tag{1b}$$

$$\frac{\partial\Theta_s(X,1,\tau)}{\partial R}=Q(\tau) \quad \text{at } X>0, \quad R=1, \quad \tau>0 \tag{1c}$$

In the fluid region:

$$\frac{\partial\Theta(X,R,\tau)}{\partial\tau}+\frac{1}{2R_{\mathrm{iw}}L}\,\mathrm{Re}_\tau\,\mathrm{Pr}\,U(R)\frac{\partial\Theta(X,R,\tau)}{\partial X}-\left(1+\frac{\mathrm{Pe}_t}{\mathrm{Pr}_t}\right)\cdot\frac{1}{R}\frac{\partial}{\partial R}\left(R\frac{\partial\Theta(X,R,\tau)}{\partial R}\right)=0 \tag{2a}$$

$$\Theta_f(0,R,\tau)=F(\tau)\quad\text{at } X=0,\quad 0\leqslant R\leqslant R_{\mathrm{iw}},\quad \tau>0 \tag{2b}$$

$$\frac{\partial\Theta_f(X,0,\tau)}{\partial R}=0\quad\text{at } X>0,\quad R=0,\quad \tau>0 \tag{2c}$$

The initial condition is taken to be:

$$\Theta(X,R,0)=0\quad\text{at } X>0,\quad 0<R<1,\quad \tau=0 \tag{3}$$

At the interface between the pipe wall and the fluid inside the pipe ($R=R_{\mathrm{iw}}$):

$$\partial\Theta_f(X,R_{\mathrm{iw}},\tau)/\partial R=k_{\mathrm{sf}}\partial\Theta_s(X,R_{\mathrm{iw}},\tau)/\partial R \tag{4a}$$

$$\Theta_s(X,R_{\mathrm{iw}},\tau)=\Theta_f(X,R_{\mathrm{iw}},\tau) \tag{4b}$$

where various dimensionless terms are defined as:

$$\Theta(X,R,\tau)=\frac{T(x,r,t)-T_{\mathrm{initial}}}{T_{\mathrm{initial}}},\quad F(\tau)=\frac{f(t)-T_{\mathrm{initial}}}{T_{\mathrm{initial}}},$$

$$Q(\tau)=\frac{q(t)r_{\mathrm{ow}}}{k_sT_{\mathrm{initial}}},\quad U=\frac{u}{u_\tau},\quad R=\frac{r}{r_{\mathrm{ow}}},\quad X=\frac{x}{\ell},\quad \tau=\frac{\alpha_f t}{r_{\mathrm{ow}}}$$

In these expressions, $F(\tau)$ is the dimensionless time-varying temperature at the entrance of the pipe, $Q(\tau)$ denotes the dimensionless time-varying outer-wall heat flux, $U(R)$ is the hydrodynamically developed velocity profile, and $u_\tau=u_m\sqrt{c_f/2}$ is the friction velocity in the pipe. The friction coefficient $c_f/2$ is approximately equal to $0.039\,\mathrm{Re}^{-0.25}$. That fits the experimental data very well for $10^4<\mathrm{Re}<5\times10^4$ [18].

The governing parameters for conjugate conduction and turbulent forced convection heat transfer in a pipe subjected to nonuniform heat flux are the Reynolds number, $\mathrm{Re}_\tau=2r_{\mathrm{iw}}u_\tau/\nu$, the Prandtl number, Pr, the turbulent Prandtl number, Pr_t, the solid-to-fluid thermal conductivity ratio, $k_{\mathrm{sf}}=k_s/k_f$, and the solid-to-fluid thermal diffusivity ratio, $\alpha_{\mathrm{sf}}=\alpha_s/\alpha_f$.

The fully developed velocity profile of turbulent flow of a Newtonian fluid in a circular pipe is obtained from the following expression for the dimensionless velocity, which is expressed in terms of the wall parameters [18],

$$U=2.5\ln\left[\frac{1.5(1+R/R_{\mathrm{iw}})}{\overline{y}\dfrac{1+2(R/R_{\mathrm{iw}})^2}{}}\right]+5.5 \tag{5}$$

where, $\overline{y}=yu_\tau/\nu=(r_{\mathrm{iw}}-r)u_\tau/\nu$.

The turbulent Peclet number, Pe_t, is given by:

$$\mathrm{Pe}_t=\frac{\nu_t}{\nu}\,\mathrm{Pr} \tag{6}$$

where $\nu_t/\nu=(K\overline{y}/6)(1+R/R_{\mathrm{iw}})[1+2(R/R_{\mathrm{iw}})^2]$. This equation is obtained from an empirical equation proposed by Reichardt [19]. Equation (5) is derived from the Nikuradse equation, $U=2.5\ln\overline{y}+5.5$, together with the ν_t/ν relational equation and $K=0.4$. The turbulent Prandtl number, Pr_t, is given by the following expression, which corresponds well to the available experimental data [18]:

$$\mathrm{Pr}_t=\frac{1}{\dfrac{1}{2\mathrm{Pr}_{t_\infty}}+\mathrm{CPe}_t\sqrt{\dfrac{1}{\mathrm{Pr}_{t_\infty}}}-(\mathrm{CPe}_t)^2\left[1-\exp\left(-\dfrac{1}{\mathrm{CPe}_t\sqrt{\mathrm{Pr}_{t_\infty}}}\right)\right]} \tag{7}$$

where $\mathrm{C}=0.3$ and $\mathrm{Pr}_{t_\infty}=0.85$.

The number of independent dimensionless parameters in the current problem is quite large. A parametric study involving all of these individual parameters requires a vast set of results and is not the principal objective of the present study. Hence the values of certain dimensionless parameters are specified as constants, i.e.

$$L=\ell/r_{\mathrm{ow}}=30\quad\text{and } R_{\mathrm{iw}}=r_{\mathrm{iw}}/r_{\mathrm{ow}}=0.8,$$

$$k_{\mathrm{sf}}=72.027\quad\text{and } \alpha_{\mathrm{sf}}=25.87\quad\text{(for steel and water)},$$

$$\mathrm{Re}=3\times10^4\quad\text{and Pr}=7.$$

3 Numerical Method

3.1 Direct Problem. The present study employs the finite-difference method to analyze the direct problem. Following discretization, the dimensionless governing equations and boundary conditions obtained from Eqs. (1*a*)–(2*d*) can be expressed in the following recursive forms:

In the wall region:

$$\frac{\Theta^n_{i,j}-\Theta^{n-1}_{i,j}}{\Delta\tau}-\frac{\alpha_{\mathrm{sf}}}{R_j}\left(\frac{\Theta^n_{i,j+1}-\Theta^n_{i,j-1}}{2\Delta R}+R_j\frac{\Theta^n_{i,j+1}-2\Theta^n_{i,j}+\Theta^n_{i,j-1}}{(\Delta R)^2}\right)-\frac{\alpha_{\mathrm{sf}}}{L^2}\left(\frac{\Theta^n_{i+1,j}-2\Theta^n_{i,j}+\Theta^n_{i-1,j}}{(\Delta X)^2}\right)=0 \tag{8a}$$

$$\frac{\Theta^n_{0,j+1}-\Theta^n_{0,j}}{\Delta R}=0\quad\text{at } i=0,\quad jw\leqslant j\leqslant J,\quad n>0 \tag{8b}$$

$$\frac{\Theta^n_{i,J}-\Theta^n_{i,J-1}}{\Delta R}=Q^n\quad\text{at } i>0,\quad j=J,\quad n>0 \tag{8c}$$

In the fluid region:

$$\frac{\Theta^n_{i,j}-\Theta^{n-1}_{i,j}}{\Delta\tau}+\frac{1}{2R_{jw}L}\,\mathrm{Re}_\tau\,\mathrm{Pr}\,U_j\frac{\Theta^n_{i+1,j}-\Theta^n_{i-1,j}}{2\Delta X}-\left(1+\frac{\mathrm{Pe}_{tj}}{\mathrm{Pr}_{jt}}\right)\cdot\frac{1}{R_j}\left(\frac{\Theta^n_{i,j+1}-\Theta^n_{i,j-1}}{2\Delta R}+R_j\frac{\Theta^n_{i,j+1}-2\Theta^n_{i,j}+\Theta^n_{i,j-1}}{(\Delta R)^2}\right)=0 \tag{9a}$$

$$\Theta^n_{0,j}=F^n\quad\text{at } i=0,\quad 0\leqslant j\leqslant jw,\quad n>0 \tag{9b}$$

$$\frac{\Theta^n_{i,1}-\Theta^n_{i,0}}{\Delta R}=0\quad\text{at } i>0,\quad j=0,\quad n>0 \tag{9c}$$

The initial condition is taken as:

$$\Theta^0_{i,j}=0\quad\text{at } i>0,\quad 0<j<J,\quad n=0 \tag{10}$$

Substituting Eq. (4*b*) into the discretization equation obtained from the energy equation [Eq. (4*a*)] at the interface between the wall and the fluid inside the pipe gives the dimensionless inner-wall temperature as:

$$\Theta^n_{i,jw}=\frac{k_{\mathrm{sf}}}{k_{\mathrm{sf}}+1}\Theta^n_{i,jw+1}+\frac{1}{k_{\mathrm{sf}}+1}\Theta^n_{i,jw-1} \tag{11}$$

In Eqs. (8*a*)–(8*c*), (9*a*)–(9*c*), (10), and (11), ΔR and ΔX are the increments in the dimensionless spatial coordinates, $\Delta\tau$ is the increment of the temporal coordinate, i is the ith grid point along the x-coordinate direction, j is the jth grid point along the r-coordinate direction, n is the nth grid point along with temporal coordinate, and $\Theta^n_{i,j}$ is the dimensionless temperature at grid point (i,j). Meanwhile, Q^n and F^n are the uniform outer-wall heat flux and the inlet temperature, respectively, at the nth grid point along

the temporal coordinate. Finally, J represents the grid point at the boundary, i.e., $R=R_{ow}$, and jw represents the grid point at the inner wall, i.e., $R=R_{iw}$.

According to the inner-wall temperature expression given in Eq. (11), the dimensionless inner-wall temperature, $\Theta^n_{i,jw}$, which is expressed by $\Theta^n_{i,jw+1}$ at the first radial grid point in the pipe wall and by $\Theta^n_{i,jw-1}$ at the final radial grid point in the fluid, will be eliminated during algebraic vector manipulation. In other words, the boundary conditions existing at the solid-fluid interface are avoided. This simplifies the subsequent analysis task significantly.

As shown below, the heat conduction and convection equations can be combined into an equivalent matrix equation, which permits all of the unknowns to be derived within a single computational iteration.

Using the inner-wall temperature expression given in Eq. (11) and the boundary conditions and initial condition given in Eqs. (8*b*), (8*c*), (9*b*), (9*c*), and (10), the recursive forms of the governing equations given in Eqs. (8*a*) and (9*a*) can be rearranged in the form of the following linear model:

$$\mathbf{T}^n = \mathbf{A}^{-1}\mathbf{T}^{n-1} + \mathbf{A}^{-1}\mathbf{B}\mathbf{C}^n = \mathbf{D}\mathbf{T}^{n-1} + \mathbf{D}\mathbf{B}\mathbf{C}^n \tag{12}$$

where

$$\mathbf{D} = \mathbf{A}^{-1}$$

Matrix $\mathbf{A}$ is a constant matrix constructed from the thermal properties and spatial coordinates of the system. The components of vector $\mathbf{T}$ are the dimensionless temperatures at discrete points within the pipe wall and the fluid. Matrix $\mathbf{B}$ is the coefficient of vector $\mathbf{C}$, which is composed of the dimensionless boundary conditions, including the inlet temperature and the heat flux on the external surface of the pipe. The aim of the present direct analysis process is to determine the dimensionless temperature at each node when all the boundary conditions and thermal properties are known. This is accomplished by using the Gauss elimination method to solve the direct problem expressed in Eq. (12) above.

In the present study, the dimensionless temperature data obtained from the direct problem are subsequently employed in the inverse problem to represent the measured temperature values of the fluid.

3.2 Inverse Problem. The aim of the inverse problem is to determine the time-varying inlet temperature and the outer-wall heat flux simultaneously by using the temperature measurements taken from within the pipe flow. It is advantageous to perform algebraic manipulations utilizing a matrix form of the model. Equation (12) can be written in expanded matrix form as:

$$\begin{Bmatrix} \mathbf{T}^1 \\ \mathbf{T}^2 \\ \vdots \\ \mathbf{T}^{N-1} \\ \mathbf{T}^N \end{Bmatrix} = \begin{bmatrix} \mathbf{D} & 0 & \cdots & & 0 \\ \mathbf{D}^2 & \mathbf{D} & \ddots & & \\ \vdots & \ddots & \ddots & \ddots & \vdots \\ \mathbf{D}^{N-1} & \ddots & \ddots & \mathbf{D} & 0 \\ \mathbf{D}^N & \mathbf{D}^{N-1} & \cdots & \mathbf{D}^2 & \mathbf{D} \end{bmatrix} [\mathbf{B}] \times \begin{bmatrix} \mathbf{C}^1 \\ \mathbf{C}^2 \\ \vdots \\ \mathbf{C}^{N-1} \\ \mathbf{C}^N \end{bmatrix} + \begin{bmatrix} \mathbf{D} \\ \mathbf{D}^2 \\ \vdots \\ \mathbf{D}^{N-1} \\ \mathbf{D}^N \end{bmatrix} \{\mathbf{T}^0\} \tag{13}$$

where N is the number of time steps to be estimated. The unknown vector $\mathbf{C}$ of each time step has two components, i.e., the inlet temperature and the outer-wall heat flux.

To stabilize the computational results, the future-time and function specification concepts are applied. The future-time unknown components are temporarily estimated for the linear function form. Numerical experiments have determined that linear function form in unknown components is superior to the constant unknown components case. The single unknown is $\mathbf{C}^n$ since $\mathbf{C}^1,\ldots,\mathbf{C}^{n-1}$ have been calculated previously. $\mathbf{C}^{n+1},\ldots,\mathbf{C}^{n+r-1}$ can be written in terms of $\mathbf{C}^n$ and $\mathbf{C}^{n-1}$ [20]:

$$\mathbf{C}^{n+j-1} = j\mathbf{C}^n - (j-1)\mathbf{C}^{n-1} \tag{14}$$

Applying the assumption given in Eq. (14), the temperatures for times $t^n, t^{n+1}\ldots$ are given by Eq. (12) as:

$$\begin{Bmatrix} \mathbf{T}^n \\ \mathbf{T}^{n+1} \\ \vdots \\ \mathbf{T}^{n+r-2} \\ \mathbf{T}^{n+r-1} \end{Bmatrix} = \begin{bmatrix} \mathbf{D} & 0 & \cdots & & 0 \\ \mathbf{D}^2 & \mathbf{D} & \ddots & & \\ \vdots & \ddots & \ddots & \ddots & \vdots \\ \mathbf{D}^{r-1} & \ddots & \ddots & \mathbf{D} & 0 \\ \mathbf{D}^r & \mathbf{D}^{r-1} & \cdots & \mathbf{D}^2 & \mathbf{D} \end{bmatrix} [\mathbf{B}] \times \begin{bmatrix} \mathbf{C}^n \\ \mathbf{C}^{n+1} \\ \vdots \\ \mathbf{C}^{n+r-2} \\ \mathbf{C}^{n+r-1} \end{bmatrix} + \begin{bmatrix} \mathbf{D} \\ \mathbf{D}^2 \\ \vdots \\ \mathbf{D}^{r-1} \\ \mathbf{D}^r \end{bmatrix} \{\mathbf{T}^{n-1}\} \Rightarrow \begin{Bmatrix} \mathbf{T}^n - \mathbf{D}\mathbf{T}^{n-1} \\ \mathbf{T}^{n+1} - \mathbf{D}^2\mathbf{T}^{n-1} \\ \vdots \\ \mathbf{T}^{n+r-2} - \mathbf{D}^{r-1}\mathbf{T}^{n-1} \\ \mathbf{T}^{n+r-1} - \mathbf{D}^r\mathbf{T}^{n-1} \end{Bmatrix}$$

$$= \begin{bmatrix} 0 & \mathbf{D} \\ -\mathbf{D} & \mathbf{D}^2 + 2\mathbf{D} \\ \vdots & \vdots \\ -(\mathbf{D}^{r-2} + 2\mathbf{D}^{r-3} + \ldots + (r-2)\mathbf{D}) & \mathbf{D}^{r-1} + 2\mathbf{D}^{r-2} + \ldots + (r-1)\mathbf{D} \\ -(\mathbf{D}^{r-1} + 2\mathbf{D}^{r-2} + \ldots + (r-1)\mathbf{D}) & \mathbf{D}^r + 2\mathbf{D}^{r-1} + \ldots + r\mathbf{D} \end{bmatrix} [\mathbf{B}] \times \begin{bmatrix} \mathbf{C}^{n-1} \\ \mathbf{C}^n \end{bmatrix} \tag{15}$$

where r is a future-time parameter indicating the number of future-time measurements used as input data. Substituting Eq. (15) into Eq. (13), the whole domain equation can be rearranged into the following form:

$$\Theta = M\Psi \tag{16}$$

where

$$\Theta = \begin{Bmatrix} \mathbf{T}^1 - \mathbf{D}^1\mathbf{T}^0 \\ \mathbf{T}^2 - \mathbf{D}^2\mathbf{T}^0 \\ \vdots \\ \mathbf{T}^r - \mathbf{D}^r\mathbf{T}^0 \\ \mathbf{T}^2 - \mathbf{D}^2\mathbf{T}^0 \\ \mathbf{T}^3 - \mathbf{D}^3\mathbf{T}^0 \\ \vdots \\ \mathbf{T}^{r+1} - \mathbf{D}^{r+1}\mathbf{T}^0 \\ \vdots \\ \mathbf{T}^N - \mathbf{D}^N\mathbf{T}^0 \\ \vdots \\ \mathbf{T}^{N+r-1} - \mathbf{D}^{N+r-1}\mathbf{T}^0 \end{Bmatrix}, \quad \Psi = \begin{bmatrix} \mathbf{C}^1 \\ \mathbf{C}^2 \\ \vdots \\ \vdots \\ \mathbf{C}^{N-1} \\ \mathbf{C}^N \end{bmatrix}$$

$$M = \begin{bmatrix} \mathbf{D} & 0 & \cdots & & \\ \mathbf{D}^2 + 2\mathbf{D} & \vdots & & & \\ \vdots & \vdots & & & \\ \mathbf{D}^r + 2\mathbf{D}^{r-1} + \ \ldots\ + r\mathbf{D} & 0 & \cdots & & \\ \mathbf{D}^2 & \mathbf{D} & 0 & \cdots & \\ \mathbf{D}^3 - \mathbf{D} & \mathbf{D}^2 + 2\mathbf{D} & \vdots & & \\ \vdots & \vdots & \vdots & & \\ \mathbf{D}^{r+1} - (\mathbf{D}^{r-1} + 2\mathbf{D}^{r-2} + \ \ldots\ + (r-1)\mathbf{D}) & \mathbf{D}^r + 2\mathbf{D}^{r-1} + \ \ldots\ + r\mathbf{D} & 0 & \cdots & \\ \vdots & \vdots & & & \\ \mathbf{D}^N & \mathbf{D}^{N-1} & \cdots & \mathbf{D}^2 & \mathbf{D} \\ \vdots & \vdots & & & \vdots \\ \mathbf{D}^{N+r-1} & \mathbf{D}^{N+r-2} & \cdots & & \mathbf{D}^r + 2\mathbf{D}^{r-1} + \ \ldots\ + r\mathbf{D} \end{bmatrix} [\mathbf{B}]$$

The unknown parameters at any time instant can be estimated simultaneously by applying the linear least-squares-error method, i.e.

$$\Psi = (M^T M)^{-1} M^T \Theta \tag{17}$$

where $(M^T M)^{-1} M^T$ is defined as a reverse matrix.

This algorithm, which combines the function specification method and the whole domain estimation technique, can estimate simultaneously all of the unknown boundary conditions over the total time interval. A major advantage of the proposed inverse approach is that the construction of the linear inverse model given in Eq. (17) requires no explicit assumptions regarding the functional forms of the unknown thermal quantities. In other words, a

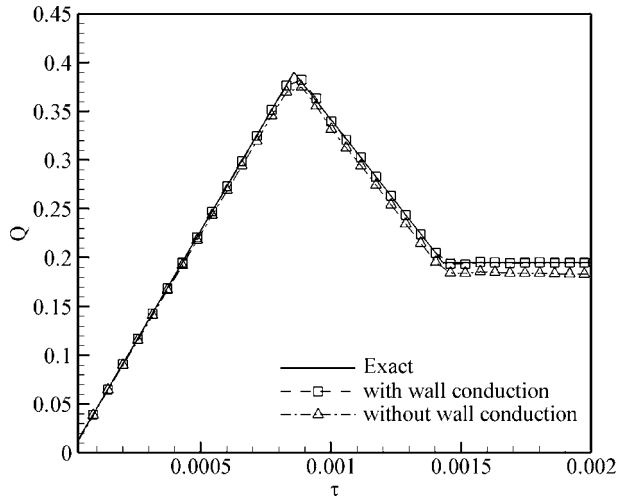

Fig. 2 Estimated dimensionless outer-wall heat flux distributions with and without wall conduction for measurement error of σ=0% and r=3

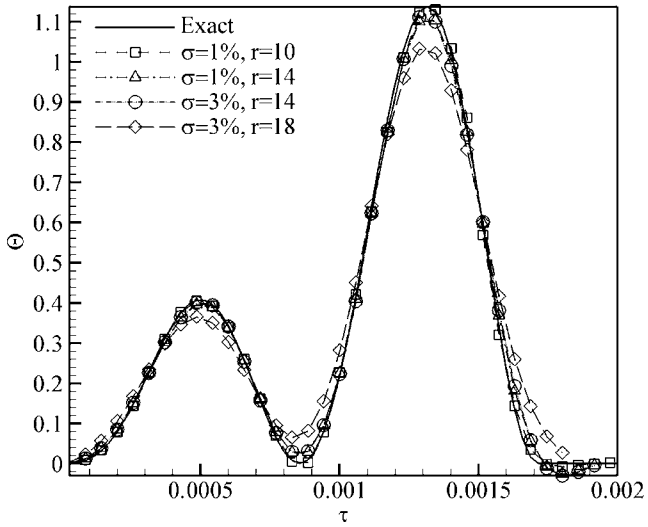

Fig. 3 Estimated dimensionless inlet temperature distributions for different values of future-time parameter with measurement errors of σ=1% and 3%

prior knowledge of these functional forms is unnecessary when utilizing the proposed inverse analysis method to determine the unknown thermal boundary conditions at discrete grid points.

In practice, the temperature measurements always contain some degree of error. The magnitude of this error depends upon the particular measuring method employed. Therefore, the simulated temperature measurements adopted in the current inverse problem are also considered to include a measurement error component. For reasons of practicality, the present study adds a random error noise to the exact temperature values computed from the direct problem. Hence, the measured dimensionless temperature, $\Theta_{measured}$, is expressed as:

$$\Theta_{measured} = \Theta_{exact}(1 + \omega\sigma) \tag{18}$$

where Θ_{exact} is the exact dimensionless temperature, σ is the amplitude of the measurement error, and ω is a random value specified between −1 and 1.

4 Results and Discussion

This paper considers the conjugate heat transfer case of fluid flowing through a pipe. Hence, the analyzed IHCP investigates the influence of heat conduction in the pipe wall in developing turbulent forced convection flow and generating heat transfer inside the pipe. Let the inlet temperature and the outer-wall heat flux distribution be described, respectively, by the following functions:

$$F(\tau) = \begin{cases} \dfrac{\tau}{1.144\times10^{-3}}\sin^2\left(\dfrac{\pi\tau}{8.58\times10^{-4}}\right) & \text{for } 0 < \tau \leqslant 1.716\times10^{-3} \\ 0 & \text{for } 1.716\times10^{-3} < \tau \end{cases}$$

$$Q(\tau) = \begin{cases} \dfrac{0.39\tau}{8.58\times10^{-4}}\square\square\square\square\square\square & \text{for } 0 < \tau \leqslant 8.58\times10^{-4} \\ 0.39\left(1 - \dfrac{\tau - 8.58\times10^{-4}}{2\times5.72\times10^{-4}}\right) & \text{for } 8.58\times10^{-4} < \tau \leqslant 1.43\times10^{-3} \\ \dfrac{0.39}{2} & \text{for } 1.43\times10^{-3} < \tau \end{cases}$$

The direct problem described above can be solved by the finite-difference method. The total simulation time of 2.288×10^{-3} (in dimensionless terms) is divided into 80 equal time steps, corresponding to a sampling frequency of 2.86×10^{-5}. The dimensionless length and radius of the pipe are both assumed to be equal to 1 and are divided into 50 and 40 equal divisions, respectively, corresponding to $\Delta X = 0.02$ and $\Delta R = 0.025$. Temperature measurement sensors are placed on the centerline of the pipe ($R = 0$) and at the inner-wall ($R = R_{iw}$) at a downstream location of $X_{mea} = 10\Delta X$. The inverse problem is then solved for the inlet temperature and the outer-wall heat flux components using the algorithm described above. Clearly, the quality of the estimated results can be readily determined since the exact solution is known.

Figure 2 shows a comparison between the predicted results and the exact solutions of the outer-wall heat flux with and without consideration of the wall conduction, respectively, for a measurement error of $\sigma = 0\%$ and $r = 3$. It can be seen that the estimated results which neglect the effect of wall heat conduction have significant divergence from the exact outer-wall heat flux solutions. And the estimations without consideration of wall conduction are always lower than the exact solutions. This result is to be expected because the heat transfer can occur in the unheated section. The magnitude and extent of upstream and downstream heating increase monotonically with an increase of k_{sf} or a decrease of R_{iw} [1–3]. In other words, increase in k_{sf} and decrease in R_{iw} contribute to provide a less accurate estimate without consideration of wall conduction.

Figure 3 presents the estimated results of the dimensionless inlet temperature, $\Theta(\tau)$, of the pipe flow for various amplitudes of measurement error. It can be seen that the estimated results are in very good agreement with the exact inlet temperature solutions when the measurement error is taken to be $\sigma = 1\%$. However, the results obtained with $r = 14$ are less accurate than those obtained with $r = 10$. In IHCP problems, it is known that the precision of the estimated results is significantly influenced by the magnitude of the measurement errors. When a value of $r = 14$ is selected, the estimated results deviate slightly from the exact solutions for measurement errors of $\sigma = 1\%$ and 3%. Figure 3 also shows that the estimated results deviate more widely for $r = 18$ than for $r = 14$ for a constant measurement error of $\sigma = 3\%$.

Figure 4 presents a comparison between the predicted results and the exact solutions of the outer-wall heat flux for measurement errors of $\sigma = 1\%$ and 3%. In general, the results reveal that for a measurement error of $\sigma = 1\%$, good agreement exists between the two sets of data for both $r = 10$ and $r = 14$. Comparing the results obtained for measurement errors of $\sigma = 1\%$ and $\sigma = 3\%$, it can be seen that, although both sets of estimated results

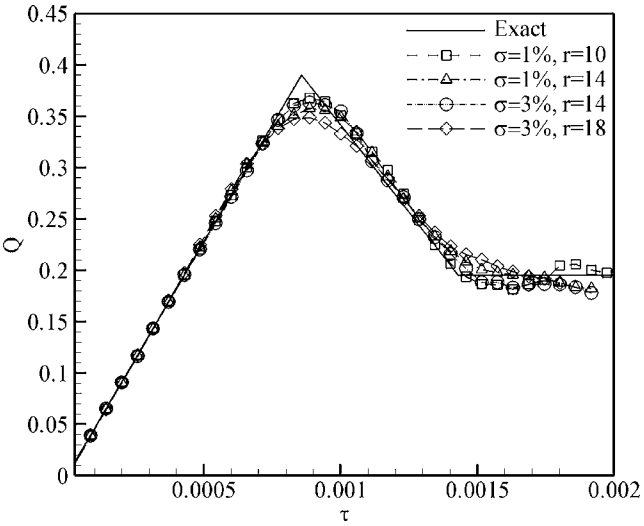

Fig. 4 Estimated dimensionless outer-wall heat flux distributions for different values of future-time parameter with measurement errors of $\sigma = 1\%$ and 3%

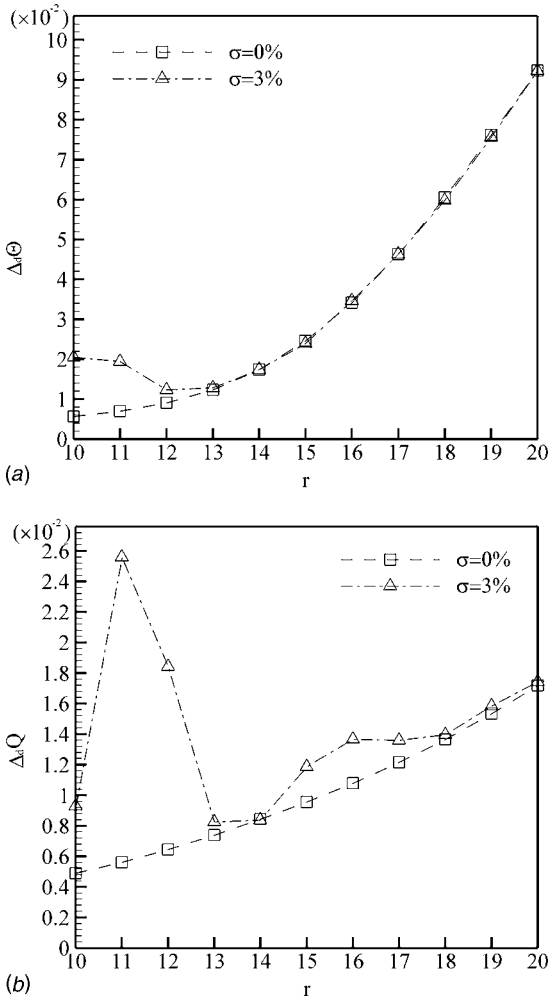

Fig. 5 Comparison between variation of deterministic bias with future-time parameter of: (a) inlet temperature, $\Delta_d\Theta$, and (b) outer-wall heat flux, $\Delta_d Q$, for measurement errors of σ =0% and 3%

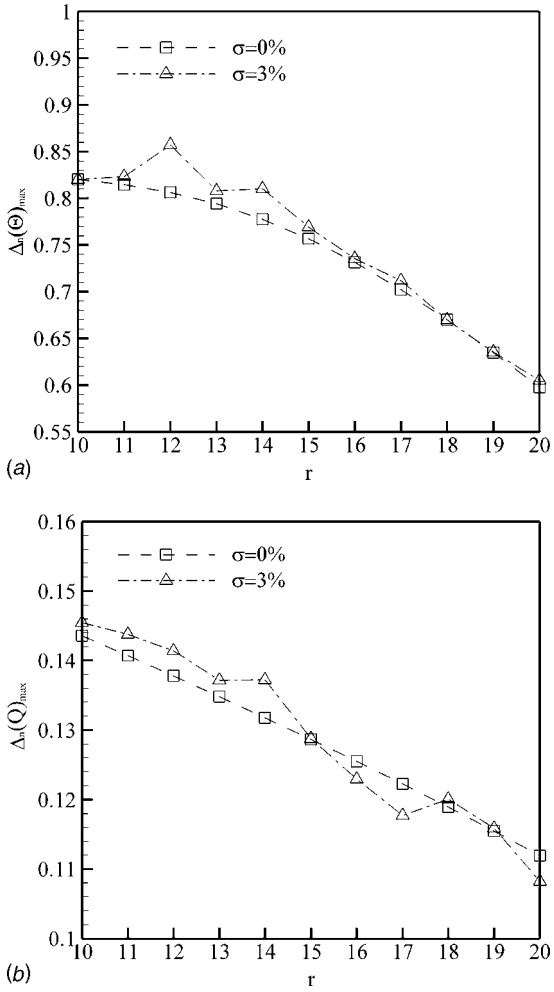

Fig. 6 Comparison between variation of maximum nonlinear bias with future-time parameter of: (a) inlet temperature, $[\Delta_n\Theta]_{max}$, and (b) outer-wall heat flux, $[\Delta_n Q]_{max}$, for measurement errors of σ=0% and 3%

provide reasonable approximations to the exact solutions when r =14, the results obtained for a measurement error of σ=1% are more accurate. Consequently, when measurement errors are taken into consideration, it is noted that there exists a slight deviation between the estimated and the exact solutions. The extent of this deviation is found to be dependent upon the magnitude of the measurement errors. It can be concluded that the presence of large measurement errors degrades the performance of the proposed inverse method.

As stated previously, the quality of the estimated results can be assessed quite simply since the exact solution is known. The quality depends on $\Delta_n\mathbf{C}^i$ (i.e., the nonlinear bias) and $\Delta_d\mathbf{C}$ (i.e., the deterministic bias) [21]. The variable $\Delta_n\mathbf{C}^i$ is given by the difference between the estimated value and the exact average value, i.e.

$$\Delta_n\mathbf{C}^i = \mathbf{C}^i_{\text{estimated}} - \overline{\mathbf{C}}_{\text{exact}} \tag{19}$$

The deterministic bias is defined as:

$$\Delta_d\mathbf{C} = \sqrt{\frac{1}{N}\sum_{i=1}^{N}(\mathbf{C}^i_{\text{estimated}} - \mathbf{C}^i_{\text{exact}})^2} \tag{20}$$

From Eqs. (19) and (20), it can be seen that a lower maximum nonlinear bias yields a more stable solution, while a higher deterministic bias generates a less accurate solution.

This study could divide the deterministic bias $\Delta_d\mathbf{C}$ into two groups, i.e., $\Delta_d\Theta$ (the deterministic bias of inlet temperature) and $\Delta_d Q$ (the deterministic bias of outer-wall heat flux). Figure 5 plots the variations of $\Delta_d\Theta$ and $\Delta_d Q$ with the future-time parameter, r, for measurement error magnitudes of σ=0% and σ=3%. The results reveal that the variations of the deterministic bias are greatly influenced by the value of the future-time parameter. The deterministic bias grows increasingly with the future-time parameter when a measurement error of σ=0% is applied. In other words, the accuracy of the estimated results decreases as the value of the future-time parameter is increased, i.e., as more future-time measurements are used as input data. However, using a lesser number of future-time measurements in an attempt to preserve the accuracy of the results may lead to fluctuations in the estimated results when measurement errors are taken into account. Figure 5 also shows that increasing the value of the future-time parameter reduces the sensitivity of the estimated results to measurement errors. It is observed that increasing the value of r yields a clear improvement in the results for σ=3% when $r \leqslant 13$, whereas its effect is not as apparent when $r > 13$.

As mentioned previously, a more stable solution is obtained from a lower maximum nonlinear bias. The future-time parameter, r, which is derived from the function specification method, acts as a stabilizing parameter. Figure 6 shows that as r increases, the maximum nonlinear bias decreases continuously when measurement errors are neglected (i.e., σ=0%). Hence, specifying a larger value of r can lead to a more stable solution. However, when an

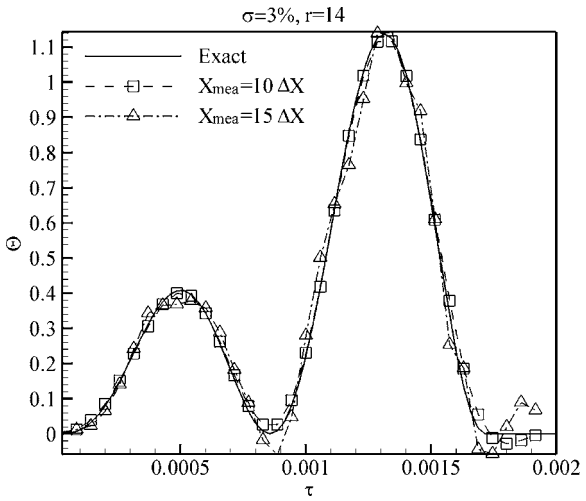

Fig. 7 Effects of sensor locations $10\Delta X$ and $15\Delta X$ on accuracy of estimated inlet temperature for measurement error of $\sigma=3\%$ and $r=14$

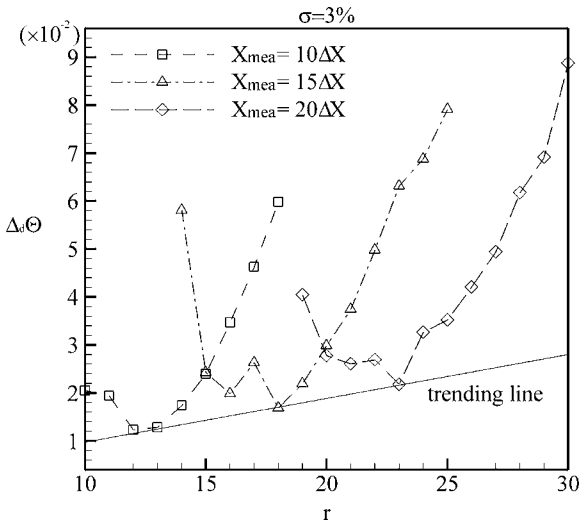

Fig. 8 Effects of measuring point location on variation of $\Delta_d\Theta$ with future-time parameter for measurement error of $\sigma=3\%$

insufficient number of future-time measurements are used, i.e., $r<14$, and a measurement error of $\sigma=3\%$ is assumed, the maximum nonlinear bias fluctuates rather than decreasing smoothly. When the future-time parameter is specified with a greater value (i.e., $r\geqslant 14$), it can be seen that there is a greater agreement between the results obtained with a measurement error of $\sigma=3\%$ and those obtained with no measurement error. This again confirms that increasing the value of the future-time parameter can reduce the sensitivity of the estimated results to measurement errors. In Figs. 5(*b*) and 6(*b*), the effects of the future data which reduces the sensitivity of estimation to measurement errors are not excellent. This may impute to the relatively weak influence of the estimated outer-wall heat flux upon the temperature field.

In order to investigate the relationship between the location of the measuring points and the accuracy of the estimated results, the sensors are placed at three different downstream locations, i.e., $X_{\text{mea}}=10\Delta X$, $15\Delta X$ and $20\Delta X$, and the results calculated for each case. Figure 7 shows the effects of the measurement location on the accuracy of the estimated inlet temperature for a measurement error of $\sigma=3\%$ and a future-time parameter of $r=14$. As expected, the results obtained when the sensors are placed at $10\Delta X$, i.e., in the vicinity of the pipe entrance, approximate the exact solutions more closely. Conversely, with the sensors located at $15\Delta X$, the estimated results are considerably less accurate.

Figure 8 shows the effect of the measuring point location on the variation of $\Delta_d\Theta$ with the future-time parameter for a measurement error of $\sigma=3\%$. It is clear that the sensitivity of the estimated results to measurement errors increases notably when the sensors are located at a greater distance from the entrance. It can be seen that the optimum value of r depends not only on the amplitude of the measurement error, but also upon the measuring point location. As shown by the trending line in Fig. 8, the deterministic bias obtained from the optimum value of r increases when the sensors are located further from the position of the unknown quantities of interest. Accordingly, the accuracy of the optimum estimated results increases as the distance between the entrance and the sensors decreases.

On the basis of the current results, it can be concluded that the optimum value of the future-time parameter, r, depends on the amplitude of the measurement errors and the distance between the unknowns and the sensors. For higher measurement errors and more distant measuring point locations, a greater volume of future data is required to damp oscillation and to obtain a stable solution.

5 Conclusion

This paper has successfully applied an inverse method to the estimation of the unknown boundary conditions associated with turbulent pipe flow. The influences of conduction effects within the pipe wall on the thermal development of the turbulent flow in a pipe with a finite heated length have been considered. The proposed inverse model is constructed using the available temperature measurements and a finite difference model of the corresponding differential heat transfer equations. This model is capable of representing the unknown boundary conditions of the pipe flow explicitly. The proposed method can be applied to a wide range of heat transfer problems on account of the nonuniform solution used in the model. The results of the inverse method can be derived within a single iteration, and demonstrate that the uniqueness of the solution can be easily identified. The proposed method has the further advantages that the unknown quantities of the thermal boundary conditions can be estimated directly and the inverse problem can be solved in a linear domain. For the above reasons, the method can provide solutions of the inverse problem very fast. It takes about 5 s of CPU time to complete the computation. The CPU times correspond to an Intel Pentium 1 GHz processor, with 512MB RAM, running under the Microsoft Fortran PowerStation 4.0 platform.

The results have indicated that increasing the value of the future-time parameter has a positive effect on the estimation stability, but a negative effect on the estimation accuracy. In other words, an increase in this parameter decreases the nonlinear bias, but increases the deterministic bias. The results have also shown that the estimated results are more accurate and robust when the temperature measurement points are located closer to the boundary of interest, i.e., the entrance of the pipe flow in the present case. The current results have revealed that the estimated results are accurate even when a measurement error of 3% is introduced. In conclusion, the proposed inverse method is an accurate, robust, and efficient technique for solving the conjugate heat transfer problem associated with turbulent pipe flow.

Nomenclature

- $\mathbf{A}$ = constant matrix constructed from thermal properties and spatial coordinates
- $\mathbf{B}$ = coefficient matrix of $\mathbf{C}$
- $\mathbf{C}$ = vector constructed from the unknown boundary conditions
- c_f = local friction coefficient

$\mathbf{F}$ = error function
F = dimensionless inlet temperature
$f(t)$ = function form of inlet temperature variation
k = thermal conductivity
ℓ = length of the pipe
Pe = Peclet number
Pr = Prandtl number
Q = dimensionless outer-wall heat flux
$q(t)$ = function form of the outer-wall heat flux
$\mathbf{R}$ = reverse matrix
R = dimensionless radial coordinate
Re = Reynolds number
r = radial coordinate
$\mathbf{T}$ = temperature vector
T = temperature
u = fluid axial velocity
u_τ = friction velocity
X = dimensionless axial coordinate
x = axial coordinate
y = distance from the wall

Greek symbols

α = thermal diffusivity
ΔX = axial step size
ΔR = radial step size
$\Delta\tau$ = time step size
ν = kinematic viscosity
ω = random variable
Θ = dimensionless temperature
σ = standard deviation of the measurement error
τ = dimensionless time

Subscripts

exact = exact temperature
f = fluid
i,j,n,J = indices
initial = initial value
iw = inner wall
jw = index of radial coordinate at inner wall
m = mean value
measured = measured temperature
ow = outer wall
s = solid
t = turbulent

References

[1] Zariffeh, E. K., Soliman, H. M., and Trupp, A. C., 1982, "The Combined Effects of Wall and Fluid Axial Conduction on Laminar Heat Transfer in Circular Tubes," *Proc. 7th Int. Heat Transfer Conf.*, Munich, Germany **4**, pp. 131–136.

[2] Bernier, M. A., and Baliga, B. R., 1992, "Conjugate Conduction and Laminar Mixed Convection in Vertical Pipes for Upward Flow and Uniform Wall Heat Flux," Numer. Heat Transfer, Part A, **21**, pp. 313–332.

[3] Faghri, M., and Sparrow, E. M., 1980, "Simultaneous Wall and Fluid Axial Conduction in Laminar Pipe-Flow Heat Transfer," ASME J. Heat Transfer, **102**, pp. 58–63.

[4] Campo, A., and Schuler, C., 1988, "Heat Transfer in Laminar Flow Through Circular Tubes Accounting for Two-Dimensional Wall Conduction," Int. J. Heat Mass Transfer, **31**, pp. 2251–2259.

[5] Chen, H. T., Lin, S. Y., and Fang, L. C., 2001, "Estimation of Surface Temperature in Two-Dimensional Inverse Heat Conduction Problems," Int. J. Heat Mass Transfer, **44**, pp. 1455–1463.

[6] Maillet, D., Degiovanni, A., and Pasquetti, R., 1991, "Inverse Heat Conduction Applied to the Measurement of Heat Transfer Coefficient on a Cylinder: Comparison Between an Analytical and a Boundary Element Technique," ASME J. Heat Transfer, **113**, pp. 549–557.

[7] Martin, T. J., and Dulikavich, G. S., 1998, "Inverse Determination of Steady Heat Convection Coefficient Distributions," ASME J. Heat Transfer, **120**, pp. 328–334.

[8] Lin, J. H., Chen, C. K., and Yang, Y. T., 2002, "An Inverse Method for Simultaneous Estimation of the Center and Surface Thermal Behavior of a Heated Cylinder Normal to a Turbulent Air Stream," ASME J. Heat Transfer, **124**, pp. 601–608.

[9] Kim, S. K., and Lee, W. I., 2002, "An Inverse Method for Estimating Thermophysical Properties of Fluid Flowing in a Circular Duct," Int. Commun. Heat Mass Transfer, **29**(8), pp. 1029–1036.

[10] Sawaf, B., Özisik, M. N., and Jarny, Y., 1995, "An Inverse Analysis to Estimate Linearly Temperature Dependent Thermal Conductivity Components and Heat Capacity of an Orthotropic," Int. J. Heat Mass Transfer, **38**(16), pp. 3005–3010.

[11] Su, Jian, Lopes, Adriane B., and Silva Neto, A. J., 2000, "Estimation of Unknown Wall Heat Flux in Turbulent Circular Pipe Flow," Int. Commun. Heat Mass Transfer, **27**, pp. 945–954.

[12] Su, Jian, and Silva Neto, A. J., 2001, "Simultaneous Estimation of Inlet Temperature and Wall Heat Flux in Turbulent Circular Pipe Flow," Numer. Heat Transfer, Part A, **40**, pp. 751–766.

[13] Park, H. M., and Lee, J. H., 1998, "A Method of Solving Inverse Convection Problem by Means of Mode Reduction," Chem. Eng. Sci., **53**(9), pp. 1731–1744.

[14] Bokar, J. C., and Özisik, M. N., 1995, "An Inverse Analysis for Estimating the Time-Varying Inlet Temperature in Laminar Flow Inside a Parallel Plate Duct," Int. J. Heat Mass Transfer, **38**(1), pp. 39–45.

[15] Li, H. Y., and Yan, W. M., 2000, "Inverse Convection Problem for Determining Wall Heat Flux in Annular Duct Flow," ASME J. Heat Transfer, **122**, pp. 460–464.

[16] Li, H. Y., and Yan, W. M., 2003, "Identification of Wall Heat Flux for Turbulent Forced Convection by Inverse Analysis," Int. J. Heat Mass Transfer, **46**, pp. 1041–1048.

[17] Yang, C. Y., and Chen, C. K., 1996, "The Boundary Estimation in Two-Dimensional Inverse Heat Conduction Problems," J. Phys. D, **29**, pp. 333–339.

[18] Kays, W. M., and Crawford, M. E., 1993, *Convective Heat and Mass Transfer*, 3rd ed., McGraw–Hill, New York, pp. 246–249.

[19] Reichardt, H., 1951, "Vollstndige Darstellung der Turbulenten Geschwindigkeitsverteilung in Glatten Leitungen," Z. Angew. Math. Mech., **31**, pp. 208–219.

[20] Beck, J. V., Blackwell, B., and Clair, C. R., 1985, *Inverse Heat Conduction-Ill-Posed Problem*, Wiley, New York.

[21] Chantasiriwan, S., 2000, "Inverse Heat Conduction Problem of Determining Time-Dependent Heat Transfer Coefficient," Int. J. Heat Mass Transfer, **42**, pp. 4275–4285.

Phuong M. Le
School of Chemical, Biological and Materials Engineering,
The University of Oklahoma,
100 East Boyd,
Norman, OK 73019

Dimitrios V. Papavassiliou
School of Chemical, Biological and Materials Engineering,
Sarkeys Energy Center,
The University of Oklahoma,
100 East Boyd,
Norman, OK 73019

Turbulent Heat Transfer in Plane Couette Flow

Heat transfer in a fully developed plane Couette flow for different Prandtl number fluids was studied using numerical simulations. The flow field was created by two infinite planes moving at the same velocity, but in opposite directions, forming a region of constant total shear stress. Heat markers were released into the flow from the channel wall, and the ground level temperature was calculated for dispersion from continuous line sources of heat. In addition, the temperature profile across the channel was synthesized from the behavior of these continuous line sources. It was found that the heat transfer coefficient for Couette flow is higher than that in channel flow for the same Prandtl numbers. Correlations were also obtained for the heat transfer coefficient for any Prandtl number ranging from 0.1 to 15,000 in fully developed turbulence. [DOI: 10.1115/1.2130404]

1 Introduction

Turbulent heat or mass transport is important for applications in several processes, such as mixing, pollutant dispersion, heat exchange, etc. The transport of heat in turbulent channel flow has been studied with both experimental [1–8] and direct numerical simulation (DNS) approaches [9–14]. However, plane Couette flow has not been investigated as fully and as deeply as plane channel flow. The main reason is its special configuration, in which one channel wall moves, or two walls travel in opposite directions, forming a constant total shear stress region across the flow field.

Even though plane Couette flow is a simple flow conceptually, it is difficult to construct an experimental procedure to accomplish it. Previous investigators have set up experiments using a running belt, a second fluid, or a moving plane to explore the characteristics of plane Couette flow. In 1956, Reichardt [15] used a running belt to study Couette flow with two moving walls. Oil and water were employed as the fluids. Reichardt was able to measure the mean velocity profile, and to determine the critical Reynolds number for transition to turbulent Couette flow. Later on, Robertson and Johnson [16] set up an apparatus with one stationary wall and one moving wall, and reported streamwise turbulence intensity and streamwise energy spectra for Couette flow. Aydin and Leutheusser [17–19] used a plane suspended above a straight stationary bench that was moving with the help of a towing carriage, and measured the mean and the fluctuating streamwise velocity. Other experiments used a moving belt and a rigid wall [20] or used a plastic band moving between vertical glass surfaces in water [21,22]. These experiments obtained measurements of the mean velocity, and most of them were limited to measurements of the root mean square of the velocity fluctuations in the streamwise direction.

Developments in computer simulation have provided the opportunity to study the flow structure in plane Couette flow using direct numerical simulations (DNS). Several papers have reported on the velocity structure of plane Couette flow [23–25]. Recently, Liu [26] and Debusschere and Rutland [27] reported results for heat transfer in plane Couette flow using DNS for fluids with Prandtl number Pr equal to 0.7. In these recent publications, several scalar quantities were reported, in addition to velocity field data, for heat transport in plane Couette flow.

Le and Papavassiliou [28] have used a Couette flow DNS and a Poiseuille flow DNS in conjunction with a Lagrangian method for tracking the trajectories of heat markers in the flow to investigate the mechanism of heat transfer in the outer region of the flow. In the present work, dispersion and heat transport from the wall in plane Couette flow are investigated using the same technique (DNS in conjunction with the Lagrangian scalar tracking method, LST). A range of fluids with different Pr (Pr=0.1, 0.7, 6, 10, 100, 200, 500, 2400, 7500, and 15,000) was studied. The main contributions of this work are (a) the investigation of the effects of the velocity boundary conditions on the mechanism of heat transfer by comparing the Couette flow results to those for plane channel flow, and (b) the development of predictive correlations for the heat transfer coefficient K^+ as a function of Pr based on results from a consistent methodology for a wide range of Pr. It is found that K^+ is higher in plane Couette flow compared to plane channel flow, a result that may have important applications in mixing processes.

2 Background

Mitrovic and Papavassiliou [29] and Mitrovic et al. [30] have described the turbulent transport of heat and mass transfer in a Poiseuille flow channel using a Lagrangian method in conjunction with DNS of the fluid flow. For the simulation of plane Couette flow, and for the calculation of temperature profiles and heat transfer coefficients, the same methodology is employed here.

2.1 Eulerian Heat Transfer. The temperature T can be decomposed into the mean temperature $\overline{T}$ and the fluctuation θ. It can be made dimensionless by normalizing with the friction temperature T^*, $T^*=q_w/(\rho C_p u^*)$, where q_w is the heat flux at the wall defined in terms of the thermal conductivity of the fluid k as

$$q_w = -k\left(\frac{d\overline{T}}{dy}\right)_w \tag{1}$$

Therefore, the dimensionless temperature T^+ can be calculated by

$$T^+ = \frac{T}{T^*} = -\frac{T\rho C_p u^*}{k\left(\frac{d\overline{T}}{dy}\right)_w} = -\Pr\frac{T}{\left(\frac{d\overline{T}}{dy^+}\right)_w} \tag{2}$$

where y^+ is the distance from the wall in viscous wall units ($y^+=yu^*/\nu$).

The heat transfer coefficient is defined as

Contributed by the Heat Transfer Division of ASME for publication in the JOURNAL OF HEAT TRANSFER. Manuscript received January 19, 2005; final manuscript received July 1, 2005. Review conducted by Louis C. Burmeister.

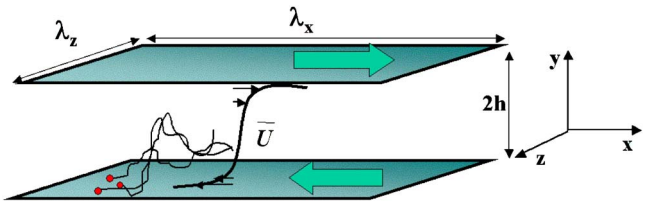

Fig. 1 Problem configuration for heat transfer in plane Couette flow

$$K = \frac{q_w}{\overline{\overline{T_b}} - \overline{\overline{T_w}}} \tag{3}$$

where the bulk temperature T_b is the average temperature across the y direction of the channel.

It can also be made dimensionless by scaling with wall parameters ($\rho C_p u^*$) and using Eq. (1)

$$K^+ = \frac{K}{\rho C_p u^*} = \frac{1}{\mathrm{Pr}}\left[\frac{d\left(\dfrac{\overline{T}}{\overline{\overline{T_b}} - \overline{\overline{T_w}}}\right)}{dy^+}\right]_w \tag{4}$$

Based on dimensional analysis, the heat transfer coefficient is often given in the form of a correlation for the Nusselt number

$$\mathrm{Nu} = C_1\,\mathrm{Re}^p\,\mathrm{Pr}^q \tag{5}$$

where C_1, p, q are constants that depend on the type of flow (e.g., flow in a pipe or a channel, flow around an immersed object, etc.).

2.2 Direct Numerical Simulation. The configuration of the problem is visualized in Fig. 1. The top wall of the channel is moving in the positive x direction with velocity $U^+=17.7386$ in wall units, and the bottom wall is moving to the negative x direction with velocity $U^+=-17.7386$ in wall units. The Reynolds number Re defined with the velocity of one of the moving walls and the half channel height h is 2660. Previous simulations have been done on plane Couette flow using different choices of computational domain size and number of grid points. Lee and Kim [23] used a computational box with $192\times129\times288$ grid points and dimensions ($4\pi h$, $2h$, $8/3\ \pi h$) in the x, y, and z directions. They observed large scale structures of the velocity that were persistent in space and time. These structures were also observed in simulations done by Papavassiliou and Hanratty [25] using a computational box with $128\times65\times128$ grid points and dimensions ($4\pi h$, $2h$, $2\pi h$), and in simulations by Komminaho et al. [24] and by Bech et al. [31].

In this current work, the DNS methodology for the initiation and the development of the Couette flow simulation was similar to that in [25]. The moving walls were taken into account by changing the Dirichlet boundary conditions. The simulation was conducted on a $256\times65\times128$ grid in the x, y, z directions, respectively. The length of the streamwise direction was double that used in [25] in order to capture the large turbulent structures in plane Couette flow. The dimensions of the computational box were ($8\pi h$, $2h$, $2\pi h$), with $h=150$ in viscous wall units (the wall units are used to create dimensionless parameters by normalizing with the friction velocity u^*, friction length $l^*=\nu/u^*$ and friction time $t^*=l^*/u^*$). The flow was periodic in the streamwise and spanwise directions, with periodicity lengths equal to the dimensions of the box in the respective directions. Statistics of the Couette flow velocity field have been reported elsewhere [28,32].

2.3 Lagrangian Scalar Tracking. The Lagrangian scalar tracking (LST) method was used to track the heat markers in conjunction with direct numerical simulation. Its basic concept is that a heated/cooled surface is formed by continuous sources/sinks of heat markers. A total of 145,161 markers were released uniformly into the flow field from a rectangular grid covering the xz plane at the bottom wall of the channel. The algorithm used for the tracking of these heat markers is based on the algorithm developed by Kontomaris et al. [33]. More about the implementation and validation of the LST methodology for channel flow can be found elsewhere [34–37]. Heat transfer across the interface between a turbulent gas and a turbulent liquid has also been simulated using LST [38,39]. The tracking of the trajectories of the heat markers was initiated after the velocity field of the DNS reached fully developed and stationary state.

Data from two runs are used in the present work: Run A tracked particles with Pr=0.1, 0.7, 6, 10, and 100 until $t^+=3000$, and Run B tracked particles with Pr=200, 500, 2400, 7500, and 15,000 until $t^+=13{,}000$. The trajectories and velocities of the particles were stored at every time unit, and the time step was $\Delta t^+=0.2$ (equal to the time step for the advancement of the velocity field).

The behavior of a marker source was determined by following the paths of a large number of scalar markers in the flow field generated with the DNS. Each marker moved due to convection and diffusion effects. It was assumed that the particle had the same velocity as the fluid on which it rode, $\vec{V}(\vec{x_o},t) = \vec{U}[\vec{X}(\vec{x_o},t),t]$, where $\vec{V}(\vec{x}_o,t)$ is the Lagrangian velocity of a marker that was released at location, $\vec{x}_o$ and $\vec{U}$ is the Eulerian velocity of the fluid at the location of the marker at time t. The marker's motion due to the convective effect was then calculated using the following equation:

$$\vec{V}(\vec{x_o},t) = \frac{\partial \vec{X}(\vec{x_o},t)}{\partial t} \tag{6}$$

The molecular diffusion effect was described by the Brownian motion theory of the marker [40], in which the rate of molecular dispersion in a laminar field is related to the molecular diffusivity D by $d\overline{X^2}/dt=2D$ for the case of dispersion in the dimension x. The diffusion effect was represented by a random walk added on the marker motion after each time step, which was estimated by a Gaussian distribution with zero mean and a standard deviation σ that depended on the Prandtl number of the fluid ($\sigma=\sqrt{2\Delta t^+/\mathrm{Pr}}$ in wall units). The effects of Pr could, thus, be simulated by modifying σ.

The building block for the implementation of LST is the probability function $P_1(x-x_o,y,t-t_o|\vec{x}_o,t_o)$. This function represents the joint and conditional probability density function for a marker to be at location (x,y) at time t, given that the marker was released at $\vec{x}_o$ and at time t_o. This probability can be interpreted physically as concentration [41]. Snapshots of the cloud resulting from an instantaneous source, which is usually called a *puff*, are captured over time. By integrating (or, in the discrete case, summing up) P_1 from time t_o to a final time t_f, the behavior of a continuous line source, represented by the probability function P_2, can be obtained, where

$$P_2(X-x_o,Y) = \sum_{t=t_o}^{t_f} P_1(X-x_o,Y,t|\vec{x_o},t_o) \tag{7}$$

The cloud from this continuous source, called a *plume*, is a series of instantaneous clouds, each of which is released at every time unit. The calculation of this function P_2 involves calculations of $145{,}161\times3000=4.35483\times10^8$ particles for run A and of $145{,}161\times13{,}000=1.88709\times10^9$ particles for run B. Earlier simulations done on channel flow [28,30,36,42] have shown a very good agreement between results obtained with LST and both experiments and simulations. The probability P_2 was calculated for each Pr using a grid that covered the flow domain and counting the number of markers that were present in each one grid cell. The grid in the normal direction was constructed either by dividing the width of the channel uniformly into 300 bins (when $\mathrm{Pr}\leqslant100$), or by using Chebyshev collocation points to generate 400 bins (when $200\leqslant\mathrm{Pr}$) in order to increase the resolution closer to

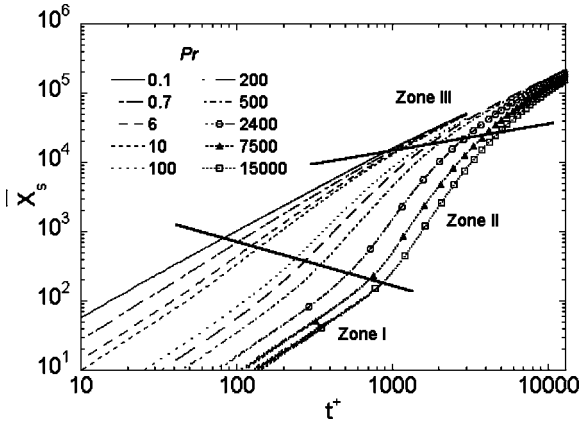

Fig. 2 Mean streamwise cloud position as function of Pr (from [32])

the wall. In the streamwise direction, the grid was stretched around the point of origin of the plume, in order to take measurements at long distances from the source. The stretching in both the positive and negative streamwise directions followed the relation $\Delta x_n = 1.06^n \Delta x_o$ with $\Delta x_o = 5$ in viscous wall units.

3 Results and Discussion

3.1 Development of a Puff. The characteristics of the behavior of a puff in plane Couette flow have been reported in Le and Papavassiliou [32], including the first and second order statistics of the marker displacement in the streamwise and normal directions. The main conclusion from those results is that a higher dispersion rate is found for Couette flow when compared to marker dispersion in Poiseuille channel flow. It was also found that the dispersion of the markers can be divided into three zones, similar to the dispersion of markers in a channel flow [42]. These zones can be seen clearly in Fig. 2, which shows the dispersion of particles in the streamwise direction (as reported in [32]). In the first zone, the puff of markers stayed together near the wall, forming a compact cloud. This is the region where the movement of the markers is dominated by molecular effects. Zone II is a transition zone, in which the markers get away from zone I, and move into the outer region of the flow field, where the marker motion is dominated by convection effects. The particles' motion in the third zone is due to turbulent convection. It was seen that this stage of dispersion occurred when the particles were distributed almost uniformly across the channel.

3.2 Development of a Plume. The behavior of the plume can be described by the probability function P_2 (Eq. (7)). In the present work, the plume is seen in two frames of reference: (a) as it is formed in the frame of reference that is stationary with respect to the center of the channel (i.e., the two moving walls move in opposite directions in this frame of reference—see Fig. 3(*a*)), and (b) as it is formed in a moving frame of reference that moves with the bottom wall of the channel (i.e., the plume is seen by an observer moving with the bottom wall—see Fig. 3(*b*)). The purpose of studying the plume with the moving frame of reference is to compare it with the corresponding plume in Poiseuille channel flow, and to other previous studies of Couette flow using a configuration with one moving wall.

Prediction of ground level temperature/concentration. The behavior of the plume in the first frame of reference, which is stationary with respect to the center of the channel, is shown in Fig. 4(*a*). The ground level temperature $T_{\max}$ is normalized with the strength of the source (i.e., the total number of markers released per time step). The temperature (or equivalently, the ground level concentration, if one considers the analogy between passive heat

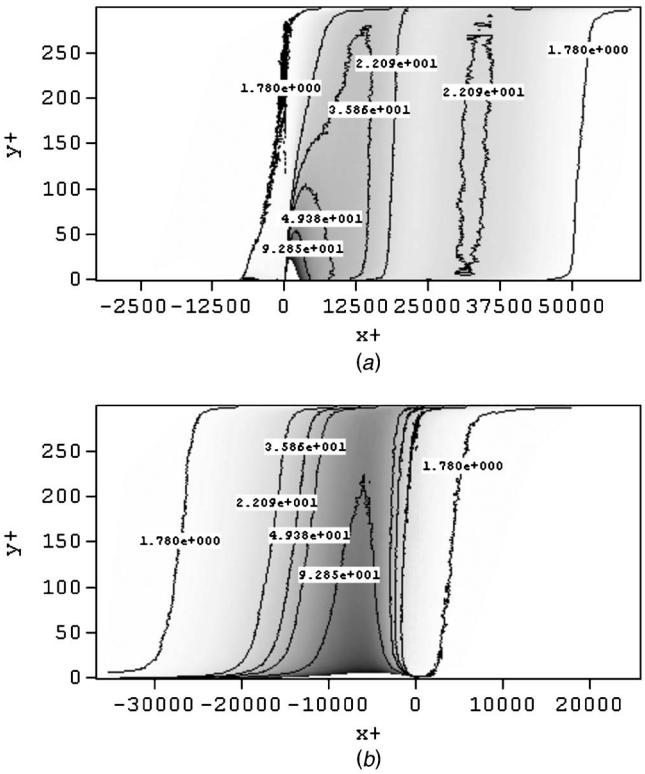

Fig. 3 Contour plots for (*a*) a plume relative to a stationary frame of reference, and (*b*) a plume relative to a moving frame of reference. In both cases Pr=100 and $t^+=3000$.

and passive mass transfer) is highest at the location $x=0$, where the particles are released continuously. Since the bottom plane is moving in the negative x direction, the mean velocity in the region near the wall is negative, and, thus, the maximum temperature is higher in the negative direction and lower in the positive direction. When Pr increases, the markers stay together longer, forming a compact cloud and resulting in higher temperature close to the wall. On the other hand, lower Pr numbers have a higher dispersion rate at the early stages after their release from the wall (note that the value of σ increases with decreasing Pr). They move quickly out of the viscous wall region and go into the bulk of the flow field, becoming more and more uniformly distributed. Therefore, the ground level temperature/concentration is lower for lower Pr.

Note that there are also markers in the positive x direction that are moving by the *leaking* of particles due to the random motion. It is also seen in Fig. 4(*a*) that at short x distances from the source, the ground level temperature/concentration is higher for low Pr markers and at longer distances from the source the ground level temperature/concentration is higher for higher Pr markers. In general, as Pr decreases, the total number of markers that can be found in the positive x direction is higher, because the lower Pr markers have larger random motion movements and can leak toward the positive x direction at farther distances (this was confirmed by counting the markers in the positive x direction, and finding that the total number of particles is higher for lower Pr). Therefore, the concentration is higher for lower Pr for a short distance. However, dispersion in the normal direction is also stronger for lower Pr markers, so at farther distances in the positive x direction the ground level concentration decreases quickly, while the markers for high Pr fluids are still staying together in the near wall region. This phenomenon of the *leaking* heat markers in the streamwise direction is similar to the phenomenon discussed (in its Eulerian analog) by Weigand et al. [43] for small Peclet

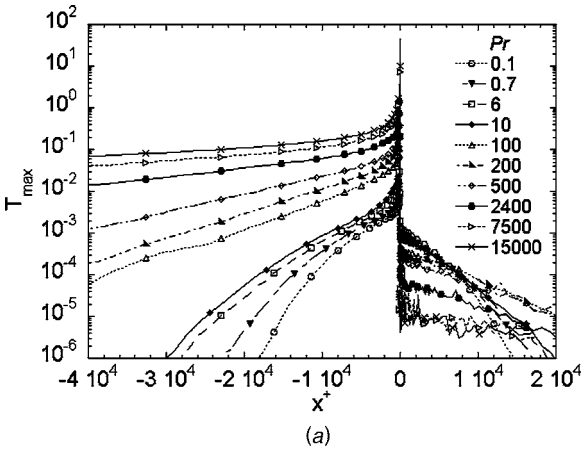

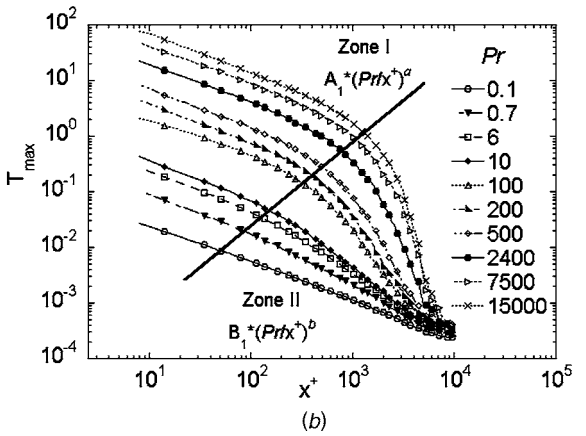

Fig. 4 Maximum temperature (concentration of markers) as function of streamwise position for (*a*) original plume and (*b*) plume relative to the velocity of the bottom moving wall

numbers and heat transfer in a duct, where it was referred to as *streamwise conduction*.

The logarithmic plot of the ground level temperature T_{max} as a function of streamwise position for the case where the frame of reference for the plume moves with the bottom wall is shown in Fig. 4(*b*). The decay of the ground level concentration is clearly distinguished into two zones. Similar to the behavior of the puff, as Pr increases, zone I is extended. The value of T_{max} is found to be dependent on the Pr and on the streamwise position. Based on Bachelor's prediction [44] that $T_{max} \sim 1/x$, T_{max} for this case will be estimated to be proportional to $(\mathrm{Pr}/x^+)^a$ and $(\mathrm{Pr}/x^+)^b$ in zones I and II, respectively. Then the normalized temperature can be calculated at any downstream location using the following correlation:

$$T_{max} = \frac{A_1 \cdot B_1 \left(\frac{\mathrm{Pr}}{x^+}\right)^{a+b}}{A_1 \left(\frac{\mathrm{Pr}}{x^+}\right)^{a} + B_1 \left(\frac{\mathrm{Pr}}{x^+}\right)^{b}} \tag{8}$$

The values of A_1, B_1, a, and b are calculated with regression and are reported in Table 1 for Pr=0.1–15,000.

The dispersion of a plume can be characterized by the plume half-width, which is defined to be the distance from the wall at which the temperature of the plume becomes half of its maximum. The half-plume width for the plume formed between the two moving walls is shown in Fig. 5(*a*). For low Pr, the dispersion is high, the markers are quickly distributed across the channel, and the half-plume width increases very fast. For high Pr, there are still a lot of particles close to the wall; half the maximum temperature

Table 1 Coefficients for the correlation that provides the ground-level temperature downstream from a plume (Eq. (8))

Pr	A_1	*a*	R^2	B_1	*b*	R^2
0.1	0.415	0.619	0.999	0.629	0.685	0.999
0.7	0.557	0.689	0.999	1.435	0.891	0.999
6	0.335	0.710	0.999	1.679	1.079	0.999
10	0.363	0.705	0.999	1.106	1.164	0.998
100	0.454	0.617	0.996	0.857	1.541	0.996
200	0.441	0.723	0.999	0.803	1.926	0.997
500	0.444	0.703	0.999	0.615	2.880	0.998
2400	0.429	0.699	0.998	0.030	3.634	0.998
7500	0.424	0.696	0.998	1.732×10^{-5}	6.678	0.995
15000	0.411	0.698	0.999	1.989×10^{-6}	7.063	0.993

lies very close to the wall. The half-plume width for the plume that is seen relative to the bottom moving wall has a trend similar to the trend seen in channel flow (Fig. 5(*b*)). For Pr=0.7 in channel flow, Poreh and Hsu [45] reported that δ_y changes with $x^{0.8}$, based on experimental measurements. Later on, Fackerell and Robins [46] found that $\delta_y \sim x^{0.75}$, and other DNS/LST results by Mitrovic and Papavassiliou [29] reported that δ_y is proportional to $x^{0.72}$. The half-plume width, δ_y, for Pr=0.7 in the Couette flow configuration increases with $x^{0.82}$, higher than what was found for

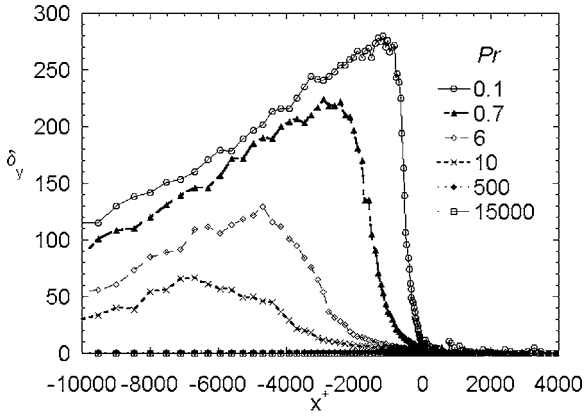

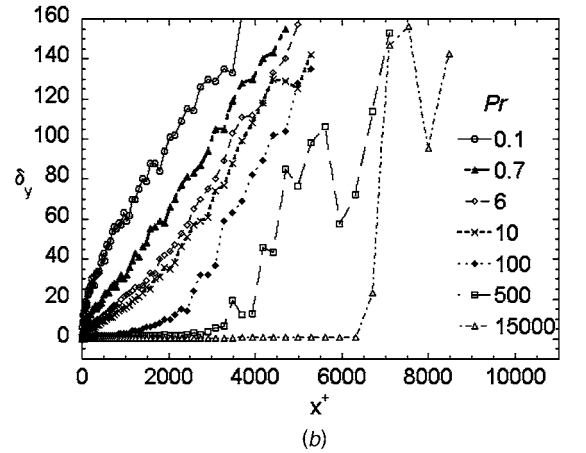

Fig. 5 Half-plume width as a function of streamwise position for (*a*) original plume and (*b*) plume relative to the velocity of the bottom moving wall

Table 2 Estimated conductive sublayer thickness at different Pr and bin size close to the wall

Pr	Estimated y_1^+ acording to Kader [3]	Number of bins used for caculation of $\left(\frac{dT}{dy}\right)_w$	Bin width Δy^+	y^+_{max} used for the calculation of $\left(\frac{dT}{dy}\right)_w$
0.1	20	20	1	20
0.7	7.14	7	1	7
6	6.604	3	1	3
10	5.570	3	1	3
100	2.585	2	1	2
200	2.052	16	0.004626-0.143063	1.182793
500	1.512	14	0.004626-0.124678	0.905855
2400	0.896	10	0.004626-0.087819	0.462399
7500	0.613	5	0.004626-0.041629	0.115644
15000	0.487	4	0.004626-0.032380	0.074016

channel flow in both experiments and simulations, meaning that the dispersion of a plume in Couette flow is faster than in channel flow.

3.3 Prediction of Mean Temperature Profiles Across the Couette Flow Channel. The mean temperature profile can be synthesized using a series of continuous line sources covering one (the bottom), or two walls of the channel (both the top and the bottom). Heat flux added to the bottom wall can be simulated by integrating P_2 over the streamwise direction

$$\overline{T}(y) \equiv \sum_{x=x_o}^{x_f} P_2(x-x_o,y|\vec{x}_o) = \sum_{x=x_o}^{x_f}\sum_{t=t_o}^{t_f} P_1(x-x_o,y,t-t_o|\vec{x}_o,t_o), \quad t_f \to \infty \text{ and } x_f \to \infty \tag{9}$$

The mean temperature profile at distance (x_1-x_o) downstream from a step change in heat flux from the wall, which occurs at x_o, can be described by

$$\overline{T}(x_1,y) \equiv \sum_{x=x_o}^{x_1} P_2(x-x_o,y|\vec{x}_o) = \sum_{x=x_o}^{x_1}\sum_{t=t_o}^{t_f} P_1(x-x_o,y,t-t_o|\vec{x}_o,t_o), \quad \text{as } t_f \to \infty \tag{10}$$

(Note that, since the velocity field is fully developed when the heat markers are released in the flow, only the thermal field is under development.) The mean temperature for the case of heat flux from both planes at a long distance $(x_1 \to \infty)$ downstream from the step change in heat from the wall, therefore, can be calculated using

$$\overline{T}(y) = \overline{T}(x_1,y) + \overline{T}(x_1,2h-y) \quad \text{as } x_1 \to \infty \tag{11}$$

and assuming that the temperature is symmetric around the centerplane (i.e., the plane $y=h$).

In the conductive wall sublayer, the mean temperature profile is expressed by $T^+=y^+$ Pr. Therefore, a linear extrapolation inside this region was used to determine the slope of the mean temperature at the wall that can be used in Eq. (2) for the calculation of the mean temperature in wall units. The bins used for the calculation of P_4, and thus the slope $(dT/dy^+)_w$, were located within the conductive sublayer region. Kader [3] suggested that the thickness of the conductive sublayer y_1^+ can be estimated by $y_1^+ \cong 12/\mathrm{Pr}^{1/3}$ for $\mathrm{Pr} \gg 1$ and $y_1^+ \cong 2/\mathrm{Pr}$ for $\mathrm{Pr} \ll 1$. The number of bins used for the calculation of $(dT/dy^+)_w$ is shown in Table 2. The number of bins is varied so that the maximum y_{max} in wall units is equal to or less than the value of y_1^+ calculated by Kader's suggestion to make sure that the bins are within the conductive sublayer. These values are also reported in Table 2.

The mean temperature profiles for all Pr fluids in the case of heat flux applied to one channel wall are shown in Figs. 6(*a*) and 6(*b*), and the mean temperature for heat flux from two channel walls is shown in Fig. 6(*c*). These temperature profiles were calculated using a frame of reference that moves with the bottom wall. All the quantities are in wall units. In the conductive sublayer, the dimensionless temperature follows the correlation $T^+=y^+$ Pr, as expected. The temperature profile of low Pr fluids for one heated wall is presented in Fig. 6(*a*). The temperature profile for Pr=0.7 is compared with the results provided in [26] showing good agreement (note that the Re in [26] is different than the Re of the present study—it is roughly three times smaller than the Re used here). As Pr increases, the temperature in the center of the channel increases.

The logarithmic region for the velocity field in Couette flow is more extended than the logarithmic region for plane channel flow, because the whole Couette flow channel is a constant stress region. However, we can now compare the logarithmic region for the temperature profile for channel and for Couette flow. The temperature profile in the logarithmic region is given by $T^+=A\ln y^+ + B$, where A depends on the flow field and B depends on the Pr [26]. The coefficients A and B are shown in Figs. 7(*a*) and 7(*b*), respectively. The A coefficient is smaller in Couette flow than in channel flow. It reaches almost a constant value for $\mathrm{Pr} \geqslant 10$. In this high Pr range, the conductive thermal sublayer is very thin close to the wall and the distance from the wall at which the logarithmic layer starts is short. For Poiseuille channel flow (using the data of Mitrovic et al. [30]), the average coefficient A for high Pr (and, thus, well-observable temperature logarithmic layers) is 4.21 with a standard deviation of 0.42, and, for Couette flow, this value is 3.02 with a standard deviation of 0.17. For low Pr fluids, the coefficients are lower. Liu [26] found A to be 2.63 and B to be 1.2

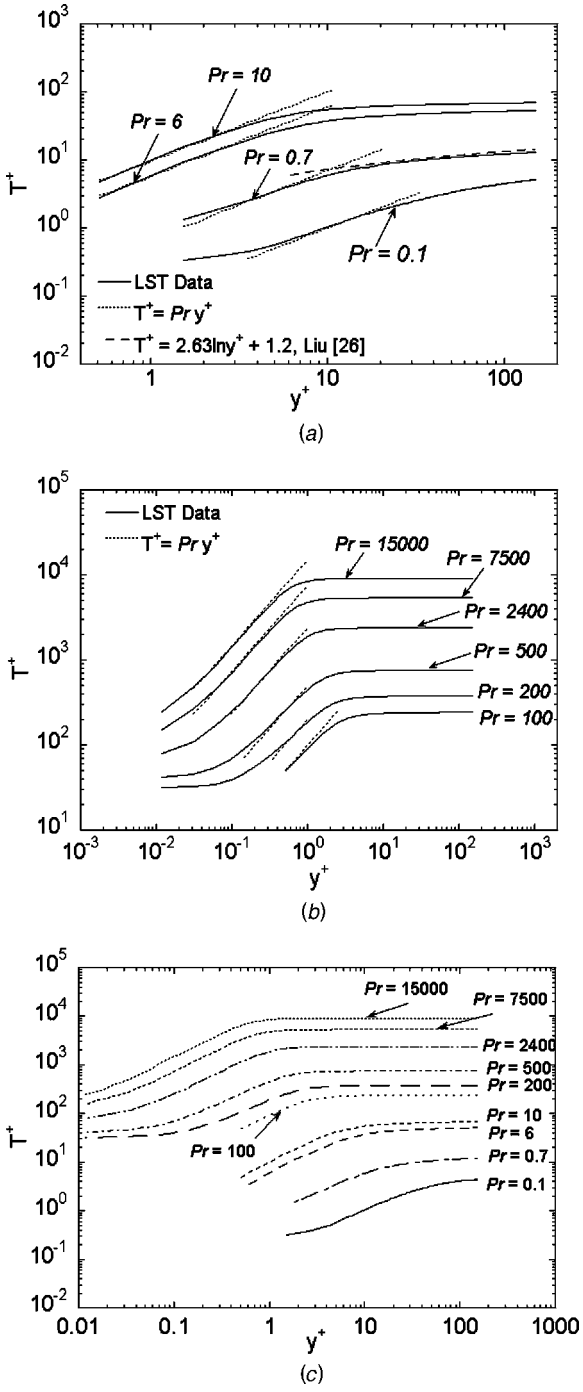

Fig. 6 Mean temperature profile with a step change in the heat flux applied to (*a*) one channel wall (Pr≤10); (*b*) one channel wall (Pr≥100), and (*c*) two channel walls

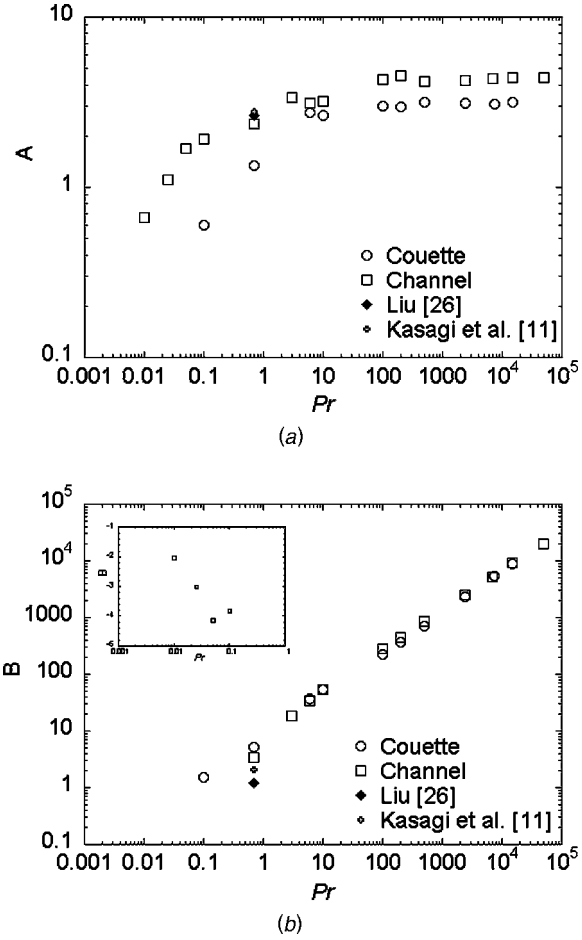

Fig. 7 Mean temperature log-law coefficients for plane Couette flow and plane channel flow (the values for plane channel flow are calculated from the data of Mitrovic et al. [30]): (*a*) coefficient A, and (*b*) coefficient B with an inset for low Pr

for Pr=0.71 for Couette flow in which one wall was heated and the other wall was cooled. Kasagi et al. [11] found $A=2.78$ for Pr=0.7 in forced channel flow. For Pr=0.7 in the current work, A is found to be 2.37 for Poiseuille flow and 1.35 for Couette flow. If A depends on the flow field, B depends strongly on the Pr number. A very small difference between the coefficients B for Couette and Poiseuille flow is seen in Fig. 7(*b*). The difference in the B coefficients from Liu [26] might be due to the difference in Re; $h^+=52.8$ in [26] versus 150 in the present study.

The heat transfer coefficient, K^+, can be calculated with Eq. (4) using the average bulk temperature. The heat transfer coefficient as a function of the streamwise position for all Pr fluids for the case of one heated wall is shown in Fig. 8(*a*), and a system of reference that moves with the bottom heated wall. The results are compared with the asymptotic solution for small x^+ and high Pr fluids that was derived theoretically by Son and Hanratty [47]

$$K^+ = 0.81(x^+)^{-1/3}\,\mathrm{Pr}^{-2/3} \tag{12}$$

Similar to the case reported for a Poiseuille channel flow in [30], the results agree with this solution for $x^+/h^+<10$, corresponding to the entry length of a scalar exchange region. As the heat markers travel downstream, the temperature across the channel becomes more uniform, and the heat transfer coefficients keep decreasing until they get to constant values, at which point the temperature profiles are fully developed. It is also seen that as Pr increases, the heat transfer coefficient decreases, indicating a better mixing in lower Pr fluids.

The heat transfer coefficients for the case where heat flux is applied to both channel walls are presented in Fig. 8(*b*) (specifically, the heat flux is applied to both walls at points $x^+\geq 0$, and the system of reference is stationary with respect to the center plane of the channel). The heat transfer coefficients start from lower values than the values in Fig. 8(*a*) at the entry region. The reason is that the marker plumes that compose the temperature profile close to the point of step change in wall heat flux are dispersed mainly in the negative x direction (see discussion about plumes in Sec. 3.2). As a result, the temperature profile, even at small distances downstream from the point of step change in heat flux, is very close to a fully developed temperature profile, which corre-

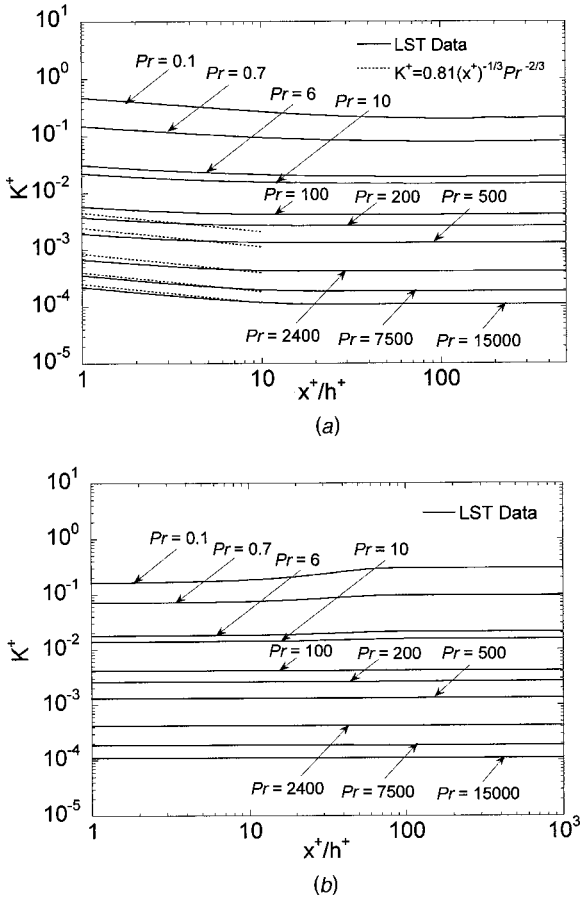

Fig. 8 Heat transfer coefficient as a function of the distance downstream from a step change in heat flux applied to (*a*) one channel wall, and (*b*) two channel walls

sponds to lower K^+ (see, for example, the values of K^+ at large x^+/h^+ in Fig. 8(*a*)). For higher Pr, the value of K^+ does not change much with x.

The heat transfer coefficients are mostly of interest at a well-mixed state, very far downstream from the entry region, where they stay constant. These coefficients are noted as K^+_∞. Plots of K^+_∞ as a function of Pr, for one heated wall and two heated walls, are shown in Fig. 9. The fully developed heat transfer coefficient decreases as Pr increases. The values can be fitted with a power

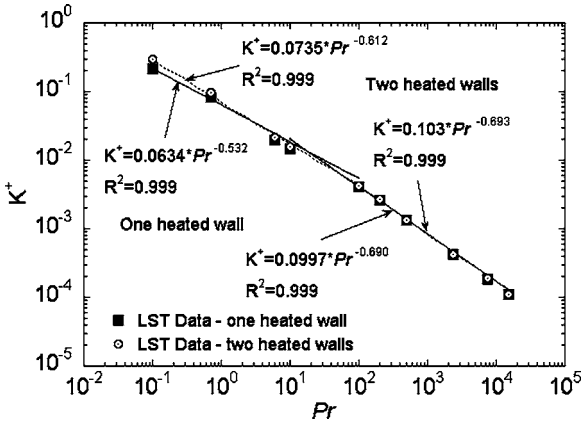

Fig. 9 Fully developed heat transfer coefficient as function of Pr for one heated wall and two heated walls

function according to Eq. (5). The trend for heat flux applied at only the bottom wall is shown in Fig. 9. The fully developed heat transfer coefficient is estimated to be

$$\mathrm{Pr} \leqslant 10: K^+_\infty = 0.0634\,\mathrm{Pr}^{-0.532}, \quad R^2 = 0.999 \tag{13}$$

$$\mathrm{Pr} \geqslant 100: K^+_\infty = 0.0997\,\mathrm{Pr}^{-0.690}, \quad R^2 = 0.999 \tag{14}$$

For a similar case in a Poiseuille channel flow, the power values were found to be −0.510 and −0.690 [30]. This indicates a similar dependence of the heat transfer coefficient on the Pr for Couette flow and for plane channel flow at high Pr. However, the moving wall helps to increase the fully developed heat transfer coefficients, since the preexponential coefficients are higher in both cases for Couette flow.

For the case of heat flux applied at both walls, K^+ is found to be

$$\mathrm{Pr} \leqslant 10: K^+_\infty = 0.0735\,\mathrm{Pr}^{-0.612}, \quad R^2 = 0.999 \tag{15}$$

$$\mathrm{Pr} \geqslant 100: K^+_\infty = 0.103\,\mathrm{Pr}^{-0.693}, \quad R^2 = 0.999 \tag{16}$$

In general, heat transfer coefficients in the case of heat flux applied at both channel walls are higher than those with heat flux applied at one channel wall (this difference is more pronounced at lower Pr—it can be within 4% for $\mathrm{Pr} \geqslant 100$). Similar to the case of heat flux applied to one channel wall, the power values are the same as in Poiseuille flow [30] and the preexponential coefficients are higher in Couette flow. The interpretation of this observation is that the mechanism of turbulent transport from the wall is the same in both cases, i.e., only a part of the spectrum (the smaller wave-numbers part) of the turbulent velocity field contributes to turbulent transport from the wall and this part depends on the fluid Pr (as Pr increases, a smaller part of the spectrum contributes, see [29,48]). However, the turbulent velocity field is different in Couette and Poiseuille flow, with turbulence intensities being higher in Couette flow, and this fact manifests itself as a larger preexponential factor.

The power values for high Pr in Eqs. (14) and (16) are close to the values measured by Shaw and Hanratty [49], who found $K^+ \sim \mathrm{Sc}^{-0.704}$ from accurate experimental measurements for turbulent mass transfer. However, the Pr dependence suggested by Eq. (14), i.e., $K^+ \sim \mathrm{Pr}^{-0.690}$, is different than other frequently used correlations. For channel flow with two fixed planes, the heat transfer coefficient for fully developed flow is usually reported with the Deissler asymptotic correlation, $K^+ \sim \mathrm{Pr}^{-3/4}$, or with Sieder-Tate's prediction, $K^+ \sim \mathrm{Pr}^{-2/3}$ for high Pr, in textbooks like Bird et al. [50] and Hinze [51]. It should be noted that several other researchers have also found differences from the Deissler and Sieder-Tate predictions [52–54].

In order to develop a predictive correlation for K^+ over the whole range of Pr, one can use a correlation similar to that for $T_{\max}$ (Eq. (8)). A regression analysis for K^+ results in the following equations:

(a) For heat flux applied to one channel wall

$$K^+_\infty = \frac{0.0233\,\mathrm{Pr}^{-1.222}}{0.255\,\mathrm{Pr}^{-0.532} + 0.0875\,\mathrm{Pr}^{-0.690}}$$

$$R^2 = 0.991 \tag{17}$$

(b) For heat flux applied to both channel walls

$$K^+_\infty = \frac{0.176\,\mathrm{Pr}^{-1.305}}{2.25\,\mathrm{Pr}^{-0.612} + 0.0784\,\mathrm{Pr}^{-0.693}}$$

$$R^2 = 0.996 \tag{18}$$

Generalized equations for heat transfer coefficients can also be obtained by using the Churchill and Usagi method [55]. They proposed the following generalized equation when the asymptotic behavior of a function at two limits is known:

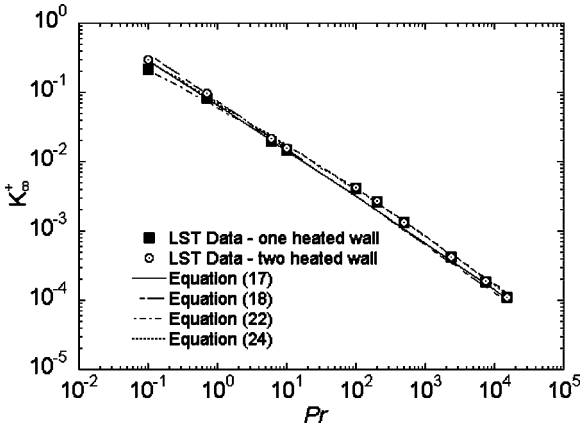

Fig. 10 Comparison of the LST results for the fully developed heat transfer coefficient with fitted correlations for one heated wall and two heated walls

$$\frac{f(w)}{f_\infty(w)} = \left[1 + \left(\frac{f_o(w)}{f_\infty(w)}\right)^n\right]^{1/n} \tag{19}$$

where $f_\infty(w)$ and $f_o(w)$ represent asymptotic expressions for large and small values of w. Using this method, the heat transfer coefficient correlation can be expressed as

$$\frac{K_\infty^+(\mathrm{Pr})}{K_\infty^+(\mathrm{Pr} \geqslant 100)} = \left[1 + \left(\frac{K_\infty^+(\mathrm{Pr} \leqslant 10)}{K_\infty^+(\mathrm{Pr} \geqslant 100)}\right)^n\right]^{1/n} \tag{20}$$

where $K_\infty^+(\mathrm{Pr} \leqslant 10)$ and $K_\infty^+(\mathrm{Pr} \geqslant 100)$ represent the asymptotic expressions for heat transfer coefficients for small Pr and large Pr. For one heated wall, these two expressions are Eqs. (13) and (14), respectively. Combining these two expressions into Eq. (20) results in the following equation for one heated wall:

$$\frac{K_\infty^+(\mathrm{Pr})}{0.0997\,\mathrm{Pr}^{-0.690}} = \left[1 + \left(\frac{\mathrm{Pr}}{17.56}\right)^{n/6.33}\right]^{1/n} \tag{21}$$

The n value is fitted in order to achieve the best results. Furthermore, the left-hand side of Eq. (21) should be unity for all $\mathrm{Pr} \geqslant 100$, since K_∞^+ for this range of Pr is approximated by the relations in the denominators. In order to satisfy this condition, the exponent n should be negative with high absolute value. If we assume the convenient exponent $n=-6.33$ for the one heated wall case, then Eq. (21) becomes

$$K_\infty^+ = \frac{0.0997\,\mathrm{Pr}^{-0.690}}{\left[1 + \left(\frac{17.56}{\mathrm{Pr}}\right)\right]^{0.158}} \tag{22}$$

with $R^2=0.999$.

This equation gives an excellent fit with the LST data. It is also better than the correlation predicted using the method suggested by Eq. (8) (i.e., Eq. (17)). Comparisons between the LST data and the heat transfer coefficients calculated by Eqs. (17) and (22) are shown in Fig. 10.

Similarly, for two heated walls, using Eqs. (15) and (16) for small and large Pr numbers into Eq. (20) gives

$$\frac{K_\infty^+(\mathrm{Pr})}{0.103\,\mathrm{Pr}^{-0.693}} = \left[1 + \left(\frac{\mathrm{Pr}}{63.47}\right)^{n/12.3}\right]^{1/n} \tag{23}$$

Assuming the convenient exponent $n=-12.3$, the equation becomes

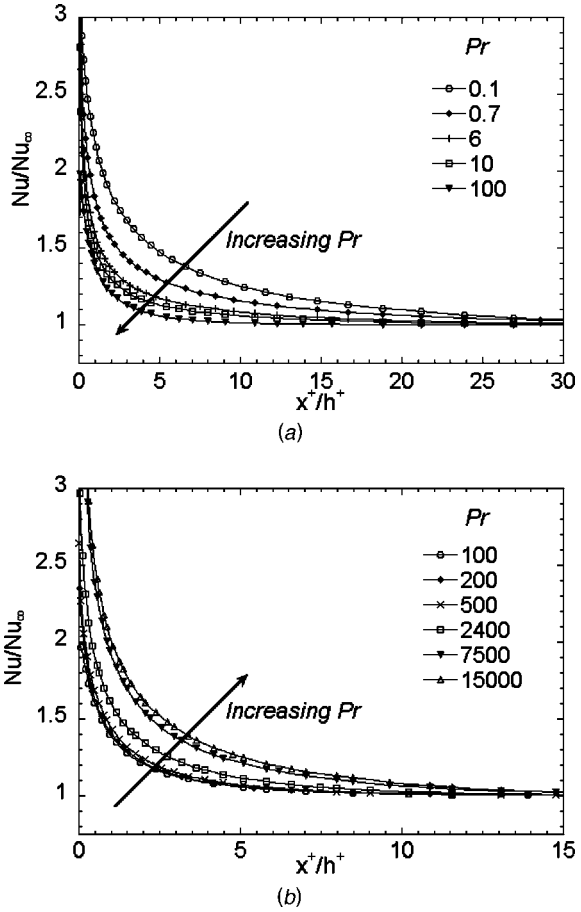

Fig. 11 Change of Nusselt number ratio with the distant downstream from a step change in heat flux applied to the bottom channel wall: (*a*) low Pr runs ($\mathrm{Pr} \leqslant 10$) and (*b*) high Pr runs ($\mathrm{Pr} \geqslant 100$)

$$K_\infty^+ = \frac{0.103\,\mathrm{Pr}^{-0.693}}{\left[1 + \left(\frac{63.47}{\mathrm{Pr}}\right)\right]^{0.081}} \tag{24}$$

with $R^2=0.999$.

The differences between LST data and calculations from Eqs. (18) and (24) are also shown in Fig. 10. Both of these two methods agree well with the data, however the Churchill and Usagi method gives better accuracy.

The Nusselt number ratio $\mathrm{Nu}/\mathrm{Nu}_\infty$ with respect to the downstream distance x^+/h^+ from a step change in heat flux from the wall is also calculated and shown in Fig. 11. The ratio for low Pr and high Pr for heat flux applied to only the bottom wall are presented in Figs. 11(*a*) and 11(*b*), respectively. The same behavior is observed in the current work and in Poiseuille channel flow [30]. For $\mathrm{Pr} \leqslant 100$, the ratio decreases as the Pr increases; and for $\mathrm{Pr} \geqslant 100$, the ratio increases as the Pr increases. Mitrovic et al. [30] suggested that this behavior can be explained by the correlations of K^+ as a function of Pr. At small distance, i.e., in the entry region, K^+ is proportional to $\mathrm{Pr}^{-2/3}$ (Eq. (12) for small x^+). For high Pr, at fully developed thermal layer (large x^+) K^+ is proportional to $\mathrm{Pr}^{-0.690}$. Therefore, the Nusselt number ratio for high Pr number fluids is

$$\frac{\mathrm{Nu}(x^+/h^+)}{\mathrm{Nu}(x^+/h^+ \to \infty)} \propto \frac{K^+}{K_\infty^+} \propto \frac{(x^+)^{-1/3}\,\mathrm{Pr}^{-2/3}}{\mathrm{Pr}^{-0.69}} \propto (x^+)^{-1/3}\,\mathrm{Pr}^{0.023} \tag{25}$$

Initially, the ratio is higher for higher Pr numbers. As x^+ increases, the Pr effect is negligible and the ratio becomes independent of Pr, and goes to 1. For low Pr number fluids, K^+ is proportional to $\mathrm{Pr}^{-0.532}$ for one heated wall. The Nusselt ratio, therefore, will go with $(x^+)^{-1/3}\mathrm{Pr}^{-0.135}$, and is expected to decrease as the Pr increases at the same location.

Even though this behavior is similar to that of Poiseuille flow, the Nusselt number ratio goes to 1 faster in Couette flow than in Poiseuille flow. For example, at $x^+/h^+=5$ and $\mathrm{Pr}=0.7$ the value of $\mathrm{Nu}/\mathrm{Nu}_\infty$ is 1.3 for Couette flow and 1.7 for Poiseuille flow (from Mitrovic et al.). For a higher Pr number, $\mathrm{Pr}=500$, $\mathrm{Nu}/\mathrm{Nu}_\infty$ is 1.1 and 1.3 for Couette and Poiseuille flow, respectively, at $x^+/h^+=5$.

4 Conclusions

The present work used direct numerical simulation in conjunction with a Lagrangian method, a convenient tool to study turbulent heat/mass transfer in a range of Pr. The effects of the velocity boundary conditions on the mechanism of heat transfer through the ground-level temperatures downstream from a continuous source of heat markers and through the half-plume widths of the plumes were observed. Together with prior investigation on the dispersion of the puff, it is found that the Couette channel flow leads to an increase to the rate of development of the thermal plume, showing a better mixing compared to mixing in Poiseuille channel flow.

Mean temperature profiles across the channel at fully developed turbulence were also presented for an extensive range of Pr numbers. Heat flux was applied at one wall or at both channel walls. Predictive correlations for the heat transfer coefficients K^+ for the case of heat transfer from one and two heated planes were determined. The heat transfer coefficients for Couette channel flow show the same trend as for Poiseuille channel flow. The exponential values are the same or close to those in Poiseuille channel flow, but the preexponential factors are higher.

Acknowledgments

The support of NSF under Contract No. CTS-0209758 is gratefully acknowledged. This work was also supported by the National Computational Science Alliance under Contract No. CTS-040023 and utilized the NCSA IBMp690 and the NCSA SGI/CRAY Origin2000. Computational support was also offered by the University of Oklahoma Center for Supercomputing Education and Research (OSCER).

Nomenclature

A,B = constants in the logarithmic law for the mean temperature

a,b = exponentials in the power law relation for the ground level temperature (see Eq. (8))

A_1,B_1 = constants in the power law relationship for the ground level temperature (see Eq. (8))

C_1 = constant in the correlation between the Nusselt number and the Prandtl and Reynolds numbers (see Eq. (5))

C_p = specific heat at constant pressure (kJ/(Kg K)

D = diffusivity (m^2/s)

$f_o(w)$ = asymptotic expression for small values of w

$f_\infty(w)$ = asymptotic expression for large values of w

h = half height of the channel

K = heat transfer coefficient ($\mathrm{kW}/(\mathrm{m}^2\,\mathrm{K})$)

K_∞ = heat transfer coefficient for a fully developed thermal region ($\mathrm{kW}/(\mathrm{m}^2\,\mathrm{K})$)

k = thermal conductivity (W/(m K))

l^* = friction length, $l^*=\nu/u^*$

n = constant in the generalized equation (see Eq. (19))

Nu = Nusselt number, $\mathrm{Nu}=K^+h^+$

Nu_∞ = Nusselt number for a fully developed thermal region

p,q = constants that appear in the correlation between the Nusselt number and the Prandtl and Reynolds numbers (see Eq. (5))

P_1 = conditional probability for a marker to be at a location (x,y) at time t, given that it was released at a known time from a known location at the wall

P_2 = joint probability for a marker to be at a location (x,y)

Pr = Prandtl number, $\mathrm{Pr}=\nu/\alpha$

q_w = heat flux from the wall (kW/m^2)

R^2 = coefficient of determination

Re = Reynolds number, $\mathrm{Re}=U_c h/\nu$

Sc = Schmidt number, $\mathrm{Sc}=\nu/D$

$\vec{V}$ = Lagrangian velocity vector of a marker (m/s)

T = temperature (K)

T^* = friction temperature, $T^*=q_w/(\rho C_p u^*)$

$\overline{T}$ = mean temperature (K)

t = time (s)

t^* = friction time, $t^*=l^*/u^*$

t_o = time instant of a marker released (s)

U = velocity (m/s)

$\vec{U}$ = Eulerian velocity vector (m/s)

$\overline{U}$ = mean velocity (m/s)

u^* = friction velocity, $u^*=(\tau_w/\rho)^{1/2}$(m/s)

$\vec{V}$ = Lagrangian velocity vector (m/s)

x,y,z = streamwise, normal and spanwise coordinates

x_1 = streamwise location

X,Y = Lagrangian displacement of a marker from the source in the x,y directions

X_s = Lagrangian displacement of a marker from the source in x directions in a stationary frame of reference

$\vec{X}$ = position vector of a marker

y_1 = thickness of conductive wall sublayer

Greek symbols

α = thermal diffusivity

δ_y = plume half-width

Δt = time step

$\Delta x,\Delta y$ = bin size in the x and y directions

θ = temperature fluctuation

λ_x = periodic streamwise length

λ_z = periodic spanwise length

ν = kinematic viscosity (m^2/s)

π = trigonometric pi ($\pi=3.14159\ldots$)

ρ = fluid density (kg/m^3)

σ = standard deviation

τ = shear stress (Pa)

Superscripts and subscripts

$\overline{(\,)}$ = ensemble average

$\vec{(\,)}$ = vector quantity

$(\,)^+$ = value made dimensionless with the wall parameters

$(\,)^*$ = friction value

$(\,)_b$ = bulk value

$(\,)_f$ = value at the final time step of the simulation

$(\,)_{\max}$ = maximum value

$(\,)_o$ = value at the instant of marker release

$(\,)_w$ = value at the wall of the channel

References

[1] Zhukauskas, A., and Shlanchauskas, A., 1973, *Heat Transfer in a Turbulent Liquid Flow*, Mintis, Vilnius.

[2] Gowen, R. A., and Smith, J. W., 1967, "The Effect of the Prandtl Number on Temperature Profiles for Heat Transfer in Turbulent Pipe Flow," Chem. Eng. Sci., **22**, pp. 1701–1711.

[3] Kader, B. A., 1981, "Temperature and Concentration Profiles in Fully Turbulent Boundary Layers," Int. J. Heat Mass Transfer, **29**(9), pp. 1541–1544.

[4] Taranov, G. S., 1970, "Study of the Statistical Characteristics of Velocity and Temperature Fields in Turbulent Flow With a Transverse Shear," Thesis (Cand.Sci.), Institute of Phys. Atmos., Acad. Sci. of the U.S.S.R.

[5] Fulachier, L., 1972, "Contribution a L'etude des Analogies des Champs Dynamique et Thermique Dans Unee Couche Limite Turbulent. Effet de L'aspiration," These (Doct.Sci), Phys. Univ. Provence, Marseille.

[6] Belov, V. M., 1976, "Experimental Investigation of Heat Transfer in a Turbulent Boundary Layer With a Step-Like Change in Thermal Boundary Conditions on the Wall," Thesis (Cand.Sci), The Bauman Higher Technical College, Moscow, Russia.

[7] Teitel, M., and Antonia, R. A., 1993a, "Heat Transfer in Fully Developed Turbulent Channel Flow: Comparison Between Experiment and Direct Numerical Simulations," Int. J. Heat Mass Transfer, **36**(6), pp. 1701–1706.

[8] Teitel, M., and Antonia, R. A., 1993b, "A Step Change in Wall Heat Flux in a Turbulent Channel Flow," Int. J. Heat Mass Transfer, **36**(6), pp. 1707–1709.

[9] Kim, J., and Moin, P., 1989, "Transport of Passive Scalars in a Turbulent Channel Flow," *Turbulent Shear Flow VI*, J. C. Adre, J. Cousteix, F. Durst, B. E. Launder, F. W. Schmidt, and J. H. Whitelaw, eds., Springer, Berlin, pp. 85–96.

[10] Lyons, S. L., Hanratty, T. J., and McLaughlin, J. B., 1991, "Direct Numerical Simulation of Passive Heat Transfer in a Turbulent Channel Flow," Int. J. Heat Mass Transfer, **34**(4/5), pp. 1149–1161.

[11] Kasagi, N., Tomita, Y., and Kuroda, A., 1992, "Direct Numerical Simulation of Passive Scalar Field in a Turbulent Channel Flow," ASME J. Heat Transfer, **114**, pp. 598–606.

[12] Kasagi, N., and Shikazono, N., 1995, "Contribution of Direct Numerical Simulation to Understanding and Modeling Turbulent Transport," Proc. R. Soc. London, Ser. A, **451**, pp. 257–292.

[13] Kawamura, H., Ohsaka, K., Abe, H., and Yamamoto, K., 1998, "DNS of Turbulent Heat Transfer in Channel Flow With low to Medium-High Prandtl Number Fluid," Int. J. Heat Fluid Flow, **19**, pp. 482–491.

[14] Kawamura, H., Abe, H., and Matsuo, Y., 1999, "DNS of Turbulent Heat Transfer in Channel Flow With Respect to Reynolds and Prandtl Number Effects," Int. J. Heat Fluid Flow, **20**(3), pp. 196–207.

[15] Reichardt, H., 1956, "Über die Geschwindigkeitsverteilung in Einer Geradlinigen Turbulenten Couetteströmung," Z. Angew. Math. Mech., **36**, pp. 26–29.

[16] Robertson, J. M., and Johnson, H. F., 1970, "Turbulence Structure in Plane Couette Flow," J. Eng. Mech. Div., Am. Soc. Civ. Eng., **96**, pp. 1171–1182.

[17] Aydin, E. M., and Leutheusser, H. J., 1979, "Novel Experimental Facility for the Study of Plane Couette Flow," Rev. Sci. Instrum., **50**(11), pp. 1362–1366.

[18] Aydin, E. M., and Leutheusser, H. J., 1987, "Experimental Investigation of Turbulent Plane Couette Flow," *ASME Forum on Turbulent Flows*, FED 51, pp. 51–54, ASME, Cincinnati.

[19] Aydin, E. M., and Leutheusser, H. J., 1991, "Plane Couette Flow Between Smooth and Rough Walls," Exp. Fluids, **11**, pp. 302–312.

[20] El Telbany, M. M. M., and Reynolds, A. J., 1982, "The Structure of Turbulent Plane Couette Flow," ASME J. Fluids Eng., **104**, pp. 367–372.

[21] Tillmark, N., and Alfredsson, P. H., 1991, "An Experimental Study of Transition in Plane Couette Flow," Adv. Turbulence, **3**, pp. 235–239.

[22] Tillmark, N., and Alfredsson, P. H., 1992, "Experiments on Transition in Plane Couette Flow," J. Fluid Mech., **235**, pp. 89–102.

[23] Lee, M. J., and Kim, J., 1991, "The Structure of Turbulence in a Simulated Plane Couette Flow," *8th Symp. On Turb. Shear Flows*, University of Munich, Munich, paper 5–3.

[24] Komminaho, J., Lundbladh, A., and Johansson, A. V., 1996, "Very Large Structures in Plane Turbulent Couette Flow," J. Fluid Mech., **320**, pp. 259–285.

[25] Papavassiliou, D. V., and Hanratty, T. J., 1997, "Interpretation of Large Scale Structures Observed in a Turbulent Plane Couette Flow," Int. J. Heat Fluid Flow, **18**, pp. 55–69.

[26] Liu, C., 2003, "Turbulent Plane Couette Flow and Scalar Transport at low Reynolds Number," ASME J. Heat Transfer, **125**, pp. 988–998.

[27] Debusschere, B., and Rutland, C. J., 2004, "Turbulent Scalar Transport Mechanism in Plane Channel and Couette Flows," Int. J. Heat Mass Transfer, **47**, pp. 1771–1781.

[28] Le, P. M., and Papavassiliou, D. V., 2005, "Turbulent Dispersion From Elevated Sources in Channel and Couette Flow," AIChE J., **51**(9), pp 2402–2414.

[29] Mitrovic, B. M., and Papavassiliou, D. V., 2003, "Transport Properties for Turbulent Dispersion From Wall Sources," AIChE J., **49**(5), pp. 1095–1108.

[30] Mitrovic, B. M., Le, P. M., and Papavassiliou, D. V., 2004, "On the Prandtl or Schmidt Number Dependence of the Turbulence Heat or Mass Transfer Coefficient," Chem. Eng. Sci., **59**(3), pp. 543–555.

[31] Bech, K. H., Tillmark, N., Alfredson, P. H., and Anderson, H. I., 1995, "An Investigation of Turbulent Plane Couette Flow at low Reynolds Numbers," J. Fluid Mech., **286**, pp. 291–325.

[32] Le, P. M., and Papavassiliou, D. V., 2004, "Turbulent Heat Transfer in Plane Channel and Plane Couette Flow," paper HT-FED2004–56130, *CD ROM Proceedings, 2004 ASME Heat Transfer/Fluids Engineering Summer Conference*, Charlotte, NC, July 11–15, ASME, New York.

[33] Kontomaris, K., Hanratty, T. J., and McLaughlin, J. B., 1993, "An Algorithm for Tracking Fluid Particles in a Spectral Simulation of Turbulent Channel Flow," J. Comput. Phys., **103**, pp. 231–242.

[34] Papavassiliou, D. V., and Hanratty, T. J., 1997, "Transport of a Passive Scalar in a Turbulent Channel Flow," Int. J. Heat Mass Transfer, **40**(6), pp. 1303–1311.

[35] Ponoth, S. S., and McLaughlin, J. B., 2000, "Numerical Simulation of Mass Transfer for Bubbles in Water," Chem. Eng. Sci., **55**, pp. 1237–1255.

[36] Papavassiliou, D. V., 2002, "Turbulent Transport From Continuous Sources at the Wall of a Channel," Int. J. Heat Mass Transfer, **45**, pp. 3571–3583.

[37] Mito, Y., and Hanratty, T. J., 2003, "Lagrangian Stochastic Simulation of Turbulent Dispersion of Heat Markers in a Channel Flow," Int. J. Heat Mass Transfer, **46**(6), pp. 1063–1073.

[38] Hasegawa, Y., and Kasagi, N., 2001, "The Effect of Schmidt Number on Air-Water Interface Mass Transfer," *Proceedings, 4th Int. Conference on Multiphase Flow 2001*-New Orleans (CD-ROM), ICMF'01, New Orleans, Louisiana.

[39] Hasegawa, Y., and Kasagi, N., 2003, "The Role of Splatting Effect in High Schmidt Number Turbulent Mass Transfer Across an Air-Water Interface," in *Turbulence, Heat and Mass Transfer 4*, edited by K. Hanjalic, Y. Nagano, and M. Tummers, 113–120, Begell House, New York.

[40] Einstein, A., 1905, "Uber die von der Molecular-Kinetischen Theorie der Warme Geforderte Bewegung von in Ruhenden Flussigkeiten Suspendierten Teilchen," Ann. Phys., **17**, pp. 549–560.

[41] Saffman, P. G., 1960, "On the Effect of the Molecular Diffusivity in Turbulent Diffusion," J. Fluid Mech., **8**, pp. 273–283.

[42] Papavassiliou, D. V., 2002, "Scalar Dispersion From an Instantaneous Source at the Wall of a Turbulent Channel for Medium and High Prandtl Fluids," Int. J. Heat Mass Transfer, **23**(2), pp. 161–172.

[43] Weigand, B., Schwartzkopff, T., Sommer, T. P., 2002, "A Numerical Investigation of the Heat Transfer in a Parallel Plate Channel With Piecewise Constant Wall Tempereature Boundary Conditions," ASME J. Heat Transfer, **124**(4), pp. 626–634.

[44] Batchelor, G. K., 1964, "Diffusion from Sources in a Turbulent Boundary Layer," Arch. Mech. Stosow., **3**(6), pp. 661–670.

[45] Poreh, M., and Hsu, K. S., 1971, "Diffusion From a Line Source in Turbulent Boundary Layer," Int. J. Heat Mass Transfer, **14**, pp. 1473–1483.

[46] Fackerell, J. E., and Robins, A. G., 1982, "Concentration Fluctuations and Fluxes in Plumes From Point Sources in a Turbulent Boundary Layer," J. Fluid Mech., **117**, pp. 1–26.

[47] Son, J. S., and Hanratty, T. J., 1967, "Limiting Relation for the Eddy Diffusivity Close to a Wall," AIChE J., **13**, pp. 689–696.

[48] Na, Y., and Hanratty, T. J., 2000, "Limiting Behavior of Turbulent Scalar Transport Close to a Wall," Int. J. Heat Mass Transfer, **43**, pp. 1749–1758.

[49] Shaw, D. A., and Hanratty, T. J., 1977, "Turbulent Mass Transfer Rates to a Wall for Large Schmidt Numbers," AIChE J., **23**(1), pp. 28–37.

[50] Bird, R. B., Steward, W. E., and Lightfoot, E. N., 1960, *Transport Phenomena*, Wiley, New York, pp. 399, 403, 361.

[51] Hinze, J. O., 1987, *Turbulence*, 2nd ed., McGraw-Hill, New York.

[52] Incropera, F. P., Kerby, J. S., Moffat, D. F., and Ramadhyani, S., 1986, "Convective Heat Transfer From Discrete Heat Sources in a Rectangular Channel," Int. J. Heat Mass Transfer, **29**(7), pp. 1051–1058.

[53] Hubbard, D. W., and Lightfoot, E. N., 1966, "Corelation of Heat and Mass Transfer in Turbulent Data for High Schmidt and Reynolds Numbers," Ind. Eng. Chem. Fundam., **5**, pp. 370–379.

[54] Petty, C. A., 1975, "A Statistical Theory for Mass Transfer Near Interfaces," Chem. Eng. Sci., **30**, pp. 413–418.

[55] Churchill, S. W., and Usagi, R., 1972, "A General Expression for the Correlation of Rates of Transfer and Other Phenomena," AIChE J., **18**, pp. 1121–1127.

Laminar Flow and Heat Transfer in the Entrance Region of Trapezoidal Channels With Constant Wall Temperature

Metin Renksizbulut[1]
e-mail: metin@uwaterloo.ca

Hamid Niazmand

Mechanical Engineering Department,
University of Waterloo,
Waterloo, Ontario, Canada N2L 3G1

Simultaneously developing three-dimensional laminar flow and heat transfer in the entrance region of trapezoidal channels have been investigated using numerical methods in the Reynolds number range from 10 to 1000. The principal and secondary velocity fields, the temperature field, and all associated heat and momentum exchange parameters have been examined. The present results for the fully developed flow region of the channels compare well with the available literature. In the entrance region, it is observed that the axial velocity profiles develop overshoots near the walls and particularly at the channel corners. It is shown that boundary-layer type of approximations, which lead to Reynolds-number-independent Poiseuille and Nusselt numbers, can be used for Reynolds numbers over 50 and after a few hydraulic diameters from the channel inlet. It is also shown that hydrodynamic entrance lengths calculated with methods based on fully developed flow data are grossly in error. New correlations are proposed for the entrance length, and for the friction and heat transfer coefficients. [DOI: 10.1115/1.2130405]

Keywords: trapezoidal channel, entrance region, friction factor, heat transfer coefficient

1 Introduction

Laminar flow and heat transfer in channels of arbitrary cross section have received considerable attention over the years due to their obvious practical importance. Shah and London [1] and Shah and Bhatti [2] have provided comprehensive reviews of a large number of these studies. In recent years, advances in manufacturing technologies, coupled with a drive toward MEMS, have renewed interest in laminar flows in relatively short channels with irregular cross sections. For short channels, the entrance region where the velocity and temperature profiles undergo rapid transformations from essentially uniform inlet profiles to fully developed parabolic profiles is of paramount importance. In the entrance region, an analytical solution of the problem is not feasible due to the nonlinear inertia terms in the momentum equations. Boundary-layer assumptions provide major simplifications and have been used extensively. In one of the earliest studies, Schiller [3] analyzed the hydrodynamic entrance region of a tube by radially patching the boundary layer velocity profile near the wall with an inviscid core. Schlichting [4,5] obtained approximate solutions using perturbation techniques and the idea of patching the Blasius boundary layer solution with a perturbed fully developed velocity profile in the axial direction. Both methods have received subsequent refinements; see, for example, Schmidt and Zeldin [6] for details.

An alternative approach in the analytical formulation of the problem is the linearization of the inertia terms of the Navier-Stokes equations. Assuming constant pressure over a given cross section and neglecting axial diffusion, Langhaar [7] developed an analytical solution for the entrance length of a circular duct. Similarly, Han [8] obtained an analytical solution for the three-dimensional (3D) flow in the entrance region of a rectangular duct. Comparable methodology was employed by Lundgren et al. [9] to predict the pressure drop in the entrance region of channels of arbitrary cross section. In recent years, numerical methods have been used extensively in the investigation of the hydrodynamic entrance problem. Yet, in many cases the boundary-layer approximations have been applied to the governing equations to reduce the computational effort (e.g., [10–13]).

Momentum and heat transfer processes in the entrance region of noncircular channels are relatively complex and, surprisingly, have not been studied in depth despite their importance to some practical engineering devices. For example, short channels with a variety of trapezoidal cross sections are commonly encountered in modern compact heat exchangers. Mini- and microfluidic devices, such as sensors, actuators, pumps, etc., all involve transport phenomena in short channels with relatively complex geometries.

In the present work, the focus is on trapezoidal channels (Fig. 1). Fully developed laminar flows in trapezoidal ducts were analyzed in considerable detail by Shah [14]. A discrete least square method was employed to develop series solutions for the velocity and temperature fields. Friction factors and Nusselt numbers for different side angles and aspect ratios were calculated. More recently, Flockhart and Dhariwal [15] used the same technique along with an experimental investigation to study pressure drop in microscale trapezoidal ducts with hydraulic diameters of $50-120\ \mu$m. The microchannels were fabricated by an etching technique resulting in trapezoidal cross sections with side angles of $\phi=54.74$ deg (silicon substrate). It was concluded that a formulation based on the conventional no-slip boundary conditions (no velocity slip, no temperature jump) adequately predicts the experimentally observed flow characteristics. Sadasivam et al. [16] also considered laminar fully developed flows through single- and double-trapezoidal (hexagonal) channels using a finite-difference method. Solutions for the velocity and temperature fields were obtained for a wide range of duct aspect ratios and side angles. Recently, Morini [17] numerically analyzed fully developed flows in rectangular and trapezoidal microchannels. However, for the latter, only one side angle ($\phi=54.74$ deg) was considered. The calculated friction coefficients for a wide range of channel aspect ratios are shown to agree well with available data.

[1]Corresponding author.

Contributed by the Heat Transfer Division of ASME for publication in the JOURNAL OF HEAT TRANSFER. Manuscript received February 22, 2005; final manuscript received July 14, 2005. Review conducted by Anthony M. Jacobi.

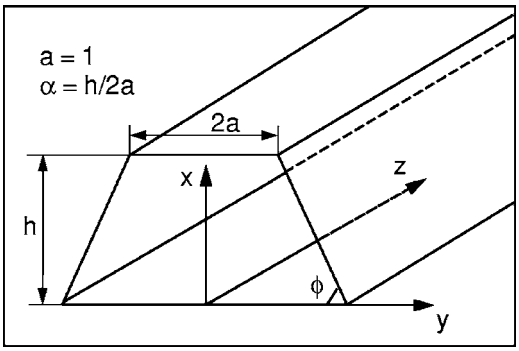

Fig. 1 Flow geometry and the coordinate system

The literature discussed thus far addresses thermally and hydrodynamically fully developed laminar flows. Under these conditions, the governing equations basically reduce to two Poisson equations, where, in many cases, analytical solutions can be found. However, much less information is available for developing flows. Lawal and Mujumdar [18,19]. studied the 3D laminar incompressible flow of a power-law fluid in ducts. They neglected molecular diffusion in the principal flow direction and decoupled the transverse and longitudinal pressure gradients. A variation of Patankar and Spalding's [20] marching procedure (as proposed by Briley [21] for this type of parabolic problems) was adopted to predict the heat transfer coefficient and pressure drop in square, trapezoidal, and pentagonal ducts. Asako and Faghri [11] and Asako et al. [12] also employed the numerical scheme of Patankar and Spalding [20] together with a coordinate transformation to map the irregular cross section onto a rectangular domain to study the entrance region of polygonal and rhombic ducts. Friction and heat transfer coefficients were obtained for boundary conditions of uniform heat flux and uniform temperature at the walls.

Farhanieh and Sunden [22] numerically studied the problem of simultaneously developing fluid flow and heat transfer in the entrance region of trapezoidal ducts. A finite volume formulation was used, and calculations were carried out with a uniform wall temperature for several channel aspect ratios and side angles. The secondary flow development, and the axial variation of the friction and heat transfer coefficients were examined in detail. However, the axial development of the flow field with its distinct overshoot feature was not addressed. One of the interesting features of the flow development from a uniform inlet velocity profile is the emergence of overshoots in the axial velocity profile such that the maximum local velocity occurs near the walls as opposed to the channel core. This effect is a function of Reynolds number and becomes more pronounced at higher Re. Furthermore, the effects of Reynolds number on the key flow parameters were not studied. It should be noted that the flow development becomes independent of Reynolds number only when boundary-layer type of approximations are adopted (axial diffusion and cross-flow pressure gradients ignored). Finally, no information regarding the entrance length was provided.

In the present work, the momentum and energy equations for 3D laminar flows in the entrance region of trapezoidal channels are solved using a control-volume-based numerical method in the Reynolds number range from 10 to 1000. Different channel side angles and aspect ratios are considered, and the results are discussed in detail. Practical engineering correlations for the entrance length, friction factor, and heat transfer coefficient are also provided. It is worth emphasizing that, in the present study, molecular diffusion of heat and momentum in the principal flow direction are included in the analysis. As indicated earlier, a parabolic treatment for the governing equations has been common practice to simplify the computational process, and therefore, most of the available literature is restricted to high Reynolds number flows. Performing calculations to obtain an estimate of the compromising accuracy associated with such an approximation is of its own value and interest.

2 Problem Formulation

The coordinate system and basic geometric variables that describe a trapezoidal channel are shown in Fig. 1. The aspect ratio and the side angle are denoted by $\alpha = h/2a$ and ϕ, respectively, where h is the channel height and a is the half-length of the top wall. The principal flow is in the z direction, and since the flow field is symmetric with respect to the x-z plane, solution is required only for half of the cross-sectional area. The laminar constant-property viscous flow under study is governed by the usual continuity, momentum, and energy equations as follows:

$$\vec{\nabla}\cdot\vec{V} = 0 \tag{1}$$

$$\rho\frac{D\vec{V}}{Dt} = -\nabla p + \mu\nabla^2\vec{V} \tag{2}$$

$$\rho c_p\frac{DT}{Dt} = k\nabla^2 T \tag{3}$$

where $\vec{V}$ is the velocity vector, T is temperature, ρ is density, p is pressure, μ is dynamic viscosity, c_p is specific heat, and k is thermal conductivity.

Inflow boundary conditions correspond to a uniform flat velocity profile such that $u=v=0$, and $w=W_i$, with a uniform inlet temperature $T=T_i$. For outflow, zero gradients along the axial flow direction are applied to all variables, $\partial f/\partial z=0$, where $f=u,v,w,T$. The channel walls are uniformly at a temperature of T_w, where the flow satisfies the no-slip boundary condition, $u=v=w=0$. Since the problem under study is considered as a mass-driven flow, the pressure is set equal to zero at the outlet, while zero gradients are assigned at all other boundaries including the inlet.

The Reynolds number $\mathrm{Re}=\rho W_i D_h/\mu$ is based on the uniform inlet velocity and the hydraulic diameter D_h defined as four times the cross-sectional flow area over the wetted perimeter. It is also specified that $\mathrm{Pr}=k/c_p\mu=1$, where Pr is the Prandtl number.

3 Solution Method

The numerical methodology is based on a transformation of the governing equations into a generalized nonorthogonal coordinate system. The equations are solved using a projectionlike method originated by Chorin [23] and developed further by Dwyer [24] and the authors. The velocity components are first calculated from the momentum equations using an alternating-direction predictor-corrector scheme based on the pressure field at the previous time step. Then the pressure correction is calculated from an equation designed to satisfy conservation of mass directly. This pressure correction equation is a Poisson-type equation solved with a matrix-free and preconditioned version of GMRES (generalized minimal residual) algorithm [25]. This method is capable of enhancing the convergence rate of the Poisson solver as compared to the traditional successive-overrelaxation solvers. Typical slow convergence of the pressure fields in duct flows is largely caused by the high aspect ratios of the computational cells that result from the flow geometry.

Further enhancement in convergence rate of the solution procedure can be achieved by implementing a pressure correction based on the average velocity defect $\Delta w'$ at each cross section of the channel such that $\Delta w' = \overline{W} - W_i$, where $\overline{W}$ is the average velocity at a given cross section and W_i is the average inlet velocity. Assuming that the local velocity defect is associated with a pressure defect, the following equation can be formed:

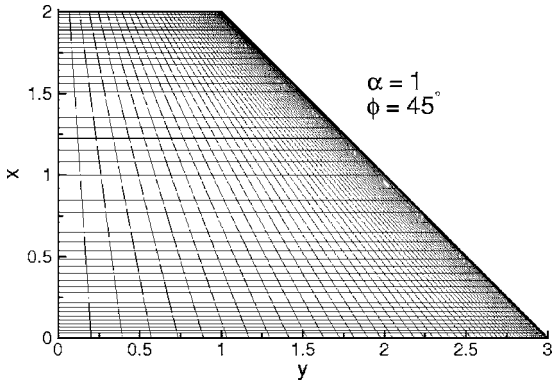

Fig. 2 Grid distribution in the *xy* plane

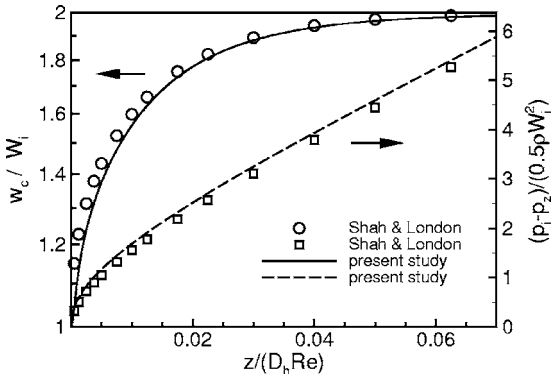

Fig. 4 Centerline velocity and pressure drop in pipe flow

$$\rho\frac{\Delta w'}{\Delta t} = -\frac{\partial p'}{\partial z} \tag{4}$$

Thus, the pressure field is updated with the above correction, and the momentum equations are solved again with the new pressure field. This procedure dramatically improves the computational efficiency [26].

Figure 2 shows a typical grid distribution used in the present work. The grid points are clustered near the channel walls and in the entrance region where large gradients exist. The effect of grid resolution on numerical accuracy was studied by performing computations at Re=100 for a channel with ϕ=45 deg, and the results are given in Table 1 and Fig. 3. Table 1 shows that the variation in the fully developed friction factor is <1% for the last three grids, and Fig. 3 shows that a grid density of 121 provides satisfactory resolution in the axial direction. Therefore, a mesh size of 51 $\times$51$\times$121 (x,y,z) was chosen with an expansion ratio of 1.06 in all directions. However, the grid density in the y direction was increased to 61 with an expansion ratio of 1.07 for α=2 to maintain the accuracy. For a given geometry, the axial extent of the computation domain was set to a minimum of twice the entrance length estimated based on the prevailing Re, which ensures that fully developed conditions are reached well before the channel exit.

Extensive code validation studies have been conducted for benchmark flows through circular and rectangular ducts. Because of space limitations, only two examples are presented here. Figure 4 shows a comparison of pressure drop and centerline velocity with data from Shah and London [1] for pipe flow. The results show reasonably good agreement. The small discrepancy between the velocity results close to the inlet can be attributed to the fact that their data are based on some linearization in the numerical scheme, which prevents the solution from predicting the velocity overshoots near the pipe wall. Such velocity overshoots close to the wall lead to lower velocities in the central region due to conservation of mass.

Figure 5 compares the calculated pressure drop in the main flow direction of a square duct with the experimental results of Beavers et al. [27]. The experimental data are provided for Reynolds numbers in the range 651<Re<1858. Present calculation at Re =1500 shows a reasonably good agreement with the experimental data. The numerical results of Han [8], and Wiginton and Dalton [28] are also included in the same figure for comparison. Furthermore, in Tables 2 and 3, different flow parameters and heat transfer rates for fully developed flow in trapezoidal ducts with various side angles and aspect ratios are compared to those of Shah and London [1]. The overall agreement is found to be very satisfactory, such that the differences are typically <1.5%.

Table 1 Grid size effect on fully developed $Po_{fd}=(fRe)_{fd}$ at different aspect ratios for trapezoidal duct with ϕ=45 deg

Grid points	$\alpha=0.5$	$\alpha=1$	$\alpha=2$
21 × 21 × 121	-	12.967	-
31 × 31 × 121	-	13.389	-
41 × 41 × 121	-	13.592	-
51 × 51 × 121	15.000	13.706	13.364
51 × 61 × 121	15.068	13.756	13.417
61 × 61 × 121	15.069	13.776	13.425
Farhanieh et al. [22]	15.145	13.782	13.307
Shah and London [1]	15.206	13.827	13.364

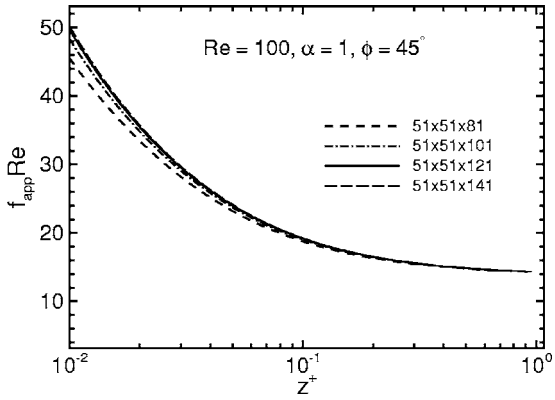

Fig. 3 Axial grid resolution

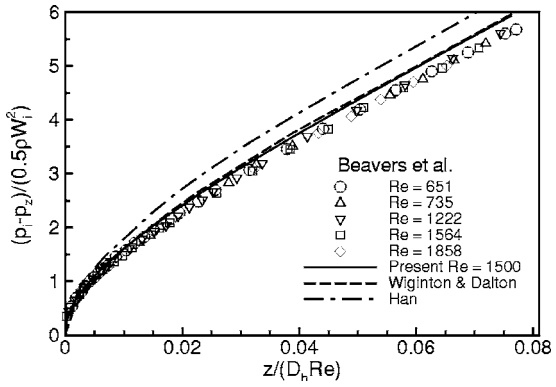

Fig. 5 Axial pressure distribution in a square duct

Table 2 Comparison of fully developed flow parameters for trapezoidal channels at different aspect ratios and side angles with Shah and London [1]

	W_{max}/W_i		$(fRe)_{fd}$		$K(\infty)$		$K_d(\infty)$		$K_e(\infty)$	
ϕ	Present	S &L	Present	S &L	Present	S &L	Present	S &L	Present	S &L
					$\alpha = 0.5$					
30	2.076	2.073	14.158	14.323	1.634	1.651	1.398	1.404	2.215	2.229
45	1.994	1.998	15.000	15.206	1.434	1.464	1.358	1.367	2.075	2.099
60	1.962	1.969	15.473	15.693	1.344	1.379	1.339	1.349	2.011	2.039
90	1.981	1.992	15.362	15.548	1.343	1.383	1.337	1.347	2.008	2.039
					$\alpha = 1$					
30	2.263	2.266	13.192	13.246	1.940	1.969	1.450	1.457	2.420	2.442
45	2.159	2.169	13.756	13.827	1.704	1.744	1.407	1.418	2.259	2.290
60	2.106	2.119	14.103	14.151	1.577	1.618	1.382	1.392	2.171	2.201
90	2.076	2.096	14.294	14.227	1.500	1.552	1.366	1.378	2.116	2.154
					$\alpha = 2$					
30	2.336	2.352	12.904	12.875	2.071	2.115	1.471	1.482	2.506	2.540
45	2.220	2.232	13.417	13.364	1.811	1.847	1.426	1.434	2.331	2.358
60	2.147	2.162	13.893	13.804	1.647	1.687	1.395	1.404	2.218	2.248
90	1.981	1.992	15.362	15.548	1.343	1.383	1.336	1.347	2.008	2.039

4 Results and Discussion

It is beneficial to start with the global features of the flow development in the entrance region by considering the velocity fields at different axial locations along the channel. In the fully developed region, nonaxial velocity components are zero and pressure is uniform over a given cross section. However, in the entrance region, the flow is three-dimensional with a nonuniform pressure field at each cross section. Figures 6(*a*)–6(*c*) show the velocity vectors and pressure contours at three axial planes ($z^+ = 5.21\times10^{-5}, 6.83\times10^{-4}, 1.50\times10^{-3}$) in a trapezoidal channel with $\phi=30$ deg and $\alpha=1$ at a Reynolds number of 100. The nondimensional axial length is defined as $z^+=z/(D_h\mathrm{Re})$, and $\rho W_i^2/2$ is used to normalize the pressure.

In Fig. 6(*a*), which is very close to the inlet, a strong secondary flow has formed toward the core of the channel. This flow is the result of large pressure gradients that develop near the walls because of the no-slip boundary condition coupled with the prescribed uniform inlet velocity profile. Note that pressure is maximum locally just inside the acute side angle ϕ. Farther downstream (Fig. 6(*b*)), the flow is more developed in the core of the channel; however, there are still large pressure gradients near the walls. The flow field shown in Fig. 6(*c*) is at a plane closer to the fully developed region as evidenced by the much weaker pressure variation over the cross section: $\Delta p = p_{\max} - p_{\min} = 3$ as compared to $\Delta p = 21$ in Fig. 6(*a*).

Strong pressure gradients that exist near the walls not only force the flow toward the core of the channel but also push the fluid near the walls in the axial direction. As shown in Fig. 7, this process causes the maximum velocities to be found near the walls rather than the channel core as would normally be expected. These unexpected velocity overshoots have been observed by other researchers as well (e.g., [1,29]). It should be noted that, in order to capture this phenomenon, it is necessary to include both the axial diffusion and transverse pressure gradients in the analysis. The velocity profiles in Fig. 7 appear to be symmetric with respect to the centerline of the cross section; however, for flows in channels with higher aspect ratios or larger side angles, asymmetry is clearer.

Velocity overshoots are more pronounced near the corners of channels because the pressure gradients are the highest at these locations. For example, in a trapezoidal duct, the region of the acute side angle contains the strongest overshoot, as clearly seen in Fig. 8. In this figure, the 3D axial velocity profiles at four axial locations are shown for the same geometry and Re as those in Figs. 5 and 6. The velocity contours in Figs. 8(*a*)–8(*c*) show

Table 3 Comparison of the fully developed Nu at different aspect ratios and side angle $\phi=90$ deg.

α	Present study	Aparecido & Cotta [33]	Shah & London [1]
0.1	5.967	5.930	5.911
0.25	4.456	4.440	4.439
0.5	3.403	3.392	3.391
1	3.033	2.978	2.976

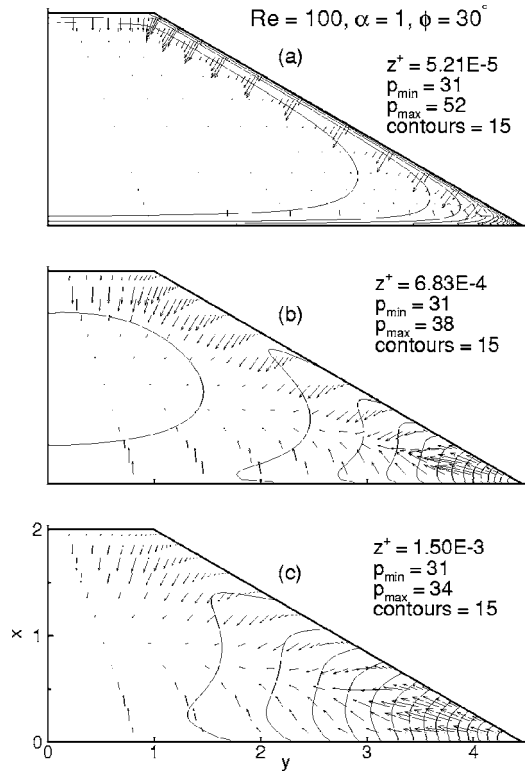

Fig. 6 Velocity vectors and pressure contours in the *xy* plane at three axial locations: (*a*) $z^+=5.21\times10^{-5}$, (*b*) $z^+=6.83\times10^{-4}$, and (*c*) $z^+=1.50\times10^{-3}$

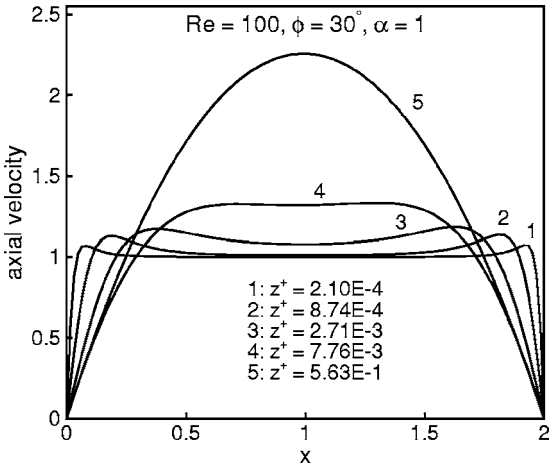

Fig. 7 Axial velocity profiles along the $y=0$ plane

clearly that the highest axial velocities are located in the side-angle region. The slight reduction in axial velocity in the core of the channel, observed in Fig. 8(*a*) very close to the inlet, is simply due to conservation of mass. Another feature of the velocity profiles in Figs. 8(*a*) and 8(*b*) is the presence of very large velocity gradients near the walls, resulting in correspondingly large friction coefficients early in the entrance region. Figure 8(*d*) shows the fully developed velocity profile. Very low velocities and gradients in the acute angle region are the notable features in this figure.

Channels with other aspect ratios and side angles develop similar flow patterns in the entrance region. Even in the limiting case of rectangular cross sections as the side angle becomes 90 deg, the maximum velocities occur in the corner regions. An example is given in Fig. 9 for a square duct.

In the following, the effects of ϕ and α on the flow patterns and on the key engineering parameters (friction factor and heat transfer coefficient) will be discussed. Furthermore, axial variations of flow parameters, such as the momentum rate and kinetic energy (both closely associated with the flow development in the entrance region), are examined. Four side angles ($\phi=30,45,60,90$ deg) and three aspect ratios ($\alpha=0.5,1,2$) will be considered. The Reynolds number associated with all cases discussed in this section is 100. The effects of Re on the flow features will be discussed later.

One of the key parameters of interest in the entrance region is the pressure drop in the principal flow direction. The present analysis indicates pressure variations in both the axial and the transverse directions in the entrance region. The transverse pressure distribution is a function of axial location and Reynolds number. As the flow approaches the fully developed region, the pressure variations in the transverse direction diminish and a uniform pressure over a given cross section is attained for all Reynolds numbers. Because of the presence of transverse pressure variations in the entrance region, a local mean pressure $\overline{p}$ is defined as

$$\overline{p} = \sum p_i dA_i / A \tag{5}$$

where p_i is the local pressure at each point on the cross-sectional plane, dA_i is the area of the associated control volume face, and A is the cross-sectional area of the channel. The nondimensional pressure drop along the channel is traditionally expressed in the form of an apparent friction factor defined as

$$\frac{\Delta\overline{p}}{\rho W_i^2/2} = \frac{4z}{D_h} f_{\text{app}} = 4z^+ f_{\text{app}}\text{Re} = 4z^+\text{Po}_{\text{app}} \tag{6}$$

where $\Delta\overline{p}$ indicates the pressure drop from the entrance, that is from $z=0$, and Po is the Poiseuille number.

In Fig. 10, the variation of f_{app}Re is shown at Re=100 for a trapezoidal channel with $\phi=45$ deg and three different aspect ratios. For the case with $\alpha=1$, the circumferentially averaged local skin friction factor $f\text{Re}=\text{Re}\tau_w/(\rho W_i^2/2)$ is also included for comparison. Unlike the fully developed region where the pressure drop is only due to the friction at the wall, in the developing region the change in momentum rate accounts for a major part of the pressure drop, as clearly seen in Fig. 10. Obviously, the apparent friction factor approaches the skin friction factor as the flow becomes fully developed. Figure 10 also shows that decreasing the aspect ratio from 2 to 1 has a minor effect on the $(f\text{Re})_{fd}$, but decreasing α further to 0.5 results in an increase of about 12% in $(f\text{Re})_{fd}$. This can be explained by considering the fact that, for

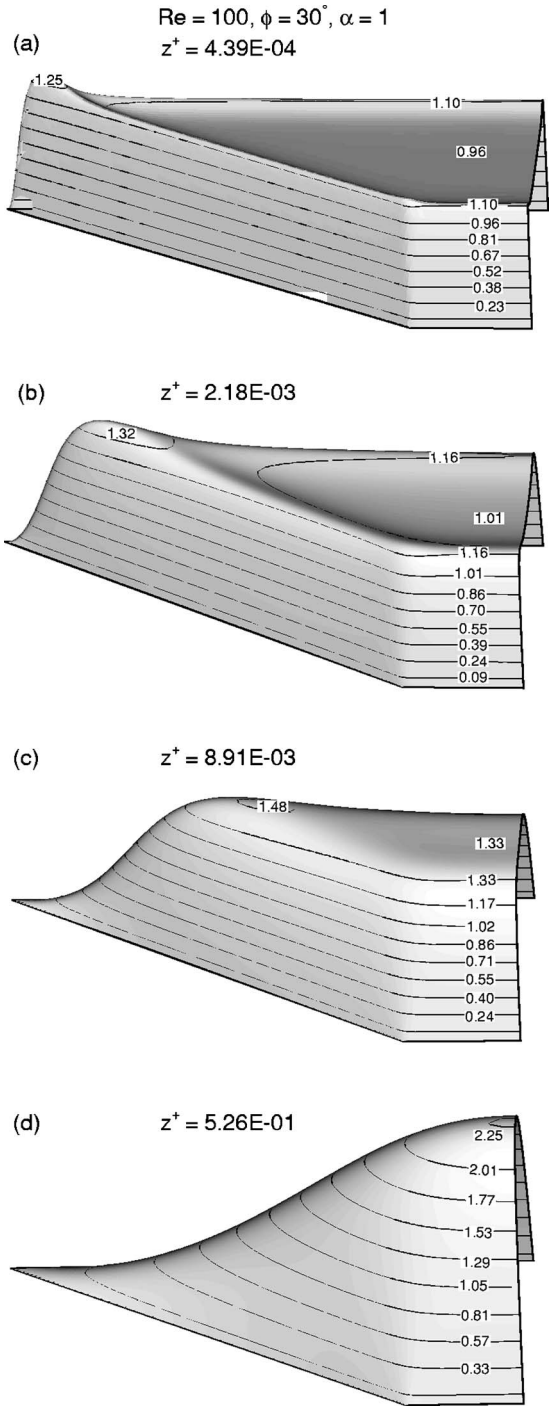

Fig. 8 Three-dimensional velocity profiles at four axial locations: (*a*) $z^+=4.39\times10^{-4}$, (*b*) $z^+=2.18\times10^{-3}$, (*c*) $z^+=8.91\times10^{-3}$, and (*d*) $z^+=5.26\times10^{-1}$

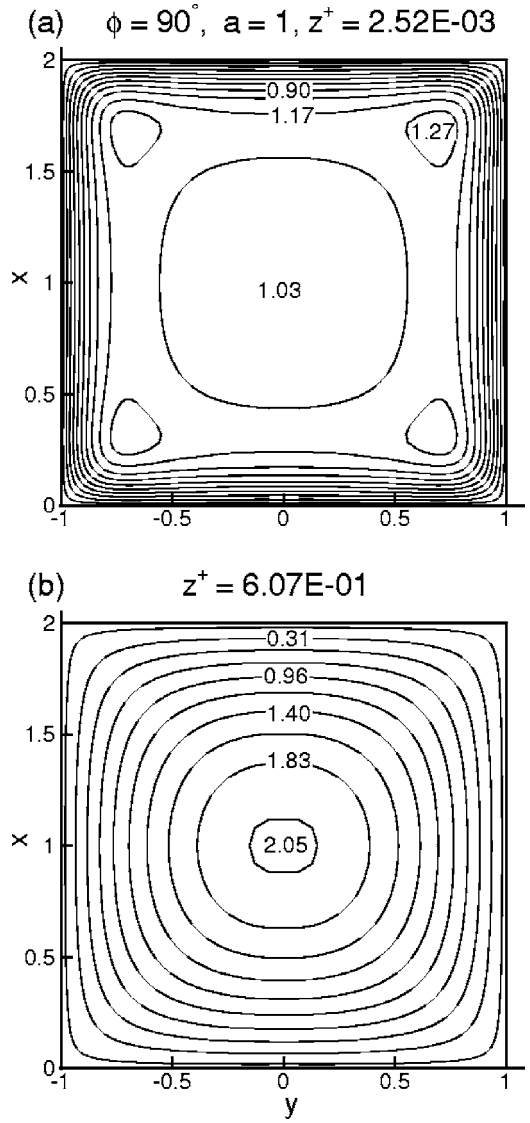

Fig. 9 Velocity contours for a square channel at two axial locations: (*a*) entrance region $z^+=2.52\times10^{-3}$ and (*b*) fully developed region $z^+=6.07\times10^{-1}$

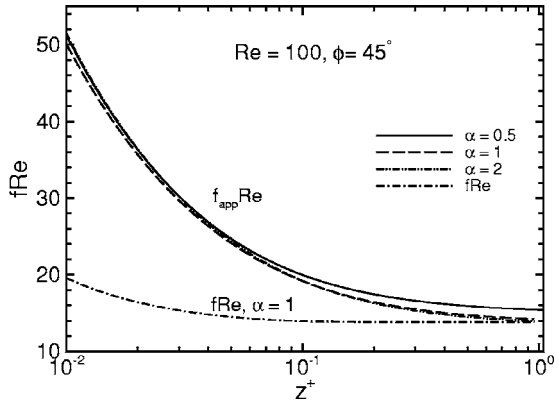

Fig. 10 Variation of apparent friction factor along the axial direction for different aspect ratios

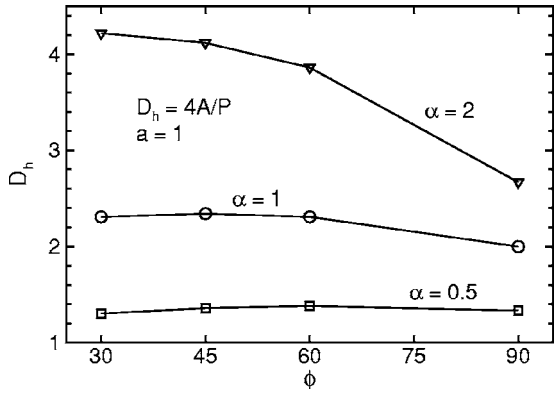

Fig. 11 Variation of hydraulic diameter (arbitrary units) with channel aspect ratio and side angle

a given ϕ, the hydraulic diameter increases significantly with increasing aspect ratio, as shown in Fig. 11. At a given Re, this leads to a higher inlet velocity in a channel with lower aspect ratio and, therefore, higher friction factor.

In Fig. 12, the variation of the apparent friction factor along channels having the same aspect ratio ($\alpha=1$) but different side angles is shown. It appears that the apparent friction factor is a weak function of ϕ for side angles >45 deg. However, at lower side angles, friction is higher in the region closer to the channel inlet but lower in the fully developed region. For clarity, consider a comparison of the $\phi=30$ deg and $\phi=90$ deg cases. As discussed earlier in relation to Fig. 8, near the channel inlet, the maximum axial velocity is located within the side-angle region (Figs. 8(*a*) and 8(*b*)). The pressure drop required to transform this velocity profile to a fully developed one (Fig. 8(*d*)) is higher than that for a channel with $\phi=90$ deg, where the velocity profile undergoes a smoother evolution. However, the fully developed value of the friction factor for $\phi=30$ deg is lower due to a higher D_h as explained before (Fig. 11).

Momentum rate and kinetic energy are also of importance in the entrance region since they are both closely related to the development of the flow field. The momentum rate in the main flow direction is given by $K_d\rho W_i^2 A$, where $K_d(z)$ is a momentum flux correction factor defined as [1]

$$K_d = \frac{1}{A}\int_A (w/W_i)^2 dA \tag{7}$$

Similarly, the kinetic energy of the fluid in the main flow direction is given by $K_e\rho W_i^3 A/2$, where $K_e(z)$ is a kinetic energy correction factor defined as

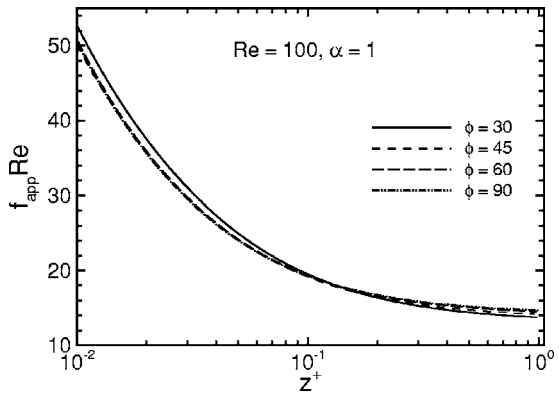

Fig. 12 Variation of apparent friction factor in the flow direction for different side angles

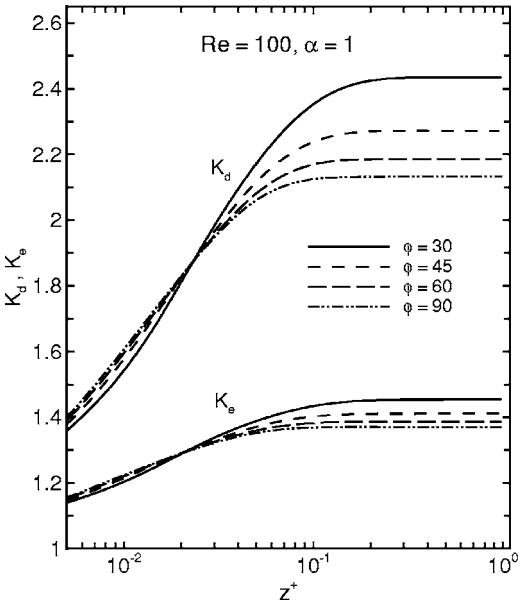

Fig. 13 Variations of the momentum flux and kinetic energy correction factors along the axial flow direction for different side angles

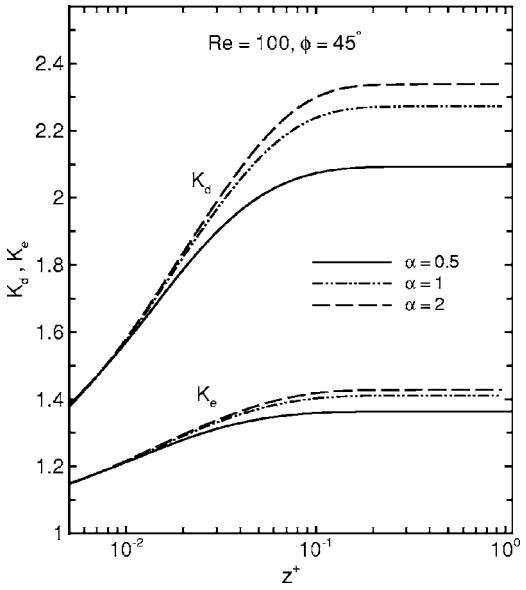

Fig. 14 Variations of the momentum flux and kinetic energy correction factors along the axial flow direction for different aspect ratios

$$K_e = \frac{1}{A}\int_A (w/W_i)^3 dA \tag{8}$$

Figure 13 shows the variations of $K_d(z)$ and $K_e(z)$ at Re=100 for a channel with $\alpha=1$ and different side angles ϕ. For a uniform inlet velocity profile, K_d and K_e are expected to increase monotonically from unity at $z=0$ to their asymptotic values, $K_d(\infty)$ and $K_e(\infty)$, in the fully developed region. The asymptotic trend observed in this figure is consistent with the fact that maximum velocities increase with decreasing ϕ at a fixed channel aspect ratio (see Table 2). However, near the inlet, this trend is reversed. As it is apparent from Eqs. (7) and (8), the deviations in K_d and K_e from unity are dependent on the amount of flow area over which $w/W_i > 1$, and near the inlet, higher velocities are found close to the walls and particularly in the side angle region.

Figure 14 shows the variations of the $K_d(z)$ and $K_e(z)$ in the flow direction for a given side angle, $\phi=45$ deg, while the aspect ratio is varied. In the fully developed region, Table 2 shows that the maximum velocity increases as the aspect ratio increases, and therefore, it is expected that the asymptotic values of K_d and K_e follow the same trend. However, K_d and K_e in the inlet region are not noticeably affected by aspect ratio changes because, near the inlet, the velocity profile development is only weakly dependent on α.

An approximate analytical method has been developed by Shah and London [1] to determine the incremental pressure drop in the fully developed region, $K(\infty)$, for ducts of arbitrary cross section using $K_d(\infty)$ and $K_e(\infty)$ such that

$$K(\infty) = 2[K_e(\infty) - K_d(\infty)] \tag{9}$$

For long ducts, total pressure drop can then be estimated based on the knowledge of fully developed friction factor and $K(\infty)$ using

$$\frac{P_o - P_L}{\rho W_i^2/2} = (f\mathrm{Re})_{fd}\frac{4L}{D_h\mathrm{Re}} + K(\infty) \tag{10}$$

where P_o is the inlet pressure and P_L is the pressure at a distance L from the inlet. In Table 2, the calculated $K(\infty)$ are listed for different aspect ratios and side angles, which show good agreement with the results of Shah and London [1].

4.1 Thermal Entrance Region. Simlar to velocity, nondimensional fluid temperature, $\theta=(T_w-T)/(T_w-T_m)$, undergoes a continuous variation from the prescribed uniform inlet value $\theta=1$ to a fully developed profile such that $\partial\theta/\partial z=0$. Here, T_w is the specified constant wall temperature, and $T_m(z)$ is the mean fluid temperature. Figures 15(*a*)–15(*d*) show the 3D temprature contours at four different axial locations corresponding to the velocity profiles in Figs. 8(*a*)–8(*d*). Each figure identifies ten isotherms uniformly distributed between the minimum temperature at the wall and the maximum temperature at that location.

Similar to the velocity profile, close to the inlet at $z^+=4.39\times10^{-4}$ in Fig. 15(*a*), the temperature profile also shows strong gradients near the walls, whereas the central region of the cross section is almost unaffected by the wall temperature. Obviously, unlike the velocity profile, which develops overshoots near the walls and especially within the side angle area (see Fig. 8(*a*)), overshoots cannot appear in the temperature profile. Under the assumption of constant wall temperature, $(T_w > T_i)$, and negligible viscous dissipation, heat can only diffuse from the wall toward the center of each cross section with the maximum temperature at the wall. Clearly, velocity overshoots near the walls close to the inlet lead to the higher temperature gradients near the walls. In Fig. 15(*b*) at the axial location $z^+=2.18\times10^{-3}$, the temperature around the central region is nearly uniform, yet, higher than that in Fig. 15(*a*), with still high temperature gradients close to the wall regions all around the cross section. Closer to the fully developed region at the axial location of $z^+=8.91\times10^{-3}$ in Fig. 14(*c*), the temperature profile varies smoothly from $\theta=0$ at the wall to its maximum of about $\theta=1.42$ in the core. In the fully developed region in Fig. 15(*d*), the uniform wall temperature extends around the side angle areas and the temperature gradients have moved to the central part of the cross section as compared to the temperature profiles closer to the inlet (Figs. 15(*a*) and 15(*b*)). This rather large area of almost zero temperature gradient around each side angle accounts for the major reduction in the heat transfer rate for this geometry as compared to the heat transfer rates for larger side angles, where the temperature gradients extend more into the side angle regions.

Despite the constant wall temperature, the heat transfer rate is

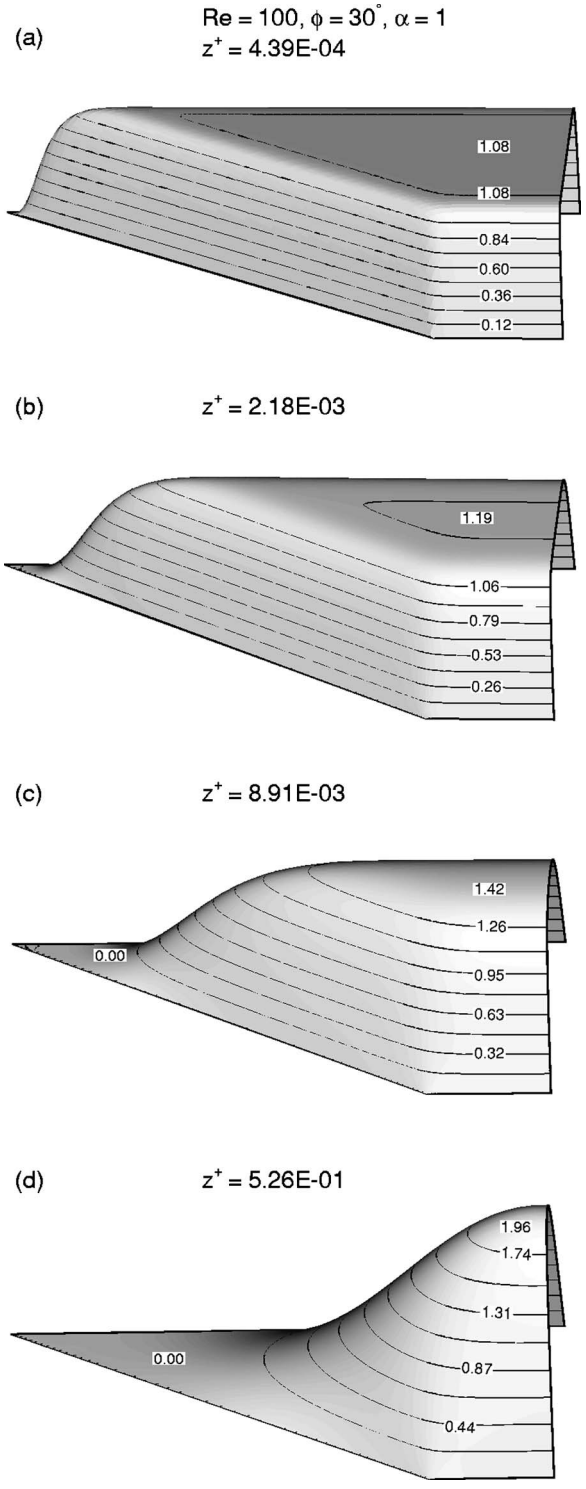

Fig. 15 Three-dimensional temperature profiles at four axial locations: (*a*) $z^+=4.39\times10^{-4}$, (*b*) $z^+=2.18\times10^{-3}$, (*c*) $z^+=8.91\times10^{-3}$, and (*d*) $z^+=5.26\times10^{-1}$

neither peripherally nor axially constant in the entrance region. The circumferentially averaged local heat transfer coefficient or the local Nusselt number is defined as

$$\mathrm{Nu}_z = \frac{h_z D_h}{k} = \frac{D_h[\overline{(\partial T/\partial n)_w}]_z}{T_w - T_m} \tag{11}$$

where $\overline{(\partial T/\partial n)_w}$ is the peripherally averaged temperature gradient at the wall at any axial location, and $T_m(z)$ is the mean fluid temperature defined as

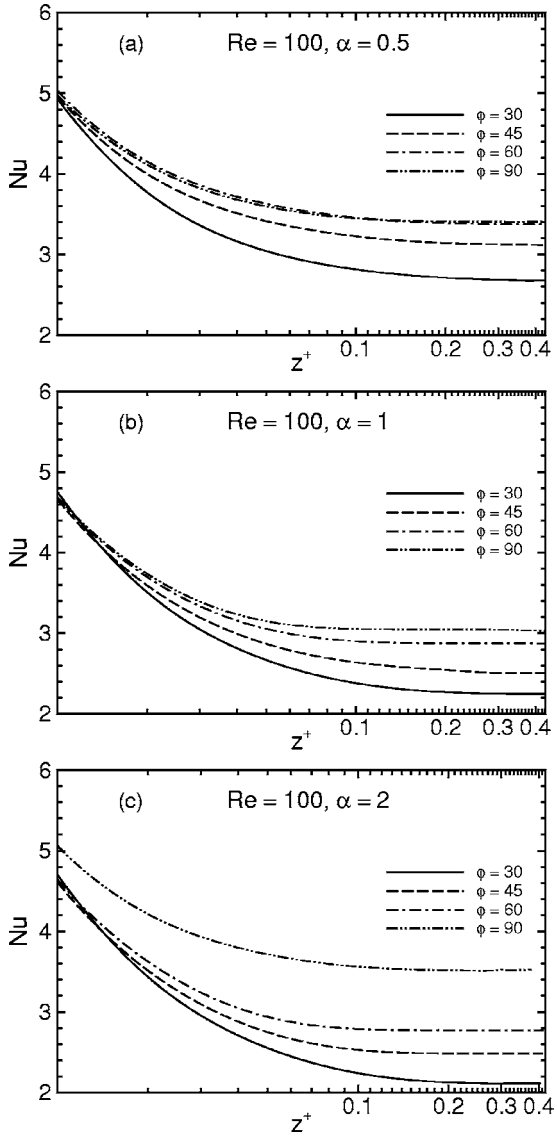

Fig. 16 Variation of Nusselt number in the main flow direction for different side angles and three aspect ratios: (*a*) $\alpha=0.5$, (*b*) $\alpha=1$, and (*c*) $\alpha=2$

$$T_m = \frac{1}{AW_i}\int_A T\vec{V}\cdot\vec{n}dA \tag{12}$$

In the present work, Pr=1 in all cases considered, and therefore, the nondimensional axial length $z_T^+=z/(D_h\mathrm{RePr})$ or the reciprocal Graetz number (commonly encountered in problems of this type) is the same as z^+ defined earlier.

The variations in the heat transfer rate along the main flow direction for channels with three different aspect ratios are shown in Figs. 16(*a*)–16(*c*) for various side angles. It is interesting to note that close to the inlet where strong temperature gradients develop very close to the wall (see Figs. 15(*a*) and 15(*b*)), the Nusselt number is almost independent of ϕ. However, as the fully developed region is approached and the temperature profile develops throughout the cross section, the geometry plays an important role on the heat transfer rates. In this region, the effect of the side angle on Nu is particularly strong, such that increasing ϕ for a given aspect ratio leads to substantial increases in Nu. On the other hand, heat transfer rates decrease with increasing aspect ratio at fixed ϕ.

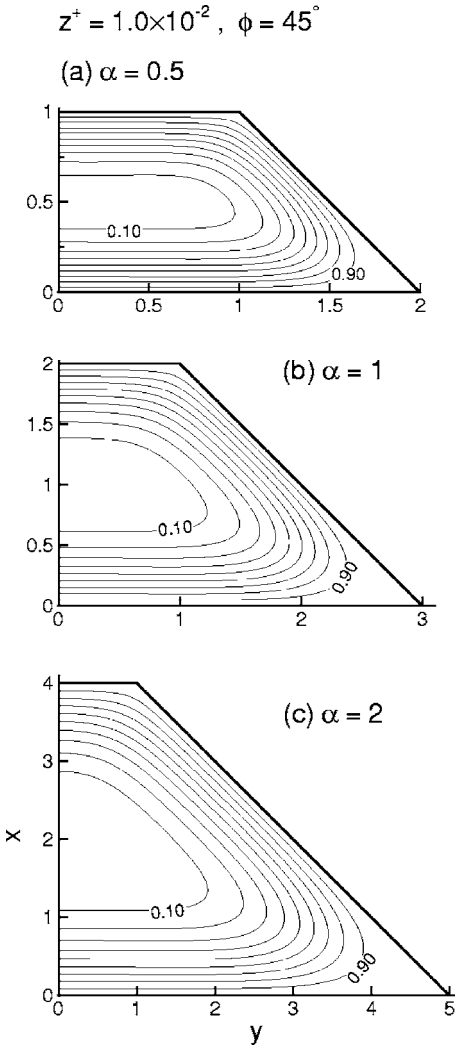

Fig. 17 Isotherms for various aspect ratios at axial location $z^+=1\times10^{-2}$ for flow at Re=100 and ϕ=45 deg: (*a*) α=0.5, (*b*) α=1, and (*c*) α=2

Since the geometry of the channel is the same for $\alpha=0.5$ and $\alpha=2$ when $\phi=90$ deg, the corresponding axial variations in Nu are the same in Figs. 16(*a*) and 16(*c*). Therefore, their comparison to those of other side angles presents a measure of the reduction in the heat transfer rates due to an increase in aspect ratio. In addition, comparison of isotherms at different aspect ratios can provide some insight about its effects on the heat transfer rates. Figures 17(*a*)–17(*c*) show a set of identical isotherms in a cross section located at $z^+=0.01$ for $\phi=45$ deg with three different aspect ratios. Clearly, the temperature gradients next to to the channel walls are stronger for cross sections with smaller aspect ratios. Also, note that the region in the vicinity of the side angle is very poor in heat transfer due to the presence of weak temperature gradients. For a given aspect ratio, this region extends in size as the side angle is reduced and causes substantial reductions in heat transfer as indicated earlier in Fig. 15(*d*).

In Table 3, the fully developed values Nu for rectangular ducts are compared to published results [1,33] for different α, and good agreement is observed.

4.2 Effects of Reynolds Number. In developing channel flows, the apparent friction factor is a function of duct geometry, boundary conditions, Reynolds number, and axial position. For heat transfer, the Prandtl number of the fluid also plays an important role. However, the present work is limited to Pr=1, which is appropriate for gases. It should be noted that the flow development becomes independent of the Reynolds number if boundary-layer type of assumptions (axial diffusion and cross flow pressure gradients ignored) are adopted, which was done in most of the prior studies of the current problem.

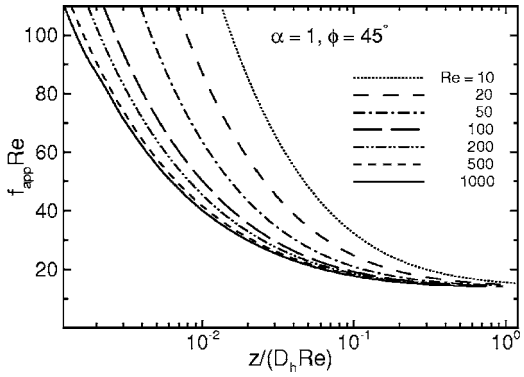

Fig. 18 Axial variation of the apparent friction factor with Reynolds number

Figures 18 and 19 show the axial variations of $Po=f_{app}Re$ and Nu as a function of Re for a trapezoidal channel with $\alpha=1$ and $\phi=45$ deg. Clearly, the values of Po and Nu in the entrance region are much larger than those in the fully developed region, which highlights the critical importance of the entrance region in determining the fluid flow and heat transfer characteristics of short channels found in many modern miniaturized devices. Figures 18 and 19 indicate that close to the inlet where the axial gradients are considerable, the effects of Re cannot be ignored. As expected, the effects of Re extend to higher axial positions at lower Re as axial diffusion gains more weight. These figures also show that the effects of Re become small only for z^+ over 0.05 and Re over 50, approximately. Although not shown here, similar trends are observed in other channel geometries.

4.3 The Entrance Length. Starting with a uniform velocity profile at the channel inlet, the hydrodynamic entrance length L is defined as the axial location where maximum velocity attains 99% of its fully developed value. In one of the earlier studies, McComas [30] developed the following entrance length correlation, which employs data associated with the fully developed region such that

$$L^+ = \frac{L}{D_h \mathrm{Re}} = \frac{(W_{\max}/W_i)^2 - 1 - K(\infty)}{4(f\mathrm{Re})_{fd}} \tag{13}$$

In Table 4, L^+ values for trapezoidal ducts with different aspect ratios and side angles are given for Re=100. Entrance lengths

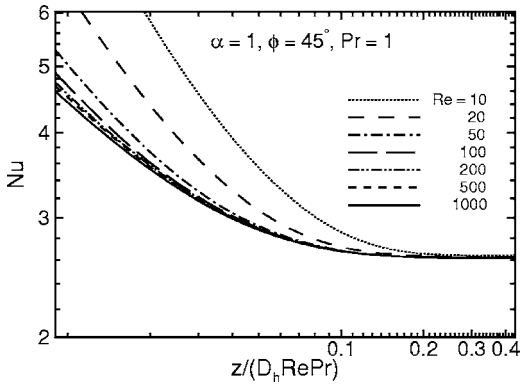

Fig. 19 Axial variation of Nusselt number with Reynolds number

Table 4 Variation of the entrance length L^+, for trapezoidal ducts with different aspect ratios and side angles at Re=100

α	ϕ	Present study	McComas (Eq.13)
0.5	30	0.133	0.0296
0.5	45	0.108	0.0257
0.5	60	0.095	0.0243
0.5	90	0.085	0.0257
1	30	0.155	0.0413
1	45	0.113	0.0356
1	60	0.088	0.0329
1	90	0.078	0.0316
2	30	0.154	0.0462
2	45	0.114	0.0394
2	60	0.088	0.0353
2	90	0.085	0.0257

calculated using Eq. (13) are also tabulated, which are almost identical with the results provided by Shah [14] using the same correlation. It is seen that in all cases, L^+ predictions based on the McComas correlation are about three times smaller than the values obtained in the present work. It should also be noted that this correlation does not yield accurate results for rectangular ducts either. For example, $L^+=0.0255$ calculated by Shah [14] using Eq. (13) for a rectangular duct with $\alpha=0.5$ is much smaller than $L^+=0.085$ calculated by Wiginton and Dalton [31] and also in the present work (see Table 4). Clearly, the McComas correlation is highly inaccurate and should not be used for entrance-length determination.

Present data in Table 4 indicates that the entrance length is a relatively weak function of the aspect ratio for a specified side angle ϕ. However, for a given aspect ratio, the entrance length increases substantially with decreasing ϕ because vorticity generated at the walls must then spread into a larger flow area before fully developed conditions can be attained.

In Table 5, the effects of Re on the entrance length are shown for a duct with $\alpha=1$ and $\phi=45$ deg. As expected, the entrance length increases substantially with increasing Reynolds number from $L\cong 1.7D_h$ at Re=10 to $11D_h$ at Re=100, and $55D_h$ at Re=500. However, consistent with the results of the previous section, the L^+ approaches essentially a constant value as Re increases beyond 100.

5 Correlations

For fully developed flows, the friction and heat transfer coefficients are functions of the duct geometry and Reynolds number. The present correlation for the friction factor, Eq. (14), is developed based on available data for sides angles $\phi=30,45,60,90$ deg and covers the full range of aspect ratios ranging from $\alpha=0$ for parallel plates to $\alpha\to\infty$ for ducts with triangular cross sections. Data for geometries not considered in the present study are taken from Shah and London [1]. Equation (14) predicts available data within ±3% as shown in Fig. 20.

Table 5 Variation of the entrance length L^+, for a trapezoidal duct with $\alpha=1$ and $\phi=45$ deg as a function of Re

Re	10	20	50	100	200	500	1000
L^+	0.167	0.128	0.117	0.113	0.111	0.109	0.109

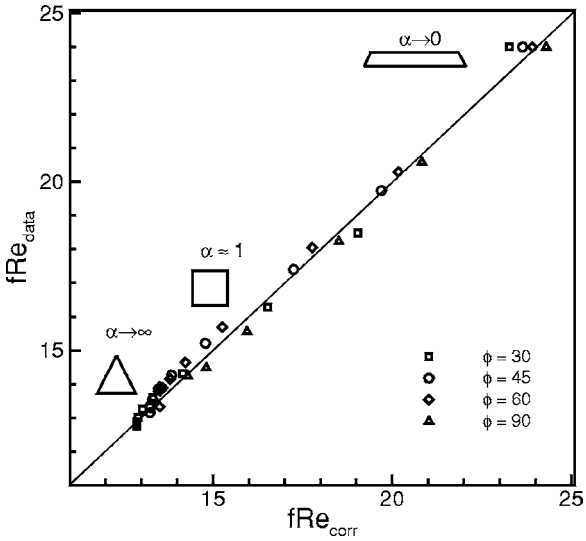

Fig. 20 Comparison of available data to the proposed friction coefficient correlation

$$(f\mathrm{Re})_{fd}=13.9\left(\frac{90^\circ}{\phi}\right)^{-0.07}+10.4\exp\left[-3.25\alpha\left(\frac{90^\circ}{\phi}\right)^{0.23}\right] \tag{14}$$

Concerning the aspect ratio α, it should be noted that flows in rectangular ducts ($\phi=90$ deg) are invariant to a 90 deg rotation of the cross section; that is, a channel with the reciprocal aspect ratio has exactly the same flow features. This ambiguity is overcome simply by defining α as the ratio of the short side to the long side of the duct, and thus, the aspect ratio (for rectangular channels only) always remains in the range $0\leqslant\alpha\leqslant 1$.

In heat transfer, the Reynolds number dependence is more pronounced at low Re, where axial conduction in the fluid cannot be readily ignored. The relative importance of axial conduction was examined by Pahor and Strnad [32] for flow between parallel plates with constant wall temperatures. They showed that axial conduction increases the heat transfer coefficient such that Nu $\to 8.117$ for Pe$\ll$1, which represents a significant increase as compared to the other asymptotic limit of Nu=7.541 for high Pe flows. This effect has been incorporated into the proposed heat transfer correlation given below for the range $0.1\leqslant\mathrm{Re}\leqslant 1000$. Available heat transfers data for the same side angles and aspect ratios as those of Eq. (14) are correlated with Eq. (15) within ±8% as shown in Fig. 21.

$$(\mathrm{Nu})_{fd}=\left[2.87\left(\frac{90^\circ}{\phi}\right)^{-0.26}+4.8\exp\left(-3.9\alpha\left(\frac{90^\circ}{\phi}\right)^{0.21}\right)\right]G \tag{15}$$

$$G=[1+0.075(1+\alpha)\exp(-0.45\mathrm{Re})] \tag{16}$$

Finally, the entrance lengths calculated in the present study are correlated with Eq. (17) as shown in Fig. 22. With this correlation, data for the same side angles as above but for a limited range of aspect ratios ($0.5\leqslant\alpha\leqslant 2$) are predicted within ±15% for $10\leqslant\mathrm{Re}\leqslant 1000$

$$\frac{L}{D_h}=\left[0.085\mathrm{Re}+\frac{0.8}{\mathrm{Re}^{0.3}}\right]\left[\left(\frac{90^\circ}{\phi}\right)^{0.6}\right][(1+\alpha)^{-0.24}] \tag{17}$$

6 Conclusions

Simultaneously developing 3D laminar flow and heat transfer in the entrance region of trapezoidal channels have been studied for $10\leqslant\mathrm{Re}\leqslant 1000$ and Pr=1. Because of the existence of high shear

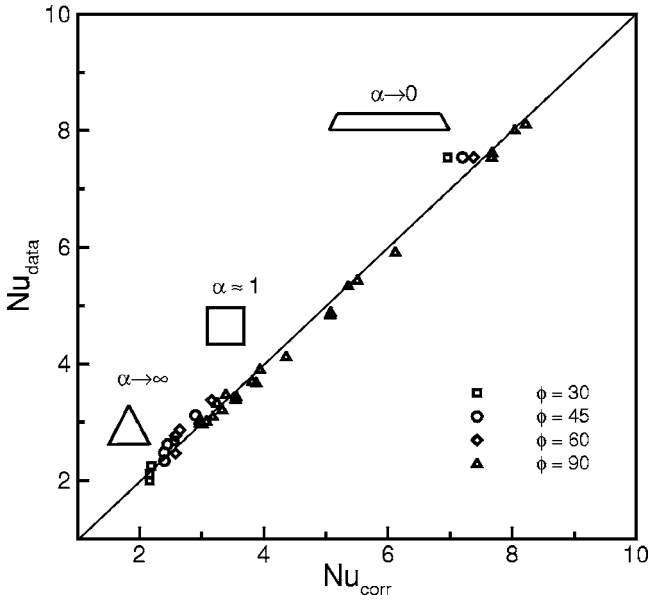

Fig. 21 Comparison of available data to the proposed heat transfer coefficient correlation

and heat transfer rates, the entrance region is particularly important for short channels. One of the interesting features of the flow development from a uniform profile at the inlet is the emergence of velocity overshoots, such that maximum axial velocities appear near the walls and especially in the corners as opposed to the channel core, which become more pronounced with decreasing side angle ϕ. Viscous dissipation has been ignored in the present work, and the walls are maintained at constant temperature; therefore, similar overshoots cannot develop in the temperature profiles.

Boundary-layer-type approximations are not valid close to the inlet. However, for Reynolds numbers over 50, and several hydraulic diameters away from the inlet, the behavior of the key flow parameters, such as the Poiseuille and Nusselt numbers, become practically independent of Re, which indicates that diffusion in the axial direction can be ignored.

Hydrodynamic entrance length is a function of both Re and geometry. For a trapezoidal cross section, the geometric effects

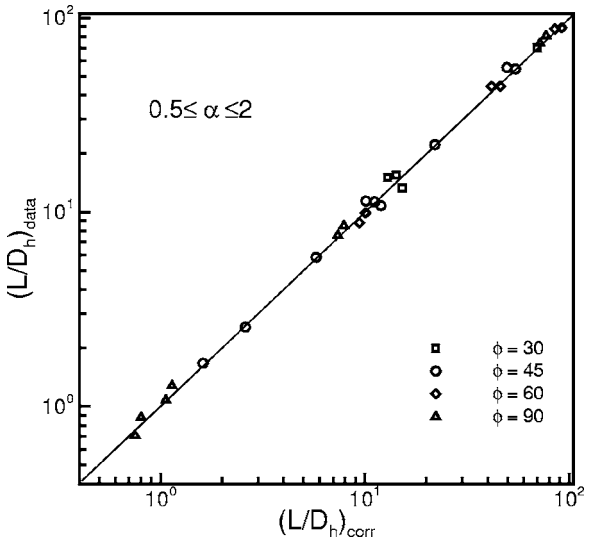

Fig. 22 Comparison of the numerical data to the proposed entrance length correlation

are such that larger aspect ratios or smaller side angles both result in longer distances from the walls to the core of the channel. Therefore, the vorticity diffusion time is increased, which leads to longer entrance lengths. Furthermore, approximate methods based on data associated with the fully developed region of the channel fail to predict the entrance length properly for trapezoidal ducts.

Based on the present solutions of the full 3D governing equations, new engineering correlations are proposed for the entrance length, as well as the friction and heat transfer coefficients for trapezoidal channels.

Acknowledgment

This work was made possible through the financial support of the Natural Sciences and Engineering Research Council of Canada.

References

[1] Shah, R. K., and London, A. L., 1978, *Laminar Flow Forced Convection in Ducts*, Academic Press, New York.
[2] Shah, R. K., and Bhatti, M. S., 1987, "Laminar Convective Heat Transfer in Ducts," *Handbook of Single-Phase Convective Heat Transfer*, S. Kakac, R. K. Shah, and W. Aung, eds., Wiley, New York, Chap. 3.
[3] Schiller, L., 1922, "Die Entwicklung der Laminaren Geschwindigkeitsverteilung und Ihre Bedeutung fur Zahigkeitsmessungen," Z. Angew. Math. Mech., **2**, pp. 96–106.
[4] Schlichting, H., 1934, "Laminare Kanaleinlaufstromung," Z. Angew. Math. Mech., **14**, pp. 368–373.
[5] Schlichting, H., 1968, *Boundary-Layer Theory*, 6th English Edition, McGraw-Hill, New York, pp. 176–177.
[6] Schmidt, F. W., and Zeldin, B., 1969, "Laminar Flows in Inlet Section of Tubs and Ducts," AIChE J., **15**(4), pp. 612–614.
[7] Langhaar, H. L., 1942, "Steady Flow in the Transition Length of a Straight Tube," ASME J. Appl. Mech., **9**, pp. A55–A58.
[8] Han, L. S., 1960, "Hydrodynamic Entrance Lengths for Incompressible Laminar Flow in Rectangular Ducts," ASME J. Appl. Mech., **27**, pp. 403–409.
[9] Lundgren, T. S., Sparrow, E. M., and Starr, J. B., 1964, "Pressure Drop due to the Entrance Region in Ducts of Arbitrary Cross-Section," ASME J. Basic Eng., **86**, pp. 620–626.
[10] Prakash, C., and Liu, Ye-Di., 1983, "Analysis of Laminar Flow and Heat Transfer in the Entrance Region of an Internally Finned Circular Duct," ASME J. Heat Transfer, **107**, pp. 84–91.
[11] Asako, Y., and Faghri, M., 1988, "Developing Laminar Flow and Heat Transfer in the Entrance Region of Regular Polygonal Ducts," Int. J. Heat Mass Transfer, **31**, pp. 2590–2593.
[12] Asako, Y., Nakamura, M., and Faghri, M., 1988, "Three-Dimensional Laminar Heat Transfer and Fluid Flow Characteristics in the Entrance Region of a Rhombic Duct," ASME J. Heat Transfer, **110**, pp. 855–861.
[13] Hwang, G. J., Cheng, Y. C., and Ng, M. L., 1993, "Developing Laminar Flow and Heat Transfer in a Square Duct With One-Walled Injection and Suction," Int. J. Heat Mass Transfer, **36**(9), pp. 2429–2440.
[14] Shah, R. K., 1975, "Laminar Flow Friction and Forced Convection Heat Transfer in Ducts of Arbitrary Geometry," Int. J. Heat Mass Transfer, **18**, pp. 849–862.
[15] Flockhart, S. M., and Dhariwal, R. S., 1998, "Experimental and Numerical Investigation Into the Flow Characteristics of Channels Etched in ⟨100⟩ Silicon," ASME J. Fluids Eng., **120**, pp. 291–295.
[16] Sadasivam, R., Manglik, R. M., and Jog, M. A., 1999, "Fully Developed Force Convection Through Trapezoidal and Hexagonal Ducts," Int. J. Heat Mass Transfer, **42**, pp. 4321–4331.
[17] Morini, G. L., 2004, "Laminar to Turbulent Flow Transition in Microchannels," Microscale Thermophys. Eng., **8**, pp. 15–30.
[18] Lawal, A., and Mujumdar, A. S., 1984, "Forced Convection Heat Transfer to a Power-Law Fluid in Arbitrary Cross-Section Ducts," Can. J. Chem. Eng., **62**, pp. 326–333.
[19] Lawal, A., and Mujumdar, A. S., 1985, "Developing Flow and Heat Transfer to Power-Law Fluids in Square, Trapezoidal and Pentagonal Ducts," Int. Commun. Heat Mass Transfer, **12**, pp. 23–31.
[20] Patankar, S. V., and Spalding, D. B., 1971, "A Calculation Procedure for Heat, Mass and Momentum Transfer in Three-Dimensional Parabolic Flows," Int. J. Heat Mass Transfer, **15**, pp. 1787–1806.
[21] Briley, W. R., 1974, "Numerical Methods for Predicting Three-Dimensional Steady Viscous Flow in Ducts," J. Comput. Phys., **14**, pp. 8–28.
[22] Farhanieh, B., and Sunden, B., 1991, "Three-Dimensional Laminar Flow and Heat Transfer in the Entrance Region of Trapezoidal Ducts," Int. J. Numer. Methods Fluids, **13**, pp. 537–556.
[23] Chorin, H. A., 1968, "Numerical Solution of the Navier-Stokes Equations," Math. Comput., **22**, pp. 745–762.
[24] Dwyer, H. A., 1989, "Calculation of Droplet Dynamics in High Temperature Environments," Prog. Energy Combust. Sci., **15**, pp. 131–158.
[25] Wigton, L. B., Yu, N. J., and Young, D. P., 1985, "GMRES Acceleration of Computational Fluid Dynamics Codes," *AIAA Computational Fluid Dynamics*

Meeting, Cincinnati, pp. 67–74.
[26] Dwyer, H. A., Cheer, A. Y., Rutaganira, T., and Shacheraghi, N., 2001, "Calculation of Unsteady Flows in Curved Pipes," ASME J. Fluids Eng., **123**, pp. 869–877.
[27] Beavers, G. S., Sparrow, E. M., and Magnuson, R. A., 1970, "Experiments on Hydrodynamically Developing Flow in Rectangular Ducts of Arbitrary Aspect Ratio," Int. J. Heat Mass Transfer, **13**, pp. 689–720.
[28] Wiginton, C. L., and Dalton, C., 1968, "Incompressible Laminar Flow in the Entrance Region of a Rectangular Duct," *12th Int. Congr. Appl. Mech.*, Stanford University, Stanford, CA.
[29] Karniadakis, G. E., and Beskok, A., 2002, *Micro Flows, Fundamentals and Simulation*, Springer-Verlag, Berlin, Chap. 4.
[30] McComas, S. T., 1967, "Hydrodynamic Entrance Lengths for Ducts of Arbitrary Cross Section," ASME J. Basic Eng., **89**, pp. 847–850.
[31] Wiginton, C. L., and Dalton, C., 1970, "Incompressible Laminar Flow in the Entrance Region of a Rectangular Duct," ASME J. Appl. Mech., **43**, pp. 854–856.
[32] Pahor, S., and Strnad, J., 1961, "A Note on Heat Transfer in Laminar Flow Through a Gap," Appl. Sci. Res., Sect. A, **10**, pp. 81–84.
[33] Aparecido, J. B., and Cotta, R. M., 1990, "Thermally Developing Laminar Flow Inside Rectangular Ducts," Int. J. Heat Mass Transfer, **33**, pp. 341–347.

Thermal Conductivity Measurements of Ultra-Thin Single Crystal Silicon Layers

Wenjun Liu

Mehdi Asheghi

Mechanical Engineering Department,
Carnegie Mellon University,
Pittsburgh, PA 15213

Self-heating in deep submicron transistors (e.g., silicon-on-insulator and strained-Si) and thermal engineering of many nanoscale devices such as nanocalorimeters and high-density thermomechanical data storage are strongly influenced by thermal conduction in ultra-thin silicon layers. The lateral thermal conductivity of single-crystal silicon layers of thicknesses 20 and 100 nm *at temperatures between 30 and* 450 K *are measured using joule heating and electrical-resistance thermometry in suspended microfabricated structures. In general, a large reduction in thermal conductivity resulting from phonon-boundary scattering is observed. Thermal conductivity of the* 20 nm *thick silicon layer at room temperature is nearly* 22 W m^{-1} K^{-1}, *compared to the bulk value,* 148 W m^{-1} K^{-1}. *The predictions of the classical thermal conductivity theory that accounts for the reduced phonon mean free paths based on a solution of the Boltzmann transport equation along a layer agrees well with the experimental results.* [DOI: 10.1115/1.2130403]

Keywords: phonon rransport, silicon, heat transfer, measurement techniques, nanoscale, ultra-thin films

1 Introduction

Ultra-thin single-crystal silicon layers have been extensively used in the past decade for microfabrication of sensors, actuators, and transistors [1–4] as well as the fundamental study of electrical and thermal transport properties [5–10]. In recent years, the characteristic dimensions of these devices, in particular transistors [9–11], have been aggressively reduced to sub-100 nm and, therefore, more and more of them are made on silicon-on-insulator (SOI) wafers with device layers of thickness 10 to 100 nm. Self-heating and thermally induced reliability are pressing issues for advanced SOI, strained-silicon, strained Si-on-SiGe-on-insulator and strained silicon on insulator field effect transistors where the devices are separated from the silicon substrate by poor thermal conducting layers [9–17]. The lateral thermal conduction in thin silicon device layers somewhat reduces the maximum temperature rise in these transistors but its conductivity is significantly reduced due to the phonon-boundary scattering [7–10,14–17]. In addition, the thermal response times and sensitivities of miniaturized thermal analysis sensors [1], convection-based micromachined inclinometer [5], MicroElectro Mechanical Systems (MEMS) differential scanning nanocalorimeters [3], and microcantilevers for high-density thermomechanical data storage [4] are governed by lateral thermal conduction along the silicon layer. There have been limited experimental data available for lateral thermal conductivity of thin silicon layers of thickness near 1 μm, over the temperature range of 10 to 300 K [7,8], and for silicon layers of thickness 78, 100, and 200 nm at room temperature [10]. More recently, thermal conductivity of silicon nanotubes with diameters of 22, 37, 56, and 115 nm have been measured in the temperature range 20 to 300 K [18]. There are no experimental data available for silicon layers of thickness in the range of 20–100 nm, in particular, above the room temperature, which are more relevant for the thermal design of the deep submicron SOI and strained-Si transistors.

In this manuscript, we provide data and phonon transport analysis that quantify the impact of phonon-boundary scattering on heat conduction in single-crystalline silicon layers of thicknesses 20 and 100 nm over the temperature range of 20–450 K. Steady-state joule heating and electrical resistance thermometry were used to measure lateral thermal conductivity of the suspended silicon/metal structures. Analyses of the heat conduction mechanisms in suspended microstructures and uncertainty in measured thermal conductivity data are presented. In addition, limitations of the above thermal conductivity measurements technique for sub-20 nm thick silicon layers are investigated and presented in the Appendix.

2 Experimental Structure and Procedure

The experimental data are collected using the microfabricated suspended structure shown in Fig. 1. Steady-state joule heating and electrical resistance thermometry were used to measure lateral thermal conductivity of the suspended structure. For thermal characterization of doped silicon or metal bridges, joule heating is achieved by directly passing an electric current through the bridge. However, for the nearly pure silicon layer, which is not electrically conductive, deposition of an additional metal layer is required. Clearly, the metal layer can introduce some level of uncertainty in the thermal conductivity experimental data for silicon layer hence its thermal conductivity must be measured independently. Two identical silicon-based suspended structures, with [Fig. 1(*b*)] and without [Fig. 1(*c*)] silicon layers were fabricated using nearly similar fabrication processes. Thermal conductivity of the suspended metal (CoFe and aluminum) structures are measured independently and subsequently used to extract thermal conductivity of thin silicon layers of thicknesses 20 and 100 nm, respectively.

2.1 Microfabrication Processes. While the final structures for thermal conductivity measurements of the 20 nm and 100 nm thick silicon layers appear to be similar (Fig. 1), the microfabrication process for these two structures are somewhat different. For the reasons that will be fully discussed in Sec. 2.3, using CoFe (instead of aluminum) layer as the heating and thermometry element is preferred. In addition, the microfabrication process described in this section was slightly modified to eliminate the impact of variation in thickness of the metal layer on the measurements of the silicon layer thermal conductivity. Hereafter,

Contributed by the Heat Transfer Division of ASME for publication in the JOURNAL OF HEAT TRANSFER. Manuscript received March 6, 2004; final manuscript received June 24, 2005. Review conducted by: Gang Chen.

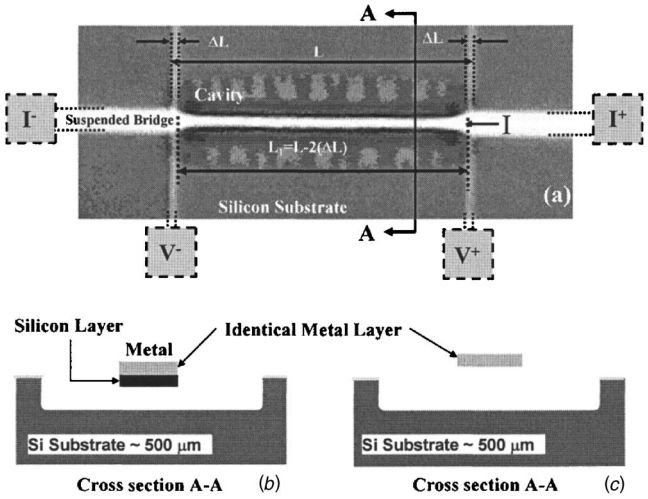

Fig. 1 (*a*) **The optical microscope image of the suspended structure. Cross sections of** (*b*) **the metal/silicon and** (*c*) **the metal (aluminum or CoFe) suspended structures, which are used to obtain the thermal conductivity data for silicon layer.**

the aluminum/silicon and CoFe/silicon suspended structures will be referred to as AS100 and CoFeS20 structures, respectively, and the corresponding microfabrication processes will be discussed in Secs. 2.1.1 and 2.1.2, respectively.

2.1.1 Microfabrication Process for the Aluminum/Silicon Suspended Structure (AS100). The starting material for microfabrication of the AS100 structure is a silicon-on-insulator (SOI) wafer with a 100 nm silicon device layer and 100 nm buried silicon dioxide layer. At the first step, silicon-dioxide layers of thickness 20 Å and 100 Å are thermally grown on wafers AS100 and A100, respectively [Fig. 2(*a*)], followed by sputtering 100 nm thick aluminum films that will be used both as a heater and thermometer in this measurements [Fig. 2(*b*)]. A 1 μm thick photoresist layer (Dupont 2556) is spun onto the wafers and developed [Fig. 2(*c*)], followed by an ion milling process to pattern silicon/aluminum structure and aluminum bridge on the AS100 and A100 wafers, respectively [Fig. 2(*d*)]. A 1 μm photoresist layer (Dupont 2556) is then spun onto the wafers and developed to define the regions on the silicon substrate that would be exposed for the subsequent isotropic reactive ion etching (RIE) process [Fig. 2(*e*)]. The (STS) machine is then used to undercut and release the aluminum/silicon and aluminum structures [Fig. 2(*f*)] followed by an ion milling process using oxygen ion coupled plasma (ICP) etcher to remove the photoresist from the suspended structures.

2.1.2 Microfabrication Process for the CoFe/Silicon Suspended Structure (CoFeS20). The starting material for microfabrication of the CoFeS20 structure is a silicon-on-insulator (SOI) wafer with a 20 nm silicon device layer and 144 nm buried silicon dioxide layer. A 20 Å thick thermal oxide layer is grown to provide electrical insulation between the silicon and CoFe layers [Fig. 3(*a*)]. As we discussed previously, certain measures were adopted to reduce the uncertainty in the measurements (due to nonuniformity in deposition of metal film) that required slight modifications in the microfabrication process. At this step, the silicon overlayer is etched away from half of the 4 in. SOI wafer [Fig. 3(*b*)], followed by sputtering 75 nm thick CoFe layer using a cvc connexion sputtering machine [Fig. 2(*d*)]. A 1 μm thick photoresist layer (Dupont 2556) is spun onto the wafers and developed [Fig. 2(*e*)], followed by an ion milling process to pattern silicon/CoFe structure and CoFe bridge [Fig. 2(*f*)]. A 1 μm photoresist layer (Dupont 2556) is then spun onto the wafers and developed to define the regions on the silicon substrate that would be exposed for the subsequent isotropic reactive ion etching (RIE) process [Fig. 2(*g*)]. The STS machine is then used to undercut and release the silicon/CoFe and CoFe structures [Fig. 2(*h*)] followed by an ion milling process to remove the photoresist from the suspended structures.

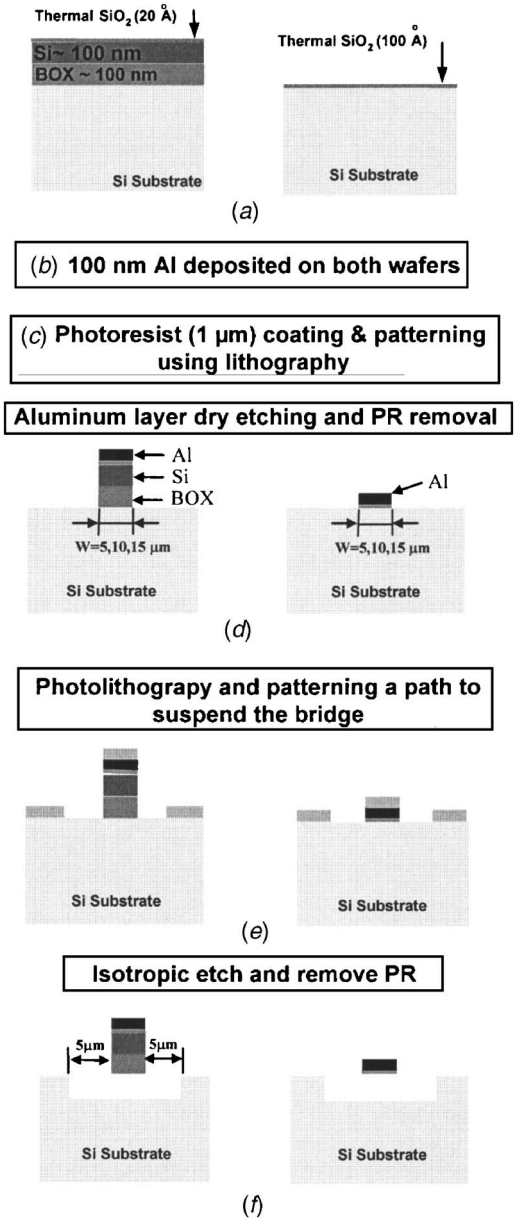

Fig. 2 Fabrication process of 100 nm silicon film

2.2 Experimental Setup and Procedure. The measurements were performed in a special model Janis ST-100 continuous flow cryostat that is capable of reaching vacuum levels on the order of 5×10^{-3} Torr. The dies were diced and separated from identical locations in the AS100 and A100 wafers. For the case of the CoFeS20 wafer, two neighboring dies at the center of the wafer with and without the CoFe metal layer were selected and diced. While the microfabrication process usually provides nearly identical film uniformity and quality over large distances, the above additional steps were also taken for further assurances. Before discussing the experimental procedure it is important to address an important issue or concern that may come to mind regarding the microfabricated suspended structures. It is clear from Fig. 1(*a*) that the width of the suspended bridge varies over its length and there was initially a concern that this might have been due to

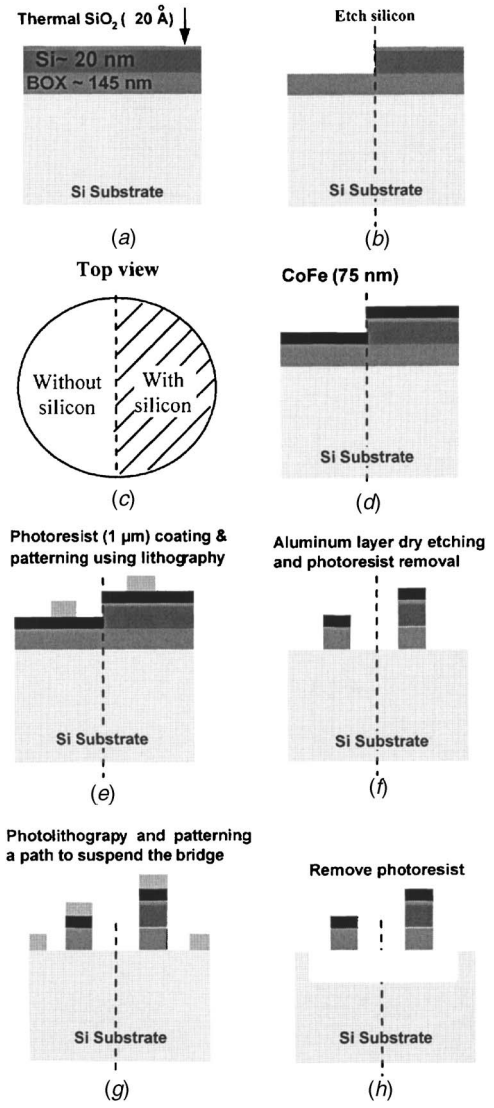

Fig. 3 Fabrication process of 20 nm silicon film

oxidization of the metal layer or the result of overetch during the surface micromachining process. This is an important factor which can directly impact the final experimental results. We resolved this matter by measuring and comparing the electrical resistivities of the suspended bridge [Fig. 2(*b*)] and an on-substrate section of the bridge, which shows no variations in width. The electrical resistances of the two structures were identical, which indicates the reduced dimension, as observed in Fig. 1(*a*), is probably due to bulging of the cantilever due to residual stress, not by oxidization/etch of the metal or silicon layer.

The dies were wire bonded in 68 pin Leadless Ceramic Chip (LCCs) chip carriers that provide electrical access to the suspended beams. The electrical resistances of the metal beam elements were measured using the four-probe measurement technique. The temperature dependency of the metal bridges electrical resistance was measured by changing the temperature of the chip carrier using a Lakeshore model 331S temperature controller (temperature stability: ±50 mK). The accuracy of the temperature sensor used for the calibration is about ±50 mK [19]. Steady-state joule heating and electrical resistance thermometry were used to measure the lateral thermal conductance of the suspended structures [20,21] in vacuum (5×10^{-3} Torr) to minimize conduction to the air. All of the volumetric heat generated in the aluminum film flows by conduction along the composite bridge structure toward the base and subsequently spreads out into the substrate. Therefore, heat transfer in the suspended structure may be assumed one dimensional along the structure. In addition, an analytical solution for heat conduction in the suspended bridge with uniform heat generation and surface heat losses due to radiation and molecular conduction was developed to quantitatively examine the effect of unwanted heat loss mechanisms from the bridge. Heat transfer analyses have shown that heat losses from the surface by both radiation and molecular gas conduction are negligible [9,20]. It can be shown that, assuming $\varepsilon=1$ and for the average temperature rise in the bridge in the order of 20°C–30°C above room temperature, the heat loss due to radiation can be neglected. In the present measurements, the average temperature rise in the bridge was kept well below 5°C. Surface heat loss being negligible was also verified experimentally as the thermal conductivity data for different bridge lengths and widths showed very little variations. An analysis of the spreading effect into the substrate was made and concluded that the base temperature can be assumed at T_0 for all practical purposes [20]. We also performed the necessary heat conduction analysis and confirmed that the portion of the beams that rest on the substrate can be assumed to have temperatures near T_0. The slight temperature rise on the order of 0.05°C, can be neglected compared to the average temperature rise in the beam, which is kept between 3°C–5°C. High resolution IR thermometry was also performed, which essentially verified the above analysis.

The governing equation for one-dimensional heat transfer in the metal (aluminum or CoFe) suspended bridge with negligible surface heat loss; and volumetric heat generation and the relevant boundary conditions are given as [20–22],

$$k_m(wd_m)\frac{d^2T}{dy^2}+I^2\frac{R_0}{L}[1+\alpha_m(T-T_0)]=0 \tag{1a}$$

$$T(y=\pm L/2)=T_0 \tag{1b}$$

where k_m is the lateral thermal conductivity of the metal film, α_m is the temperature coefficient of the electrical resistance, T_0 is the temperature of the substrate, I is the applied electrical current, and R_0 is the electrical resistance (at $T=T_0$) for the metal bridge. The dimensions w, d_m, and L are the width, thickness, and length of the metal bridge, respectively. The above equation also assumes that the ratio of the thermal resistance across (normal to) the thickness of the bridge, $R_{\perp,th}$, to the thermal resistance along (parallel to) the length $R_{\parallel,th}$, of the bridge is on the order of $\sim d_m/L$, which is much smaller than unity. This condition assures that the one-dimensional heat conduction assumption is indeed valid over the entire length of the bridge except, possibly, in the regions that are away from the base, by nearly $\sim d_m$. Let $\Theta=1+\alpha_m(T-T_0)$ in the equation and the boundary conditions, they reduce to,

$$\frac{d^2\Theta}{dy^2}+\gamma_m^2\Theta=0 \tag{2a}$$

$$\Theta(y=\pm L/2)=1 \tag{2b}$$

where $\gamma_m^2=I^2R_0\alpha_m/(wLd_mk_m)$. This equation can be solved to yield

$$\Theta(y)=\cos(\gamma_m y)/\cos(\gamma_m L/2) \tag{3a}$$

or

$$T(y)=T_0-\frac{1}{\alpha_m}\left(1-\frac{\cos(\gamma_m y)}{\cos(\gamma_m L/2)}\right) \tag{3b}$$

Integrating the above equation from $-L/2$ to $+L/2$, the average temperature of the bridge is given by

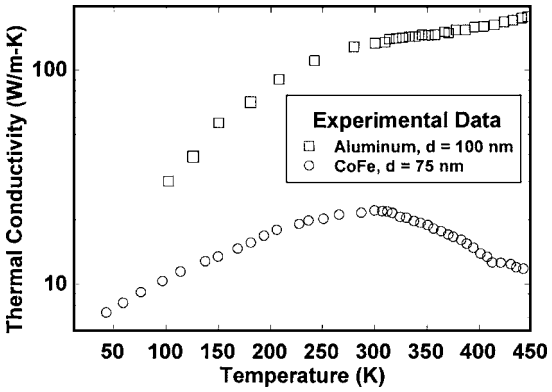

Fig. 4 Temperature dependent thermal conductivity data of the 100 nm thick aluminum and 75 nm CoFe layers as a function of temperature, which are subsequently used to obtain the thermal conductivity data for 100 nm and 20 nm thick silicon layers, respectively. The uncertainties in the data are less than 5%, which is on the order of size of the "symbols." As a result, the uncertainty bars are not shown in this plot.

$$\overline{T} = T_0 - \frac{1}{\alpha_m}[1 - (2/\gamma_m L)\tan(\gamma_m L/2)] \tag{4}$$

The average electrical resistance of the bridge under bias is, therefore, given by

$$\overline{R}_m = R_{0,m}[(2/\gamma_m L)\tan(\gamma_m L/2)] \tag{5}$$

The lateral thermal conductivity of the metal k_m can be obtained by the measured data using Eq. (5) for the electrical resistance.

There is also a slight underetch at the bases of the suspended beams $\Delta L \sim 4\ \mu\text{m} - 10\ \mu\text{m}$, which can cause some ambiguity in defining the thermal boundary conditions described by Eq. (1*b*) for the governing heat conduction equation given by Eq. (1*a*). We attempted to account for this via evaluating the average temperature of the bridge by integrating Eq. (3) from $(-L/2+\Delta L)$ to $(+L/2-\Delta L)$. This represents the length of the aluminum suspended bridge confined between the points of the voltage measurement Fig. 1(*a*).

The governing equation for one-dimensional heat transfer in the combined metal silicon [Fig. 1(*b*)] suspended bridge with volumetric heat generation in the metal film is very similar to Eq. (1*a*) and is given by

$$(k_m d_m + k_s d_s) w \frac{d^2T}{dy^2} + I^2 \frac{R_0}{L}[1 + \alpha_m (T - T_0)] = 0, \tag{6}$$

where d_s and k_s are the thickness and the thermal conductivity of the silicon layer, respectively. Equations (1*b*) through (5) are still valid except that the parameter γ_m^2 must now be replaced by $\gamma_{s,m}^2 = I^2 R_0 \alpha_m / [wL(k_m d_m + k_s d_s)]$. Therefore, the average electrical resistance of the silicon/metal bridge is given by

$$\overline{R}_{s,m} = R_{0,(s,m)}[(2/\gamma_{s,m} L)\tan(\gamma_{s,m} L/2)] \tag{7}$$

Given the measured thermal conductivity of the metal k_m the thermal conductivity of the silicon layer k_s can be obtained by comparing the measured electrical resistivity data and predictions of Eq. (7) for the electrical resistance.

A total number of three aluminum ($w=16\ \mu$m, $L=500\ \mu$m, and $w=20\ \mu$m, $L=300$, $500\ \mu$m) and three CoFe ($w=5$, $10\ \mu$m, $L=100\ \mu$m, and $w=15\ \mu$m, $L=200\ \mu$m) bridge structures were characterized. Experiments were conducted in vacuum and for a temperature range of 30 K to 450 K. Figure 4 shows the measured lateral thermal conductivities of the 100 nm thick aluminum and 75 nm thick CoFe layers. It becomes immediately clear that the thermal conductivity of the CoFe metal layer is by far smaller

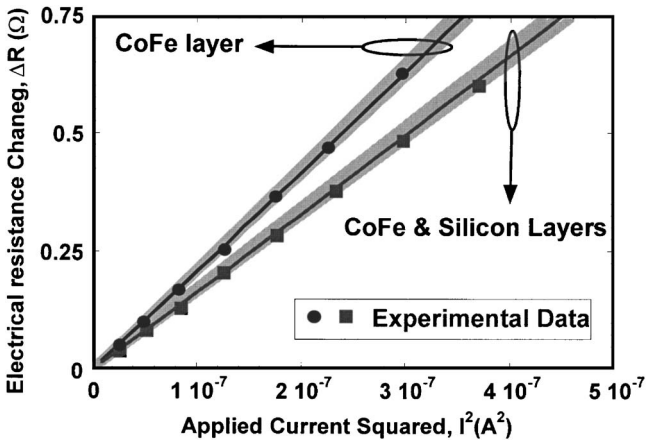

Fig. 5 Curve fits for thermal conductance along the length of the CoFe and CoFe+silicon suspended structures using Eqs. (5) and (7) to the electrical resistivity data at room temperature. The fitted thermal conductivity data for CoFe layer is subsequently used to extract the thermal conductivity of the 20 nm thick silicon layer. The uncertainties in the measured electrical resistivity data are less than 2%, which is on the order of size of "symbols." The gray shaded areas show the ±5% and ±7% variations in thermal conductance of the CoFe and CoFe +silicon structures based on the predictions of the Eqs. (5) and (7).

than that of the aluminum layer and therefore more suitable for the present thermal conductivity measurements. In particular, the fact that thermal conductivity of the CoFe film is reduced at higher temperatures, compared to the aluminum layer, has a strong impact on both the feasibility of the present measurements for ultrathin silicon layers and uncertainty of the results. This matter will be further examined in the following sections. The thermal conductivity data for aluminum and CoFe metal layers are subsequently used in Eq. (7) to extract the lateral thermal conductivities of the silicon film as a function of temperature from the combined aluminum/silicon or CoFe/silicon structures. Figure 5 shows a plot of the electrical resistances of the CoFe $\overline{R}_{\text{CoFe}}$, and CoFe/Silicon, structures as a function of the applied electrical current squared I^2. Given the thermal conductivity of the CoFe layer k_{CoFe}, the thermal conductivity of the silicon layer k_s can be obtained by comparing the measured electrical resistivity data and predictions of Eq. (7) for the electrical resistance. The applied currents were adjusted such that the average temperature rise did not exceed 3°C–5°C. While the increased current level would increase the sensitivity of the measurements, it would also adversely affect the measurements in three aspects. First, if the average temperature rise of the bridge exceeds 15°C–30°C, then the radiation loss from the suspended bridge become increasingly important. Since the emissivity of the structures has not been measured independently, then the radiation loss cannot be determined and properly accounted for. The elevated temperatures also imply that one should specifically account for both the temperature dependence of the thermal properties of the metal and silicon layers. This is due to the fact that Eq. (7) neglects the variation in thermal conductivities of the metal and silicon with temperature. For the case of CoFe/silicon structure, nonlinear behavior in the plots of $\overline{R}_{\text{CoFe}}$ versus I^2 was observed for excessive temperature rise of 20°C, for the measurements near room temperature. In addition, the metal bridges rapidly deteriorate at high current levels and small nonlinearity in the electrical resistivity versus temperature may cause significant error in the measurements.

2.3 Experimental Uncertainty. A careful consideration of the experimental uncertainty is not only important for the present measurements but also helps to understand the limitation of this

particular technique for thermal conductivity measurements of the sub-20 nm thick silicon layers. Equations (6) and (7) can be used to perform both the sensitivity and uncertainty analyses. Basically, the impact of variations in dimensions of the suspended structure Temperature Coefficient of Resistance (TCR) thickness of the silicon layer, and thickness and thermal conductivity of the metal layer on the thermal conductivity of the silicon layer can be investigated (see the Appendix). During the design of the mask, specific patterns were designed that allowed accurate measurements of the bridge widths, and lengths within ±1% of w and ±0.1% of L, respectively. The temperature coefficient of electrical resistances of aluminum and CoFe, is measured to be $\sim 1.0 \times 10^{-3}$ K^{-1} and 2.13×10^{-3} K^{-1} at 300 K with the estimated error of ±2%, which is due to the fact that the temperature sensor was slightly farther away from the LCC chip carrier. The measured currents and voltages are accurate within ±0.01% and ±0.1%, respectively. Uncertainty in the measured thermal conductivity and thickness of the metal layer are the major source of uncertainty in determination of the silicon layer thermal conductivity. Assuming that the thicknesses of the silicon and metal layers are roughly the same, the uncertainty of the measurements will be greater if the thermal conductivity of the metal layer is significantly larger than that of the silicon layer at a given temperature. For example, the thermal conductivity of the 100 nm thick aluminum layer is about three times larger than that of silicon, at room temperature. As a result, any uncertainty in thermal conductivity measurements of the metal layer (which could be the result of variations in thickness of the metal) will be magnified threefold in the final results for the thermal conductivity of silicon layer. For example, the thermal conductivity of aluminum layer increases from 130 W m^{-1} K^{-1}, at room temperature, to 180 W m^{-1} K^{-1}, at 450 K. In the meantime, thermal conductivity of the 100 nm thick silicon layer reduces from 65 W m^{-1} K^{-1} to nearly 40 W m^{-1} K^{-1} over the same temperature range. As a result, the estimated uncertainties for 100 nm thick silicon at 300 K and 450 K are 15% and 22%, respectively. The uncertainty significantly reduced ($\sim$9%) at lower temperatures as the thermal conductivities of the aluminum dropped to 50 W m^{-1} K^{-1}, while the silicon thermal conductivity increased to 100 W m^{-1} K^{-1} at temperatures around 100 K.

When CoFe layer is used as a heating and thermometry element, the uncertainty is less than 10% for the entire high temperature range. This is due to the fact that the ratio of thermal conductivities of the CoFe and 20 nm thick silicon layers remains constant over temperatures from 300 K to 450 K. It is clear that the low thermal conductivity CoFe metal alloy (20 W m^{-1} K^{-1} at room temperature) of thickness near 75 nm can produce more reliable data for thermal conductivity measurement of the 20 nm thick silicon layer, in particular at high temperatures.

The Appendix describes a detailed sensitivity analysis that provides guidelines to minimize the contribution of the metal heater/thermometer bridge to the thermal conductivity of the thin silicon layers of thickness less than 100 nm. In general, low thermal conductivity metal alloys are excellent candidates and can significantly reduce uncertainty in the thermal conductivity measurements of thin silicon layers. In addition, the temperature coefficient of electrical resistance of CoFe was measured and found to be nearly twice of that of aluminum film, which doubled the sensitivity of the measurements. Alternative fabrication schemes and processes are under investigation to nearly eliminate the contribution of the metal layer. One way to accomplish this is by reducing the width of the metal bridge compared to the width of the suspended silicon layer.

3 Theory and Experimental Results

The modified form of the conductivity integral [23], which separately accounts for the contributions of transverse and longitudinal phonon modes, along with an analytical solution to the Boltzmann transport equation in the thin layers is used for prediction of thermal conductivity as a function of the layer thickness and temperature [7–9]

$$k = \frac{1}{3} \sum_{j=L,T,TU} \nu_j^2 \int_0^{\theta_j/T} C_{V,j}(x,T)[\tau_j(x,T) \times F(\delta)]dx \qquad (8)$$

where the subscripts $j=L$, T, TU refer to the single longitudinal and the two transverse phonon modes, respectively, ν_j is the appropriate phonon group velocity, θ_j is the Debye temperature of the solid, $x=\hbar\omega/k_BT$ is the nondimensional phonon frequency, C_j is phonon specific heat per unit volume and per nondimensional phonon frequency. The Boltzmann constant is $k_B=1.38 \times 10^{-23}$ J K^{-1}, and Planck's constant divided by 2π is $\hbar=1.602 \times 10^{-34}$ Js. Table 1 outlines all the relevant parameters in evaluation of the thermal conductivity integral [Eq. (8)]. The boundary scattering reduction function [24]

$$F(\delta) = 1 - \frac{3}{8\delta} + \frac{3}{2\delta}\int_1^{\infty} \left(\frac{1}{t^3} - \frac{1}{t^5}\right)\exp(-\delta \times t)dt \qquad (9)$$

depends on $\delta=d_s/\Lambda_b$ which is the ratio of the layer thickness d_s and the appropriate phonon mean free paths for transverse or longitudinal modes $\Lambda_b=\nu \times \tau_b$. The relaxation time in the absence of phonon-boundary scattering τ_b is what was previously determined for bulk silicon [24]. This expression assumes that phonons are diffusely scattered or emitted from the boundaries of the layer, which may slightly overestimate the conductivity reduction at temperatures below 20 K [7–9]. The fraction of phonons diffusely reflected, therefore, depends strongly on the surface roughness and the wavelength of the phonons under consideration.

The temperature-dependent thermal conductivity data and predictions of Eq. (8), as shown in Fig. 6, are in good agreement. This indicates that boundary scattering is responsible for the strong reduction in thermal conductivity, compared to the bulk silicon. The maximum thermal conductivity for the 100 nm thick silicon occurs at 100 K. As expected, the maximum thermal con-

Table 1 The coefficients for phonon scattering rate, group velocity, and Debye temperature

Scattering Rate	Fitting Parameter
$\tau_{isotopes}^{-1} = A_{isotopes}\omega^4$	$A_{isotopes} = 1.32 \times 10^{-45}$ s^3
$\tau_T^{-1} = B_T\omega T^4 + \tau_{isotopes}^{-1}$	$B_T = 9.3 \times 10^{-13}$ K^{-3}
$\tau_{TU}^{-1} = \dfrac{B_{TU}\omega^2}{\sinh(x_\omega)}, \omega_1 < \omega < \omega_2$	$B_{TU} = 5.5 \times 10^{-18}$ s
$\tau_L^{-1} = B_L\omega^2 T^3 + \tau_{isotopes}^{-1}$	$B_L = 2 \times 10^{-24}$ s K^{-3}

Group Velocity		
ν_T	ν_{TU}	ν_L
5860 m s^{-1}	2000 m s^{-1}	8480 m s^{-1}

Debye Temperature		
Θ_T	Θ_{TU}	Θ_L
180 K	210 K	570 K

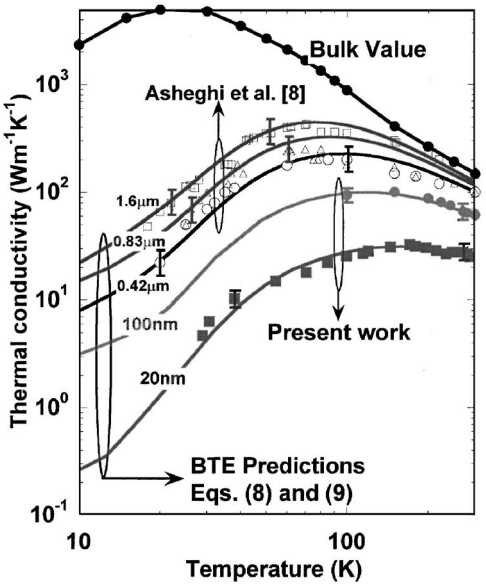

Fig. 6 The temperature dependent thermal conductivity data for the silicon layers of 20 and 100 nm thickness. The estimated uncertainties for 20 nm thick silicon layer are on the order of 12%, 8% at 30 K and 300 K. For 100 nm silicon layer, the estimated uncertainties are on the order of 9% and 15% at 100 K and 300 K, respectively.

ductivity (~130 K) shifts toward higher temperatures for the 20 nm thick silicon layers. The maximum thermal conductivity for the bulk silicon (5000 $W\,m^{-1}\,K^{-1}$ at $T=30$ K) separates the low-temperature region, where scattering is dominated by imperfections and surfaces, from the high-temperature region, where phonon-phonon scattering is dominant. In the ultrathin silicon layers, phonon-boundary scattering remains significant even at high temperatures, as shown in Figs. 7 and 8.

Figure 7 shows the measured lateral thermal conductivities of silicon layers as a function of thickness near room temperature. Previous [9,10] and present experimental data agree very well with the predictions, except for the silicon layer of thickness, $d_s = 78$ nm [10]. Thermal conductivity of the 20 nm and 100 nm thin

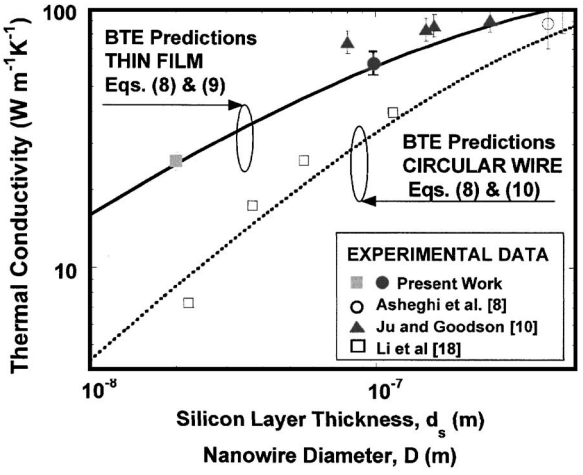

Fig. 7 Thermal conductivity of silicon layer and wires, at room temperature, as a function of thickness. Predictions based on Boltzmann transport equation (BTE) agree reasonably well with the experimental data [8,10] for thin silicon film. For nanowires, the predications are different from the reported data [18] for $D=22$ nm by nearly 30%.

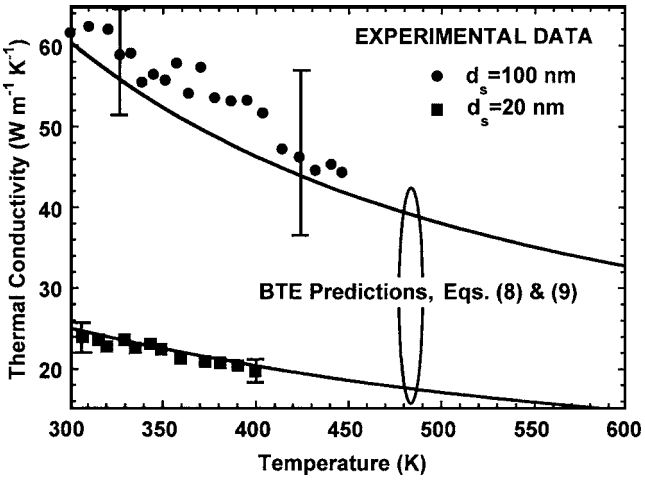

Fig. 8 Lateral thermal conductivity data and predictions for thin silicon layers at high temperatures. The estimated uncertainties for 20 nm thick silicon layer are on the order of 8%, 6% at 300 K and 400 K. For 100 nm silicon layer, the estimated uncertainties are in the order of 15% and 22% at 300 K and 450 K, respectively

silicon layers at room temperature are 22 $W\,m^{-1}\,K^{-1}$ and 60 $W\,m^{-1}\,K^{-1}$, respectively, which are nearly 85% and 60% less than the reported bulk value of 148 $W\,m^{-1}\,K^{-1}$. It is worthwhile to mention that no additional fitting parameters are used for getting agreement between the experimental data and predictions using Eqs. (8) and (9).

In addition, the graph depicts the thermal conductivity data for individual silicon nanowires of various diameters [18], which agree reasonably well (except for $D=22$ nm) with the predictions of phonon-boundary scattering using Eq. (8) and the boundary scattering reduction function for wires with circular cross section [24]

$$F_o(\delta_o) = 1 - \frac{12}{\pi} \cdot \int_0^1 (1-t^2)^{1/2} S_4(\delta_o \times t) dt \qquad (10)$$

where

$$S_n(u) = \int_1^\infty e^{-ut}(t^2-1)^{1/2} \cdot t^{-n} dt$$

depends on $\delta_o = D/\Lambda_b$, where D is the nanowire diameter.

It is suggested that the confinement of acoustic phonons and corresponding change in phonon dispersion and therefore the group velocity may lead to an increase in phonon scattering rates and, thus drastic reduction in thermal conductivity [25–27] for silicon nanowire of thickness on the order of 10 nm–20 nm. It was further claimed in Ref. [28] that for a 20 nm silicon nanowire, the overall phonon group velocity would be reduced by 40% compared with the bulk value. At the same time, changes in phonon dispersion could also modify the density of states and phonon scattering rate. For the silicon nanowire, the scattering rate for phonon-electron scattering is small compared to that of the umklapp and mass difference scattering, however, the mass-difference scattering rate is strongly increased at phonon frequency about 5×10^{13} rad/s [25,28].

In order to shed light on these matters, we followed the procedure described by Bannov et al. [26] to obtain the phonon dispersion curves for 20 nm thick silicon film and nanowire of 20 nm diameter [29]. The spatial confinement in these nanostructures leads to many dispersion branches, their flattening and corresponding decrease of the phonon group velocity. It is concluded that the changes in the phonon dispersion modes for nanowire is

more pronounced compared to that of the thin film layer of comparable thickness. This may partially explain why the thin film thermal conductivity data and predictions, Eq. (8), agree well, while the predictions using Eq. (10), overestimates the nanowire thermal conductivity data by as much as 30%–40%. It is certainly worthwhile to modify the scattering rates based on the modified phonon dispersion to examine its impact on the thermal conductivity of nanowire and ultra-thin silicon layers. However, the final results will be more or less qualitative as the phonon confinement effect can also manifest itself by altering the phonon scattering rates.

The predictions of the Boltzmann Transport Equation (BTE) for silicon nanotubes (not shown here) overestimates the experimental data for a 20 nm diameter nanotube [19] at low temperatures. In contrast, the BTE predictions for a 20 nm thickness silicon layer agree well with experimental data even at 30 K. However, relatively large uncertainty in the experimental data makes it difficult to make a conclusive statement about the impact of phonon confinement effect for thin silicon layer. Perhaps, thermal conductivity measurements of 5 nm–10 nm thick layer and/or nanotubes in the temperature range of 1 K–10 K will be helpful in resolving this controversy.

4 Conclusions

The lateral thermal conductivity of single-crystal silicon layers of thicknesses 20 mm and 100 mm at temperatures between 30 K and 300 K is measured, using joule heating and electrical-resistance thermometry in suspended microfabricated structures. The experimentally measured thermal conductivity and predictions based on the kinetic theory for phonon transport along thin silicon layers agree well and show significant reduction compared to the bulk value for the entire temperature range. The thermal conductivity of the 20 mm thick silicon layer, at room temperature, is nearly 22 $W\,m^{-1}\,K^{-1}$, which is significantly smaller than the bulk value, 148 $W\,m^{-1}\,K^{-1}$. Careful analyses of the heat conduction and uncertainty in the measured thermal conductivity data are presented. In addition, the limitations of the above technique for thermal conductivity measurements of silicon layers were carefully investigated.

Acknowledgment

This work is supported by a grant from National Science Foundation (NSF-0103082) for Nanotechnology Interdisciplinary Research Team (NIRT). The authors would like to acknowledge support from the Data Storage System Center (DSSC) that provided nearly unlimited resources for fabrication of the nanostructures, at Carnegie Mellon University. Dr. Sadegh M. Sadeghipour provided helpful comments and extensive editorial assistance in the publication of this paper.

Appendix

The uncertainty and sensitivity analyses described here provides guidelines to minimize the contribution of the metal heater/thermometer bridge to the thermal conductivity measurements of the thin silicon layers as well as insight on the limitations of the present experimental techniques for thermal conductivity measurements of sub-100 nm thickness silicon layers.

A.1 Uncertainty Analysis. Metal and oxide layer's thickness and thermal conductivity variations; and nonuniformity caused by fabrication process could largely impact the uncertainty in silicon thermal conductivity data. In order to estimate the uncertainty in the results one can start with the linearized form of Eq. (7) given by

$$\Delta R = R_0\left(\frac{L^3}{12}\cdot\frac{I^2\rho}{w^2d^2k}\right) \tag{A1}$$

where $R=R_0(1+\alpha\times\Delta T)$. Rearranging the above equation one can arrive at the following expressions for the thermal conductivity of silicon/metal and metal structures, respectively:

$$k_{s,m} = \frac{1}{\alpha_{s,m}\Delta T_{s,m}}\left(\frac{L^3}{12}\frac{\rho I_{s,m}^2}{w^2(d_s+d_m)^2}\right) \tag{A2a}$$

$$k_m = \frac{1}{\alpha_m\Delta T_m}\left(\frac{L^3}{12}\frac{\rho I_m^2}{w^2d_m^2}\right) \tag{A2b}$$

The thermal conductivity of the silicon layer can be obtained using the following expression:

$$k_s = \frac{d_s+d_m}{d_s}k_{s,m} - \frac{d_m}{d_s}k_m \tag{A3}$$

By inserting equations (A2*a*) and (A2*b*) into the above equation, one can obtain an appropriate equation for the sensitivity analysis

$$k_s = \frac{C}{\alpha}\left(\frac{C_1}{d_s+d_m} - \frac{C_2}{d_m}\right) \tag{A4a}$$

where

$$C = \frac{I^2L^3\rho}{12w^2d_s};\quad C_1 = \frac{1}{\Delta T_{s,m}};\quad C_2 = \frac{1}{\Delta T_m} \tag{A4b}$$

The above expression assumes that $I\approx I_{s,m}\approx I_m$, $\alpha\approx\alpha_s\approx\alpha_{s,m}$, and that there are very small uncertainties associated with the measurements of d_s, w, L, and ρ compared to d_m and α. The uncertainty in thermal conductivity of the silicon layer can be represented by [30]

$$U_{k_s} = \sqrt{\left(\frac{\partial k_s}{\partial\alpha}U_\alpha\right)^2 + \left(\frac{\partial k_s}{\partial d_m}U_{d_m}\right)^2} \tag{A5}$$

Using Eq. (A4) one can arrive at the following expression for the uncertainty in thermal conductivity of silicon layer:

$$U_{k_s} = \frac{C}{\alpha} \times \sqrt{\left[\left(\frac{C_2}{\alpha\cdot d_m} - \frac{C_1}{\alpha(d_s+d_m)}\right)U_\alpha\right]^2 + \left[\left(\frac{C_2}{d_m^2} - \frac{C_1}{(d_s+d_m)^2}\right)U_{d_m}\right]^2} \tag{A6}$$

The uncertainties reported in Figs. 4–7 are obtained using the above equation (see Sec. 2.3). Since $d_m\sim10^{-7}$ nm$\ll\alpha\sim10^{-3}$ K^{-1}, the above equation can be further simplified by ignoring the first term

$$U_{k_s} = \frac{1}{d_s}\frac{I^2L^3\rho}{12w^2\alpha}\left(\frac{C_2}{d_m^2} - \frac{C_1}{(d_s+d_m)^2}\right)U_{d_m} \tag{A7}$$

It becomes clear that for a given thickness of the metal layer d_m, the uncertainty in the thermal conductivity of the silicon layer will increase if the thickness of the silicon layer is decreased. This is consistent with the trend shown in Fig. 9, which indicates that the thickness of the metal layer should be kept comparable or smaller than the thickness of the silicon layer to obtain a reasonable margin of uncertainty in the silicon thermal conductivity data.

A.2 Sensitivity Analysis. This section provides guidelines to minimize the contribution of the metal layer to the thermal conductivity measurement of thin silicon layer of thickness less than 100 nm. Equation (A3) can be used to investigate the impact of the variations in thickness of the metal layer on the uncertainty of the thermal conductivity data for the silicon layer. From Fig. 9, it becomes clear that 5% uncertainty in the thickness of the metal layer (d_m=75 nm) results in nearly ±10% uncertainty in the measurement of the thermal conductivity of 20 nm thick silicon layer

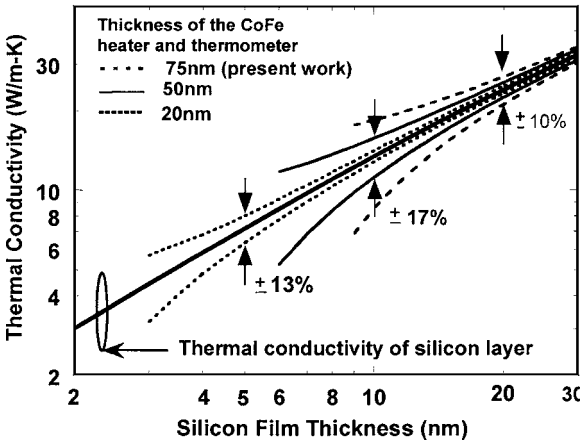

Fig. 9 The uncertainty related to 5% variation of the metal film thickness (d_m=75 nm) results in nearly ±10% uncertainty in the measurement of the thermal conductivity of 20 nm thick silicon layer at room temperature. For thermal conductivity measurements of 10 nm and 5 nm thick silicon layers with uncertainty on the order of ~±15%, metal layer thickness should be reduced to 50 nm and 20 nm, respectively.

at room temperature. For thermal conductivity measurements of 10 nm thick silicon layer with ±17% uncertainty, a 50 nm thick metal layer is required. For thinner silicon layers $d_s \sim 5$ nm, even thinner metal layer is required $d_m \sim 20$ nm to maintain a reasonable level of uncertainty $\sim \pm 13\%$. While there are no fundamental limitations on thermal characterization of structures with total thickness of less than 10 nm using the present technique, the fabrication of these structures in the suspended form becomes ever increasingly more difficult. In addition, at such small dimensions accurate measurements of the thicknesses of different components of the suspended structure becomes very crucial.

In the present study, the bridges are diced from two adjacent dies, which are nearly 3 mm apart. Uncertainty in the measured thermal conductivity and thickness of the metal layer can be largely reduced (or even eliminated) if the bridges are fabricated as close as possible, preferably in the ~ 100 μm range. It becomes clear that for thermal conductivity measurements of silicon layers of thickness in the range of 5 nm–15 nm, even small variations in the dimensions and transport properties of the metal layer cannot be tolerated. Alternative fabrication schemes and processes are under investigation to nearly eliminate the contribution of the metal layer to the experimental measurements. One way to accomplish this is by reducing the width of the metal bridge compared to the width of the suspended silicon layer.

Nomenclature

C = Phonon specific heat per unit volume, $\mathrm{J\,m^{-3}\,K^{-1}}$
D = Nanowire diameter, m
d = Thickness of the layer, m
F = Mean free path reduction ratio due to phonon boundary scattering for thin film, Eq. (9)
F_0 = Mean free path reduction ratio due to phonon boundary scattering for circular wire, Eq. (10)
I = Applied electrical current, A
k = Thermal conductivity, $\mathrm{W\,m^{-1}\,K^{-1}}$
k_B = Boltzmann constant $= 1.38 \times 10^{-23}$ $\mathrm{J\,K^{-1}}$
L = Length of the suspended bridge, m
ΔL = Length of the under/over etch portion of bridge, m
R_0 = Electrical resistance of the metal bridge at T_0, Ω
$\overline{R}$ = Average electrical resistance, Ω
ΔR = Electrical resistance change, Ω
T = Temperature, K
T_0 = Temperature of the substrate, K
$\overline{T}$ = Average temperature of the bridge, K
v = Group velocity of phonon, $\mathrm{m\,s^{-1}}$
w = Width of the suspended bridge, m
x = Nondimensional phonon frequency $= \hbar\omega/k_B T$
y = y direction along the length of the suspended bridge, m

Greek

α = Temperature coefficient of the electrical resistance, $\mathrm{K^{-1}}$
γ = Parameter defined in equation (2a)
δ = Dimensionless parameter for thin film $= d_s/\Lambda_b$
δ_0 = Dimensionless parameter for circular wire $= D/\Lambda_b$
θ = Debye temperature, K
Λ = Bulk phonon mean free path, m
ρ = Electrical resistivity, Ω m
Θ = Temperature variable, K
τ = Phonon relaxation time, s
ω = Phonon angular frequency, $\mathrm{s^{-1}}$
$\hbar$ = Planck's constant divided by $2\pi = 1.055 \times 10^{-34}$, J s

Subscript

b = Bulk silicon
CoFe = CoFe suspended structure
j = Particular phonon mode
L = Longitudinal phonon
m = Metal suspended structure
m,s = Metal/silicon suspended structure
s = Silicon layer
T = Low frequency transverse phonons
TU = High frequency transverse phonons

References

[1] Furuya, M., Fujiwara, S., and Kimura, M., 2002, "Miniaturized Thermal Analysis Sensor Using Micro-Heaters on SOI Substrate," Trans. Instit. Electrical Eng. Japan, **122-E**, pp. 207–211.

[2] Billat, S., Glosch, H., Kunze, M., Hedrich, F., Frech, J., Auber, J., Lang, W., Sandmaier, H., and Wimmer, W., 2001, "Convection-Based Micromachined Inclinometer Using SOI Technology," *14th IEEE International Conference on MicroElectroMechanicalSystems*, Interlaken, Switzerland, pp. 159–161.

[3] Olson, E. A., Yu, M., Efremov, E., Zhang, M., Zhang, Z., and Allen, L. H., 2003, "The Design and Operation of a MEMS Differential Scanning Nanocalorimeter for High-Speed Heat Capacity Measurements of Ultrathin Films," J. Microelectromech. Syst., **12**, pp. 355–364.

[4] King, W. P., Kenny, T. W., Goodson, K. E., Cross, G. L. W., Despont, M., Dürig, U., Rothuizen, H., Binnig, G., and Vettiger, P., 2001, "Atomic Force Microscope Cantilevers for Combined Thermomechanical Data Writing and Reading," Appl. Phys. Lett., **78**, pp. 1300–1302.

[5] Savin, A. M., Prunnila, M., Kivinen, P. P., Pekola, J. P., Ahopelto, J., and Manninen, A. J., 2001, "Efficient Electronic Cooling in Heavily Doped Silicon by Quasiparticle Tunneling," Appl. Phys. Lett., **79**, pp. 1471–1473.

[6] Pescini, L., Tilke, A., Blick, R. H., Lorenz, H., Kotthaus, J. P., Eberhardt, W., and Kern, D., 1999, "Suspending Highly Doped Silicon-on-Insulator Wires for Applications in Nanomechanics," Nanotechnology, **10**, pp. 418–420.

[7] Asheghi, M., Leung, Y. K., Wong, S. S., and Goodson, K. E., 1997, "Phonon-Boundary Scattering in Thin Silicon Layers," Appl. Phys. Lett., **71**, pp. 1798–1800.

[8] Asheghi, M., Touzelbaev, M. N., Goodson, K. E., Leung, Y. K., and Wong, S. S., 1998, "Temperature Dependent Thermal Conductivity of Single-Crystal Silicon Layers in SOI Substrates," ASME J. Heat Transfer, **120**, pp. 30–36.

[9] Asheghi, M., Kurabayashi, K., Kasnavi, R., and Goodson, K. E., 2002, "Thermal Conduction in Doped Single-Crystal Silicon Films," J. Appl. Phys., **91**, pp. 5079–5088.

[10] Ju, Y. S., and Goodson, K. E., 1999, "Phonon Scattering in Silicon Films With Thickness of Order 100 nm," Appl. Phys. Lett., **74**, pp. 3005–3007.

[11] Rim, K., Koester, S., Hargrove, M., Chu, J., Mooney, P. M., Ott, J., Kanarsky, T., Ronsheim, P., Ieong, M., Grill, A., and Wong, H.-S. P., 2001 "Strained Si NMOSFETs for High Performance CMOS Technology," *Symposium on VLSI Technology Digest of Technical Papers*, Kyoto, Japan, pp. 59–60.

[12] Hoyt, J. L., Nayfeh, H. M., Eguchi, S., Aberg, I., Xia, G., Drake, T., Fitzgerald, E. A., and Antoniadis, D. A., 2002, "Strained Silicon MOSFET Technology," *IEEE International Electron Devices Meeting*, San Francisco, CA, pp. 23–26.
[13] Jenkins, K. A., and Rim, K., 2002, "Measurement of the Effect of Self-Heating in Strained-Silicon MOSFETs," IEEE Electron Device Lett., **23**, pp. 360–362.
[14] Etessam-Yazdani, K., and Asheghi, M., 2004, "Ballistic Phonon Transport on Strained Si/SiGe Nanostructures With an Application to Strained-Silicon Transistors," *IEEE ITherm Conference*, June 2004, Las Vegas, NV.
[15] Liu, W., and Asheghi, M., 2004, "Thermal Modeling of Self-Heating in Strained-Silicon MOSFETS," *IEEE ITherm Conference*, June 2004, Las Vegas, NV.
[16] Asheghi, M., Behkam, B., Yazdani, K., Joshi, R., and Goodson, K. E., 2002, "Thermal Conductivity Model for Thin Silicon-on-Insulator Layers at High Temperatures," Presented at the *IEEE International SOI Conference Proceedings*, Oct. 7–10, Williamsburg, VA, pp. 51–52.
[17] Asheghi, M., Sverdrup, P., and Goodson, K. E., 1999, "Thermal Modeling of Thin-Film SOI Transistors," *IEEE International SOI Conference Proceedings*, Oct. 4–7, Rohnert Park, CA, pp. 28–29.
[18] Li, D., Wu, Y., Kim, P., Shi, L., Yang, P., and Majumdar, A., 2003, "Thermal Conductivity of Individual Silicon Nanowires," Appl. Phys. Lett., **83**, pp. 2934–2936.
[19] F Band temperature sensor: Lake shore: http://www.lakeshore.com/temp/sen/sdts.html accuracy: ±20 mK$<$10 K; ±55 mK (10 K to 500 K).
[20] Tai, Y. C., Mastrangelo, C. H., and Muller, R. S., 1988, "Thermal Conductivity of Heavily Doped Low Pressure Chemical Vapor Deposited Polycrystalline Silicon Films," Appl. Phys. Lett., **63**, pp. 1442–1447.
[21] Zhang, S, Yang, Y., Sadeghipour, M. S., and Asheghi, M, 2003, "Thermal Characterization of the 144 nm GMR Layer Using Microfabricated Suspended Structures," *ASME Summer Heat Transfer Conference*, Paper no. HT2003-40270, July 21–23, Las Vegas, Nevada.
[22] Reifenberg, J., England, Voss, R. J., Rao, P., Schmitt, W., Yang, Y., Liu, W., Sadeghipour, S. M., and Asheghi, M. "Thermal Conductivity Measurement of Thin Aluminum Layers Using Steady-State Joule Heating and Electrical Resistance Thermometry in Suspended Bridges," *ASME International Mechanical Engineering Congress & Exposition*, IMECE-42055, November 15–21, 2003, Washington, D. C.
[23] Holland, M. G., 1963, "Analysis of Lattice Thermal Conductivity," Phys. Rev., **132**, pp. 2461–2471.
[24] Sondheimer, E. H., 1952, "The Mean Free Path of Electrons in Metals," Adv. Phys., **1**, pp. 1–42.
[25] Nishiguchi, N., 1996, "Electron Scattering due to Confined and Extended Acoustic Phonons in a Quantum Wire," Physica B, **58**, pp. 1494–1497.
[26] Bannov, N., Aristov, V., and Mitin, V., 1995, "Electron Relaxation Times due to the Deformation-Potential Interaction of Electrons With Confined Acoustic Phonons in a Free-Standing Quantum Well," Phys. Rev. B, **51**, pp. 9930–9942.
[27] Zou, J., and Balandin, A., 2001, "Phonon Heat Conduction in a Semiconductor Nanowire," J. Appl. Phys., **89**, pp. 2932–2938.
[28] Balandin, A., and Wang, K., 1998, "Significant Decrease of the Lattice Thermal Conductivity due to Phonon Confinement in a Free Standing Semiconductor Quantum Well," Phys. Rev. B, **58**, pp. 1544–1549.
[29] Liu, W., and Asheghi, M., 2005, "Phonon Confinement Effects in Silicon Film and Nanowire," in preparation.
[30] Holman, J. P., 1984, *Experimental Methods for Engineers*, McGraw-Hill, New York, pp. 50–57.

Journal of Heat Transfer

Technical Briefs

Computation of the Logarithmic Mean Temperature Difference

Antonio Gomiz

The original formula for the computation of the logarithmic mean temperature difference in finite precision floating-point arithmetic may suffer from serious round-off problems when both temperature differences are very close to each other. An alternative, mathematically equivalent, yet simple formula showing better numerical properties is presented. [DOI: 10.1115/1.2130406]

Keywords: logarithmic mean temperature difference, LMTD, floating-point arithmetic

Computation of the LMTD

The logarithmic mean temperature difference (LMTD, ΔT_{lm}) is the driving temperature in heat transfer processes carried out by double pipe and similar heat exchangers when a number of conditions are assumed, particularly, when the fluid heat capacities and the side heat transfer coefficients are constant.

The computation of the LMTD is a basic step of one of the simplest and most used methods for sizing heat exchangers (see, for example, [1–3]). The LMTD is defined by the following expression:

$$\Delta T_{lm}(\Delta T_1,\Delta T_2) = \begin{cases} (\Delta T_1 - \Delta T_2)/\ln(\Delta T_1/\Delta T_2), & \Delta T_1 \neq \Delta T_2 \\ \Delta T_1, & \Delta T_1 = \Delta T_2 \end{cases} \tag{1}$$

where ΔT_1 and ΔT_2 are the fluid temperature differences at both ends of the heat exchanger. In spite of its simplicity, this expression should not be implemented directly as the following examples show. (A hat $\hat{}$ on the arithmetic operators and functions serves the purpose of differentiating the floating-point versions from their infinite precision counterparts.)

Using four-digit precision arithmetic in base 10 and usual rounding, given $\Delta T_1 = 31.94$ and $\Delta T_2 = 31.9$, Eq. (1) yields

$$\Delta T_{lm} = (31.94 \hat{-} 31.9) \hat{/} \hat{\ln}(31.94 \hat{/} 31.9) = 0.04 \hat{/} \hat{\ln} 1.001$$

$$= 0.04 \hat{/} 9.995\text{e}-4 = 40.02$$

However, the correct result to four digits is 31.92, so the relative error is about 25%.

Contributed by the Heat Transfer Division of ASME for publication in the JOURNAL OF HEAT TRANSFER. Manuscript received April 15, 2004; final manuscript received January 31, 2005. Review conducted by: Karen Thole.

Since the problem is inherent to the use of finite precision floating-point arithmetic, extending the precision does not provide a solution, perhaps rendering it more unlikely but not impossible.

Consider an energy balance operation for a heat recovery process, where both fluid heat capacities are (practically) the same, computed with double precision IEEE floating-point arithmetic and usual rounding, see [4–7]. It is frequent to observe some accumulated round-off error, for instance, $\Delta T_1 = 31.900000000000004$ instead of just $\Delta T_1 = 31.9$. Then (due to rounding the actual value of the trailing 4 is 2^{-48}, not $4 \cdot 10^{-15}$)

$$\Delta T_{lm} = \{(31.9 + 2^{-48}) \hat{-} 31.9\} \hat{/} \hat{\ln} \{(31.9 + 2^{-48}) \hat{/} 31.9\}$$

$$= 2^{-48} \hat{/} \hat{\ln}(1 + 2^{-52}) = 2^{-48} \hat{/} 2^{-52} = 16$$

which is off by nearly −50%. You can check it quickly with a standard PC and a high level language, like MATLAB®.

Therefore, the original formula should not be used as an algorithm and alternatives must be considered; see [8] for more examples of apparently simple computations.

A typical approach consists of returning $(\Delta T_1 + \Delta T_2)/2$ if ΔT_1 and ΔT_2 are sufficiently near; just consider a two-term series expansion of $f(x) = (x - \Delta T_2)/\ln(x/\Delta T_2)$ at $x = \Delta T_1$, see [1], Sec. 1.3.1. However, this introduces the additional problems of testing when ΔT_1 and ΔT_2 are close enough, and that the resulting algorithm yields a function which is neither smooth nor even continuous, something undesirable when using a number of iterative methods.

Before deriving any alternative algorithm, it is essential to take into account some properties of floating-point arithmetics.

Computer Arithmetics

In a typical, well-designed computer arithmetic, the floating-point operations are related to their infinite precision counterparts with the simple expressions

$$x \hat{\circ} y = (x \circ y)(1 + \delta)$$

$$\hat{f}(x) = f(x)(1 + \eta) \tag{2}$$

where $\circ$ is a placeholder for the arithmetic operators $+$, $-$, $*$, and $/$, f is any of the elementary functions ln, sin, etc., and δ, η, are tiny numbers, see [4–7]. For example,

$$31.94 \hat{-} 31.9 = (31.94 - 31.9)(1 + \delta_1) \Rightarrow \delta_1 = 0$$

$$31.94 \hat{/} 31.9 = (31.94/31.9)(1 + \delta_2) \Rightarrow \delta_2 = -2.536\text{e}-4$$

$$\hat{\ln}\, 1.001 = (\ln 1.001)(1 + \eta) \Rightarrow \eta = -3.333\text{e}-7$$

Why the Original LMTD Formula Fails

The LMTD can be regarded as a function of the form $f_a(x) = (x - a)/\ln(x/a)$, where a is a nonzero constant and x takes values with the same sign as a. Such functions have a removable singu-

larity at $x=a$, so that they can be made continuous by simply defining $f_a(a)=\lim_{x\to a} f_a(x)=a$ (use L'Hospital's rule). Note that x and a are interchangeable: $f_a(x)=f_x(a)$.

Applying the relations (2) to see how f_a compares to its floating-point version $\hat{f}_a$

$$\begin{aligned}\hat{f}_a(x) &= (x\hat{-}a)\hat{/}\hat{\ln}(x\hat{/}a) = \{(x-a)(1+\delta_1)\}\hat{/}\hat{\ln}\{(x/a)(1+\delta_2)\}\\ &= \{(x-a)(1+\delta_1)\}\hat{/}[\ln\{(x/a)(1+\delta_2)\}(1+\delta_3)]\\ &= \frac{(x-a)(1+\delta_1)}{\ln\{(x/a)(1+\delta_2)\}(1+\delta_3)}(1+\delta_4) = \frac{x-a}{\ln\{(x/a)(1+\delta_2)\}}E\end{aligned}$$

where $E=(1+\delta_1)(1+\delta_4)/(1+\delta_3)$, it becomes clear that the actual function being evaluated does not have the corresponding removable singularity, unless $\delta_2=0$, for example, when $a=1$. In some cases $\ln\{(x/a)(1+\delta_2)\}$ will be closer to zero than it should be as x-a approaches zero and the LMTD will be overestimated, as in the first example. In other cases, $\ln\{(x/a)(1+\delta_2)\}$ will be farther from zero than it should be and the LMTD will be underestimated, as in the second example.

An Alternative Formula

The previous observation suggests bringing the removable singularity back: just modify the original formula so that the quotient x/a also appears in the numerator

$$f_a(x) = \frac{x-a}{\ln(x/a)} = a\frac{x/a-1}{\ln[(x/a)/1]} = a\cdot f_1(x/a) \tag{3}$$

Since x and a are interchangeable, it is possible to choose the argument of f_1, either x/a or a/x, whichever is greater than 1. The reason will be made clear below.

The alternative formula is now stated as follows. If ΔT_1 and ΔT_2 are identical there is nothing to do, otherwise interchange ΔT_1 and ΔT_2 if necessary so that $\Delta T_1>\Delta T_2$ and define $r=\Delta T_1/\Delta T_2$, then

$$\Delta T_{lm}(\Delta T_1,\Delta T_2) = \begin{cases}\Delta T_2[(r-1)/\ln r], & r\neq 1\\ \Delta T_1, & r=1\end{cases} \tag{4}$$

Recomputing the first example with Eq. (4), the relative error of the new LMTD estimate

$$\begin{aligned}\Delta T_{lm} &= 31.9\hat{*}[(31.94\hat{/}31.9\hat{-}1)\hat{/}\hat{\ln}(31.94\hat{/}31.9)]\\ &= 31.9\hat{*}[(1.001\hat{-}1)\hat{/}\hat{\ln}\,1.001] = 31.9\hat{*}(0.001\hat{/}9.995e-4)\\ &= 31.9\hat{*}1.001 = 31.93\end{aligned}$$

is only about 0.031%, and for the second example

$$\begin{aligned}\Delta T_{lm} &= 31.9\hat{*}[\{(31.9+2^{-48})\hat{/}31.9\hat{-}1\}\hat{/}\hat{\ln}\{(31.9+2^{-48})\hat{/}31.9\}]\\ &= 31.9\hat{*}[\{(1+2^{-52})\hat{-}1\}\hat{/}\hat{\ln}(1+2^{-52})]\\ &= 31.9\hat{*}[2^{-52}\hat{/}(2^{-52}-2^{-105})] = 31.9\hat{*}(1+2^{-52}) = 31.9+2^{-47}\end{aligned}$$

is a small multiple of 2^{-53}, the unit roundoff of the IEEE double precision format; see [4] or [6].

It is not difficult to explain why the modified algorithm is much more accurate than the original (for further details, including proofs, on different but essentially equivalent problems refer to [6], Sec. 1.14.1, and [7], Theorem 4).

Note that f_1 relates to its floating-point counterpart $\hat{f}_1$ much better than f_a did

$$\begin{aligned}\hat{f}_1(x) &= (x\hat{-}1)\hat{/}\hat{\ln}(x) = \{(x-1)(1+\delta_1)\}\hat{/}\{\ln(x)(1+\delta_2)\}\\ &= \frac{(x-1)(1+\delta_1)}{\ln(x)(1+\delta_2)}(1+\delta_3) = \frac{x-1}{\ln(x)}E = f_1(x)\cdot E\end{aligned} \tag{5}$$

Since $E=(1+\delta_1)(1+\delta_3)/(1+\delta_2)$ is very close to 1, it turns out that $\hat{f}_1(x)$ is a very accurate estimate of $f_1(x)$. Hence, the original problem, the evaluation of a function of the form $f_a(x)=(x-a)/\ln(x/a)$, has been reduced to another simpler and better behaved problem, namely, the evaluation of $f_1(x)=(x-1)/\ln(x)$. However, the value being passed to f_1 is not x/a but $x\hat{/}a=(x/a)(1+\delta)$. To assess how this perturbation will affect the result it is necessary to resort to a few properties of f_1 (the proofs only require elementary calculus)

(a) $f_1(y)>0,\ y\in\,]0,+\infty[$.
(b) $f_1'(y)>0,\ y\in\,]0,+\infty[;\ f_1'(1)=0.5;\ f_1'(y)<0.5,\ y\in\,]1,+\infty[$.
(c) $f_1''(y)<0,\ y\in\,]0,+\infty[$.
(d) $0<y\cdot f_1'(y)/f_1(y)<1,\ y\in\,]0,+\infty[$.

The absolute error which results from computing $f_1(\hat{y})$ instead of $f_1(y)$, where $\hat{y}=y(1+\delta)$, is $f_1(\hat{y})-f_1(y)=f_1'(\mu)(\hat{y}-y)$, with $y<\mu<\hat{y}$ or $\hat{y}<\mu<y$. Since it is possible to assume that $y>1$, the rounded value cannot be less than 1, so $\hat{y}\geqslant 1$. Hence, $\mu>1$ and $f_1'(\mu)<0.5$. Then, using (b)

$$\begin{aligned}|f_1(\hat{y})-f_1(y)| &= |f_1'(\mu)(\hat{y}-y)| = |f_1'(\mu)|\cdot|\hat{y}-y| < 0.5|\hat{y}-y|\\ &= 0.5|y(1+\delta)-y| = 0.5\cdot|\delta|\cdot y\end{aligned}$$

More interestingly, the relative error

$$\begin{aligned}\left|\frac{f_1(\hat{y})-f_1(y)}{f_1(y)}\right| &= \left|\frac{f_1'(\mu)(\hat{y}-y)}{f_1(y)}\right| = \left|\frac{y\cdot f_1'(\mu)}{f_1(y)}\right|\cdot\left|\frac{\hat{y}-y}{y}\right|\\ &= \left|\frac{y\cdot f_1'(\mu)}{f_1(y)}\right|\cdot\left|\frac{y(1+\delta)-y}{y}\right| = \left|\frac{y\cdot f_1'(\mu)}{f_1(y)}\right|\cdot|\delta|\end{aligned}$$

can be bound similarly. If $y<\mu<\hat{y}$ then (c) implies $f_1'(y)>f_1'(\mu)$ and using (d)

$$\left|\frac{f_1(\hat{y})-f_1(y)}{f_1(y)}\right| = \left|\frac{y\cdot f_1'(\mu)}{f_1(y)}\right|\cdot|\delta| < \left|\frac{y\cdot f_1'(y)}{f_1(y)}\right|\cdot|\delta| < |\delta| \tag{6}$$

On the other hand, if $\hat{y}<\mu<y$ then (b) implies $f_1(\hat{y})<f_1(y)$ and using (c) and (d)

$$\begin{aligned}\left|\frac{f_1(\hat{y})-f_1(y)}{f_1(y)}\right| &= \left|\frac{f_1(\hat{y})}{f_1(y)}\right|\cdot\left|\frac{f_1(\hat{y})-f_1(y)}{f_1(\hat{y})}\right| < \left|\frac{f_1(\hat{y})-f_1(y)}{f_1(\hat{y})}\right|\\ &= \left|\frac{\hat{y}\cdot f_1'(\mu)}{f_1(\hat{y})}\right|\cdot\left|\frac{\hat{y}-y}{\hat{y}}\right|\\ &< \left|\frac{\hat{y}\cdot f_1'(\hat{y})}{f_1(\hat{y})}\right|\cdot\left|\frac{y\delta}{y(1+\delta)}\right| < \left|\frac{\delta}{1+\delta}\right|\\ &\cong |\delta|\cdot|1-\delta|\end{aligned} \tag{7}$$

In any case, the relative error in the computation of $f_1(x\hat{/}a)$ is not magnified. Finally, the combination of Eqs. (5)–(7) and Eq. (2)—due to the final multiplication—allows to infer that the modified algorithm yields high relative accuracy.

Conclusion

This paper highlights the importance of numerical analysis issues in even the simplest calculations. It shows how a careful treatment of mathematical formulas, in particular the LMTD, can not only enhance the accuracy of computed results but also avoid potentially costly errors.

References

[1] Hewitt, G. F., *Handbook of Heat Exchanger Design*, 1992, Begell House, New York.
[2] Incropera, F. P., and DeWitt, D. P., 1996, *Fundamentals of Heat and Mass Transfer*, 4th ed., Wiley, New York.
[3] Kakaç, S., and Liu, H., 2002, *Heat Exchangers, Selection, Rating and Thermal*

Design, 2nd ed., CRC Press LLC, Boca Raton, FL.
[4] Kahan, W., "Documents Relating to IEEE Standard 754 for Binary Floating-Point Arithmetic," http://www.cs.berkeley.edu/~wkahan/ieee754status/
[5] Overton, M. L., 2001, *Numerical Computing With IEEE Floating Point Arithmetic*, Society for Industrial and Applied Mathematics, Philadelphia, PA.
[6] Higham, N. J., 2002, *Accuracy and Stability of Numerical Algorithms*, 2nd ed., Society for Industrial and Applied Mathematics, Philadelphia, PA.
[7] Goldberg, D., 2001, *What Every Computer Scientist Should Know About Floating-Point Arithmetic*, ACM Computing Surveys, 1991. An edited version is available as Appendix D of the Numerical Computation Guide by Sun Microsystems, 2001 at http://docs.sun.com/db/doc/806-7996
[8] Forsythe, G. E., 1970, *Pitfalls in Computation, or Why a Math Book Isn't Enough*, Technical Report CS 147, Computer Science Department, Stanford University.

Entropy Generation in Counter Flow Gas to Gas Heat Exchangers

Hany Ahmed Mohamed
Associate Professor
Mechanical Engineering Department,
Faculty of Engineering,
Assiut University, Assiut, Egypt
e-mail: hah@aun.eun.eg

Analysis of heat transfer and fluid flow thermodynamic irreversibilities is realized on an example of a counter flow double pipe heat exchanger utilizing turbulent air flow as a working fluid. During the process of mathematical model creation and for different working and constructing limitations, total thermodynamic irreversibility is studied. The present work proves that the irreversibility occurred due to unequal capacity flow rates (flow imbalance irreversibility). It is concluded that the heat exchanger should be operated at effectiveness, ε, greater than 0.5 and the well operating conditions will be achieved when ε approaches one where low irreversibility is expected. A new equation is adopted to express the entropy generation numbers for imbalanced heat exchangers of similar design with smallest deviation from the exact value. The results obtained from the new equation are compared with the exact values and with those obtained by Bejan (Bejan, A., 1997, Advanced Engineering Thermodynamics, Wiley, New York).
[DOI: 10.1115/1.2130407]

Keywords: entropy generation number, balance heat exchanger, imbalance heat exchanger, irreversibility

1 Introduction

Analysis of irreversibility in heat exchangers should be considered as an important topic due to its relation with heat transfer and fluid flow (pressure drop). It is essential to determine which parameters led to the increase of the irreversibility of the heat exchanger, especially due to the flow imbalance.

Bejan [1–4] had done extensive analyses on irreversibility of the heat exchanger for minimizing the size. His approach uses the concept of entropy generation minimization. Aceves-Saborio et al. [5] took into account the irreversibility associated with the use of the materials, but did not include the irreversibility due to the pressure drops. Tondeur and Kvaalen [6] have shown that in the case of heat exchangers or separation devices involving a given heat transfer and achieving a specified transfer duty, the total entropy produced is minimal when the local rate of entropy production is uniformly distributed along space variables and time. De Oliveira et al. [7] have shown that in the case of an optimal heat exchanger the thermal and viscous contributions to the entropy generation should be equal. The ratio of thermal and viscous contribution to the exergy destruction ranges between one and three when the Reynolds number or hydraulic diameter is optimized. However, it is not shown that this is the case when both Reynolds number and hydraulic diameter are together optimized. Lozano and Valero [8] have developed a theory to allocate exergetic and monetary cost. In their theory they define a matrix containing all irreversibilities, including irreversibilities associated with the building of installations and the disposal of waste materials.

Contributed by the Heat Transfer Division of ASME for publication in the JOURNAL OF HEAT TRANSFER. Manuscript received October 2, 2004; final manuscript received April 13, 2005. Review conducted by N. K. Anand.

The irreversibility balance deserves to be calculated first in the thermodynamic of any heat exchanger, because it establishes the level (order of magnitude) below which the joint minimization of heat transfer and fluid flow irreversibilities no longer make sense. In other words, it would no longer make sense to invest heat exchanger area into minimizing the total irreversibility.

Analysis of heat transfer and fluid flow thermodynamic irreversibilities is realized on an example of a counter flow double pipe heat exchanger where the working fluid is air. The balanced and imbalanced counter flow heat exchangers are selected for the present study. A new equation to represent the entropy generation number for a counter flow imbalance heat exchanger is deduced. The results obtained from the new equation are compared with the exact values and with that obtained by another author.

2 Model Descriptions

A schematic drawing for the heat exchanger model selected for the study is shown in Fig. 1. The inner pipe carries the cold stream and the outer tube carries the hot stream with inlet and exit temperature and pressure T_1, P_1, T_2 and P_2, respectively. The thermal insulation of the heat exchanger is assumed to be perfect. The two sides are indicated by the subscripts 1 and 2. ΔT_1 and ΔT_2 represent the temperature difference of the two streams at the ends of the heat exchanger.

A Balanced heat exchanger implies that the thermal capacity flow rates, $\dot{m}C_p$, are the same on the two sides of the heat transfer surface:

$$\dot{m}_1 C_{p_1} = \dot{m}_2 C_{p_2} = \dot{m} C_p \tag{1}$$

where $\dot{m}_1$, $\dot{m}_2$, C_{P1}, and C_{P2} are the mass flow rates and the specific heats on the two sides, respectively. On the other hand, the capacity flow rates of the **imbalanced** heat exchanger are not the same on the two sides of the heat transfer surface.

3 Analysis and Discussions

The entropy generation rate of the isolated thermodynamic system is:

$$\Delta \dot{S}_s = \dot{m}_1 \cdot C_{p_1} \ln \frac{T_{1,o}}{T_1} + \dot{m}_2 \cdot C_{p_2} \ln \frac{T_{2,o}}{T_2} - \dot{m}_1 \cdot R \ln \frac{P_{1,o}}{P_1} - \dot{m}_2 \cdot R \ln \frac{P_{2,o}}{P_2} \tag{2}$$

where R is the gas constant and $P_{1,o}$, $P_{2,o}$, $T_{1,o}$ and $T_{2,o}$ are the exit pressures and temperatures of the two streams, respectively. Dimensionless entropy generation rate or entropy generation number, Ns, is defined by dividing the previous equation with the capacity flow rate as:

$$Ns = \frac{\Delta \dot{S}_s}{\dot{m}_2 \cdot C_{P2}} \tag{3}$$

The above equation gives the exact values of entropy generation number for the balanced and imbalanced heat exchangers. However, The values of $T_{1,o}$ and $T_{2,o}$ are related by the definition of the effectiveness for heat exchangers, ε which is:

$$\varepsilon = \frac{\dot{m}_1 C_{p_1}(T_{1,o} - T_1)}{\dot{m}_2 C_{p_2}(T_2 - T_1)} = \frac{T_2 - T_{2,o}}{T_2 - T_1} \tag{4}$$

The entropy generation numbers for balanced and imbalanced heat exchangers are studied at the following selected values of the different parameters:

$$T_1 = 300 \text{ K}, \quad P_1 = 0.1 \text{ MPa}, \quad L = 1 \text{ m},$$

$$\text{Tr} = T_1/T_2 = 0.2 - 0.9, \quad rd = d_1/d_2 = 0.3 - 0.7,$$

$$rP = P_1/P_2 = 0.1 - 1, \quad SL = 4L/d_1 = 20 - 50,$$

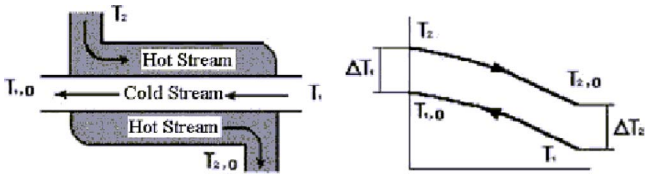

Fig. 1 Schematic drawing for the double pipe heat exchanger model

$$\varepsilon = 0.1 - 0.9, \quad \text{and} \quad \mathrm{Re}_2 = 1 \times 10^4 - 1 \times 10^6$$

Where L, Re_2, SL, d_1 and d_2 are the heat exchanger length, Reynolds number for the air flowing through the outer side, inner passage slenderness ratio ($SL = 4L/d_1$) and inner diameters of the double pipe, respectively. $P_{1,o}$ and $P_{2,o}$ are calculated from the selected values of different parameters given above for turbulent flows, neglecting the entrance and the discharge losses, using the following equations:

$$G = \frac{\mathrm{Re} \cdot \mu}{Dh} \tag{5}$$

$$\dot{m} = G \cdot A \tag{6}$$

$$\dot{m}_1 \cdot C_{P1}(T_{1,o} - T_1) = \dot{m}_2 \cdot C_{P2}(T_2 - T_{2,o}) \tag{7}$$

$$f = 0.046\,\mathrm{Re}^{-0.2} \tag{8}$$

$$\Delta P = 2 \cdot f \cdot \frac{L}{Dh} \cdot \frac{G^2}{\rho} \tag{9}$$

$$P_o = P - \Delta P \tag{10}$$

The parameters in the above equations without subscript 1 or 2 can be applied to both sides of the heat exchanger. The parameters G, Dh, A, f, Po, ΔP, ρ and μ are the mass velocity, hydraulic diameter, flow area, friction coefficient, flow exit pressure, pressure drop through flow passage and air density and dynamic viscosity, respectively. Fluid properties were taken from tables of thermophysical properties of [9] at average temperature of each stream. Calculations reveal that values of Re1 are always greater than 1×10^4 for all values of the selected parameters.

3.1 Balanced Heat Exchanger. As mentioned in previous section, the balance irreversibility deserves to be calculated first in the thermodynamic of any heat exchanger, because it establishes the level (order of magnitude) below which the joint minimization of heat transfer and fluid flow irreversibilities no longer make sense.

The thermal capacity flow rates of the two sides for the balanced heat exchangers are equal as shown in Eq. (1). Thus, from Eqs. (2) and (3), the exact value of the entropy generation number for balanced heat exchanger can be written as:

$$Ns = \ln\frac{T_{1,o}}{T_1} + \ln\frac{T_{2,o}}{T_2} - \frac{R}{C_{P1}}\ln\frac{P_{1,o}}{P_1} - \frac{R}{C_{P2}}\ln\frac{P_{2,o}}{P_2} \tag{11}$$

The results for balanced heat exchanger of the entropy generation number utilizing Eq. (11) are presented in Figs. 2–4. Figure 2 shows the effect of the heat exchanger effectiveness on the entropy generation number, Ns, at $rP = 1$, $rd = 0.5$, $SL = 20$ and $\mathrm{Re}_2 = 5 \times 10^4$ for different temperature ratios, Tr. It is shown that this effect is almost symmetrical parabolic for all temperature ratios. The values of the entropy generation number increase to peak values then decrease to lower values by increasing the effectiveness. It is clearly shown that the minimum values of the entropy generation number occur at maximum and minimum effectiveness and the peak values occur at effectiveness of about 0.5. These effects can be explaines as, from Eqs. (5)–(10), constant Re_2 means that approximately constant pressure drops for balanced heat exchangers. Thus, Ns values depend only on the temperature ratio according to Eq. (11). Increasing Tr increases $(T_2 - T_1)$ leading to increase $T_{1,o}$ and decrease $T_{2,o}$ with the same values for constant ε according to Eq. (4). Therefore, Ns increases by increasing Tr according to Eq. (11) where T_2 is higher than T_1. Also, from Eqs. (4) and (11) for constant Tr, it can be shown that Ns has a parabolic variation with ε values.

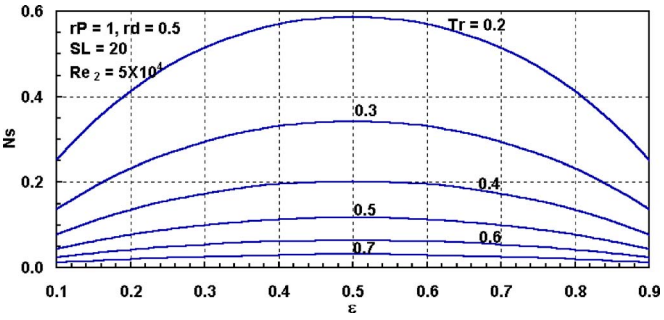

Fig. 2 Effect of the heat exchanger effectiveness on the entropy generation number at various temperature ratios for balanced heat exchangers

Similar variations of Ns with ε are displayed in Fig. 3 for various Reynolds numbers of the air flowing through the outer side from 1×10^4 to 1×10^6, at Tr=0.5, $SL = 20$, $rP = 1$ and $rd = 0.5$. It is noted that the variation in Ns due to the effect of the Reynolds number is very small compared with that induced by varying the temperature ratios. This is normal, where increasing Re increases the pressure drop (Eqs. (5)–(10)) leading to an increase in Ns value according to Eq. (11). This increase in Ns value

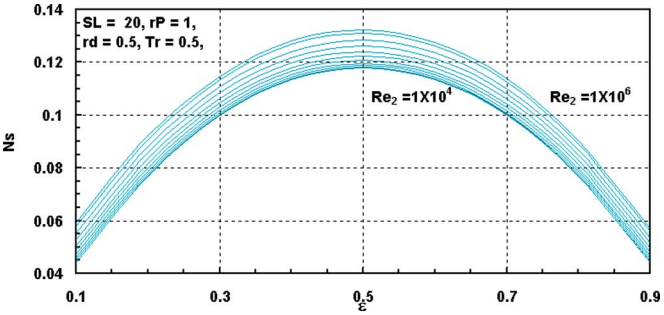

Fig. 3 Effect of the heat exchanger effectiveness on the entropy generation number at various values of hot stream Reynolds number for balanced heat exchangers

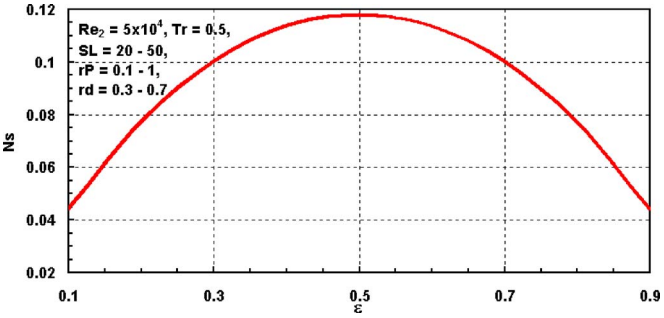

Fig. 4 Effect of the heat exchanger effectiveness on the entropy generation number at various *rd*, *rP* and *SL* for balanced heat exchangers at constant $\mathrm{Re}_2 = 5 \times 10^4$

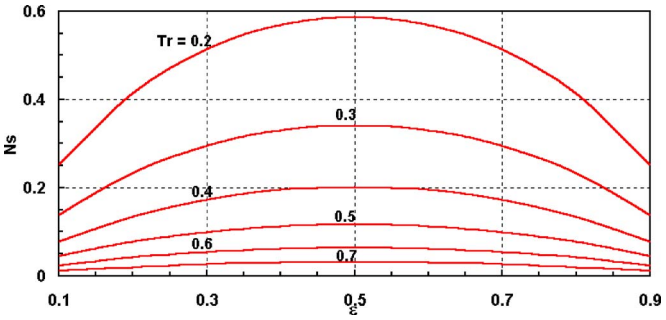

Fig. 5 Entropy generation number in a balanced counter flow heat exchanger at zero pressure drops

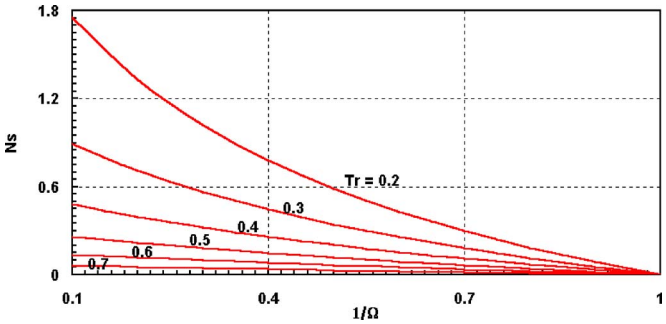

Fig. 6 The entropy generation number for imbalanced counter flow heat exchangers as dependent on Ω and Tr at zero pressure drop

is small compared with that induced by varying the temperature ratios because the pressure terms in Eq. (11) multiplied by R/C_p (less than 1).

Figure 4 shows that there is no effect on the variation of the entropy generation numbers with the heat exchanger's effectiveness through various ranges of *SL* (from 20 to 50), *rP* (from 0.1 to 1) and *rd* (from 0.3 to 0.7) at Tr=0.5 and $\mathrm{Re}_2=5\times10^4$. This is expected where the pressure drops depend mainly on the Re value (Eqs. (5)–(10)).

It is concluded that the entropy generation number for balanced heat exchangers is not affected by *rP*, *rd* and *SL* and mainly depends on the Tr and Re. Minimum values of the entropy generation number are located at maximum and minimum effectiveness while their peak values are located at effectiveness of about 0.5.

3.2 Balanced Heat Exchangers with Negligible Pressure Drop Irreversibility. For balanced counter flow heat exchanger, Eq. (4) gives

$$T_{1,o}=T_1+\varepsilon(T_2-T_1)\ \text{and}\ T_{2,o}=T_2-\varepsilon(T_2-T_1)$$

Hence, by neglecting pressure drop Eq. (11) becomes:

$$Ns=\ln\left(\frac{T_{1,o}}{T_1}\right)+\ln\left(\frac{T_{2,o}}{T_2}\right)=\ln\left(\frac{T_{1,o}T_{2,o}}{T_1T_2}\right)$$
$$=\ln\left[\frac{[T_1+\varepsilon(T_2-T_1)][T_2-\varepsilon(T_2-T_1)]}{T_1T_2}\right]$$
$$=\ln\left[1+\frac{\varepsilon(1-\varepsilon)(\mathrm{Tr}-1)^2}{\mathrm{Tr}}\right] \tag{12}$$

The behavior of *Ns*, for different temperature ratios, Tr, is illustrated in Fig. 5. The entropy generation number is zero when $\varepsilon\to0$ and $\varepsilon\to1$ and it is maximum at $\varepsilon=0.5$, where $dNs/d\varepsilon=0$ from the above equation. The maximum entropy generation number increases when the temperature ratio Tr increases. It is reasonable to expect that the entropy generation number, i.e., irreversibility, decreases when $\varepsilon\to1$. The behaviors of *Ns* when $\varepsilon\to0$ is perfectly clear and logical; it is a well known result although not in terms of entropy generation numbers. Decreasing ε to small values means less heat transferred and obviously the entropy production number decreases toward zero. There is no heat requirement to call for an "absent" exchanger ($\varepsilon=0$). The heat exchanger is very badly designed or deeply scaled and the working conditions are inappropriately chosen for ε to become small. This shows that the heat exchanger should be operated at ε greater than 0.5 and the well operating conditions will be achieved when ε approaches from one where low irreversibility is expected.

3.3 Flow Imbalance Irreversibility with Negligible Pressure Drop. Consider first an imbalanced counter flow heat exchanger with thermal capacity flow rate ratios as:

$$\Omega=\frac{\dot m_1C_{P1}}{\dot m_2C_{P2}}>1.0 \tag{13}$$

Since, according the definition of the heat exchanger effectiveness given in Eq. (4)

$$T_{1,o}=T_1+\frac{\varepsilon(T_2-T_1)}{\Omega}\quad\text{and}\quad T_{2,o}=T_2-\varepsilon(T_2-T_1) \tag{14}$$

then by substituting into Eq. (2), it is possible for zero pressure drops ($\Delta P_1=\Delta P_2=0$) to obtain the equation for overall entropy generation number for imbalanced heat exchangers as:

$$Ns=\Omega\ln\left(\frac{T_{1,o}}{T_1}\right)+\ln\left(\frac{T_{2,o}}{T_2}\right)$$
$$=\ln\left[[1-\varepsilon(1-\mathrm{Tr})]\left[1+\frac{\varepsilon(1-\mathrm{Tr})}{\Omega\mathrm{Tr}}\right]^{\Omega}\right] \tag{15}$$

Then for the ideal case when $\varepsilon=1$, and $\Delta P_1=\Delta P_2=0$

$$Ns=\ln\left[\mathrm{Tr}\left(1+\frac{(1-\mathrm{Tr})}{\Omega\mathrm{Tr}}\right)^{\Omega}\right] \tag{16}$$

Figure 6 shows the dependence of *Ns* on Ω and temperature ratio Tr. Flow imbalance irreversibility increases with the increase of Ω and decrease of temperature ratio Tr. For balanced counter flow heat exchangers ($\Omega=1$) flow irreversibility does not exist ($Ns=0$) according to Eq. (16). Therefore, it can be concluded that the irreversibility occurs due to the unequal capacity flow rates (flow imbalance irreversibility) only.

4 Imbalanced Heat Exchangers

In the present work, a new equation representing approximately the entropy generation number is desired by assuming the relative pressure drops ($\Delta P/P$) along each stream are sufficiently small and the conductive thermal resistance of the wall which separates fluids is negligible. In this case the pressure terms $\ln(P_{1,o}/P_1)$ and $\ln(P_{2,o}/P_2)$ are approximately equal ($-\Delta P_1/P_1$) and ($-\Delta P_2/P_2$), respectively. Taking into account these approximations a new equation is obtained as a result from the substitutions of Eqs. (4)–(10) into Eq. (3). This new equation, Eq. (17), is given for the two streams of the heat exchanger together as follows:

$$Ns=\left\{\left(\frac{0.1421\mu_1^{0.2}R}{\rho_1C_{P1}}\right)\left(\frac{m_1^{1.8}L}{\Omega P_1d_1^{4.8}}\right)\right.$$
$$\left.\times\left[1+\left(\frac{\rho_1\mu_2^{0.2}}{\rho_2\mu_1^{0.2}}\right)\left(\frac{rPrd^{4.8}}{mr^{2.8}(1-rd)^3(1+rd)^{1.8}}\right)\right]\right\}$$
$$+\left\{\ln\left[[1-\varepsilon(1-\mathrm{Tr})]\left[1+\frac{\varepsilon(1-\mathrm{Tr})}{\Omega\mathrm{Tr}}\right]^{\Omega}\right]\right\} \tag{17}$$

The first term on the right hand side represents the contribution of

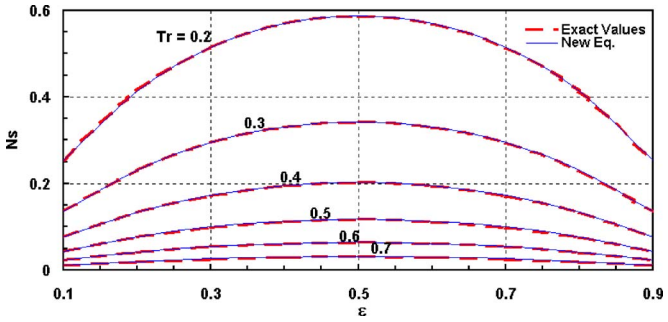

Fig. 7 Comparisons between *Ns* values obtained from the new equation with the corresponding exact one at *SL*=20, $Re_2=5\times10^4$, *rP*=1, *rd*=0.5, Ω=1 and different Tr

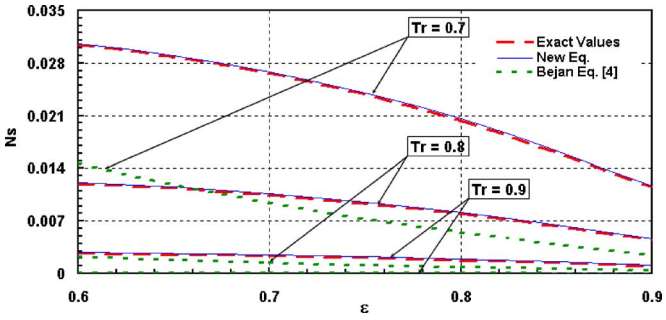

Fig. 8 Comparisons between the new and Bejan [4] equations with the corresponding exact values at *SL*=20, $Re_2=5\times10^4$, *rP*=1, *rd*=0.5, Ω=1, Tr=0.7–0.9 and ε=0.6–0.9

the pressure terms and the second term represents the contribution of the temperature terms. Comparisons between the values of the entropy generation numbers obtained from this equation with that obtained from Eq. (3) (exact values for imbalanced heat exchangers), are presented in Fig. 7 against the effectiveness of the heat exchanger at *SL*=20, $Re_2=5\times10^4$, *rP*=1, *rd*=0.5, Ω=1 and different temperature ratios. It is clearly shown that the value obtained from the new equation, Eq. (17), approximately equals the corresponding exact one in all cases.

4.1 Comparison Between the New Equation and Another One. The equation deuced by Bejan [4] for one side of the heat exchanger surface, which it is considered for the comparison, is

$$Ns_1 = \frac{\tau^2}{St_1}\left(\frac{Dh}{4L}\right)_1 + \frac{R}{Cp}g_1^2 f_1\left(\frac{4L}{Dh}\right)_1 \tag{18}$$

where $\tau^2=(T_2-T_1)^2/T_1T_2$, g_1 is a mass velocity ($g_1=G_1/(2\rho P_1)^{0.5}$) and St_1 is Stanton number ($St_1=\overline{h}_1/(C_{P1}G_1)$). Where $\overline{h}_1$ is inner side heat transfer coefficients based on A_1 in the present work taken as:

$$\overline{h}_1 = \frac{\dot{m}_1 C_{P_1}(T_{1,o}-T_1)}{\pi d_1 L\left(\frac{(T_2+T_{2,o})-(T_1+T_{1,o})}{2}\right)}$$

At *SL*=20, $Re_2=5\times10^4$, *rP*=1, *rd*=0.5, Ω=1, Tr=0.7–0.9 and ε=0.6–0.9, the values obtained from Bejan [4] (Eq. (18)) for one heat exchanger side, are compared with values determined from Eq. (3) and Eq. (17) in Fig. 7 for the two sides. The double values of the entropy generation obtained from the Bejan [4] equation have bigger deviations from the exact values compared to those obtained from the new equation. The figure also shows that the new equation can be used to express the entropy generation numbers with smallest deviation from the exact value. Figures 7 and 8 also show that the entropy generation number for imbalanced heat exchangers decreased as increasing Tr values and it has a parabolic variation with ε. The new equation, Eq. (17), was adapted from the exact one (Eq. (3)) by assuming $(\Delta P/P)$ is small but Bejan equation (Eq. (18)) was adapted by assuming $(\Delta P/P)$, $(\Delta T/T)$ are small and $(1-\varepsilon)\ll1$. Therefore the new equation (Eq. (17)) is more accurate and considers a wider range of temperature ratios compared with the Bejan Eq. (18).

4.2 Minimum Irreversibility in Imbalanced Heat Exchangers. The minimization of irreversibility in heat exchangers with specified mass flow demand is very important from a practical point of view. In Eqs. (2) and (3), it is clear that the entropy generation number has contributions from three sources of irreversibility, namely, from temperature difference during stream to stream heat transfer, Ns_T, the pressure drop along the first stream and the pressure drop along the second stream. Figure 9 shows that the values of the entropy generation number due to the last two contributions, Ns_P, is too low compared with that received from the first one, Ns_T, so it can be neglected. Then the first source can be used to find minimum entropy generation number.

As clear from Figs. 10 and 11 and as it is concluded in Sec. 3.3 for the ideal case (when ε=1, and $\Delta P_1=\Delta P_2=0$), the entropy generation number decreased with the increase of Tr and the decrease of Ω. Therefore, by taking these figures into consideration, the minimum entropy generation number at constant Tr depends mainly on the effectiveness, ε, of the heat exchanger and Ω. The maximum entropy generation number occurs at locations where $\varepsilon=\Omega/(1+\Omega)$ (which can be reached by differentiating the temperature contribution term in Eq. (17) with respect to ε).

Different working regimes have opposite influence on the entropy generation number in the system. Therefore the most wanted combination of the effects of different parameters on minimal ir-

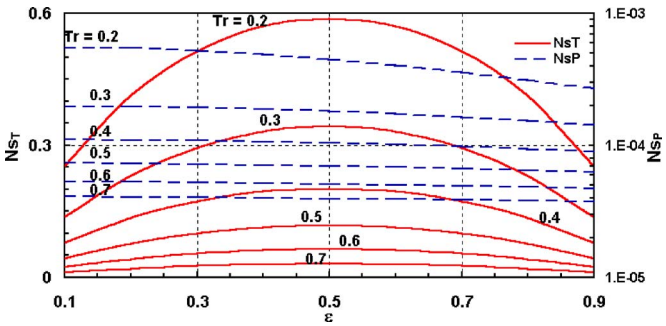

Fig. 9 Entropy generation number due to temperature difference, Ns_T, and pressure drops, Ns_P, against ε at Ω=1 for different Tr

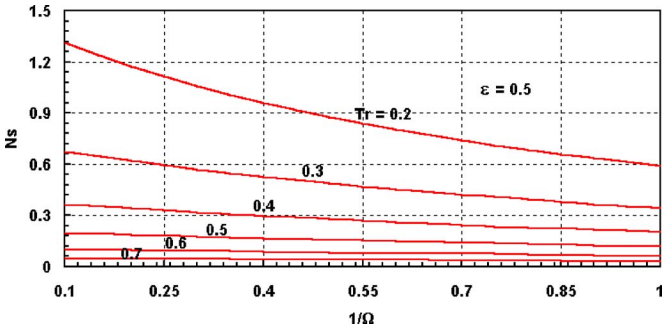

Fig. 10 Entropy generation number, *Ns*, against 1/Ω at ε=0.5 for different Tr

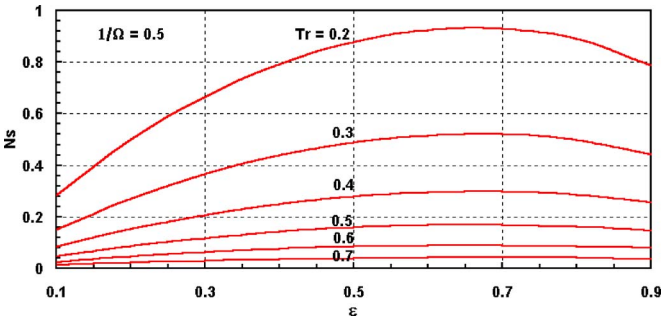

Fig. 11 Entropy generation number, *Ns*, against ε at $1/\Omega = 0.5$ for different Tr

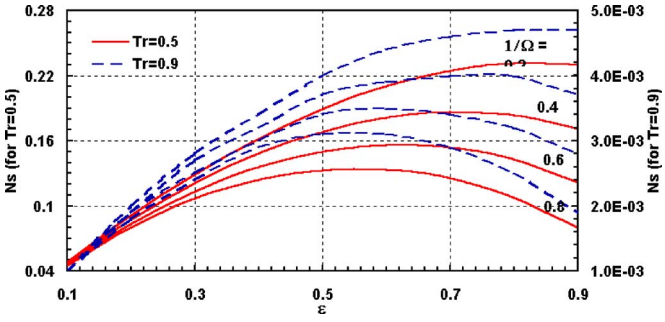

Fig. 14 Entropy generation number, *Ns*, against ε at Tr $= 0.5, 0.9$ for different $1/\Omega$

reversibility should be determined. To facilitate this combination of similar heat exchangers, guide charts (Figs. 12–14) are presented in a form of *Ns* against ε curves for different Ω and Tr.

The above analyses show that increase in the heat exchanger effectiveness, ε, increases the entropy generation numbers, *Nst*, to peak value, depending on the temperature ratios, and then decreases *Nst* to minimum value when ε approaches from one. These peak values are obtained at ε equal 0.5 for balanced heat exchangers and ε greater than 0.5 for the unbalanced heat exchanger, at different temperature ratios. However, small effectiveness means low rate of heat transfer, thus, it is recommended that the heat exchanger should be operated at ε greater than 0.5 and the well operating conditions will be achieved when ε approaches from one where low irreversibility is expected.

5 Conclusions

1. It is concluded that the values of entropy generation number, *Nst*, for heat exchangers are not significantly affected by varying *rP*, *rd* and *SL* values but mainly depend upon the Tr. The maximum value of the entropy generation number, *Nst*, increases when the temperature ratio Tr decreases.
2. The effect of values of pressure drops on the entropy generation number is so small compared with the effect of temperature difference that in general heat transfer irreversibilities are dominant for heat exchangers.
3. Neglecting pressure drops locates the peak value for the irreversibility for balanced heat exchangers at $\varepsilon = 0.5$, and at $\varepsilon = \Omega/(1+\Omega)$ for imbalanced heat exchangers.
4. The heat exchanger should be operated at ε greater than 0.5 and the well operating conditions will be achieved when ε approaches from one where low irreversibility is expected.
5. The new equation, Eq. (17), suggested in this work can be used to express the entropy generation numbers for unbalanced heat exchangers of similar design with only a small deviation from the exact values for unbalanced heat exchangers.
6. The guide charts presented in this work can be used to determine the most wanted combination of the effects of different parameters to obtain minimal irreversibility.

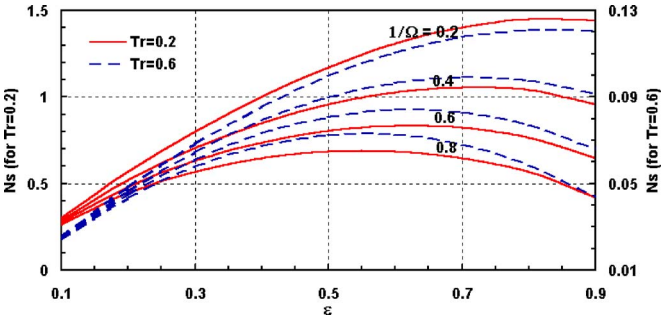

Fig. 12 Entropy generation number, *Ns*, against ε at Tr $= 0.2, 0.6$ for different $1/\Omega$

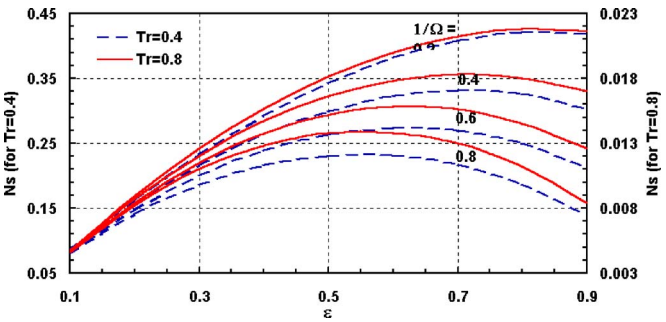

Fig. 13 Entropy generation number, *Ns*, against ε at Tr $= 0.4, 0.8$ for different $1/\Omega$

Nomenclature

A = passage flow area, m^2
CP = specific heat at constant pressure, kJ/kg K
Dh = hydraulic diameter, m
f = friction coefficient
G = mass velocity, kg/m2 s
g = dimensionless mass flow rate, $g = G/(2\rho P)^{0.5}$
$\bar{h}$ = convection heat transfer coefficient, kW/m2 K
L = heat exchanger length, m
$\dot{m}$ = mass flow rate, kg/s
mr = inner to outer side mass flow rate ratio
Ns = entropy generation number
Ns_P = entropy generation number associated with the pressure drops
Ns_T = entropy generation number associated with the temperature difference.
P = air pressure, Pa
R = gas constant, kJ/kg K
Re = Reynolds number, $\mathrm{Re} = G \cdot Dh/\mu$
rd = inner diameters ratio of the double pipe
rP = inner to outer side inlet pressure ratio
SL = inner passage slenderness ratio
St = stanton number, $\mathrm{St} = \bar{h}/(C_P G)$
T = air temperature, K
Tr = inner to outer side inlet air streams temperature ratio

Greek Symbols

ΔP = difference between inlet and exit pressures, Pa

$\Delta \dot{S}_s$ = rate of entropy generation for the isolated system, kW/K
ΔT = temperature difference, K
ε = heat exchanger effectiveness
μ = dynamic viscosity, Pa s
ρ = air density, kg/m^3
τ^2 = dimensionless temp. parameter, $\tau^2=(T_2-T_1)^2/T_1T_2$
Ω = inner to outer side capacity flow rates ratio

Subscripts and Superscripts

1, 2 = inner and outer sides
o = air stream exit condition

References

[1] Bejan, A., 1977, "The Concept of Irreversibility in Heat Exchanger Design: Counter Flow Heat Exchangers for Gas-to-Gas Applications," ASME J. Heat Transfer, **99**, pp. 374–380.
[2] Bejan, A., 1982, *Entropy Generation Through Heat and Flow*, Wiley, New York.
[3] Bejan, A., 1996, "Entropy Generation Minimization: The New Thermodynamics of Finite-Size Devices and Finite-Time Processes," J. Appl. Phys., **79**, pp. 1191–1218.
[4] Bejan, A., 1997, *Advanced Engineering Thermodynamics*, Wiley, New York.
[5] Aceves-Saborio, S., Ranasinghe, J., and Reistad, G. M., 1989, "An Extension to the Irreversibility Minimization Analysis Applied to Heat Exchangers," ASME J. Heat Transfer, **111**, pp. 29–36.
[6] Tondeur, D., and Kvaalen, E., 1987, "Equipartition of Entropy Production. An Optimality Criterion for Transfer and Separation Processes," Ind. Eng. Chem. Res., **26**, pp. 50–56.
[7] De Oliveira, S., Schwarzer, B., Le Goff, P., and Tondeur, D., 1994, "Optimum Entropy, Exergy and Economics of a Heat Exchanger," Int. Chem. Eng., **34**(3), pp. 351–352.
[8] Lozano, M. A., and Valero, A., 1993, "Theory of the Exergetic Costs," Energy, **18**(9), pp. 939–960.
[9] Incorpera, F. P., and Dewitt, D. P., 1996, *Introduction to Heat Transfer*, 3rd ed., Wiley, New York.

Active Thermal Control of Distributed Parameter Systems Excited at Multiple Frequencies

Christoph C. Richter
Institut für Thermodynamik,
Technische Universität Braunschweig,
Hans-Sommer-Straße 5,
38106 Braunschweig, Germany
e-mail: ch.richter@tu-bs.de

John H. Lienhard V
Department of Mechanical Engineering,
Massachusetts Institute of Technology,
77 Massachusetts Avenue, Room 3-162,
Cambridge, MA 02139-4307
e-mail: lienhard@mit.edu

In testing packaged high-power integrated circuits, active thermal control is useful in providing die-level temperature stability. A time-varying heat load is applied to the surface of the package to compensate for the time-varying test power sequence applied to the die. An earlier study determined the proper control heat load for a single-frequency sinusoidal variation in die power subject to a finite allowed temperature variation on the die. Actual test power sequences contain many frequencies at various phase angles, each contributing to the temperature variation of the die. In the present study, we develop a method of controlling multiple frequency test sequences subject to a finite temperature tolerance. It is shown that the total control power may be minimized assigning temperature tolerances to the highest frequencies in the test power sequence. [DOI: 10.1115/1.2130408]

Keywords: conduction, control, electronics, heat transfer, temperature

1 Introduction

Precise temperature control of high-power microprocessor devices during testing is very important in order to properly classify the device performance [1]. The device manufacturer specifies a temperature and an allowed deviation from it during the testing procedure (e.g., 85°C−0/+2°C). A temperature deviation larger than the prescribed one might lead to an improper classification of the tested integrated circuit device (e.g., a 2 GHz device is classified as a 1.8 GHz device) due to reduced signal propagation speeds at higher temperatures [2]. The test process applies computer-controlled electrical signals to the device, and, for high-power devices, this may result in die-average power density in the range of 100 kW/m^2. The frequency components of the die-average power that are energetic enough to affect die temperature range from zero to a hundred hertz or so.

Feedback control of the die temperature is usually not possible, owing to the lack of an accessible die-level temperature sensor. An alternative approach to thermal management in automatic testing equipment was proposed and tested by Sweetland, Lienhard, and Slocum [2,3]. In this approach, the surface of the device under test is heated with laser radiation while simultaneously cooled by forced convection. Through modulation of the laser power, the device temperature can be dynamically stabilized to within a set tolerance.

A significant complication in this scheme arises from the time required for temperature signal propagation from the device package surface to the die, upon which the power is actually dissipated. Figure 1 provides a cross-sectional view of a typical high-power microprocessor device. Sweetland and Lienhard [4] analyzed the effect of the conductive time lag on the control power for sinusoidal die power, showing that it tends to increase the required laser power substantially, and leads to optical powers several times larger than the die power. Minimization of the required laser power, which can amount to hundreds of watts or more, is of great importance in order to limit both the electrical power consumed by the control system and the added load on the test facility's cooling system.

This paper extends the analysis of Sweetland and Lienhard [4] to multifrequency waveforms, with the aim of determining optimal control power for multifrequency test power sequences. We show that the control profile calculation with specified die temperature tolerance presented in [4] is not suitable for nonsinusoidal die power profiles, and we develop a new approach for this situation.

2 Single Frequency Die Power Profiles

The mathematical method follows the one-dimensional model of Sweetland and Lienhard [4]. Figure 1 shows a typical cross section of a high-power microprocessor device. For transient response, the physical model of such a device is reduced to the one-dimensional model shown in Fig. 2 as detailed in [4]. The most important parts for the thermal analysis are the silicon die and the integrated heat spreader (IHS) which is typically made from plated copper. A thin layer of a thermal interface material or grease is used to optimize the heat exchange between die and IHS. As in the previous work, the interface material is taken to have thermal resistance, but negligible heat capacity; and losses to the device substrate are set to zero, giving an upper bound on control power. As in the earlier study, die's heat generation is taken to be uniform over its area, so that attention may be focused on the analysis of frequency effects on the control scheme (see [5] for numerical studies of nonuniform die heating).

The steady periodic transient response can be found using a complex temperature approach [6]. All steady components of power and temperature be may set to zero, by superposition, and attention will be directed to the time-varying response. It is assumed that the solution to the temperature profile in the complex plane takes the form

$$W(x,t) = X(x)e^{i\omega t} \tag{1}$$

where $i=\sqrt{-1}$ is the imaginary number and ω is the frequency of die power variation; x is measured from the convection side of the IHS. The one-dimensional conduction equation in the IHS can be written

$$\frac{\partial^2 W(x,t)}{\partial x^2} = \frac{1}{a_t}\frac{\partial W(x,t)}{\partial t} \tag{2}$$

where a_t is the thermal diffusivity of the IHS material. The general solution for this equation is known to be

$$X(x) = c_1 e^{-xL(i+1)} + c_2 e^{xL(i+1)} \tag{3}$$

where $L \equiv \sqrt{\omega/2a_t}$ is the unsteady diffusion scale in the IHS.

2.1 IHS Temperature Response. The transient temperature response of the IHS can be found by decomposing the model shown in Fig. 2 into two subsystems and superimposing the results [4], removing all steady components of optical heating, cooling, and die heating. The transient component of die power is a single frequency profile of the form

Contributed by the Heat Transfer Division of ASME for publication in the JOURNAL OF HEAT TRANSFER. Manuscript received August 4, 2004; final manuscript received February 10, 2005. Review conducted by Ramendra P. Roy.

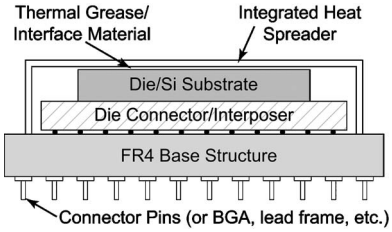

Fig. 1 Typical cross section of a high-power microprocessor device

$$q_d(t) = Q_d \cos(\omega t) \tag{4}$$

where Q_d is the die power density. In this first step of the analysis, the die power is applied directly to the die side of the IHS ignoring the influences of the die and the thermal interface material. The convection side of the IHS is subject to convective boundary conditions, an average heat transfer coefficient h_c with an air temperature $T_{\text{air}}=0$ K, by superposition, and a control power flux

$$q_c(t) = Q_c \cos(\omega t + \alpha) \tag{5}$$

where Q_c is the control power density and α is a phase shift. Of special interest is the die side or back-face (BF) temperature of the IHS which can be found to be

$$\begin{aligned} T_{\text{BF}}(t) = {} & \frac{2Q_c e^{bL}}{kL(A^2+B^2)}\{[A\cos\alpha + B\sin\alpha]\cos(\omega t) \\ & + [B\cos\alpha - A\sin\alpha]\sin(\omega t)\} + \frac{Q_d e^{-bL}}{kL(P^2+R^2)}\{[U\cos(bL) \\ & + V\sin(bL)]\cos(\omega t) + [U\sin(bL) - V\cos(bL)]\sin(\omega t)\} \\ & + \frac{Q_d e^{bL}}{kL(P^2+R^2)}\{[P\cos(bL) + R\sin(bL)]\cos(\omega t) \\ & + [R\cos(bL) - P\sin(bL)]\sin(\omega t)\} \end{aligned} \tag{6}$$

where b is the IHS thickness and k its thermal conductivity. A, B, P, R, U, and V are mathematical constants as defined in [4] and are given in the Appendix. It should be noted that the constants only depend on bL, which is a dimensionless frequency parameter, and the Biot number for the convection side of the IHS, $\text{Bi}_{\text{IHS}}=h_c b/k$.

2.2 Temperature Response of Die. The die normally has small thermal resistance and can be treated as isothermal for the frequencies of interest. Its temperature response can be described by a lumped capacitance model [4]

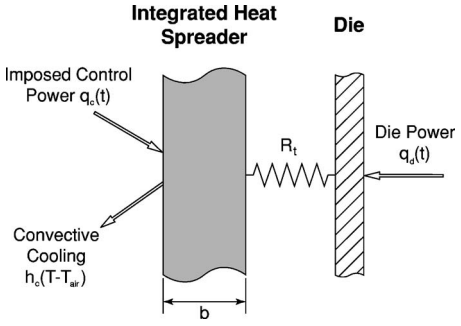

Fig. 2 Schematic diagram of simplified device for transient analysis

$$mc_p\frac{dT_{\text{DIE}}}{dt} = Q_d\cos(\omega t) - \frac{T_{\text{DIE}} - T_{\text{BF}}}{R_t} \tag{7}$$

where m is the die mass per unit area and c_p is the specific heat capacity of the die at constant pressure; R_t is the thermal contact resistance of the interface material. This equation neglects the heat capacity of the thermal interface material between the die and the IHS. The die is lumped because the Biot number $b_{\text{DIE}}/(R_t k_{\text{DIE}})$ is small (in the example below, its value is 0.032).

For ideal die temperature control [$T_{\text{DIE}}(t)=\text{const}$ and $dT_{\text{DIE}}/dt=0$], Eq. (7) can be written as

$$T_{\text{BF}}(t) = -Q_d R_t\cos(\omega t) \tag{8}$$

where the steady component T_{DIE} is set to zero, again by superposition. To compute the control power density amplitude and phase shift Q_c and α that are required to produce the IHS back-face temperature given in Eq. (8), Eq. (6) can be used. The result is

$$\begin{aligned} & \left\{\frac{2Q_c e^{bL}}{A^2+B^2}[A\cos\alpha + B\sin\alpha] + C_1 Q_d + Q_d kLR_t\right\}\cos(\omega t) \\ & + \left\{\frac{2Q_c e^{bL}}{A^2+B^2}[B\cos\alpha - A\sin\alpha] + C_2 Q_d\right\}\sin(\omega t) = 0 \end{aligned} \tag{9}$$

with the additional definitions

$$C_1 = \frac{e^{-bL}[U\cos(bL) + V\sin(bL)] + e^{bL}[P\cos(bL) + R\sin(bL)]}{P^2+R^2} \tag{10}$$

$$C_2 = \frac{e^{-bL}[U\sin(bL) - V\cos(bL)] + e^{bL}[R\cos(bL) - P\sin(bL)]}{P^2+R^2} \tag{11}$$

Equation (9) must hold true for any time t. Therefore, the sine and cosine terms have to vanish separately. Using this requirement, the phase shift α can be computed as

$$\alpha = \arctan\left(\frac{C_1 B + BkLR_t - C_2 A}{C_2 B + AkLR_t + C_1 A}\right) \tag{12}$$

The phase shift α is always picked so that the control power density, Q_c, becomes positive

$$Q_c = -\frac{A^2+B^2}{2e^{bL}[A\cos\alpha + B\sin\alpha]}\{C_1 + kLR_t\}Q_d \tag{13}$$

2.3 Control Profile Calculation With Specified Die Temperature Tolerance. Sweetland and Lienhard [4] assume in their analysis a back-face IHS temperature profile $T_{\text{BF}}(t)$ and use this profile to compute the optimal control power for control to a prescribed temperature tolerance. This method yields a small control power density but not the optimal control power density. Instead of assuming a back-face IHS temperature, the die temperature profile $T_{\text{DIE}}(t)$ is assumed to be

$$T_{\text{DIE}}(t) = \frac{\Delta T}{2}\cos(\omega t + \beta) \tag{14}$$

where ΔT is the prescribed temperature tolerance for the device under test (ΔT is defined as the peak-to-peak amplitude of the die temperature profile to be consistent with [4]) and β is an unknown phase shift. In order to compute the control power profile, the back-face IHS temperature profile has to be known. This profile can be computed by using Eq. (14) in Eq. (7) and rearranging the resulting equation to T_{BF}

$$T_{\mathrm{BF}}(t) = -\left\{\frac{\omega}{\lambda}\frac{\Delta T}{2}\cos\beta + \frac{\Delta T}{2}\sin\beta\right\}\sin(\omega t) - \left\{\frac{\omega}{\lambda}\frac{\Delta T}{2}\sin\beta - \frac{\Delta T}{2}\cos\beta + Q_d R_t\right\}\cos(\omega t) \quad (15)$$

where $\lambda = 1/mc_pR_t$ ($1/\lambda$ is the lumped-capacity time constant associated with Eq. (7)). To derive Eq. (6) it was assumed that the die power is applied at the back face of the IHS neglecting the thermal contact resistance R_t. Equation (7) can be used to find the actual heat flux from the die into the IHS. This heat flux takes on the form

$$q_{\mathrm{BF}}(t) = Q_{\mathrm{BF}}\cos(\omega t + \gamma) \quad (16)$$

with

$$Q_{\mathrm{BF}} = \frac{1}{2}\sqrt{4Q_d^2 + 4Q_d\omega mc_p\Delta T\sin\beta + (\omega mc_p\Delta T)^2} \quad (17)$$

$$\gamma = \arctan\left(-\frac{\omega mc_p\Delta T\cos\beta}{\omega mc_p\Delta T\sin\beta + 2Q_d}\right) \quad (18)$$

Using this corrected heat flux, Eq. (6) can be written as

$$T_{\mathrm{BF}}(t) = \left\{\frac{2Q_c e^{bL}}{A^2+B^2}[A\cos\alpha + B\sin\alpha] + \frac{kL}{\lambda}\omega\frac{\Delta T}{2}\sin\beta - kL\frac{\Delta T}{2}\cos\beta + Q_d kLR_t + (C_1 + C_2\tan\gamma)\left(Q_d + \omega mc_p\frac{\Delta T}{2}\sin\beta\right)\right\}\cos(\omega t) + \left\{\frac{2Q_c e^{bL}}{A^2+B^2}[B\cos\alpha - A\sin\alpha] + \frac{kL}{\lambda}\omega\frac{\Delta T}{2}\cos\beta + kL\frac{\Delta T}{2}\sin\beta + (C_2 - C_1\tan\gamma)\left(Q_d + \omega mc_p\frac{\Delta T}{2}\sin\beta\right)\right\}\sin(\omega t) \quad (19)$$

This equation has to hold true for any time t, which yields a phase shift α

$$\alpha = \arctan\left(\frac{-(C_2^*\lambda B + C_1^*\omega A)\Delta T\cos\beta + (C_1^*\omega B - C_2^*\lambda A)\Delta T\sin\beta + (C_1 B + BkLR_t - C_2 A)\lambda 2Q_d}{(C_1^*\omega B - C_2^*\lambda A)\Delta T\cos\beta + (C_2^*\lambda B + C_1^*\omega A)\Delta T\sin\beta + (C_2 B + AkLR_t + C_1 A)\lambda 2Q_d}\right) \quad (20)$$

where C_1^* and C_2^* are defined as

$$C_1^* = kL + \lambda mc_pC_1 \quad \text{and} \quad C_2^* = kL + \omega mc_pC_2 \quad (21)$$

The control power for this control case can be computed by substituting Eq. (20) into

$$Q_c = -\frac{A^2+B^2}{2e^{bL}[A\cos\alpha + B\sin\alpha]}\left\{\frac{kL}{\lambda}\omega\frac{\Delta T}{2}\sin\beta - kL\frac{\Delta T}{2}\cos\beta + Q_d kLR_t + (C_1 + C_2\tan\gamma)\left(Q_d + \omega mc_p\frac{\Delta T}{2}\sin\beta\right)\right\} \quad (22)$$

which is derived from Eq. (19) by forcing sine and cosine terms to vanish separately. The phase shift α is again picked so that the control power density Q_c becomes positive.

The solution for α and Q_c is still dependent on the unknown phase shift β. To find the optimal control power, Eq. (22) has to be minimized with respect to β. This can be done by substituting Eq. (20) into Eq. (22) and setting the first derivative with respect to β of this equation to zero. This yields

$$\beta = -\arctan\left(\frac{[\omega C_1 + \lambda C_2 + (kL + \lambda mc_pC_1)\omega R_t]kL + \omega mc_p(C_1^2 + C_2^2)\lambda}{[\lambda C_1 - \omega C_2 + (kL + \omega mc_pC_2)\lambda R_t]kL}\right) \quad (23)$$

Using this equation for β in Eq. (20) simplifies the phase shift α to

$$\alpha = \arctan\left(\frac{C_1 B + BkLR_t - C_2 A}{C_2 B + AkLR_t + C_1 A}\right) \quad (24)$$

This phase shift is identical to that previously derived for control at constant die temperature (Eq. (12)): The resulting phase shift is not dependent on the prescribed temperature tolerance ΔT. Using Eq. (22) and setting the control power density to zero ($Q_c = 0\ \mathrm{W/m^2}$), allows us to compute the maximal temperature fluctuation (peak-to-peak) for a given die power profile, which occurs when no control power is applied

$$\Delta T_{\max} = \frac{(kLR_t + C_1)\lambda 2Q_d}{(kL + \omega mc_pC_2)\lambda\cos\beta - (kL + \lambda mc_pC_1)\omega\sin\beta} \quad (25)$$

It is interesting to note that the control power density Q_c is linearly dependent on the prescribed temperature tolerance ΔT for the optimal control case

$$Q_c = Q_{c0} - Q_{c1}\Delta T \quad (26)$$

where

$$Q_{c0} = -\frac{A^2+B^2}{2e^{bL}[A\cos\alpha + B\sin\alpha]}\{C_1 + kLR_t\}Q_d \quad (27)$$

$$Q_{c1} = \frac{A^2+B^2}{4e^{bL}[A\cos\alpha + B\sin\alpha]}\left\{\left(kL\frac{\omega}{\lambda} + \omega mc_pC_1\right)\sin\beta - (kL + \omega mc_pC_2)\cos\beta\right\} \quad (28)$$

The constant part of the control power density Q_{c0} is the control power that has been calculated previously for control to constant die temperature (Eq. (13)). The linear coefficient Q_{c1} is not dependent on the die power density, Q_d, but will increase with an increase in the frequency of die power fluctuation ω. This result is of special importance for the discussion of nonsinusoidal control power profiles.

Using the method presented in [4] to compute the optimal control profile for a prescribed temperature tolerance, the phase shift β was found to be

$$\beta = \arctan(-\omega mc_pR_t) \quad (29)$$

This phase shift will yield a small, but not optimal, control power density as can be seen in the following example.

Example. A dimensional example for the control of a single-

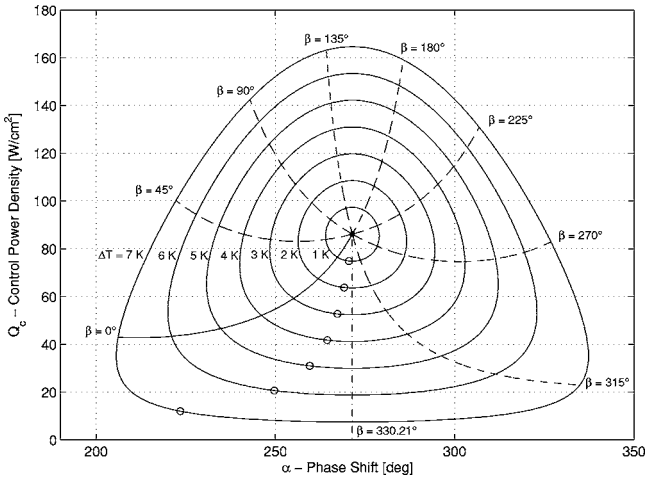

Fig. 3 Control power densities and phase shifts for single frequency die power profile (ω=5 Hz and Q_c=10 W/cm^2) and multiple prescribed temperature tolerances ΔT. The problem properties are given in Tables 1 and 2. The circles ○ mark the points computed using the method given in [4].

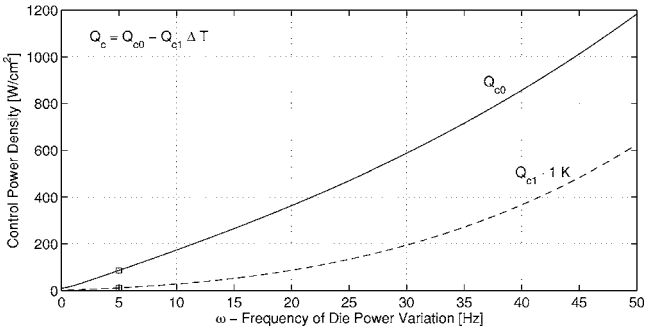

Fig. 4 Control power density for optimal control of a single frequency die power profile with Q_d=10 W/cm^2 and frequencies from zero to 50 HZ

frequency die power profile to a prescribed temperature tolerance is given in Fig. 3. The material data for this example is given in Table 1, and further properties, including the geometry, are presented in Table 2. (The geometrical values are representative and are chosen only for purposes of illustration.) The die power profile is given by Eq. (4) with a frequency of 5 Hz and a die power density magnitude of Q_d=10 W/cm^2. The prescribed temperature tolerance is varied from 0 K to 7 K in increments of 1 K. The center point in Fig. 3 marks the solution for a constant die temperature $\Delta T \equiv 0$. Every ring around this center point represents the solution for a single prescribed temperature tolerance and phase shifts $0 \leqslant \beta \leqslant 2\pi$. The optimal solution is represented by the vertical line at β=330.21 deg: Note that the intersection points of the optimal solution and the rings are equally spaced; this follows from Eq. (26). The points computed using the method proposed by Sweetland and Lienhard [4] are marked with circles. It can be seen that they are relatively close to the optimal solution in terms of the control power density Q_c but yield different phase shifts α. The maximal temperature fluctuation for this example can be computed from Eq. (25), giving $\Delta T_{\max}$=7.67 K.

Figure 4 shows the effect of die power frequency variation on the required control power. The upper line indicates the control power needed to obtain a constant die temperature Q_{c0}. This power grows rapidly with rising frequency due to the fact that the thermal mass of the IHS has to be driven over the same temperature difference faster at higher die power frequency. Clearly, control to zero fluctuation will become impractical owing to the very high control powers required. Commercially available diode lasers will be limited to optical powers of a few hundred watts or so, facilitating heat fluxes in the range of several hundred watts per square centimeter at most [2,3].

The lower line in Fig. 4 shows the control power that can be saved by allowing the die temperature to fluctuate with a representative peak-to-peak amplitude of ΔT=1 K. This lower line will be the same for all die power densities Q_d since $Q_{c1} \neq f(Q_d)$. The net control power with a fluctuation Q_c in Eq. (26) can be seen to decrease as the allowed tolerance ΔT is increased, a fact that will be important for control of a nonsinusoidal die power profile.

Table 1 Material properties for examples

Material	Density	Specific Heat	Thermal Conductivity
Copper (IHS)	8950 kg/m^3	385 J/kg·K	386 W/m·K
Silicon (Die)	2330 kg/m^3	699 J/kg·K	148 W/m·K

Table 2 Problem properties and geometry for examples

Problem Properties			Geometry		
Average heat transfer coefficient	h_c	1200 W/m^2	IHS thickness	b	1.8 mm
Thermal contact resistance	R_t	0.42 K·cm^2/W	Die thickness	b_{DIE}	0.2 mm
Air temperature	T_{air}	0 K			

3 Nonsinusoidal Die Power Profiles

The computation of control power profiles for the more realistic case of nonsinusoidal die power is based on the equations derived in the previous section. Instead of using the die power profile defined in Eq. (4), this profile now becomes a series. In general, this may be an infinite series, but significant power will be associated with only the first N terms, where N must be determined on a case by case basis. The die power profile may thus be written as a truncated series

$$q_d(t) = \sum_{n=1}^{N} (Q_d)_n \cos(\omega_n t + \varphi_n) \tag{30}$$

where n denotes the nth frequency and φ_n its phase shift. The control power profile for this more realistic die power profile is

$$q_c(t) = \sum_{n=1}^{N} (Q_c)_n \cos(\omega_n t + \varphi_n + \alpha_n) \tag{31}$$

In order to control the die temperature to a prescribed total temperature tolerance, a die temperature profile of the following form is assumed:

$$T_{\mathrm{DIE}}(t) = \sum_{n=1}^{N} \frac{\Delta T_n}{2} \cos(\omega_n t + \varphi_n + \beta_n) \tag{32}$$

The difficulty in controlling a nonsinusoidal die power profile arises from this equation. The prescribed temperature tolerance ΔT is the peak-to-peak amplitude of Eq. (32). There is no a priori basis for dividing this total tolerance among the amplitudes and phase shifts of the individual frequencies ΔT_n. If the individual tolerances ΔT_n are specified, then the corresponding control power for frequency ω_n may be calculated by using the same method as for a single frequency to find $(Q_c)_n$ and α_n. An optimal division of the total tolerance among the component frequencies may be calculated analytically only for certain simple cases, and in general it must be found by numerical interation.

An upper bound on the amplitude of Eq. (32) is given by

Table 3 Results for square wave die power profile with a prescribed temperature tolerance $\Delta T=2$ K

	n	1	2	3	4	peak-to-peak
Frequency	ω_n	5 Hz	15 Hz	25 Hz	35 Hz	amplitude
Control power phase shift	α_n	271.45°	292.90°	309.72°	324.84°	
Die temperature phase shift	β_n	330.21°	305.86°	293.91°	287.72°	
Maximal temperature fluctuation	$(\Delta T_{max})_n$	9.77 K	2.17 K	0.90 K	0.48 K	9.62 K
Prescribed temperature tolerance	ΔT_n					
before optimization		0 K	0.62 K	0.90 K	0.48 K	1.94 K
after optimization		0 K	0.69 K	0.90 K	0.48 K	2.00 K
Control power density	$(Q_c)_n$	109.59 W/cm^2	76.76 W/cm^2	0 W/cm^2	0 W/cm^2	371.60 W/cm^2
for control to $\Delta T=0$ *K*	$(Q_{c0})_n$	109.59 W/cm^2	112.60 W/cm^2	119.79 W/cm^2	130.14 W/cm^2	

$$\Delta T=\sum_n \Delta T_n \tag{33}$$

which can be used for an initial guess of the temperature tolerances, ΔT_n. Some iteration will usually be necessary to get from this initial guess to the optimal solution. The proposed process of splitting the total temperature tolerance follows from one main conclusion from the previous section: The possible gain in control power for a specific temperature tolerance is larger the higher the frequency. In other words, applying a temperature tolerance to a higher frequency will lead to a larger reduction of the required control power than applying the same temperature tolerance to a lower frequency. Therefore, the following steps will yield an optimized control power profile:

1. Sort the frequency data according to their frequencies, ω_n (where $n=1,\ldots,N$), starting with the lowest frequency that gets the index $n=1$. Compute the maximal temperature fluctuation for the uncontrolled case $(\Delta T_{\max})_n$ for each frequency using Eq. (25).
2. The total prescribed temperature tolerance ΔT can now be split into temperature tolerances for each frequency ΔT_n. This can be done using Eq. (33) as follows. The splitting process starts with the highest frequency ($n=N$). If the total prescribed temperature tolerance is larger than the maximal temperature fluctuation for this frequency n, its prescribed temperature tolerance is simply

$$\Delta T_n=(\Delta T_{\max})_n \tag{34}$$

and this temperature tolerance is subtracted from the total prescribed temperature tolerance. This step is repeated for the next lower frequency until the remaining total prescribed temperature tolerance is smaller than the maximal temperature fluctuation $(\Delta T_{\max})_n$. If that is the case, the temperature tolerance ΔT_n becomes

$$\Delta T_n=\Delta T-\sum_{n+1}^{N}(\Delta T_{\max})_n \tag{35}$$

All remaining lower frequencies have to be controlled to $\Delta T_n=0$ K.
3. The control power computed in steps 1 and 2 is too large, because it is based on the upper bound Eq. (32). The actual amplitude of the die temperature can now be computed by evaluating Eq. (32). The difference between the actual amplitude and the prescribed temperature tolerance is then added to the lowest frequency for which $\Delta T_n\neq 0$. This step has to be repeated until the difference is smaller than a desired accuracy ε.

Knowing the temperature tolerances for each frequency n, the required phase shifts α_n and β_n as well as the control power densities, $(Q_c)_n$, can be computed from Eqs. (22)–(24), respectively. The control power profile can be evaluated from Eq. (31).

Comparison of the uncontrolled $(\Delta T)_{\max}$ for the highest frequency N in the truncated series to the overall tolerance gives an indication of whether the series has been truncated at too low a value of N. The sensitivity of the result to the chosen N may be checked by changing the value of N.

Example. A square wave die power profile and a triangular wave die power profile are used as dimensional examples for the control of a nonsinusoidal die power profile. The square wave profile can be written as

$$q_d(t)=\frac{4Q}{\pi}\sum_{n=1}^{4}\frac{1}{2n-1}\cos\left((2n-1)\omega\cdot 2\pi\cdot t-\frac{\pi}{2}\right) \tag{36}$$

where Q is the amplitude of the square wave[1] and ω its frequency in hertz. The die power profile is assumed to have an amplitude $Q=10$ W/cm^2 with a frequency of $\omega=5$ Hz. Further properties are given in Tables 1 and 2. Table 3 provides an overview of the results. The first two lines give the phase shifts α_n and β_n and the third line the maximal temperature fluctuations for the uncontrolled case $(\Delta T_{\max})_n$. The next two lines are the temperature tolerances ΔT_n before and after the optimization described previously. Note that the prescribed temperature tolerances for the first two frequencies equal the maximal temperature fluctuations for these frequencies. The temperature tolerance for the third frequency is changed during the optimization process to match the actual die temperature magnitude and the prescribed total temperature tolerance with an accuracy $\varepsilon=10^{-4}$ K. The temperature tolerances ΔT_n before the optimization sum up to the prescribed total temperature tolerance ΔT according to Eq. (33) whereas the sum of the temperature tolerances ΔT_n after the optimization is larger than ΔT. The next line gives the control power densities $(Q_c)_n$ after the optimization process. The control power densities for the first two frequencies are zero since these two frequencies are allowed to fluctuate uncontrolled $(\Delta T_n=(\Delta T_{\max})_n)$. The last line shows the control power densities $(Q_{c0})_n$ that are required to control the die temperature to be constant $(T_{\mathrm{DIE}}=0)$.

Figure 5 shows the temperature and power profiles for this example. The upper figure shows the convection-side and the backface temperature profile of the IHS along with the die temperature profile. The lower figure shows the die power and the control power profile. The die power profile has the form of a square wave whereas the control power profile only consists of two frequencies as given in Table 3. The control power necessary to control a single frequency die power profile with the same power density and frequency is, according to Fig. 3, $Q_c=63.64$ W/cm^2. This control power is about a third of the power required to con-

[1]Half the peak-to-peak amplitude.

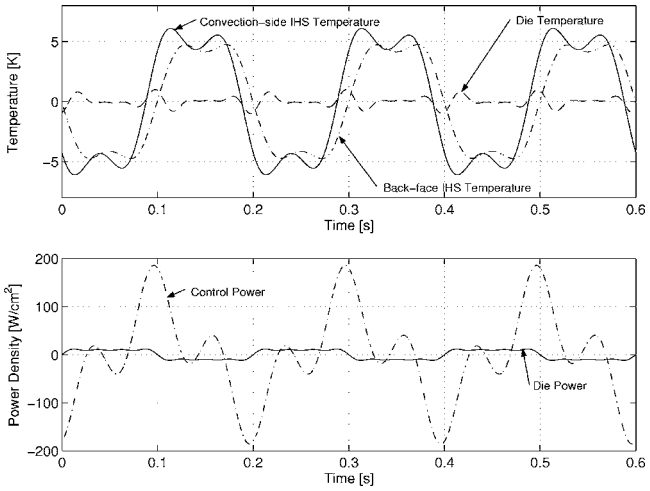

Fig. 5 Temperature and power profiles for square wave die power profile and a prescribed temperature tolerance of $\Delta T = 2$ K. Properties are given in Tables 1 and 2.

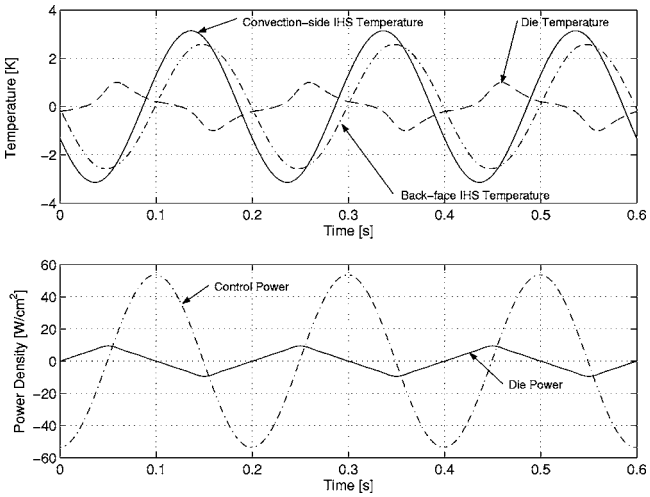

Fig. 6 Temperature and power profiles for triangular wave die power profile and a prescribed temperature tolerance of $\Delta T = 2$ K. Properties are given in Tables 1 and 2.

trol a square wave die power profile. The reason for this large difference can be found in the relatively sharp edges in the square wave die power profile which drive the temperature faster than a sine wave does.

The second example is for a triangular wave die power profile of the form

$$q_d(t) = \frac{8Q}{\pi^2}\sum_{n=1}^{4}\frac{1}{(2n-1)^2}\cos\left((2n-1)\omega\cdot 2\pi\cdot t + (-1)^n\frac{\pi}{2}\right) \tag{37}$$

The die power density is again set to $Q_d = 10\ \mathrm{W/cm^2}$ and the frequency to $\omega = 5$ Hz. The results for this example are summarized in Table 4. Only the temperature tolerance for lowest frequency ΔT_4 is not equal to its maximal (uncontrolled) temperature fluctuation, $(\Delta T_{\max})_1$, and is changed during the optimization process. The phase shifts α_n and β_n are the same as for the square wave die power profile since they are only dependent on the frequencies ω_n. Figure 6 shows the temperature and power profiles for this example. The required control power of $Q_c = 53.63\ \mathrm{W/cm^2}$ is even smaller than for a single frequency die power profile.

4 Summary

The temperature control in a distributed-parameter thermal system presented in [4] has been extended to nonsinusoidal input power profiles. A method for determining the optimal control power has been developed for a single frequency power input and was extended to find the optimal control power profile for nonsinusoidal input power profiles. It is shown that control tolerances should be assigned to the highest frequencies first, so as to limit the total power required. The control power scheme developed in this paper could help to reduce optical laser power and therefore costs for the proposed control method.

Acknowledgment

C.C.R. would like to thank the German Academic Exchange Service and the German National Academic Foundation for financial support of this work. J.H.L. gratefully acknowledges partial support from Teradyne, Inc.

Nomenclature

A, B, P, R, U, V = Mathematical constants, see the Appendix
a_t = Thermal diffusivity, $\mathrm{m^2/s}$
$\mathrm{Bi_{IHS}}$ = Biot number for top side of IHS $h_c b/k$
b = IHS thickness, m
C_1, C_2 = Mathematical constants, Eqs. (10) and (11)
C_1^*, C_2^* = Mathematical constants, Eq. (21)
c_1, c_2 = Mathematical constants, Eq. (3)
c_p = Specific heat capacity at constant pressure, J/kg K
h_c = Average convective transfer coefficient $\mathrm{W/m^2\ K}$

Table 4 Results for triangular wave die power profile with a prescribed temperature tolerance $\Delta T = 2$ K

	n	1	2	3	4	peak-to-peak
Frequency	ω_n	5 Hz	15 Hz	25 Hz	35 Hz	amplitude
Control power phase shift	α_n	271.45°	292.90°	309.72°	324.84°	
Die temperature phase shift	β_n	330.21°	305.86°	293.91°	287.72°	
Maximal temperature fluctuation	$(\Delta T_{max})_n$	6.22 K	0.46 K	0.11 K	0.04 K	6.70 K
Prescribed temperature tolerance	ΔT_n					
before optimization		1.38 K	0.46 K	0.11 K	0.04 K	1.95 K
after optimization		1.44 K	0.46 K	0.11 K	0.04 K	2.00 K
Control power density	$(Q_c)_n$	53.63 W/cm²	0 W/cm²	0 W/cm²	0 W/cm²	107.26 W/cm²
for control to $\Delta T = 0$ K	$(Q_{c0})_n$	69.77 W/cm²	23.89 W/cm²	15.25 W/cm²	11.84 W/cm²	

i = The imaginary number $\sqrt{-1}$
k = Thermal conductivity, W/m K
L = Unsteady diffusion scale in IHS $\sqrt{\omega/2a_t}$, 1/m
m = Die mass per unit area, kg/m^2
n = Index for nonsinusoidal die power profiles
Q_{BF} = Power density of heat flux from die into IHS, Eq. (17), W/m^2
Q_c = Control power density, W/m^2
Q_{c0} = Constant part of control power for optimal control case, Eq. (27), W/m^2
Q_{c1} = Linear coefficient of control power for optimal control case, Eq. (28), W/m^2 K
Q_d = Die power density, W/m^2
$q_{BF}(t)$ = Heat flux from die into IHS, Eq. (16), W/m^2
$q_c(t)$ = Control power flux, Eqs. (5) and (31), W/m^2
$q_d(t)$ = Die power flux, Eqs. (4) and (30), W/m^2
R_t = Thermal contact resistance, K m^2/W
$T_{BF}(t)$ = Back-face IHS temperature, Eq. (6), K
$T_{DIE}(t)$ = Die temperature, K
ΔT = Prescribed temperature tolerance, K
ΔT_{max} = Maximal temperature fluctuation for uncontrolled case, Eq. (25), K
t = Time, s
$W(x,t)$ = Complex temperature solution, Eq. (1)
$X(x)$ = Real part of complex temperature solution, K
x = Distance from convection-side of IHS, m

Greek Symbols

$\alpha, \beta, \gamma, \varphi$ = Phase shifts, rad
λ = Lumped frequency response of die $1/mc_pR_t$, 1/s
ω = Frequency of die power variation, rad/s

Appendix: Mathematical Constants

The following mathematical constants are taken from [4]:

$$A = \frac{\mathrm{Bi}_{IHS}}{bL}\cos(bL)(e^{2bL}+1) - [\cos(bL)+\sin(bL)] + e^{2bL}[\cos(bL)-\sin(bL)]$$

$$B = \frac{\mathrm{Bi}_{IHS}}{bL}\sin(bL)(e^{2bL}-1) - [\cos(bL)-\sin(bL)] + e^{2bL}[\cos(bL)+\sin(bL)]$$

$$P = e^{bL}[\cos(bL)-\sin(bL)] - \frac{e^{-bL}}{D}[G\cos(bL)+N\sin(bL)]$$

$$R = e^{bL}[\sin(bL)+\cos(bL)] + \frac{e^{-bL}}{D}[G\sin(bL)-N\cos(bL)]$$

$$U = \frac{P\cdot E + R\cdot F}{D}$$

$$V = \frac{P\cdot F - E\cdot R}{D}$$

where

$$D = h_c^2 + 2h_c kL + 2(kL)^2$$

$$E = 2(kL)^2 - h_c^2$$

and $F = 2h_c kL$

References

[1] Pfahnl, A. C., Lienhard, V. J. H., and Slocum, A. H., 1999, "Thermal Management and Control in Testing Packaged Integrated Circuit (IC) Devices," *Proc. 34th Intersociety Energy Conversion Conf.*, paper no. 1999-01-2723.
[2] Sweetland, M., Lienhard, V. J., and Slocum, A. H., 2005, "A Convection/Radiation Temperature Control System for High Power Density Electronic Device Testing" (unpublished).
[3] Sweetland, M., 2001, *Design of Thermal Control Systems for Testing of Electronics*, PhD thesis, Massachusetts Institute of Technology, Cambridge, MA.
[4] Sweetland, M., and Lienhard, V. J. H., 2003, "Active Thermal Control of Distributed Parameter Systems With Application to Testing of Packaged (IC) Devices," ASME J. Heat Transfer, **125**, pp. 165–174.
[5] Richter, C. C., 2004, "Active Thermal Control of Distributed Parameter Systems Excited at Multiple Frequencies," Diplomarbeit, Massachusetts Institute of Technology, Cambridge, MA.
[6] Baehr, H. D., and Stephan, K., 2004, *Wärme und Stoffübertragung*, Springer, Berlin.

Viscous Fluid Displacement by the Growing Bubble

Abdullah Abbas Kendoush
Department of Heat Transfer,
Center of Engineering Physics,
Division of Physical Sciences and Research,
Ministry of Sciences and Technology,
Baghdad, Iraq
e-mail: kendoush@yahoo.com

Equations were derived for the forces experienced by the growing bubble in displacing the liquid radially. The derivation was based on integrating the viscous dissipation function over the entire surface of the bubble. The resulted equations were applicable to bubbles in boiling and in cavitation. The derived equations were validated by applying them to the heterogeneous nucleation and growth of bubbles from cavities in pool boiling and in cavitation. The derived equations approached asymptotically the familiar equation of heterogeneous nucleation and growth of bubbles.
[DOI: 10.1115/1.2130409]

Keywords: heat transfer, boiling, cavitation, bubble growth, analytical solution, viscous dispersion

1 Introduction

Flow systems involving a mixture of gas or vapor bubbles and liquid have many applications in chemical and mechanical engineering industries and in nuclear-power generation. In all these applications, bubbles exhibit frictional dissipation due to the viscosity of the liquid.

The viscous dissipation at the surfaces of gas bubbles is quite different from that of vapor bubbles originating from their own liquids in superheated and non-equilibrium states. Vapor bubbles grow in size as they rise through the liquid. These bubbles accelerate during their rise in superheated liquids. They experience drag in their trajectory besides other forces, e.g., impulse due to virtual mass, gravity, lift, history, and buoyancy. These forces are either in the direction of motion or opposite to it. There are other forces that act in the radial direction of the bubble, e.g., pressure forces, surface tension, and fluid displacement force. Determination of these forces on the growing bubble is equally important for the exact prediction of the parameters associated with boiling, flashing flow, and cavitation.

Basically there are three different mechanisms that control the rate of growth of a bubble. These mechanisms are referred to as inertia-controlled, thermal diffusion-controlled, and mass diffusion-controlled growth. Theoretical studies of the thermal diffusion-controlled growth of a vapor bubble in a uniformly superheated liquid have been reported earlier by Plesset and Zwick [1], Scriven [2], and Bankoff [3]. All the results agree that the bubble grows as a function proportional to the square root of time.

A unified theory for the thermal diffusion-controlled growth and collapse of bubbles is produced by Riznic, Kojasoy, and Zuber [4]. They integrated the energy equation and produced closed form solutions for the growth and collapse at high and low Jakob (Ja) numbers. They also showed that for large Ja number, the radius of the bubble depends upon the first power of Ja number.

Contributed by the Heat Transfer Division of ASME for publication in the JOURNAL OF HEAT TRANSFER. Manuscript received January 23, 2005; final manuscript received July 26, 2005. Review conducted by Jacob Chung.

The significant contribution to the understanding of thermohydrodynamics of growing and collapsing bubble derives from two careful analytical and numerical studies by Magnaudet and Legendre [5] and Legendre et al. [6]. These papers considered the possible forces encountered during growing and collapsing bubbles, namely, viscous, virtual mass, buoyancy, and history. They mentioned the fluid displacement force, but in association with the virtual mass.

In general, not enough attention has been paid to the effects of the displacement forces of the liquid on the growing bubble. Therefore, we decided to undertake the task of obtaining some analytical expressions of relatively simple form regarding this phenomenon.

2 Theoretical Analysis

Assume that the fluid is incompressible, neglect the boundary layer separation at the bubble surface, and let the bubble maintains a spherical shape during growth. Assume a stationary bubble of radius a growing in a uniformly superheated liquid. The flow field around this bubble is purely radial and given by Leal [7] as follows

$$V_r = \left(\frac{a}{r}\right)^2 \frac{da}{dt} \tag{1}$$

Here r is the polar coordinate and t is time. The main assumption of Eq. (1) is that the volume rate of production of vapor must be equal to the rate of increase of bubble size. The total rate of viscous dissipation E due to this radial motion of the liquid is given by Taylor [8] and utilized previously by Kendoush [9] as follows:

$$E = \frac{1}{2}\int_0^{\pi} \mu_f \left[\frac{\partial}{\partial r}(V_r)^2\right]_{r=a} 2\pi a^2 \sin\theta d\theta \tag{2}$$

Here μ_f is the absolute viscosity of liquid and θ is the polar coordinate. Substituting Eq. (1) into Eq. (2) and completing the integration leads to the following:

$$E = 8\pi\mu_f a\left(\frac{da}{dt}\right)^2 \tag{3}$$

The displacement force in the liquid due to the growing bubble acts radially in the entire region around the surface of the bubble. It is given as follows:

$$F = E\left(\frac{da}{dt}\right)^{-1} \tag{4}$$

This is a new equation that can be applied to bubble growth controlled by thermal diffusion, mass diffusion, or inertia. For bubble growth controlled by thermal diffusion and at high Ja numbers (Ja$>$16), Riznic et al. [4] derived the following equation under the following assumptions:

- Moving boundary during phase change
- Neglecting effects of inertia and of surface tension
- Time dependent interface temperature

$$a = \pi \mathrm{Ja}\left(\frac{\alpha t}{3}\right)^{1/2} \tag{5}$$

where α represents the thermal diffusivity of liquid and the Jakob number ($\mathrm{Ja}=\rho_f Cp\Delta T/\rho_g \lambda$) represents the ratio of the maximum bubble radius to the thickness of the superheated film around the bubble (Boucher and Alves [10]). High Ja number fluids are associated with a thin layer of superheated liquid around the bubble and vice versa. Here ρ_f and ρ_g are the density of liquid and vapor respectively, Cp is the specific heat of liquid, ΔT is the temperature excess, and λ is the latent heat of evaporation.

The differentiation of Eq. (5) gives

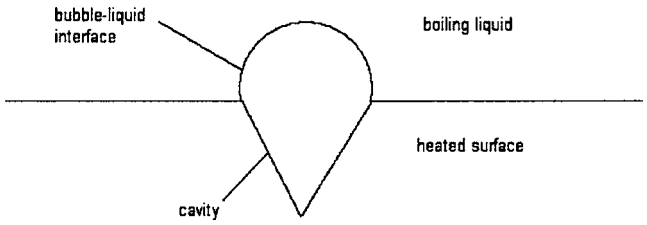

Fig. 1 Ideal cavity on the heated surface

$$\frac{da}{dt} = \frac{\pi}{2}\mathrm{Ja}\left(\frac{\alpha}{3t}\right)^{1/2} \tag{6}$$

Substituting Eqs. (5) and (6) into Eq. (4) gives the displacement force at high Ja number as follows:

$$F_H = \frac{4}{3}\pi^3\mu_f\alpha(\mathrm{Ja})^2 \tag{7}$$

For low Ja numbers, Ja$<$16, Riznic et al. [4] derived the following equation under the same assumptions mentioned above:

$$a = (2\alpha\mathrm{Jat})^{1/2} \tag{8}$$

The differentiation of Eq. (8) leads to

$$\frac{da}{dt} = \left(\frac{\alpha\mathrm{Ja}}{2t}\right)^{1/2} \tag{9}$$

Substituting Eqs. (8) and (9) into Eq. (4) gives the displacement force at low Ja number

$$F_L = 8\pi\mu_f\alpha\mathrm{Ja} \tag{10}$$

3 Validation and Discussion

The forces derived earlier shall be applied to the case of the heterogeneous nucleation and growth of bubbles in pool boiling. The nucleation is based on adopting an ideal cavity as shown in Fig. 1. As the bubble grows, its radius of curvature changes. The radius of curvature equals to the radius of the cavity opening. This means that the contact angle is 90°.

The mechanical equilibrium equation of the bubble whose inside vapor pressure is P_g is given by the following:

$$P_g = P + \frac{2\sigma}{a} + \frac{F}{2\pi a^2} \tag{11}$$

where σ is the surface tension of the bubble, P is the local hydrostatic pressure of the liquid, and F should be provided either from Eq. (7) or (10) depending on the magnitude of the Ja number. Note that a hemispherical bubble (Fig. 1) was considered in Eq. (11). A more general case of Eq. (11) is given below

$$P_g = P + \frac{2\sigma}{a} + \frac{F}{x\pi a^2} \tag{12}$$

where x represents the fraction of the surface area of the bubble that emerges from the mouth of the cavity. The fraction x is a function of the contact angle. Figure 2 illustrates the forces acting on a spherically shaped growing bubble.

For the bubble to grow at the mouth of the cavity, the surface temperature T_s must be higher than the saturation temperature by the following amount:

$$T_s = T_{\mathrm{sat}} + \frac{dT}{dP}(P_g - P) \tag{13}$$

Here T_{sat} is the saturation temperature. Using the equation of Clausius-Clapeyron along the P-T saturation curve, yields

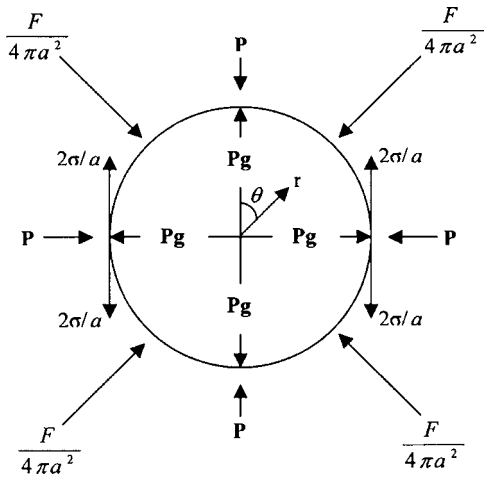

Fig. 2 Forces acting on a spherical vapor bubble

$$\frac{dP}{dT} = \frac{\lambda}{(\nu_g - \nu_f)T_{\mathrm{sat}}} \tag{14}$$

Here ν_g and ν_f are the specific volume of vapor and liquid, respectively. If $\nu_g \gg \nu_f$ and, since $\upsilon_g = 1/\rho_g$, then

$$\frac{dT}{dP} = \frac{T_{\mathrm{sat}}}{\lambda\rho_g} \tag{15}$$

and Eq. (13) becomes the following:

$$T_s = T_{\mathrm{sat}} + \frac{T_{\mathrm{sat}}}{\lambda\rho_g}\left[\frac{2\sigma}{a} + \frac{F}{2\pi a^2}\right] \tag{16}$$

In this equation, a hemispherical bubble was assumed at the mouth of the cavity. Equation (16) reduces to the familiar equation of heterogeneous nucleation (Theofanous et al. [11]) upon letting $F \to 0$, that is

$$T_s - T_{\mathrm{sat}} = \frac{2\sigma T_{\mathrm{sat}}}{a\lambda\rho_g} \tag{17}$$

Thus the present solution is valid by its asymptotic approach to Eq. (17). The conditions under which $F \to 0$ are the following: Gas bubbles rising in liquids saturated with the same gas of the bubble exhibit no significant diffusion of gas from liquid into the bubble interior, thus the bubble will not be able to displace liquid around it.

Multiplying both sides of Eq. (16) by h (the boiling heat transfer coefficient, kW/m^2 K) gives the following:

$$q = \frac{hT_{\mathrm{sat}}}{\lambda\rho_g}\left(\frac{2\sigma}{a} + \frac{F}{2\pi a^2}\right) \tag{18}$$

where q is the heat flux, kW/m^2 [$=h(T_s - T_{\mathrm{sat}})$]. Prosperetti and Plesset [12] derived the following equation for the time rate of change of bubble radius caused by fluid inertia:

$$\frac{da}{dt} = \left[\frac{2}{3}\frac{P_g - P}{\rho_f}\right]^{1/2} \tag{19}$$

Substituting Eq. (19) into Eq. (18) by considering Eq. (4) gives

$$q = \frac{hT_{\mathrm{sat}}}{\lambda\rho_g}\left[\frac{2\sigma}{a} + \frac{4\mu_f}{a}\left[\frac{2}{3}\frac{P_g - P}{\rho_f}\right]^{1/2}\right] \tag{20}$$

Kang [13] used water to study boiling heat transfer from a vertical tube with different rough surfaces. For an 11 K superheat, the quantity $P_g - P$ becomes equal to 6×10^4 N/m^2 with P is the atmospheric pressure. Using the water properties at 373 K in Table 1 and for a bubble radius $a = 3$ μm, Eq. (20) becomes the following:

Table 1 Physical properties of water at atmospheric pressure

	373K	298K
ρ_g (kg/m^3)	0.5899	0.0296
ρ_f (kg/m^3)	958.3	996.0
μ_f (Ns/m^2)	283.1x10^{-6}	9x10^{-4}
σ (N/m)	0.0588	0.0718

$$q = 11.66h \tag{21}$$

Bubble radii of 3.5 μm and 4 μm were used in Eq. (20) and plotted in Fig. 3 that shows a comparison between Eq. (20), the experimental data of Kang [13], and the correlation of Cornwell and Houston [14]. The present solution is closer to the experimental data than the correlation of Cornwell and Houston [14]. Upon the increase in the bubble radius a tendency is noticed toward the rougher surface of the heating tube, as small bubbles originate from minute crevices in relatively smooth surfaces. Note that ε in Fig. 3 represents the average tube surface roughness in rms value.

For further comparison with data of the thermal-controlled bubble growth, Koumoutsos et al. [15] performed experimental and theoretical studies on flow boiling. They photographed bubbles in forced-convection nucleate boiling. The heat flux in flow boiling can be given as follows:

$$q = U\lambda\rho_f \tag{22}$$

where U is the mean liquid velocity at the bubble surface. Equating this equation to Eq. (20) yields the following formula for the radius of the bubble:

$$a = \frac{hT_{\text{sat}}\left(2\sigma + 4\mu_f \dfrac{da}{dt}\right)}{U\lambda^2\rho_f\rho_g} \tag{23}$$

Divide through out by a_o (the initial bubble radius) to get the following:

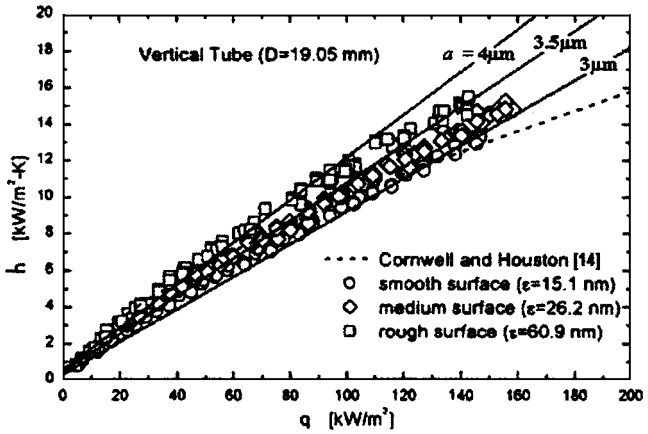

Fig. 3 Comparison of the present solution (—), Eq. (20) with the experimental data of Kang [13] (○◇□) and the correlation of Cornwell and Houston [14] (-------) for boiling bubble

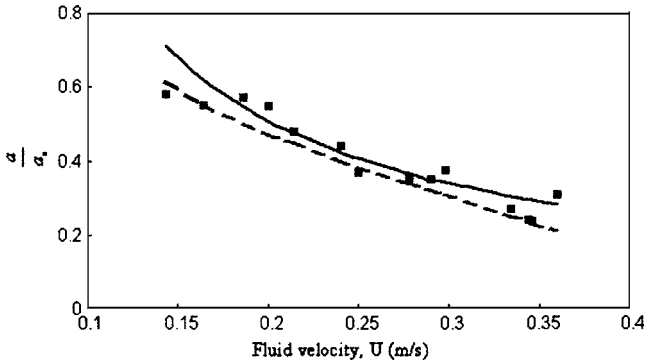

Fig. 4 Comparison of the present solution (—), Eq. (24) with the experimental (■■■) and the theoretical (----) results of Koumoutsos et al. [15] for flow boiling bubble

$$\frac{a}{a_o} = \frac{hT_{\text{sat}}\left(2\sigma + 4\mu_f \dfrac{da}{dt}\right)}{a_o U\lambda^2\rho_f\rho_g} \tag{24}$$

Koumoutsos et al. [15] reported a superheat of 15 K that gives $P_g - P = 7\times10^4$ N/m^2. For $a_o = 1.6$ nm and the water properties at 373 K of Table 1, Eq. (24) is calculated and displayed in Fig. 4 where the agreement of the present solution with the experimental data and theoretical solution of Koumoutsos et al. [15] is noticeable.

For the mass diffusion-controlled bubble growth normally encountered in cavitation, we present the following comparison with the theoretical results of Daily and Johnson [16] that was mentioned by Brennon [17]. Substituting Eq. (19) into Eq. (11) gives the following:

$$P_g - P - \frac{4\mu_f}{a}\left[\frac{2}{3}\frac{P_g - P}{\rho_f}\right]^{1/2} = \frac{2\sigma}{a} \tag{25}$$

Let $y = P_g - P$, this equation becomes as follows:

$$y - \frac{4\mu_f}{a}\left[\frac{2}{3}\frac{y}{\rho_f}\right]^{1/2} = \frac{2\sigma}{a} \tag{26}$$

Using the physical properties of water at 298 K from Table 1, this equation was solved for y at different values of a by using MATLAB and the solution is shown by the solid line in Fig. 5. The dashed line is the solution of Daily and Johnson [16] which represents the locus of peaks as shown in their Fig. 2.4 of Brennon [17]. The agreement between the two solutions is agreeable.

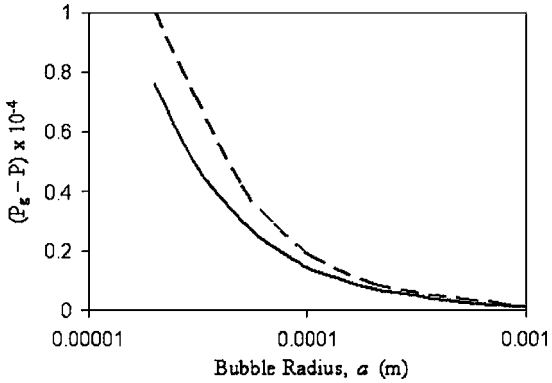

Fig. 5 Comparison of the present solution (—), Eq. (26) with the solution of Daily and Johnson [16] (----) for cavitating bubble

One of the conditions under which the liquid displacement force becomes important and must be accounted for is the exact prediction of the number of bubbles nucleated either homogeneously or heterogeneously as a result of flash evaporation occurred in the core of the water-cooled nuclear power reactors after depressurization following the hypothetical loss of coolant accident.

The importance of the derivation of an explicit formula for the liquid displacement force around the growing bubble justifies the modest mathematical analysis of this paper.

4 Conclusions

A method of calculating analytically the forces due to the displacement of liquid caused by the growing bubble has been presented. This method was based on integrating the viscous dissipation function over the surfaces of the bubble. The derived equations were applied successfully to cases of pool boiling and flow boiling where bubbles are nucleated heterogeneously and expanded from solid surface cavities. The derived solution was also applied to bubble growth due to mass diffusion in the process of cavitation.

Nomenclature

a = bubble radius, m
Cp = specific heat at constant pressure, kJ/kg K
E = viscous dissipation integral, Nm/s
F = liquid displacement force, N
h = boiling heat transfer coefficient, kW/m^2 K
Ja = Jakob number, dimensionless
P = pressure, N/m^2
q = heat flux, kW/m^2
r = polar coordinate, m
t = time, s
T = temperature, K
U = mean liquid velocity, m/s
V_r = radial component of fluid velocity, m/s
x = fraction of bubble area, dimensionless

Greek

α = thermal diffusivity, m^2/s
ε = average tube surface roughness in rms value.
θ = polar coordinate
λ = latent heat of evaporation, kJ/kg
μ = dynamic viscosity, kg/ms
ν = specific volume, m^3/kg
ρ = density, kg/m^3
σ = surface tension, N/m

Subscripts

f = liquid
g = vapor
H = high Jakob number
L = low Jakob number
s = surface
sat = saturation

References

[1] Plesset, M. S., and Zwick, S. A., 1954, "The Growth of Vapor Bubbles in Superheated Liquids," J. Appl. Phys., **25**, pp. 493–500.
[2] Scriven, L. E., 1959, "On the Dynamics of Phase Growth," Chem. Eng. Sci., **10**, pp. 1–13.
[3] Bankoff, S. G., 1966, "Diffusion-Controlled Bubble Growth," Adv. Chem. Eng., **6**, pp. 1–60.
[4] Riznic, J., Kojasoy, G., and Zuber, N., 1999, "On Spherically Phase Change Problem," Int. J. Fluid Mech. Res., **26**, pp. 110–145.
[5] Magnaudet, J., and Legendre, D., 1998, "The Viscous Drag Force on a Spherical Bubble With a Time-Dependent Radius," Phys. Fluids, **10**, pp. 550–554.
[6] Legendre, D., Borce, J., and Magnaudet, J., 1998, "Thermal and Dynamic Evaluation of a Spherical Bubble Moving Steadily in a Superheated or Subcooled Liquid," Phys. Fluids, **10**, pp. 1256–1272.
[7] Leal, L. G., 1992, *Laminar Flow and Convective Transport Processes*, Butterworth-Heinemann, Boston.
[8] Batchelor, G. K., (editor), 1963, *The Scientific Papers of Sir Geoffrey Ingram Taylor*, Vol. 3, Cambridge University Press, Cambridge, UK, pp. 303–308.
[9] Kendoush, A. A., 2001, "Hydrodynamic Model for Bubbles in a Swarm," Chem. Eng. Sci., **56**, pp. 235–238.
[10] Boucher, D. F., and Alves, G. E., 1963, "Dimensionless Numbers," Chem. Eng. Prog., **59**, pp. 75–83.
[11] Theofanous, T. G., Tu, J. P., Dinh, A. T., and Dinh, T. N., 2002, "The Boiling Crisis Phenomenon. Part I: Nucleation and Nucleate Boiling Heat Transfer," Exp. Therm. Fluid Sci., **26**, pp. 775–783.
[12] Prosperetti, A., and Plesset, M. S., 1978, "Vapour-Bubble Growth in a Superheated Liquid," J. Fluid Mech., **85**, pp. 349–368.
[13] Kang, M.-G., 2001, "Diameter Effects on Nucleate Pool Boiling for a Vertical Tube," ASME J. Heat Transfer, **123**, pp. 44–404.
[14] Cornwell, K., and Houston, S. D., 1994, "Nucleate Pool Boiling on Horizontal Tubes: A Convection Based Correlation," Int. J. Heat Mass Transfer, **37**, pp. 303–309.
[15] Koumoutsos, N., Moissis, R., and Spyridonos, A., 1968, "A Study of Bubble Departure in Forced-Convection Boiling," ASME J. Heat Transfer, **90**, pp. 223–230.
[16] Daily, J. W., and Johnson, V. E. Jr., 1956, "Turbulence and Boundary Layer Effects on Cavitation Inception From Gas Nuclei," Trans. ASME, **78**, pp. 1695–1706.
[17] Brennon, C. E., 1995, *Cavitation and Bubble Dynamics*, Oxford University Press, Oxford, UK.

Natural Convection From Two Thermal Sources in a Vertical Porous Layer

Nawaf H. Saeid
School of Mechanical Engineering,
University of Science Malaysia,
14300 Nibong Tebal,
Pulau Pinang, Malaysia

Numerical study of natural convection flow induced by two isothermally heated elements located on adiabatic vertical plate immersed in a Darcian porous medium is carried out in the present article. The natural convection is affected by the Rayleigh number, the separation distance between the elements, their temperature ratio, and the length of the upper element. The numerical results are presented as average Nusselt number versus Rayleigh number for wide ranges of the governing parameters. It is found that the heat transfer from the lower element is not affected by the presence of the upper element for equal temperatures of the elements. The heat transfer from the lower element can be enhanced by increasing the temperature of the upper element due to the suction effect. The average Nusselt number along the upper heated element is found to increase with the increase of any of the governing parameters. [DOI: 10.1115/1.2136367]

Keywords: heat transfer, natural convection, multiple heat sources, porous media, finite volume method

Introduction

Free convection heat transfer along vertical/inclined heated/cooled plate has been studied extensively for both pure fluids and porous media by various authors. The laminar boundary layer approximation is generally used in the analysis due to its wide range of engineering applications. Representative studies participating to this area and convection heat transfer, in general, can be found in the recent books [1–5]. Many authors have carried out studies on free convection about vertical flat plate in porous media. Johnson and Cheng [6] have studied the transient boundary layer flow in a porous medium and obtained similarity solutions for specific variations of wall temperature in time and position. Bejan and Khair [7] obtained similarity solutions for steady-state natural convection heat and mass transfer in boundary layer flow about vertical plates in porous media. Cheng and Pop [8] used the integral method to investigate the transient free-convection boundary layer in a porous medium adjacent to a semi-infinite vertical plate with step change in wall temperature or surface heat flux. Jang and Ni [9] used the finite difference method to investigate the transient free convection with mass transfer from an isothermal vertical flat plate embedded in a porous medium. They found that the final steady-state temperature and concentration profiles are in good agreement with the similarity solution of Bejan and Khair [7] and obtained a simple relation for the propagation of the leading-edge effect. Murthy et al. [10] studied the effect of double stratification on free-convection heat and mass transfer in a Darcian fluid-saturated porous medium using the similarity solution technique of the boundary layer model. Various essential characteristics of steady free and mixed convection in a two-dimensional horizontal or vertical porous layer have been reported in papers by Prasad et al. [11], Lai et al. [12] and Lai and Kulacki [13].

Free convection along a single heat source has been considered in the above-mentioned studies. In practice, quite often the free convection from one heat source affects another one, which may be placed in the wake of the lower one. These kinds of convection from multiple heat source problems have been addressed by, for example, Sparrow and Faghri [14] and Jaluria [15,16]. Their results indicate the dependence of the heat transfer coefficient for an element, located in the wake of another, on the energy inputs/temperatures of the elements and their locations. The purpose of the present study is to investigate the convection heat transfer from an isothermal heat source placed in the wake of another one, when both the heat sources are located on an adiabatic vertical plate immersed in a porous media. The applications include, for example, electronic cooling, high-performance insulation for buildings, grain storage, solar power collectors, and geothermal energy systems. The effects of the separation distance between the elements, the temperature of the heat sources, and the lengths of the heat sources on the natural convection are studied, and results are presented.

Governing Equations

A schematic diagram of a two-dimensional natural convection flow from two isothermal heat sources in vertical porous layer bounded between two vertical walls is shown in Fig. 1.

In the porous medium, Darcy's law is assumed to hold, and the fluid is assumed to be a normal Boussinesq fluid. The viscous drag and inertia terms in the governing equations are neglected, which are valid assumptions for low Darcy and particle Reynolds numbers. The continuity, Darcy, and energy equations for steady flow in an isotropic and homogeneous porous medium can be written as

$$\frac{\partial u}{\partial x}+\frac{\partial v}{\partial y}=0 \tag{1}$$

$$\frac{\partial u}{\partial y}-\frac{\partial v}{\partial x}=\frac{-g\beta K}{\nu}\frac{\partial T}{\partial x} \tag{2}$$

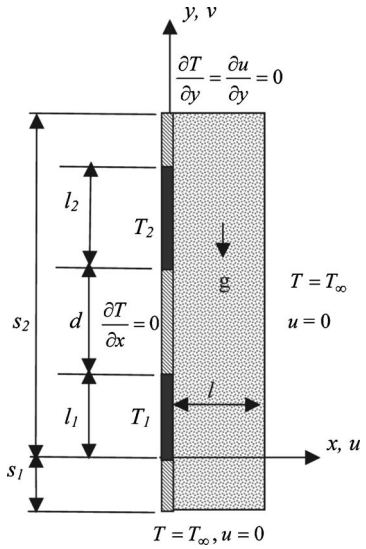

Fig. 1 Schematic diagram of the physical model and coordinate system

Contributed by the Heat Transfer Division of ASME for publication in the JOURNAL OF HEAT TRANSFER. Manuscript received September 1, 2004; final manuscript received October 2, 2005. Review conducted by Yogesh Jaluria.

Table 1 Values of $\overline{Nu_1}/\sqrt{Ra}$ for single heat source with different values of Ra

Ra	100	200	300	400	500	600	700	800	900	1000
$\overline{Nu_1}/\sqrt{Ra}$	0.637	0.707	0.743	0.767	0.784	0.797	0.807	0.816	0.823	0.832

$$u\frac{\partial T}{\partial x}+v\frac{\partial T}{\partial y}=\alpha\left(\frac{\partial^2 T}{\partial x^2}+\frac{\partial^2 T}{\partial y^2}\right) \tag{3}$$

where u and v are the velocity components along the x- and y-axes, T is the fluid temperature, g is the gravitational acceleration, β is the coefficient of thermal expansion, K is the permeability of the porous medium, ν is the kinematic viscosity, and α is the effective thermal diffusivity of the porous medium.

Equations (1)–(3) may be written in terms of the stream function defined as $u=\partial\psi/\partial y$ and $v=-\partial\psi/\partial x$. Subsequent nondimensionalization using

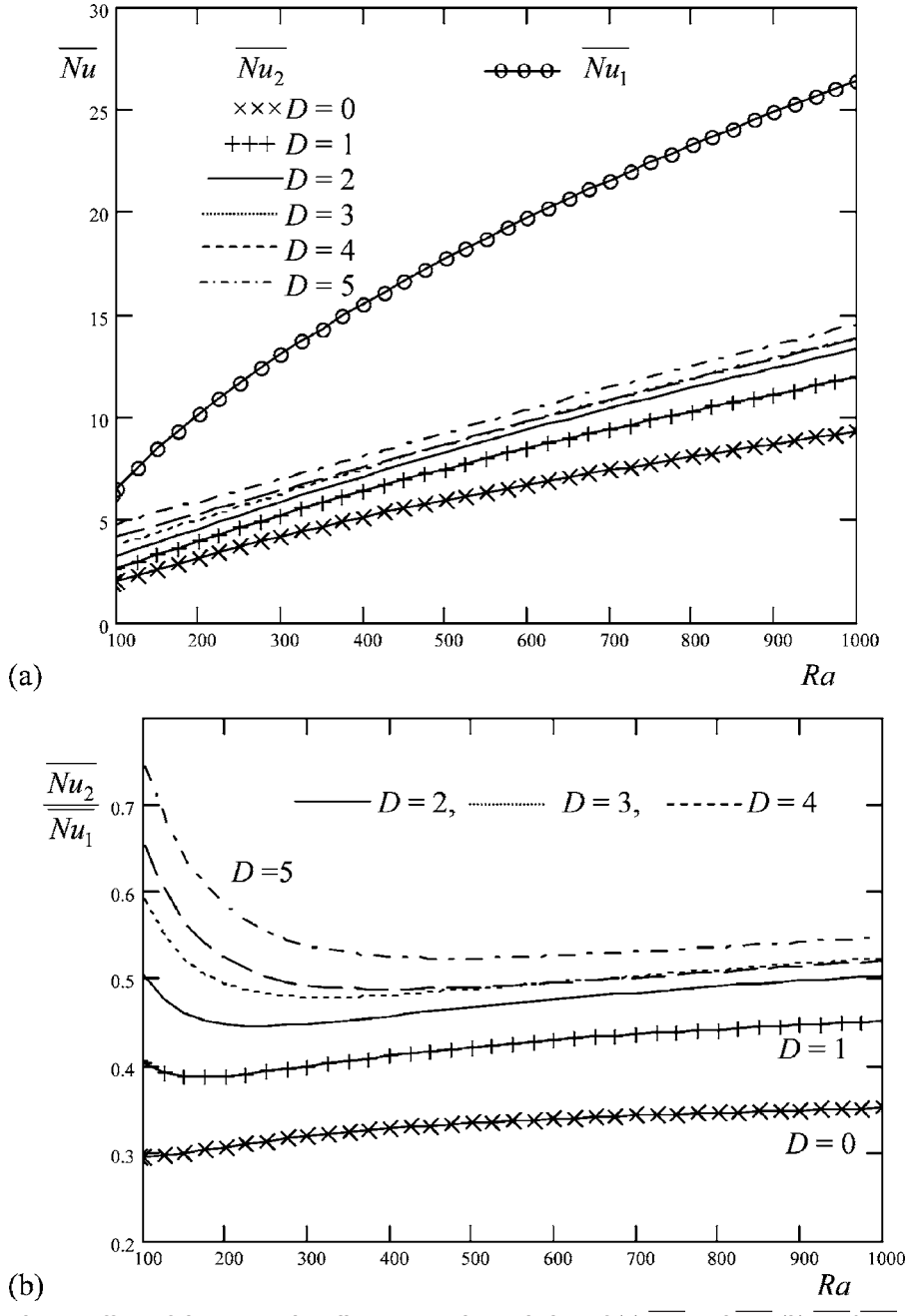

Fig. 2 Effect of the separation distance on the variation of (*a*) $\overline{Nu_1}$ and $\overline{Nu_2}$ (*b*) $\overline{Nu_2}/\overline{Nu_1}$, with Rayleigh number, for $L_2=1$ and $\Theta=1$

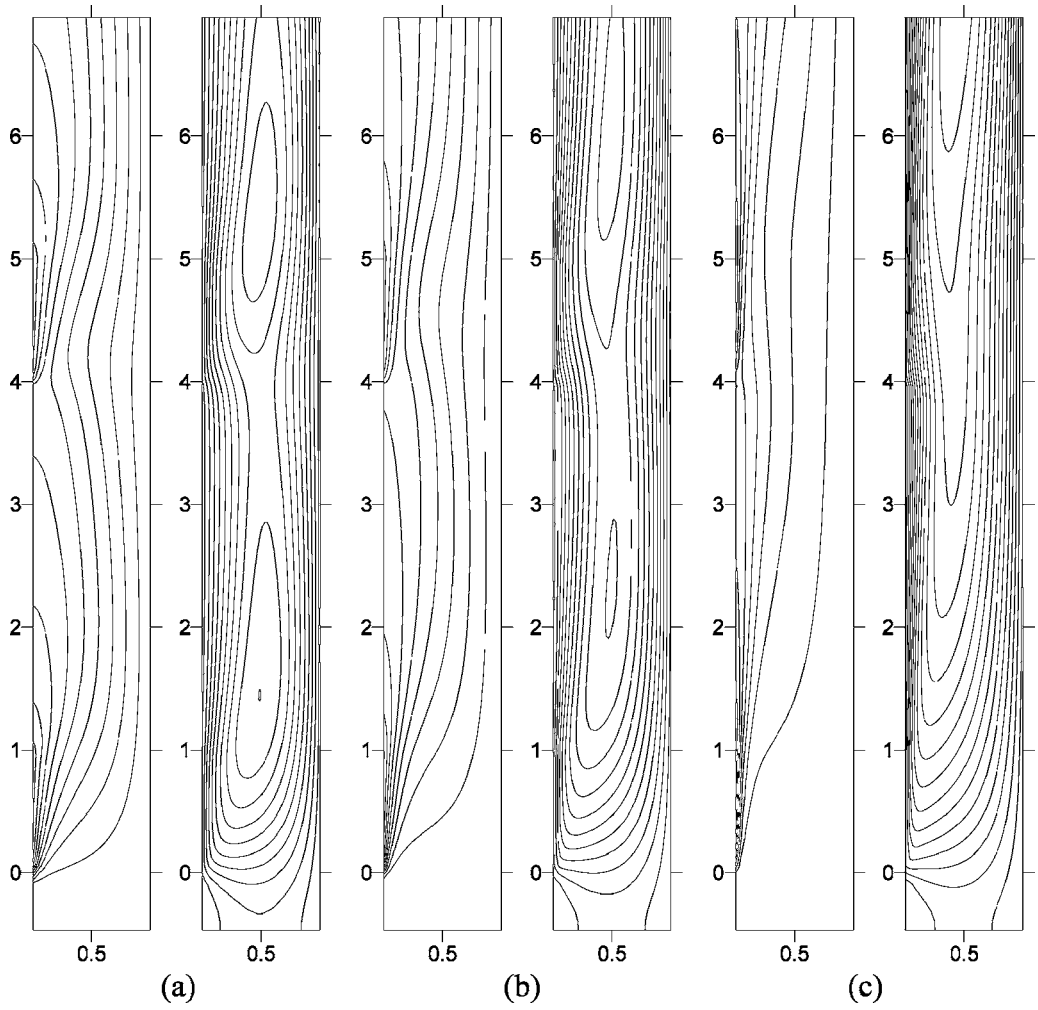

Fig. 3 Isotherms (left), stream lines (right) for L_2=1, Θ=1 and D=3: (*a*) Ra=100 ($\Delta\theta$=0.1, $\Delta\Psi$=1), (*b*) Ra=250 ($\Delta\theta$=0.1, $\Delta\Psi$=2), (*c*) Ra=1000 ($\Delta\theta$=0.1, $\Delta\Psi$=5) (only important region is shown)

$$\theta = \frac{T - T_\infty}{T_1 - T_\infty}; \quad \Theta = \frac{T_2 - T_\infty}{T_1 - T_\infty}; \quad \Psi = \frac{\psi}{\alpha} \tag{4}$$

together with nondimensionalization of all the lengths based on the length of the lower heat source (l_1) and denoting them by respective capital letters, leads to the following dimensionless forms of the governing equations:

$$\frac{\partial^2\Psi}{\partial X^2} + \frac{\partial^2\Psi}{\partial Y^2} = -\mathrm{Ra}\frac{\partial\theta}{\partial X} \tag{5}$$

$$\frac{\partial\Psi}{\partial Y}\frac{\partial\theta}{\partial X} - \frac{\partial\Psi}{\partial X}\frac{\partial\theta}{\partial Y} = \frac{\partial^2\theta}{\partial X^2} + \frac{\partial^2\theta}{\partial Y^2} \tag{6}$$

where Ra is the Rayleigh number for porous medium defined as $\mathrm{Ra} = g\beta K(T_1 - T_\infty)l_1/\nu\alpha$, and the dimensionless boundary conditions are

$$\Psi(0,Y) = 0; \quad \theta(0,Y) = 1 \text{ at } 0 \leqslant Y \leqslant 1; \quad \theta(0,Y) = \Theta \text{ at } (1+D) \leqslant Y \leqslant (1+D+L_2) \text{ and otherwise } \partial\theta(0,Y)/\partial X = 0 \tag{7a}$$

$$\Psi(L,Y) = 0; \quad \theta(L,Y) = 0 \tag{7b}$$

$$\partial\Psi(X,-S_1)/\partial Y = 0; \quad \theta(X,-S_1) = 0 \tag{7c}$$

$$\partial^2\Psi(X,S_2)/\partial Y^2 = 0; \quad \partial\theta(X,S_2)/\partial Y = 0 \tag{7d}$$

The physical quantities of particular interest in this problem are the average heat transfer coefficients along the heat sources, defined by

$$\overline{h_1} = \frac{1}{l_1}\int_0^{l_1} \frac{-k}{(T_1 - T_\infty)}\left(\frac{\partial T}{\partial x}\right)_{x=0} dy \tag{8a}$$

$$\overline{h_2} = \frac{1}{l_2}\int_{l_1+d}^{l_1+d+l_2} \frac{-k}{(T_2 - T_\infty)}\left(\frac{\partial T}{\partial x}\right)_{x=0} dy \tag{8b}$$

where k is the effective thermal conductivity of the porous medium. From Eq. (8), the average Nusselt number along the heat sources can be calculated as

$$\overline{\mathrm{Nu}_1} = \frac{\overline{h}_1 l_1}{k} = -\int_0^1 \left(\frac{\partial\theta}{\partial X}\right)_{X=0} dY \tag{9a}$$

$$\overline{\mathrm{Nu}_2} = \frac{\overline{h_2} l_2}{k} = \frac{-1}{\Theta}\int_{1+D}^{1+D+L_2} \left(\frac{\partial\theta}{\partial X}\right)_{X=0} dY \tag{9b}$$

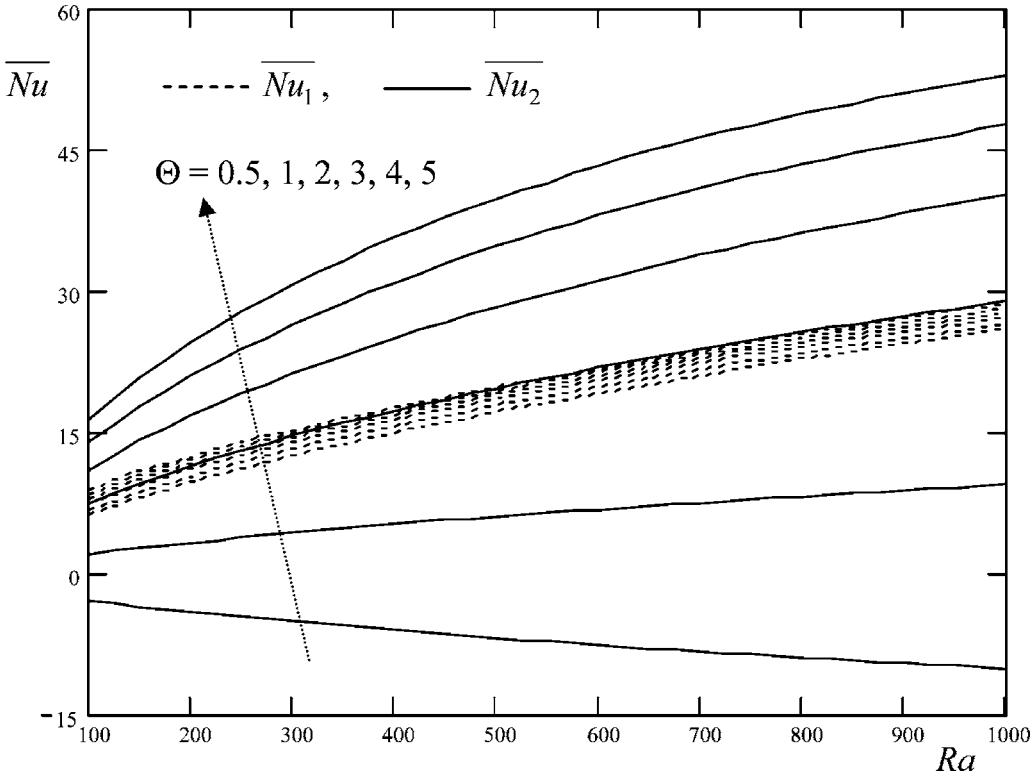

Fig. 4 Effect of the upper element temperature on the variation of $\overline{Nu_1}$ and $\overline{Nu_2}$ with Rayleigh number, for $L_2=1$ and $D=0$

Numerical Scheme

Equations (5) and (6) subjected to the boundary conditions (7) are integrated numerically using the finite volume method [17]. The central differencing scheme is used for the diffusion terms of the energy equation (6) as well as for the momentum equation (5). The quadratic upwind differencing QUICK scheme [18] is used for the convection terms formulation of the energy equation (6). The linear extrapolation, known as mirror node approach, is used for the boundary conditions implementation. The resulting algebraic equations were solved line by line using the tridiagonal matrix algorithm iteration. The iteration process is terminated under the following condition:

$$\frac{\sum_{i,j} |\phi_{i,j}^{n} - \phi_{i,j}^{n-1}|}{\sum_{i,j} |\phi_{i,j}^{n}|} \leq 10^{-5} \tag{10}$$

where ϕ is the general dependent variable which can stands for either θ or Ψ and n denotes the iteration step. In the present study, it is assumed that the width of the solution domain is equal to the heat source length, or $L=1$. The lengths on the upstream and downstream sides of the heat sources (S_1 and S_2), are taken as 0.5 and 15, respectively, to ensure the correct boundary conditions (7*c*) and (7*d*). The mesh size used is (30×250) along X- and Y-axis, respectively. The developed code is essentially a modified version of a code built and validated in previous work [19,20].

To check the accuracy of the present numerical method, the results of the present numerical scheme for the case of single heat source with different Rayleigh numbers were obtained and presented in Table 1. The average Nusselt number defined in Eq. (9) is calculated using the boundary and the next two grid values of the nondimensional temperature in the X direction. The grid independence test is performed for equal spacing mesh with two different sizes (30×250) and (60×500) for the domain defined above. The maximum difference in the results is found to be $<3\%$; therefore, the mesh size (30×250) is used to generate the results. Moreover, the value of $\overline{Nu_1}/\sqrt{Ra}=0.888$ is known from the similarity solution of the boundary layer equations based on the Darcy model of the present problem, which is found by Cheng and Minkowycz [21]. It can be seen from Table 1 that the value $\overline{Nu_1}/\sqrt{Ra}=0.888$ is approached at high values of Rayleigh number, where the boundary layer theory is applicable. These results provide confidence to the accuracy of the developed code for predicting the free convection along single heat source; therefore, it is used to generate results for the two heat sources.

Results and Discussion

For two heat sources, the results are generated to show the effect of the four governing parameters D, L_2, Θ, and Ra on the average Nusselt number along both the heated elements. The variations of the average Nusselt number with the Rayleigh umber, for wide range of the governing parameters are depicted in Figs. 2, 4, and 5.

The effect of the separation distance on both $\overline{Nu_1}$ and $\overline{Nu_2}$ is shown in Figs. 2(*a*) and 2(*b*) for $L_2=1$ and $\Theta=1$. It is found that $\overline{Nu_1}$ is not affected by D for the whole range of Ra since both the elements are kept at same temperature as shown in Fig. 2(*a*). The effect of the separation distance on $\overline{Nu_2}$ is clear and increasing the separation distance leads to increase in $\overline{Nu_2}$ for the whole range of Ra as can be seen from Fig. 2(*a*). The increase in $\overline{Nu_2}$ is more when D is increased from $D=0$ to $D=1$, than that obtained by increasing D from $D=1$ to other values for the whole range of Ra. It is evident that the fluid velocity and temperature around the isothermal upper element increase with decreasing D. The present results show that the increase in the velocity near the upper element, which is trying to enhance the heat transfer when the two

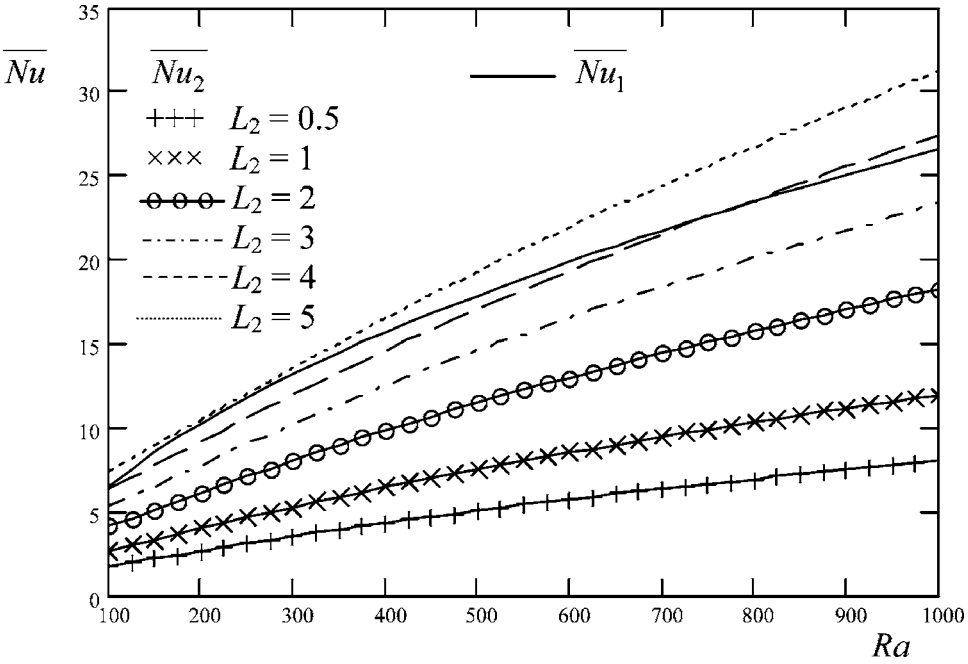

Fig. 5 Effect of the upper element length on the variation of $\overline{Nu_1}$ and $\overline{Nu_2}$ with Rayleigh number, for $\Theta=1$ and $D=1$

elements near each other, has less influence on $\overline{Nu_2}$ than the increase in temperature in the same region, which leads to reduce $\overline{Nu_2}$.

The effect of D on the ratio $\overline{Nu_2}/\overline{Nu_1}$ for different Ra is shown in Fig. 2(*b*). It can be seen from this figure that for small values of Ra the ratio $\overline{Nu_2}/\overline{Nu_1}$ increases with increasing Ra for $D=0$. It can also be seen that for $D=1$ to $D=5$, the ratio $\overline{Nu_2}/\overline{Nu_1}$ decreases with increasing Ra for small values of Ra, where the conduction mode is dominated as it is evident from Fig. 3(*a*). It reaches a minimum value at moderate value of Ra, when the convection currents start to play a role, as shown in Fig. 3(*b*), after which $\overline{Nu_2}/\overline{Nu_1}$ is increasing with Ra, when the convection mode is dominated as shown in Fig. 3(*c*). To check the accuracy of the results, the solution domain is enlarged to $S_2=30$ and the mesh size is increased to (30×500). The maximum difference found in the values of both $\overline{Nu_1}$ and $\overline{Nu_2}$ is $<0.6\%$, which indicates satisfaction of gradient boundary condition at the top boundary.

The variations of $\overline{Nu_1}$ and $\overline{Nu_2}$ with Ra are shown in Fig. 4 for different values of Θ and fixed values of $L_2=1$ and $D=0$. Figure 4 shows that $\overline{Nu_2}$ is lower than $\overline{Nu_1}$ when $\Theta=0.5$ and $\Theta=1$ for the entire range of Ra considered in the analysis. Negative values of $\overline{Nu_2}$ were observed when $\Theta=0.5$, which means that the upper heat source is receiving the heat (heat sink) even if its temperature is higher than the opposite vertical wall. In contrast to that, $\overline{Nu_2} > \overline{Nu_1}$ for $\Theta\geqslant2$ and for the whole range of Ra. It is important to note that Ra is defined based on the temperature and length of the lower element and the effective Raleigh number near the upper element is $Ra_2=Ra\times\Theta\times L_2$. Therefore, the increase in $\overline{Nu_2}$ with increasing Θ is due to increase in the value of effective Raleigh number near the upper element.

It is interesting to observe from Fig. 4 that $\overline{Nu_1}$ increases as Θ is increased. These results are of practical significance since increasing the temperature of the upper element can enhance the heat transfer from the lower element especially when the separation distance is small. For high values of Θ, the convection currents along the upper element will be developed and the buoyancy forces will work as suction forces on the fluid near the lower element causing the increase in $\overline{Nu_1}$.

Finally, the effect of the length of the upper heated element is studied. In this case, the temperature of the two elements are assumed to be equal and the separation distance is fixed at $D=1$. The results in Fig. 5 show that the variation of $\overline{Nu_1}$ with Ra is not effected by changing L_2 and it is similar to that shown in Fig. 2(*a*). On the other hand, $\overline{Nu_2}$ is increasing with increasing length of the upper element for the whole range of Ra as shown in Fig. 5. It is important to note here that the effective Raleigh number near the upper element Ra_2 is increasing with increasing length of the upper element, which leads to increase $\overline{Nu_2}$.

Conclusions

The natural convection flow, induced by two isothermal heated elements located on vertical plate immersed in a Darcian porous medium, is studied numerically in this paper. The full two-dimensional governing equations are considered instead of the boundary layer equations. In additional to the Rayleigh number, the effects of the separation distance between the elements, source temperature, and the length of the upper element on the heat transfer from both heat sources were investigated. Wide ranges of these governing parameters are selected, and their effects on the average Nusselt number along the lower and upper heated elements are presented. It is found that the heat transfer from the lower element is not affected by the presence of the upper element for the case when temperatures of both the elements are equal. The heat transfer from the lower element can be enhanced by increasing the temperature of the upper element due to suction effect especially when the separation distance is small. The average Nusselt number along the upper heated element is found to increase with the increase of any of the governing parameters.

References

[1] Nield, D. A., and Bejan, A., 1999, *Convection in Porous Media*, 2nd ed., Springer, New York.

[2] Vafai, K., ed., 2000, *Handbook of Porous Media*, Marcel Dekker, New York.

[3] Pop, I., and Ingham, D. B., 2001, *Convective Heat Transfer: Mathematical and Computational Modelling of Viscous Fluids and Porous Media*, Pergamon, Oxford.

[4] Gebhart, B., Jaluria, Y., Mahajan, R. L., and Sammakia, B., 1988, *Buoyancy-Induced Flows and Transport*, Hemisphere, New York.
[5] Jaluria, Y., and Torrance, K. E., 2003, *Computational Heat Transfer*, 2nd ed., Taylor & Francis, New York.
[6] Johnson, C. H., and Cheng, P., 1978, "Possible Similarity Solutions for Free Convection Boundary Layers Adjacent to Flat Plates in Porous Media," Int. J. Heat Mass Transfer, **21**, pp. 709–718.
[7] Bejan, A., and Khair, K. R., 1985, "Heat and Mass Transfer by Natural Convection in a Porous Medium," Int. J. Heat Mass Transfer, **28**, pp. 909–918.
[8] Cheng, P., and Pop, I., 1984, "Transient Free Convection About a Vertical Flat Plate Embedded in a Porous Medium," Int. J. Eng. Sci., **22**, pp. 253–264.
[9] Jang, J. Y., and Ni, J. R., 1989, "Transient Free Convection With Mass Transfer From an Isothermal Vertical Flat Plate Embedded in a Porous Medium," Int. J. Heat Fluid Flow, **10**, pp. 59–65.
[10] Murthy, P. V. S. N., Srinivasacharya, D., and Krishna, P. V. S. S. S. R., 2004, "Effect of Double Stratification on Free Convection in a Darcian Porous Medium," ASME J. Heat Transfer, **126**, pp. 297–300.
[11] Prasad, V., Lai, F. C., and Kulacki, F. A., 1988, "Mixed Convection in Horizontal Porous Layers Heated From Below," ASME J. Heat Transfer, **110**, pp. 395–402.
[12] Lai, F. C., Prasad, V., and Kulacki, F. A., 1988, "Aiding and Opposing Mixed Convection in a Vertical Porous Layer With a Finite Wall Heat Source," Int. J. Heat Mass Transfer, **31**, pp. 1049–1061.
[13] Lai, F. C., and Kulacki, F. A., 1991, "Experimental Study of Free and Mixed Convection in Horizontal Porous Layers Locally Heated From Below," Int. J. Heat Mass Transfer, **34**, pp. 525–541.
[14] Sparrow, E. M., and Faghri, M., 1980, "Natural Convection Heat Transfer From the Upper Plate of a Collinear, Separated Pair of Vertical Plates," ASME J. Heat Transfer, **102**, pp. 623–629.
[15] Jaluria, Y., 1982, "Buoyancy-Induced Flow Due to Isolated Thermal Sources on a Vertical Surface," ASME J. Heat Transfer, **104**, pp. 223–227.
[16] Jaluria, Y., 1986, "Mixed Convection Flow Over Localized Multiple Thermal Sources on a Vertical Surface," Phys. Fluids, **29**, pp. 934–940.
[17] Patankar, S. V., 1980, *Numerical Heat Transfer and Fluid Flow*, McGraw-Hill, New York.
[18] Hayase, T., Humphrey, J. A. C., and Greif, R., 1992, "A Consistently Formulated QUICK Scheme for Fast and Stable Convergence Using Finite-Volume Iterative Calculation Procedures," J. Comput. Phys., **98**, pp. 108–118.
[19] Saeid, N. H., 2004, "Analysis of Mixed Convection in a Vertical Porous Layer Using Non-Equilibrium Model," Int. J. Heat Mass Transfer, **47**, pp. 5619–5627.
[20] Saeid, N. H., and Pop, I., 2005, "Mixed Convection From Two Thermal Sources in a Vertical Porous Layer," Int. J. Heat Mass Transfer, **48**, pp. 4150–4160.
[21] Cheng, P., and Minkowycz, W. J., 1977, "Free Convection About a Vertical Flat Plate Embedded in a Porous Medium With Application to Heat Transfer From a Dike," J. Geophys. Res., **82**, pp. 2040–2044.